# Bored tunnel lining behaviour in discontinuous rock

## Case study: Railway tunnel in Middle-East

D. Dobrovinski

TU Delft

Royal HaskoningDHV
Enhancing Society Together

# Bored tunnel lining behaviour in discontinuous rock

## Case study: railway tunnel in Middle-East

by

D. Dobrovinski

to obtain the degree of Master of Science
at the Delft University of Technology,
defended publicly on Wednesday March 25th, 2020.


| | | |
|---|---|---|
| Student number: | 4512928 | |
| Thesis committee: | Dr. ir. W. Broere, | TU Delft, chair |
| | Dr. ir. D.J.M. Ngan-Tillard, | TU Delft |
| | Ir. K.J. Reinders, | TU Delft |
| | Ir. C.J. Lantinga, | Royal Haskoning DHV |
| | Ir. P.S. Jovanovic, | Royal Haskoning DHV |
| | Ir. G.R.N.G. Colard, | Royal Haskoning DHV |


An electronic version of this thesis is available at `http://repository.tudelft.nl/`.

TU Delft

Royal HaskoningDHV
Enhancing Society Together

# Preface

This research was initiated with the objective to prove my worthiness for a Master's degree from Delft University of Technology and in order to obtain the entitlement of being called a Geotechnical Engineer in the near future. However, this study would not result in the document as it is now, if I would have done this alone.

First of all, I want to thank God for surrounding me with people that supported me prior to and during the study. Not only did they accept my shortcomings, they also did everything in their power to guide me through the graduation period. Using their talents, sharing their ideas and their knowledge to make the best of it. Help me God, while applying the acquired skills and gained knowledge in this world as you would wish for us.

Bless you family and friends that stood by my side in this, in my opinion, sometimes prolonging and challenging period. Father Dimitri, thank you for your prayers and spiritual advice. Valentina, my beloved wife and life-time coach, the patience needed to hear me out and amplify me all the evenings knows no bounds. Father, you always supported and inspired me to obtain the best qualification by saying: "after your graduation you can become whatever you want, for my part a garbage man, as long as you want it". Mother, Mila, Polina, your warm reception on Sundays often felt like a real day off, especially during the weeks when I was so busy that I forgot what weekends were.

I want to thank my graduation committee from the university. Mr. Broere, several times you came up with excellent suggestions for the Plaxis models. Dominique, I'm grateful for your personal approach not only during the graduation, but also as the coordinator of the master Geo-Engineering. Whenever I had a question, Mrs. Reinders, you found time to get together and thoroughly discuss the matter.

Last but not least I want to express my appreciation toward my supervisors from Royal Haskoning DHV. Predrag, nobody could make me as enthusiastic as you did when you spoke about bored tunnels. Honestly, I didn't expect my graduation subject to be about bored tunnels initially. Carolina, you continuously gave me brilliant feedback on my reporting style to satisfy the academic staff. Gilles, the amount of effort that you put into this research is tremendous. Not only are you an exemplary international lead-engineer, you are a fantastic companion as well. Peter, you came across as a fair section manager, who made it possible for me to attend the World Tunnel Congress in Naples. Finally, I denote my gratitude to those who helped me along the way by sharing their expertise with me.

*D. Dobrovinski*
*Rotterdam, March 2020*

*Those who think they know something*
*do not yet know as they ought to know*

1 Corinthians 8:2

# Abstract

In a bored railway tunnel project in the Middle-East, difficulties in terms of ovalization, water leakages and settlement of several lining rings located in a fault zone were observed at the end of the construction stage. The present research attempted to find the cause for this lining behaviour. The determination of critical loading conditions, the application of the longitudinal beam model and the analytical and numerical modelling (in Plaxis) of a monolith tunnel lining in abrupt ground property transition were analyzed. Thereby, the global lining stiffness reduction due to joints was also considered.

The literature review led to the following expected factors that caused difficulties in the Middle-East case: the squeezing and submerged ground conditions, the rock mass disturbance and the improper backfilling of the rings. Additionally, the ring stiffness reduction due to joints was an essential factor for lining behaviour.

The geotechnical conditions, the lining design and the observed difficulties in the case were defined in the next section. Critical missing information, such as geotechnical properties of the fault zone material and limited monitoring data, led to essential assumptions. The settlements were expected to be caused by rock mass disturbance and improper backfilling. These altered the water flow during and after the boring operations and led to lowering of the groundwater level and increase of effective stresses. The water leakages were caused by ring ovalization in the soft fault zone, leading to opening of joints.

The analysis for this research was divided in 2D transversal, 2D longitudinal and 3D modelling of the lining in and around the fault zone. The 3D model was seen as the integral model, which took into account the transversal and longitudinal behaviour of the lining. However, most of the behaviour of the lining was analyzed by carrying out parametric analysis for both directions in 2D. Moreover, the 2D models were used to validate the results of the 3D model to identify the influence of the third dimension.

The assessment of the results from these analyses led to the following conclusions. The behaviour of the tunnel lining in small width fault zones was governed by the transversal action. The ovalization was mainly influenced by the ground stiffness, the vertical to horizontal stress ratio, the backfilling stiffness and the ring stiffness. Using Erdmann's analytical solution, the approximate lining forces can be determined. However, this overestimated the ground pressures acting on the lining, especially in cases where vertical to horizontal stress ratios were not equal to 0.5. This was because the 2D transversal behaviour did not take into account the longitudinal arching effect, which depended mostly on the stiffness ratio between ground types. The final conclusion was that the global reduction of lining stiffness due to the joints led to a discrepancy with regard to the distribution of the longitudinal displacements. A complementary analysis using a numerical model taking into account the joint structure and discontinuous behaviour between rings would probably allow a better prediction of longitudinal displacements.

# Contents

# 1 Introduction

In this chapter the research background, the objectives, the research questions, the study methodology, the relevant case facts and the report outline are presented in the mentioned order.

## 1.1. Thesis background

The traditional TBM's developed by marketleader Herrenknecht AG were the open mode ones, which main purpose was to cut through (relatively) hard rock in dry conditions. Driven by the need for TBM's in weaker rock masses and soils, came the concept of closed mode TBM's (DAUB, 2010). The open mode shields cannot provide a full face support and therefore gain their advantages in stable rock and unsaturated conditions. Whereas the closed mode provides full face support and holds out the groundwater inflow into the TBM.

In the past, the design of a bored tunnel alignment would generally be chosen in such manner that optimal ground and water conditions were found. If difficult conditions for the TBM would be encountered during desk study, one would shift the alignment to the least severe route. Nowadays, comparable challenges are counteracted by means of TBM enhancement instead of evading geological barriers. However, several case studies indicate that it would be valuable to have a closer look at the ground and lining behaviour in discontinuous rocks under critical conditions after lining installation.

This research was initiated based on observed difficulties in a railway tunnel project in the Middle-East, focusing on one particular section of the tunnel alignment located in a fault zone. At this location, excessive deformations of the tunnel lining were measured at the end of the construction stage in hardened backfill material. The available measurements, geotechnical and structural data made it possible to calibrate models of the tunnel lining in the fault zone. However, project information stayed confidential due to legal matters.

Based on this case, the thesis focused on the ground and tunnel lining behaviour in hardened backfill material in fault zones of unfavorable geotechnical environment. Simulations of the lining behaviour were made to understand the loading conditions prevailing on the tunnel, which required a three dimensional model to integrated both transversal and longitudinal models. The additional aim of this thesis was to find the critical loading combination(s) acting on the tunnel in fault zones.

## 1.2. Thesis objectives

The main objective of this thesis was to understand the behaviour of the lining in fault zones with unfavorable conditions in hardened backfilling material. A fault zone is defined as a fracture in rock conditions with displacement of the rock mass along the fault plane (Waltham, 2009).

In this research, the quantification of the behaviour of the lining was mainly looked at in terms of stresses and displacements. The ground behaviour was in the form of i.a. failure modes, potential to be activated, which as a result would act on the lining. It was inevitable to identify the aspects of the boring process that influenced the behaviour of the ground and therefore the tunnel lining.

Besides the loading conditions of the ground surrounding the tunnel lining, there were other loads that could have acted on the lining. For instance, jacking forces resulted from the advancement of the TBM could have a significant influence on the lining stress distribution (as described by Blom, 1995). All loading conditions relevant to the stage at the end of the construction phase were carefully taken into account. Prior to this, the lay-out of the lining, joints and the types of lining deformation were investigated.

The loading conditions mentioned earlier were an important part of the input for the design of a lining. Several analytical closed form solutions and a numerical model to calculate lining forces and displacements were investigated to gain knowledge about their applicability.

This study focused on the application of Plaxis, due to its wide availability and progressive character in the field of geotechnical engineering. The relevant constitutive models to find the expected ground behaviour, the lining design and interface modelling were investigated.

A clear overview of the subjects that were out of scope for the present research led to a restricted literature study. The following subjects were out of scope:

- Lining other than segmental lining, such as shotcrete or insitu casted concrete lining;
- Seismic design analysis, e.g. active faults, based on geophysical measurements in the case;
- Rock in unsaturated conditions;
- The focus for this research was the lining behaviour after the backfill material was hardened [1];
- Ultimate Limit State, the focus was on the displacements and serviceability (SLS) rather than the failure mechanism of the lining.

In the following section the research questions are illustrated. Answering these questions leads to an achievement of the main objectives.

## 1.3. Research questions

To achieve the research objectives the main research question was formulated as:

*What is the behaviour of a segmental bored tunnel lining in hardened backfill material in fault zones between different unfavorable geotechnical units in saturated rock formations at the end of the construction phase?*

To answer the main question properly and based on the earlier mentioned objectives, the following sub-questions are introduced:

1. Which critical conditions, specifically in the Middle-East case study, make a bored tunnel construction difficult?
2. What are the available analytical and numerical methods to design tunnel linings, specifically in and around fault zones?
3. Can the stress and displacement distribution around and of the tunnel lining in and around fault zones under critical loading combinations be reliably modelled in Plaxis?

To provide pointed guidance to answer the research questions, the methodology for this research is presented in the following section.

[1] Aspects from the construction phase that could have influenced the final phase were considered. Parameters needed from the construction phase were obtained based on available data and simple calculations

## 1.4. Research methodology

For each subquestion, there were certain factors to be analyzed. These made it possible to answer the subquestion comprehensively. It was necessary to define the:

1. 
   - present fault zone, potential failure mechanisms and loading conditions on the lining in the case;
   - difficulties with the lining that occurred in the case;
   - influencing factors of the boring process on the lining and the difficulty for the case specific conditions;
   - potential failure mechanisms of the ground and loading conditions on the lining to occur at the end of the construction phase in hardened backfill material.

2. 
   - conventional lining and joint design and the applied design in the case;
   - method to schematize and calculate failure modes of the lining at the end of the construction phase in hardened backfill material;
   - method to calculate stresses in the lining and displacements of the lining consequent to potential loading conditions.

3. 
   - modelling technique(s) for different loading conditions, lining and interfaces in the case;
   - normative loading conditions in the fault zone and adjacent rock in the case;
   - stresses and displacements distribution in transverse and longitudinal direction of the tunnel alignment consequent to potential loading conditions;
   - discrepancy between analytical and numerical calculations and measurement data.

In the following section, the case facts for the Middle-East project are presented.

## 1.5. Case facts

The considered case was a bored railway tunnel project in the Middle-East executed in the last decade. The tunnel alignment is almost 12 km long, of which 8 km was bored by means of a 10.04 m diameter Double Shield TBM and the rest by New Austrian Tunnelling Method (NATM). The geology in the concerning region mainly consisted of calcareous rocks. More particularly, the encountered rocks were dolomite, limestone, marl and combinations of these. Overall, the following geotechnical conditions were considered:

- High overburden, consisting of locations with over 200 m of rock above the lining;
- Large water pressures, measured water level of almost 60 m above the lining invert;
- Saturated conditions, measured rock mass permeability implied submerged circumstances;
- Fault zones, potential to be encountered according to study of geological maps;
- Karst or cavity formation, due to the dissolving property of limestone;

In spite of the acknowledgement of the above mentioned conditions, difficulties with the lining occurred in hardened backfill material during the construction phase. The lining of the main tube has an outer diameter of 9.7 m, consisting of 6 + 1 segments each having a width and thickness of respectively 1.6 m and 0.4 m. Particularly significant ovalization was observed, entailing leakages and having for consequence that the tunnel did not meet the clearance requirements. Notably, these difficulties occurred in a fault zone.

At least ten rings underwent ovalization, which substantiated that the fault zone consisted of a width of at least 16 meters. Furthermore, settlements of the lining were measured. Figure 1.1 shows the measured deformations (discontinuous line) with respect to the designed position (solid line) of the most critical ring. The maximal vertical displacement and effective convergence of this ring are resp. 23 and 18 centimeters. The first and last ring that were measured have a convergence of 12 and 6 centimeters and a maximal vertical displacement of resp. 15 and 10 centimeters. Moreover, leakages were observed and water pressures were measured which confirmed the presence of a significant water level in the rock mass.

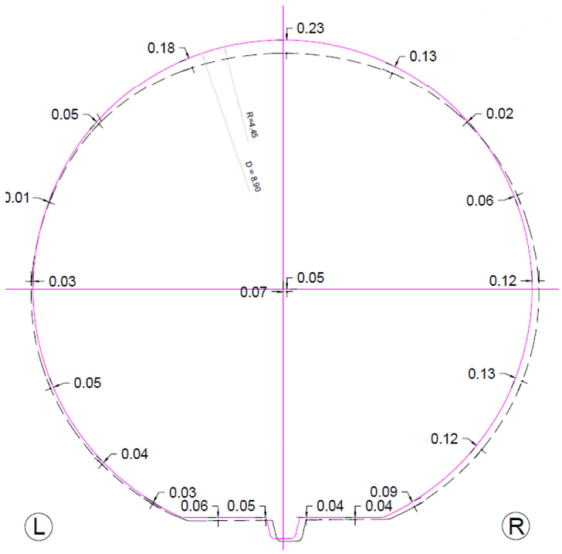


Figure 1.1: Deformed tunnel lining in the Middle-East case

To measure the present water pressures acting on the tunnel lining, inspectors drilled through the lining. During the drilling gauge it was observed that after full penetration of the lining, the drill end jumped beyond the lining until it was stopped by the inner part of the lining. This could have meant improper backfilling at the top, presence of very loose material above the lining or even a (karstic) cavity. As a result of the drilling activity, water gushed out of the hole under high pressure as shown in figure 1.2.

Figure 1.2: Water gushing into the tunnel in the Middle-East case

A top view of the fault zone where the deformed rings were observed is shown in figure 1.3 (red area). The upper section of the figure shows the geological profile as was encountered in the northern tunnel tube, while the lower part shows the geological profile as encountered in the southern tube. The southern tunnel tube, which was secondly executed, is the tube where excessive deformations were measured.

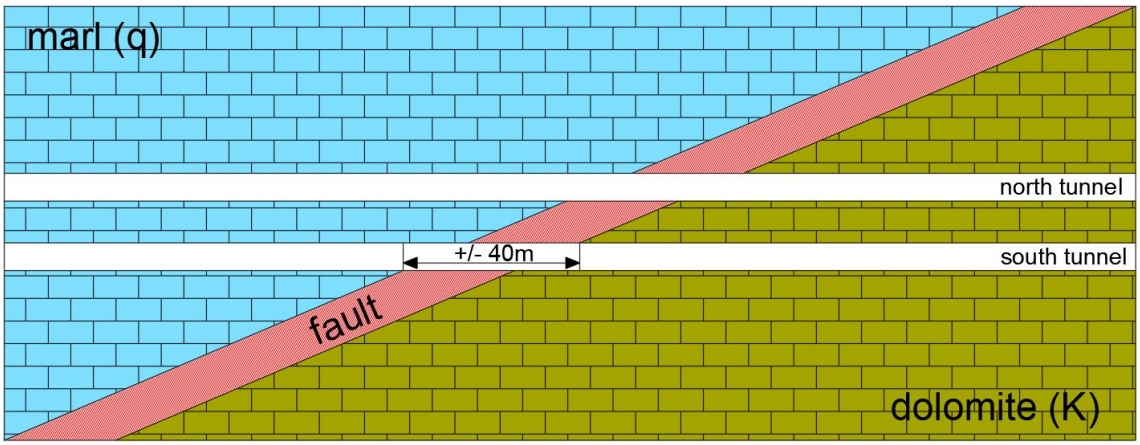


Figure 1.3: Identified fault zone from a top view where excessively deformed rings were measured in the Middle-East project

By investigating the particular case in the Middle-East, a calibrated numerical model based on measured deformations of the lining was developed. This model was used to further analyze the behaviour of the tunnel lining in the fault zone in the longitudinal direction. Based on obtained ground properties from the site investigations, the general potential ground behaviour was either squeezing, swelling or/and block fall. The prevailed mechanism(s) are elaborated in the analysis section of this research. More detailed case information is provided in chapter 3.

## 1.6. Outline of the report

This report presents the research of longitudinal behaviour of segmental lining of a bored tunnel in critical ground conditions based on the Middle-East case. Additionally, the critical loading combinations, with focus on longitudinal behaviour in geological fault zones, was examined. Specifically, the report consists of the following chapters:

- The **literature study**, which provides all important design aspects to obtain a representative model for the longitudinal behaviour and critical loading combinations of a tunnel lining. This starts with an additional study of concerning rock mass properties and behaviour, followed by an overview of the aspects of the boring process which influence the lining design. After this, the lining design with some applicable analytical solutions to verify the numerical model is studied in more detail. Finally, the relevant design features for the Plaxis models are presented.
- The **case study**, that is meant to present the specific properties and conditions of the Middle-East project. Hence, the general ground and water conditions as well as the tunnel lining design are summed up. Furthermore, the critical location where deformation measurements were obtained, with its geological profile, rock mass parameters and observed difficulties with the lining are described.
- The **analysis**, in which three analysis models, consisting of transversal 2D, longitudinal 2D and 3D model, are described. This includes the modelling assumptions, model geometry, sensitivity analyses, model calibration and validation.
- The **discussion of results**, where the results of the analysis are presented and discussed. Moreover, the limitations of the models are summed up in this section.
- The **conclusions**, which answers the previously mentioned research questions.
- The **recommendations**, in which certain modelling aspects for follow-up research are proposed.

# 2

# Literature study

The case specific information from the Middle-East project was concisely presented in section 1.5. Based on this, the literature study was restricted to the conditions relevant to the case. The literature study consists of description of rock mass behaviour, the boring process factor that could influence lining behaviour, the lining design and the numerical modelling of a tunnel in rock.

## 2.1. Geotechnical design

This section starts with a description of the specifications of a rock mass, which consists of the intact rock, discontinuities, weathering, classification index and stresses. Followed by the difficult conditions which were expected to be relevant to the Middle-East case and the failure modes, with clear illustrations of the different types of failure modes. The paragraph is concluded with an explanation of typical rock mass behaviour.

### 2.1.1. Rock mass

The definition of a rock mass is the total insitu bulk of rock containing different structural features, such as discontinuities and weathering (Brown and Brady, 2006). In this section the intact rock, discontinuities, weathering, classification index and stresses in the rock (relevant to the Middle-East case) are described.

#### Intact rock

A general description of **carbonate rocks** (such as limestone and dolomite), is that it constitutes of over 50% carbonate minerals (Bell, 1981). Figures 2.1(a) and 2.1(b) illustrate what limestone and dolomite looks like. Bell presented a classification of ranges of carbonate rocks where the largest induration is for a recrystallised rock, while the smallest is between a mudstone and a carbonate gravel (smallest and largest grain size respectively). Thick layers of limestone commonly serve as stable rock for construction works, while thin-bedded layers are more prone to dissolution activities (karst). Groundwater flow catalyzes dissolution of the carbonate rock. Commonly, the cavities are filled with soft deposits that run into the hole.

(a) (b)

Figure 2.1: (a) Illustration of a limestone; (b) Illustration of a dolomite

**Marl** belongs to the category argillaceous rock, in other words mudrock, with the prefix of being calcareous (Bell, 2000). As shown in figure 2.2(a) marl has components of a mudrock and of a calcareous rock. Depending on the ratio of clay and carbonate content in rock, it varies more towards limestone or mudstone. In figure 2.2(b) an illustration of marl is presented. The clay minerals, as shown on the left side of the figure, consist of illite and chlorite, while the rest are calcareous minerals as calcite and dolomite. Among these minerals, chlorite often shows swelling potential. When attempting to give a visual description, according to Goodman, marl is very fine-grained rock with traits of soft soil (Goodman, 1981). Moreover, marls are often highly fractured and subject to weathering as described by Bell.

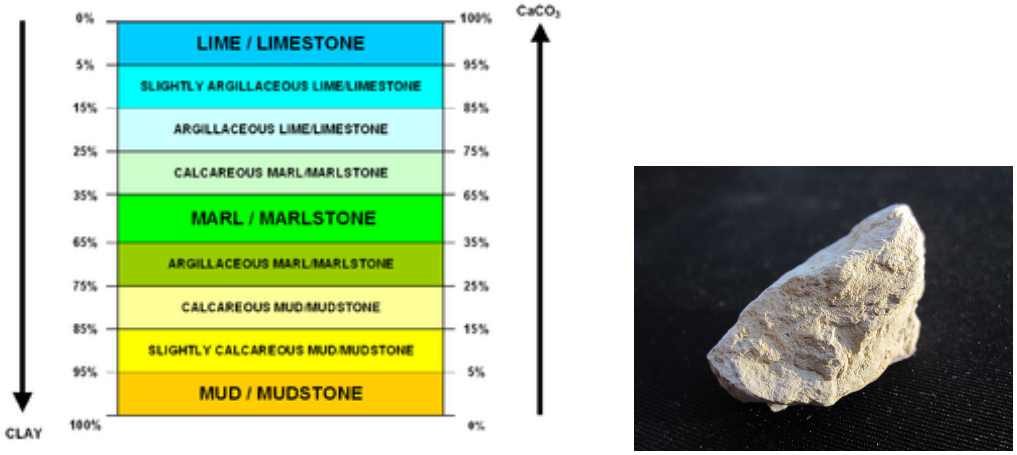


(a) (b)

Figure 2.2: (a) Distribution of carbonate and clay between limestone and mudstone;
(b) Illustration of a marl

## Discontinuities

A **joint** can be described as a fracture in the rock mass along which (almost) no displacement occurs (Bell, 1981). Joints have several properties that define their behaviour, which are orientation, spacing, persistence, roughness, strength, aperture and the filling material (as described in Zhang, 2016). The encountered fractures vary extremely (mentioned in section 3.2), for this reason only the fractures relevant to this research are described here.

A **fault** is a fracture along which adjacent ground layers are displaced deferentially with respect to each other. Faults can become transition zones as they are often not restricted to a clean break but can develop over a certain width (Bell, 1981). Faults can be of different type, such as: a normal fault, a reverse or thrust fault and a strike-slip fault. Relatively large displacements along the fault plane result in zones of crushed (often contains boulders) and/or weathered soil-like rock with various extensions (figure 2.3).

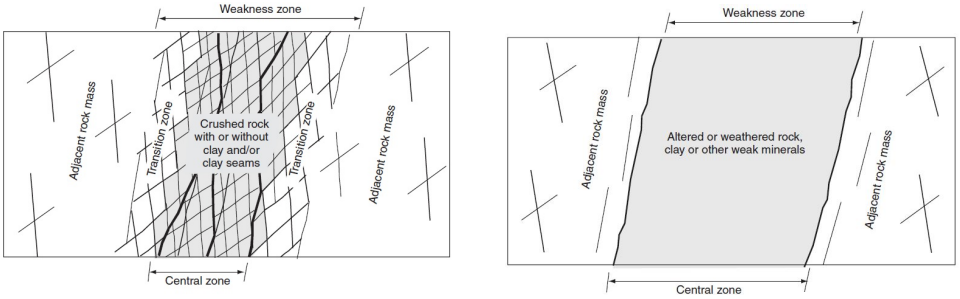


(a) (b)

Figure 2.3: (a) Fault zone with crushed rock; (b) Fault zone with totally weathered rock (from Palmstrom and Stille, 2014)

Fault zones can include various types of material, varying from strong to weak, such as angular fragments, recemented grains (breccia), rock flour or gouge material (which contains mostly clay) as mentioned in Price, 2009. In figure 2.4, illustrations of different types of weak and fault zone materials are shown.

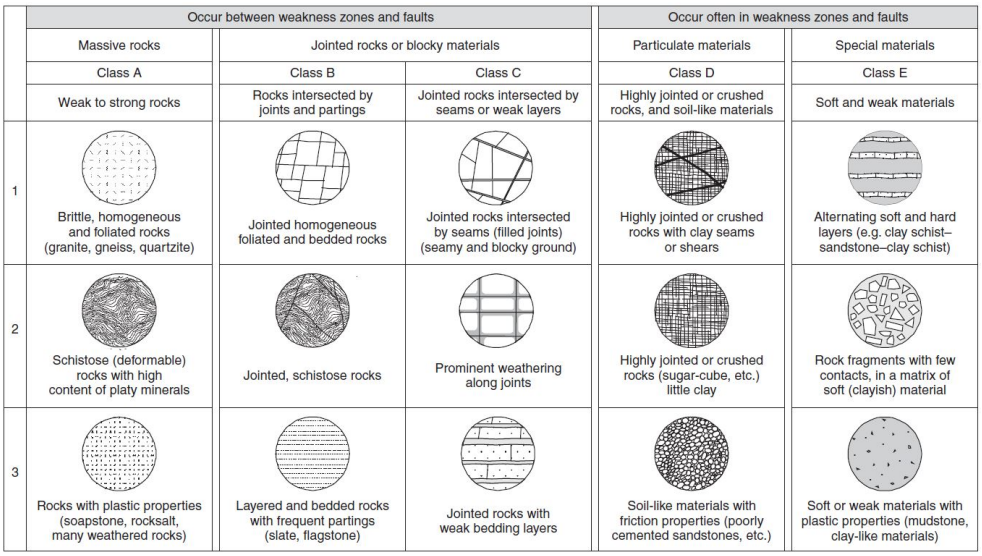


Figure 2.4: Illustration of different types of weak- and fault zone material (Palmstrom and Stille, 2014)

Due to the high variability of the different types of material it is hard to model the fault material as a homogeneous layer (which is often done to facilitate the modelling). Therefore, it is extremely difficult to estimate representative properties to the fault material. Not only the quantity of e.g. strength and deformability, but also drainage conditions and permeability the material are uncertain.

## Weathering

This describes a process in which alteration of the initial state of the rock mass occurs (Price, 2009). In general there are three different weathering processes that can occur, which includes organic, mechanical and chemical weathering. For instance, chemical weathering is a well known process in limestones (karst). Commonly, as was stated by Price, the weathering process has an impact on greatest part of the rock at shallow depth. Weathering processes occur in all type of environment, though it is strongest in hot and wet atmospheres.

Overall, weathering leads to the weakening of the rock mass which translates to the reduction of the rock mass properties. For instance, when comparing the engineering properties of a fresh / unweathered marl with a highly weathered marl, the decrease ratio may be a factor 10 depending on the considered parameter (example of values in tables shown by Bell, 1981). An even worse degree of weathering is when the rock is so weathered that the behaviour is comparable to residual soil. However, the weathering phenomena is generally captured by means of the rock mass classification indices (as described in Hudson and Harrison, 2000).

The complication with weathered rock is the possible variability over a quite small area and in the depth. Furthermore, a weathered rock will act more as a soil with increasing degree of weathering. This implies that it is harder to guarantee stability during the boring process, as well as the increment of ground pressure on the lining.

## Classification index

Due to the variability of discontinuities and the degree of weathering, a rock masses can as well be classified with an index. The most often applied classification indices are Deere's Rock Quality Designation (RQD), Bieniawski's Rock Mass Rating (RMR), Marinos' Geological Strength Index (GSI) and Barton's method (Q-value). These indices can be used to empirically estimate stresses and displacements due to an excavation, which are based on correlations with field data. To better understand the use of these parameters and the correlation between the parameters, one can refer to Zhang, 2016 and Singh and Goel, 2011.

Between most of the different classification indices correlations have been established (Bieniawski, 1973). A comparison between these classification methods RMR, GSI and Q is shown in figure 2.5. In the analysis, the GSI and RMR and their correlation will be used to predict the failure mode of a rock mass (section 4.2.1).

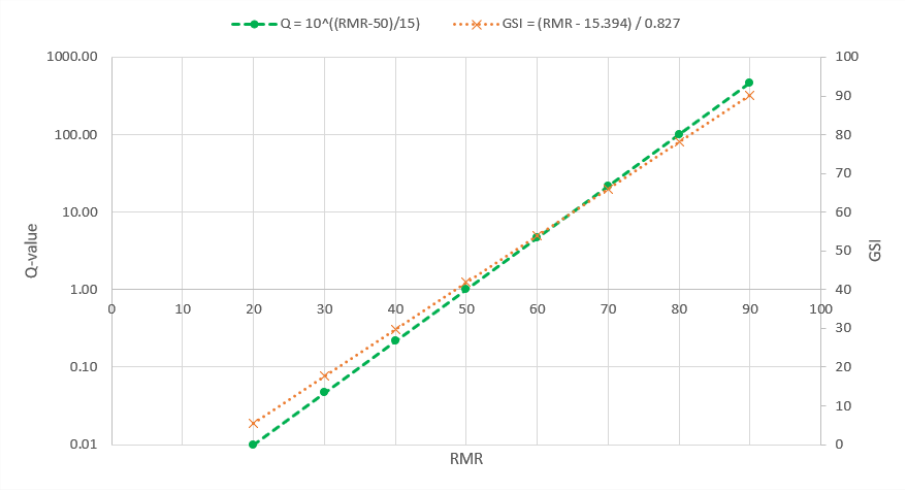


Figure 2.5: Example of a correlation between RMR, GSI and Q-values (Singh and Goel, 2011)

### Stresses

Stresses can be caused by gravity, tectonics, erosion or man-induced (Price, 2009). Generally, they are divided into vertical and horizontal stress. The lateral stress ratio (k), which is the ratio between horizontal and vertical stress, is often implemented to describe their relation. Vertical stresses are often unknown and estimated based on the static weight of the overburden thickness, while horizontal stresses derived from the vertical stress and an estimated stress ratio. Stresses next to fault often deviate from far field stress. The stress in the rock next to a normal fault (as in the Middle-East case), often has an active pressure ($k_a$) which differs from rock far away from the fault (as described by Price).

## 2.1.2. Difficult conditions

There are lots of difficult ground conditions that can be encountered in discontinuous rock during the TBM boring process. From Barla and Pelizza, 2000; Waltham, 2009 and Palmstrom and Stille, 2014, it can be concluded that the following criteria lead to difficult conditions:

- Excessively strong competent rock;
- Abrasive rock;
- Rock mass with high permeability;
- High overburden;
- High groundwater table;
- High temperature in the ground;
- Fault zones or other weak zones;
- High content of swelling minerals in rock;
- Dissolution of rock material.

Some particular conditions can be challenging during the boring process, rather than for the final design of the tunnel lining. Examples of these conditions are strong competent rock and high abrasiveness, which both can result in borability limits in terms of crushing the rock to allow further advancement and exceeding wear of the cutting tools. Several conditions or combinations of conditions can result in particular failure modes of the rock mass that are described in the next section. The purpose is to understand the conditions and failure modes that can occur after ring installation and hardening of the backfilling material.

### 2.1.3. Failure modes

In literature many different terms for the same failure mode can be found. Therefore the publication of Palmstrom and Stille, 2014, which seems to describe all failure modes in one document, is used for this research. Palmstrom divided the types of failure modes in three groups, namely gravity driven, stress induced and water influenced. The failure modes corresponding to these three groups are presented below.

Most of the previously mentioned failure modes occur immediately after excavation, with exception of rupturing, squeezing, slaking and swelling. These failure modes are typically time-dependent and can develop during an extended amount of time. However, slaking and swelling will only occur in under water conditions, while running ground occurs in dry sand or gravel which is not the case in the Middle-East project. Although, squeezing and swelling are often mentioned under one failure mode, those factors do not occur at once. Squeezing typically occurs in plastic rock containing clay-minerals with low swelling capacity, while swelling occurs in rock containing clay minerals with high swelling potential such as chlorite (as mentioned in section 3.1). As it is a continuation of slabbing and rock burst, the condition for rupturing is that either of these failure features should initially take place. Lastly, the buckling failure is a mechanism that happens in anisotropic rock.

By using graphs, correlations and empirical relations provided by literature, the conditions for the previously mentioned failures modes can be estimated. Singh presented conditions for different RMR-values of rock masses to be compared with the ratio between intact rock strength and in situ stress (Singh and Goel, 2011) and is presented in appendix A. Comparable research was done by Bhasin and Grimstad, only using the Q-values. Singh presented another empirical approach to predict squeezing conditions by using correlations with Q-values, the tunnel width and its depth. These correlations are used in the analysis (section 4) to predict ground behaviour for the Middle-East case. In figure 2.6 the different failure modes are illustrated to better understand their mechanism.

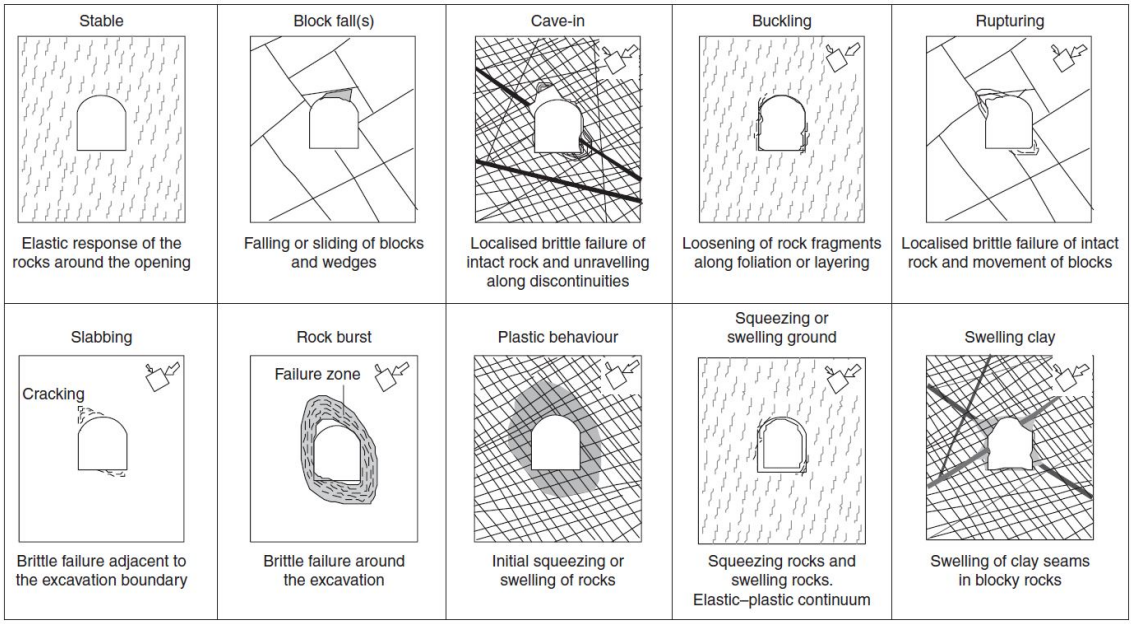


Figure 2.6: Illustration of different failure modes in certain rock masses as presented by Palmstrom and Stille, 2014

### 2.1.4. Behaviour

According to Hudson, rock is often modelled as a Continuous Homogeneous Isotropic Linear Elastic (CHILE) material (Hudson and Harrison, 2000). The validity should be questioned at all times and the explanation for this is explained in the following parts.

Depending on the randomness and degree of fractures in the rock mass, it can not simply be modelled as a **continuum** (Marinos et al., 2012). In case of predominating weak fractures, the rock mass might fail along these discontinuities. However, commonly the location of the predominant discontinuities are unknown. Therefore, implementing a non-continuous ground model can create apparent accuracy. Rather, the whole layer of rock can be modelled as continuous with a conservative reduction rate of the properties.

Moreover, rock is often embedded in a stratified manner, depending on its geological history. Therefore, it is not righteous to call it homogeneous material but rather **heterogeneous** material. Nevertheless, if appropriate division between layers is done, the material can be separately modelled using homogeneous geotechnical units. Comparable to the assumption of a continuous ground, the rock can be modelled with conservative parameters. Which in case of tunnel would be, amongst others, an increase in deformability.

Furthermore, a typical property of rock is **anisotropy**. For instance, laminated rock type (such as slate) is highly anisotropic. More specifically to this case, the valid property of limestone is isotropic behaviour, but for marls this is often not a righteous assumption (Saraglou and Tsiambaos, 2008). Due to the lack of knowledge about the possible anisotropy, it would create an apparent accuracy to assume a certain degree of anistropy. For this again, a safe decision is to choose conservative properties in all directions.

According to Carranza-Torres, rock behaves as an **non-linear elasto-plastic** medium rather than linear elastic (Carranza-Torres and Fairhurst, 1999). Depending on the strength of the rock mass, the available support pressure and the time of placement, a plastic zone around the opening with a certain thickness (BTS, 2004) can develop. This plastic zone actually represents an area around the opening which has failed, because the developed stresses exceed the strength of the rock. This plastic zone thickness can be calculated with Hoek and Brown parameters (Zhou and Li, 2011) as well as with other rock mass classification indices. This behaviour is shown in figure 2.7(a).

An interesting feature of the ground is that redistribution of ground stresses after tunnel lining installation results in an **arching effect**. This arching often leads to a reduced rock load acting on a deep tunnel, rather than the full overburden (introduced in Terzaghi, 1946). An illustration of the principle of arching is shown in figure 2.7(b). The rock load factor $H_p$ depends on the classification of the rock mass, which varies between weak highly fractured rock to strong competent rock.

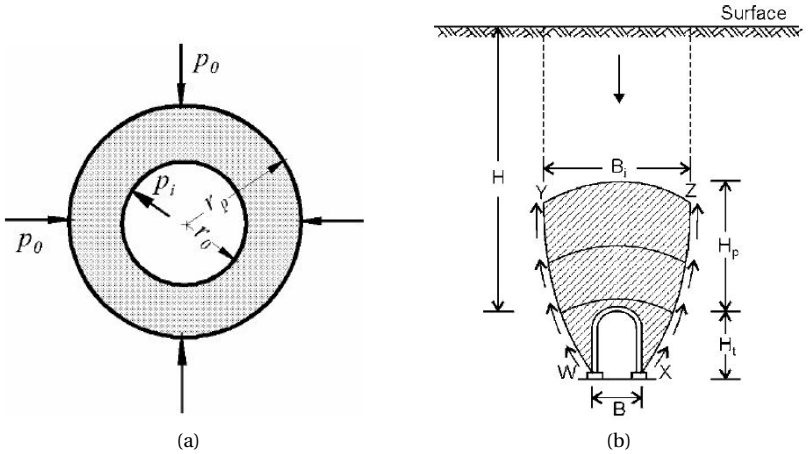


Figure 2.7: (a) Illustration of developed plastic zone in rock mass due to opening (Hoek et al., 2000);
(b) Illustration of Terzaghi arching theory with $H_p$ depending on rock mass classification (Terzaghi, 1946)

## 2.2. Boring process

In this section, more attention is given to the most important features of a bored tunnel during the final stage of the construction phase, with focus on specific features that influence the design of the tunnel lining. This includes the backfilling, the disturbance of the rock mass, the jacking forces acting on the lining and some ground improvement techniques to overcome particular unfavorable ground conditions.

### 2.2.1. General

The discontinuous rock mass in the Middle-East project was in submerged conditions in the area of study, which could have led to excess water inflow into the tunnel with an open shield TBM. The boring process with a TBM consists of the following stages (Maidl et al., 2012):

- Cutting = to make advancement into the rock mass possible an opening is cut;
- Advancement = advancement into the rock mass is done by hydraulic jacks (or grippers);
- Muck transport = extracted rock mass due to cutting has to be transported through the TBM;
- Placement lining = after advancement of the TBM the lining is placed behind it by a segment erector;
- Backfilling = after installation of a ring element, the overcut is filled with gravel and/or grout.

For this research, from the above mentioned five principles, particularly four are important for the design of a bored tunnel lining in the final stage of the construction phase. However, an additional principle is mentioned regarding the ground improvement before cutting. These are:

1. The boring process or **cutting** of the TBM leads to certain **disturbance** of the initial conditions of the rock mass. This is described in the section "Rock mass disturbance" that can be found below in section 2.2.2;
2. The **advancement** in which **thrust forces from the jacks** are transferred to the installed lining can lead to a so called longitudinal beam effect of the tunnel, while it consists of separate segments (Lengkeek, 1996). This mechanism is described in more detail in the sections below in section 2.2.3;
3. The **placement of the lining** is of significant importance for the distribution of forces within it. Small misplacement, in terms of rotated or displaced segments, can result in eccentric loading which generally leads to local peak stresses. These excessive stresses can result in damage of the lining, followed by leakages. However, the difficulties observed in the Middle-East case did not concern damage to the lining and therefore will not be considered in more detail in the literature review;
4. Due to the tapered shape of the TBM, the circular excavation presents an overcut. In other words, the excavated cavity has a larger diameter than the final lining in case of segmental lining. This overcut has to be compensated, or **backfilled**, to prevent deformations of the lining and surrounding rock mass. A more detailed description of this implementation aspect is given in section 2.2.4;
5. Additionally, in bad ground conditions it is possible to implement **ground improvement** techniques to reduce or even overcome unfavorable ground conditions during the boring process. These conditions can be unstable rock, weak zones (e.g. faults) or cavities (karst).

### 2.2.2. Rock mass disturbance

According to Marinos et al., 2012, the disturbance due to excavation by a TBM is compared to that of an excellent quality controlled blasting. In terms of Hoek and Brown parameters, this leads to a disturbance factor of zero (D = 0). This factor takes into account the loss of the interlocking between rock blocks, caused by the opening of discontinuities in a rock mass. However, even in intact rock cracks can develop, which happens when tangential stresses in the rock are larger than half the UCS value (Goodman, 1981).

Due to the tunnel excavation, often local rock failure occurs. This can be explained by the increased amount of joints, leading to the reduction of rock strength. Depending on the degree of disturbance to the rock mass surrounding the excavation whole, the tunnel cutting can cause a plastic zone around the opening (more detailed description of the plastic zone is given in section 2.1.4). Additionally, the increase of discontinuities due to rock mass disturbance, can lead to the increase in permeability. This increase combined with the excavated opening, can lead water flow towards the tunnel, acting as a sort of drainage (Singh and Goel, 2011).

### 2.2.3. Jacking forces

For the TBM to be able to move forward, thrust forces are applied to the cutter head combined with pushing forces against the lining that is already in-place. From the results of several measurements and researches, engineers found out that the thrust (normal) forces applied to the lining are almost fully directed and caught in the lining (Blom, 1995). Due to this pre-stress phenomena, the shear stiffness in the ring joints of the lining (figure 2.12) increases. Due to this increase in stiffness, the lining can be approximated as a whole or in terms of structural mechanics as a beam (Blom, 1995).

### 2.2.4. Backfilling

Tunnelling with TBM's leads to a circular annular gap. This gap is created due to an overcut formed by the TBM which has a larger diameter than the lining. The tapered shape and the design of the shield is shown in figure 2.8. The location from where this gap starts is directly behind the TBM shield. This gap has to be filled, to guarantee embedment, reduce settlements (of which 45% are long term deformations) and sealing the lining against (ground) water (Thewes and Budach, 2009). The backfill injection can be done either via grout lines in the tailskin or through holes in the segments. The backfilling material should also have the right properties to ensure outstanding pumpability, stability and prevent erosion of the ground. The embedment is needed to evenly distribute ground pressure from the adjacent ground onto the lining (BTS, 2004). Transmitting stresses improves with enhancing properties of a material, that is why the backfill material should have at least the same properties as the surrounding ground. Furthermore, the backfilling material does not have any strength requirements since it is not taken into account for structural stability (Maidl et al., 2008).

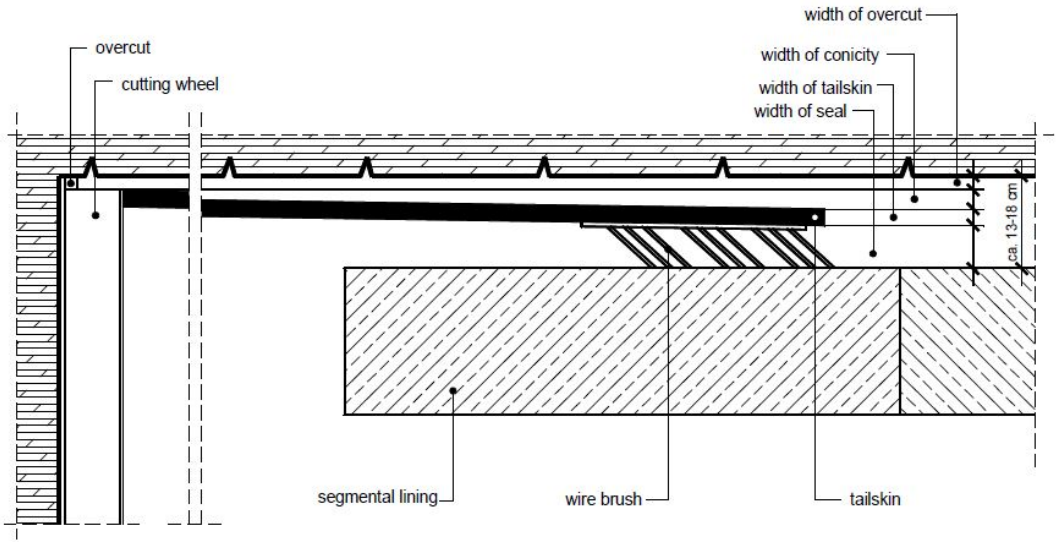


Figure 2.8: Illustration of detail of annular gap grouting behind TBM shield (Thewes and Budach, 2009)

In the application of open shield TBM's, typically pea gravel is used as backfilling material. The pea gravel is used to obtain excellent filling of the crown area, which is commonly hard to fill (Thewes and Budach, 2009). Another alternative, is to combine pea gravel with mortar. In the latter application, mortar is injected at the bottom of the overcut, followed by filling the rest of the gap with pea gravel under pressurized air through the segmental lining. The crown is completed with mortar because it is unfeasible to carry this out properly using gravel. In case of soils and weak rocks, the gap is fully filled with mortar under a pressure that is sufficient to overcome ground and water pressures (Maidl et al., 2012). Secondary injection of grout is most often necessary at 40 to 100 m distance behind the TBM.

However, one needs to take into account the fact that the gravel around the tunnel could function as a drainage layer for the fractured rock surrounding it, which in turn could increase the flow of water behind the lining leading to potential leakages. This can be prevented by injecting full round waterstopping material at certain distances along the tunnel alignment. Another solution to prevent unwanted water flow towards the tunnel is by systematic grouting of the gap and the rock mass surrounding the lining, with the help of grout injection (filling up joints with grout) using grout lances. An illustration of backfilling with pea gravel and grout is shown in figure 2.9.

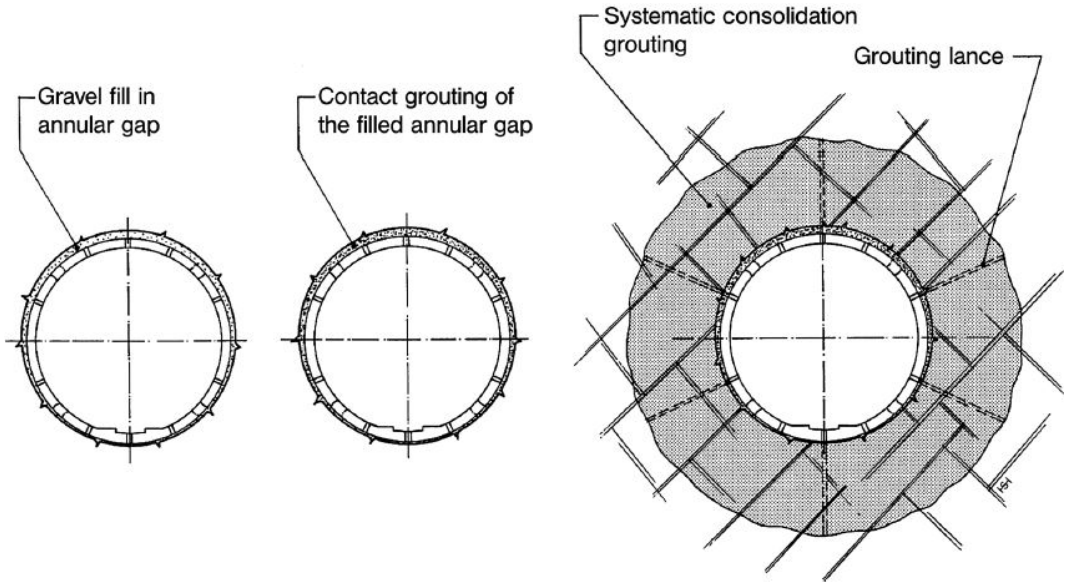


Figure 2.9: Illustration of backfilling material and grouting surrounding rock mass (Maidl et al., 2012)

### 2.2.5. Ground improvement

In poor ground conditions, ground improvement techniques are needed to make TBM tunnelling feasible or at least more efficient. Examples of poor conditions with corresponding control measures for deep rock tunnelling are:

- Loose or weathered (squeezing) rock. The zone of loose material can be pre-grouted to avoid collapses during tunnelling. This is done by bonding the particles together or in other words improving the quality of the rock mass (Maidl et al., 2013);
- Large rock blocks. These can be stabilized by means of rock bolt installation, which is done prior to tunnelling. This is also called forepoling (Price, 2009);
- Water inflow or high pressures. A mitigating measure for this is either draining out the water if possible, or filling the voids in the rock mass. This can be done with grout for a permanent solution or for a temporary solution by freezing a certain zone prior to tunnelling (Singh and Goel, 2011);
- Karst features. A mitigating measure is to fill the cavities or fissures with appropriate material such as grout (Maidl et al., 2013).

However, in reality the exact location of these poor ground conditions is not known. Therefore, probe drilling in front of the TBM face or exploratory tunnels are executed (Maidl et al., 2013). An illustration of probe drilling is shown in figure 2.10. The principle with probe drilling is to take ground samples at several distances and angles with respect to the shield front. Typically, a TBM with probe drilling tools can as well inject grout into these holes (figure 2.11(a)). This is done in stages, starting with short distance grouting, than grouting of the weak layer which was discovered during probe drills. If the TBM does not have probe drilling and grouting tools at its disposal, or the rock is not suitable for probe drills, one can cut a small service tunnel parallel to the bored tunnel to both investigate the ground material ahead of the TBM as well as improve the ground via freezing or grouting holes (figure 2.11(b)).

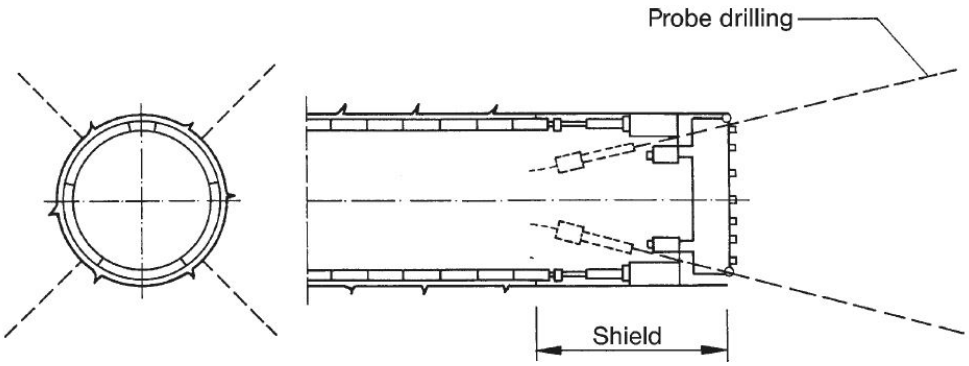


Figure 2.10: Illustration of probe drilling from a TBM in front of the face (Maidl et al., 2012)

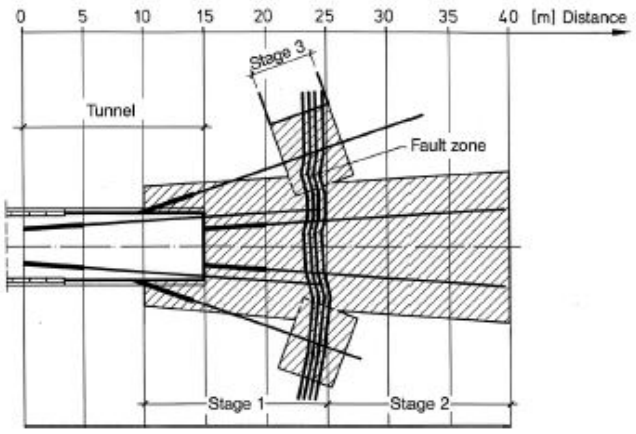


(a)

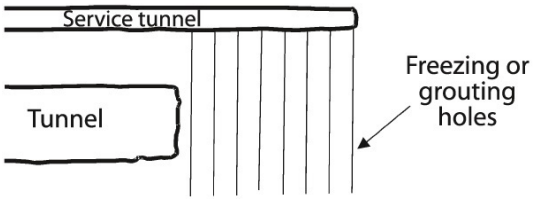


(b)

Figure 2.11: (a) Illustration of pre-grouting in a fault zone (Maidl et al., 2012);
(b) Illustration of exploratory/service tunnel to freeze or grout ground (Price, 2009)

## 2.3. Lining design

The tunnel lining serves as support for the surrounding rock mass (when the rock mass is not self supporting), water pressures and as abutment for thrust forces coming from the TBM (Maidl et al., 2012). In this section, the different features of the lining design are presented, mainly in terms of the lining lay-out, joints, loading conditions, failure modes and different closed form solutions to calculate stresses and deformations of the lining.

### 2.3.1. Lay-out

The typical attributes for a lining are the diameter, thickness, width, the amount of reinforcement, the amount of segments in a ring and the shape of the segments. The general definitions used for segmental lining are illustrated in figure 2.12.

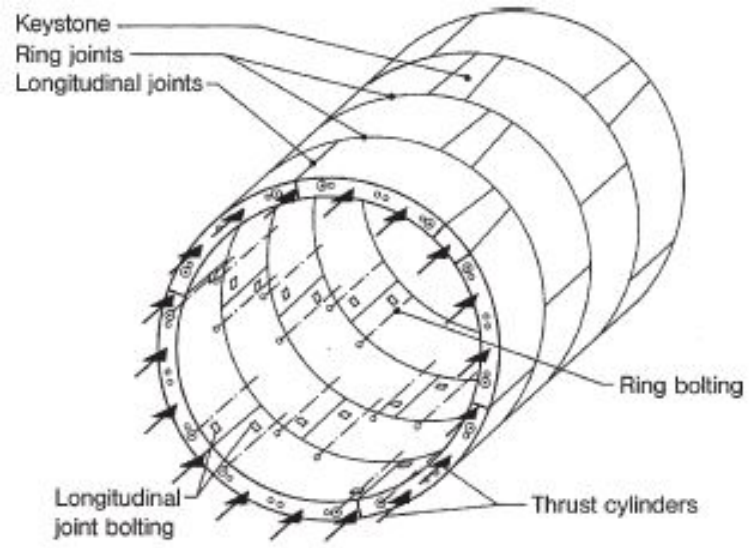


Figure 2.12: Presentation of definitions used for segmental lining Maidl et al., 2012

- The **diameter** of the lining is most commonly a given input, which depends on the clients requirements. Among others, the requirements are the design capacity for traffic intensity and the free space profile of the tunnel.
- Maidl states that the lining **thickness** is mainly determined by the needed capacity and area to transfer thrust forces from the TBM. Additionally, an enlarged tunnel diameter requires a thicker lining for structural capacity, leading to diameter - thickness dependency. However, Blom demonstrated that the normative load is the grout pressure that pushes on the tunnel during the boring process (Blom, 2002). This is only in case of closed shield TBM's in submerged conditions (water pressure is obstructed by the grout pressure). In the past the lining was designed on ground pressure, which is why many analytical solutions were developed in the 80's and 90's. However, this study focuses on the extreme loading conditions from the ground and water, which are later compared to thrust forces. Typically, the thickness of the lining segments varies between 20 to 60 cm.
- The **width** of the segments should be as large as possible to decrease the number of segments (reduction of transport, faster tunnelling and reduction of joint lengths). However, this is limited by structural damages due to more concentrated loading of the lining segments (from production and installation deflection), as well as by the increased thrust forces necessary for a longer drive length needed per segmental ring. Another reason to limit the width of the segments, could be the practical aspect to fit cross passages at a prescribed distance (Mortier et al., 2018). The normal magnitude of lining width is between 1.0 to 2.0 m.

- Segments can be divided into **shapes** with flat ring joints or staggered ring joints. Within the segments with flat ring joints, distinction is made between tapered and parallel rings. Typically, block segment rings contain several segments (from five to eight) with an additional smaller one (key-stone) that is installed as the final segment (figure 2.12). The main differences between the type of segments are:
  - The guarantee of watertightness (block segments);
  - The rigidity of the tunnel tube as a whole (hexagonal segments);
  - Optimization of ring assembly, with guiding rods and jointing dowels (rhomboidal/trapezoidal segments);
  - The need for backfilling in dry ground (expanding ring);
  - The ability to reduce stresses acting on the ring by convergence (yielding lining).

### 2.3.2. Joints

As shown in figure 2.12 the tunnel lining consists of longitudinal and ring joints. The actual sealing is provided by rubber gaskets in the joints, which are compressed and create watertightness of the tunnel. The longitudinal joints are compressed by means of ground and water pressures. The ring joints are pressurized as a result of jacking forces, which can be unevenly distributed. To allow for the efficient distribution of the forces, packing material (kaubit or plywood) is often used. However, most of the contact in the joints is concrete to concrete. The types of available joints are concisely described below and shown in figure 2.13.

#### Longitudinal joints

- Flat contact can transfer axial and shear forces as well as bending moments based on friction between the segments;
- Convex-convex contact provides larger compressive strength, but additional measures for stability during installation are necessary;
- Convex-concave contact provides greater stability during installation, but increases risk of spalling;
- Tongue and groove has the risk for spalling due to small inaccuracies, while assembly guidance is advised.

#### Ring joints

- Flat joint can be implemented with or without additional connection (e.g. bolts);
- Tongue and groove, like with longitudinal joints (convex-concave and tongue and groove), have a large risk of spalling in case of inaccuracies. It provides increased mechanical coupling;
- Cam and socket is a principle comparable to the tongue and groove. However, the loading is even more concentrated due to local coupling by means of the cam and socket system;
- Additional connection can consist of temporarily or permanently installed bolts or dowels. Generally, it is temporary to assure stable connections during the construction stage and removed after grout is hardened. In case of permenantly needed connections, they must be secured against loosening and protected against corrosion.

Most commonly, the flat contact joints are implemented. For this reason, taking into account the geotechnical engineering objectives of this research, the joints that will be implemented in the model are flat contact joints.

## Joint behaviour

Generally, joints result in a decrease of rigidity (stiffness) of the tunnel as whole. To take into account the behaviour of joints in a structural calculation of the lining, different theories are developed. Two of these, being relevant to this study, are described concisely below.

*Ring joints*

Based on measured stresses in the rings in the second Heinenoord tunnel, it has been demonstrated that jacking forces are conducted in the longitudinal direction and result in prestressing of the rings (van Oosterhout et al., 1999). This leads to additional coupling between rings when adjacent rings experience uneven internal or external loading distribution. The friction that prevents relative displacement between two adjacent rings is then translated into shear forces.

Van der Horst showed that the prestress effect leads to fully plastic behaviour of the packing material. The result of the plastic behaviour is pure concrete to concrete contact in ring joints during shearing (van der Horst, 1998). The concrete to concrete contact results in increased shear capacity to prevent differential displacement of rings (due to jacking forces leading to increased shear friction), resulting in a stiffer behaviour of the rings compared to individual ring analysis as traditionally done in a transversal 2D analysis. Moreover, Blom, 1995 analyzed the tunnel lining behaviour modelling it is an elastically supported beam, which can be modelled with beam theory of Bouma, 1993. Conclusively, this shows that tunnel lining behaviour is a 3D phenomena rather than 2D.

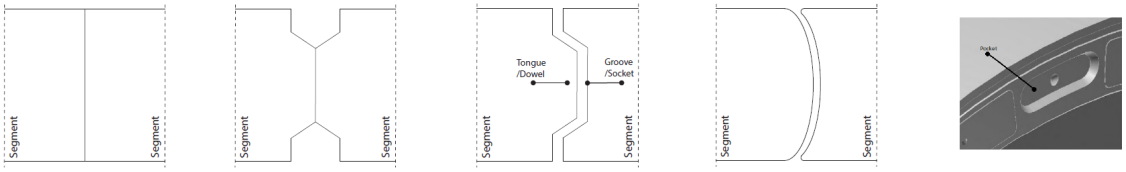


Figure 2.13: Illustration of several joint types, being from left to right: flat, reduced flat, tongue - groove, convex-concave and cam-pocket joints which has the same principle as the pin-socket (Kunst, 2017)

*Longitudinal joints*

The theoretical mechanical behaviour of longitudinal joints has been, amongst others, described by Janßen. The method of the calculation of the mechanical behaviour of joints is described in detail in Janßen, 1983 and the applicability is validated in the study by Luttikholt, 2007. This study concluded that the Janßen method is a realistic approximation of the joint behaviour.

In short, the Janßen relation represents the rotational stiffness of a joint that is modelled as a concrete beam (figure 2.14). Linear elastic material and full surface contact are assumed. No effect of additional reinforcement nor 3D-effect is taken into account. The beam cannot take into account tension forces and the joint dimensions are rectangular, with joint thickness equal to the joint height. When the joint rotates sufficiently, an opening is developed represented by a non-linear condition. The rotation of the joint depends on the active bending moment, the stiffness and the height of the joint.

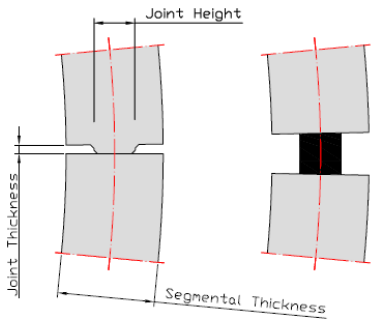


Figure 2.14: Illustration of assumptions for joint calculation by Janßen (Luttikholt, 2007)

### 2.3.3. Loading conditions

Different loading conditions are found in literature, for which the basic distinction is made between deep or shallow tunnels and between loose ground or solid rock. The loading conditions (found in DAUB, 2013; BTS, 2004 and ITA WG2, 2000) are described below:

- Ground pressure. Depends on the depth of the tunnel and ground properties. Stiffer ground results in less pressure (arching effect). The amount of transmitted shear stress depends on the interface bonding between the structure and ground. This can vary between slip (no shear transmission) or bond (full shear transmission);
- Water pressure. Depends on the inflow of water into the tunnel. More inflow results in a reduction of pressures. Fully sealed lining means the full water table acts on the lining;
- Subgrade reaction, which is the stiffness response of the surrounded ground delivered in case of ground - lining interaction;
- Self weight of tunnel;
- Construction loads, such as jacking forces. Jacking forces are (partly) permanent axial loads as described in section 2.3.2.

Because the objective of this research is focused on the final stage of the construction phase of the tunnel, the grouting pressure will not be taken into account. Other loads such as the adjacent tunnel and external loads such as Tunnel Technical Installations, car accidents or fire are assumed to be irrelevant to this study as well.

### 2.3.4. Deformation mechanisms

In this section some typical deformation modes are presented below and presented in figure 2.15 (more detailed information can be found in COB-L500, 2000). As the objective is to focus on the geotechnical behaviour and stress - displacement distribution of the lining, the deformation modes of the lining are of main interest in this research rather than the failure mechanism of the lining. The following modes are considered:

- Ovalization of lining, which typically occurs in non-isotropic stress distribution in the lining;
- Global ring displacement, which can be due to settlement or buoyancy (during liquid grout phase);
- Joint displacement, this can be elastic or elasto-plastic displacement depending on the stresses acting on the joint. This can lead to failure mechanisms such as shear buckling and snap through;
- Expansion or creep of the lining, generally as a result of temperature differences;
- Joint clearances, due to redundant tolerances in the joint interlocking.

The displacements depend, among others, on the subgrade reaction module of the rock mass, the amount of pre-stressing in the joints (resulting in shear resistance) and the deformability of the lining (including the reduction of stiffness due to joints). Buoyancy is not accounted for in this research, because the grout is assumed to be entirely hardened in the final stage of the construction phase.

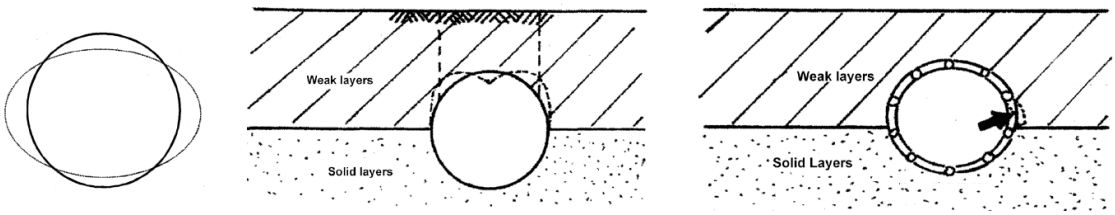


Figure 2.15: Illustration of different lining deformation modes, from left to right: ovalization, snap through and shear buckling (COB-L500, 2000)

### 2.3.5. Models

Before any Finite Element (FE) applications were developed, bored tunnels were calculated and designed manually. However, analytical and sometimes empirical solutions are used to verify the FEM results. In BTS, 2004 a distinction is made between design methods for tunnel lining in soft ground or massive rock and in jointed rock masses. These methods are shortly described in this section.

Typically, analytical solutions are implemented for soft ground and massive rock. Whereas for jointed rock masses, empirical methods are often implemented. As can be noticed, many authors have tried to estimate stresses and displacements of the lining with analytical solutions. The different type of solutions are divided in a continuum, bedded-beam, convergence-confinement, longitudinal bedded-beam and empirical model. The general principles of these models are shown in figure 2.16. The authors that have developed these models are:

*Continuum model (CM)*:
- Morgan, 1961;
- Wood, 1975;
- Curtis, 1976;
- Erdmann, 1983;
- Lo and Hefny, 1996;
- COB-L500, 2000.

*Convergence-confinement model (CCM)*:
- Einstein - Schwartz, 1979;
- Palmstrom and Stille, 2014;

*Bedded-beam model (BBM)*:
- Duddeck - Erdmann, 1985.

*Jointed rock, (semi-) empirical methods (EM)*:
- Bieniawski, 1984;
- Barton et al, 1974;
- Hoek et al., 2000.

*Longitudinal bedded-beam model (LBBM)*:
- Blom, 1995;
- Hoefsloot, 2009;

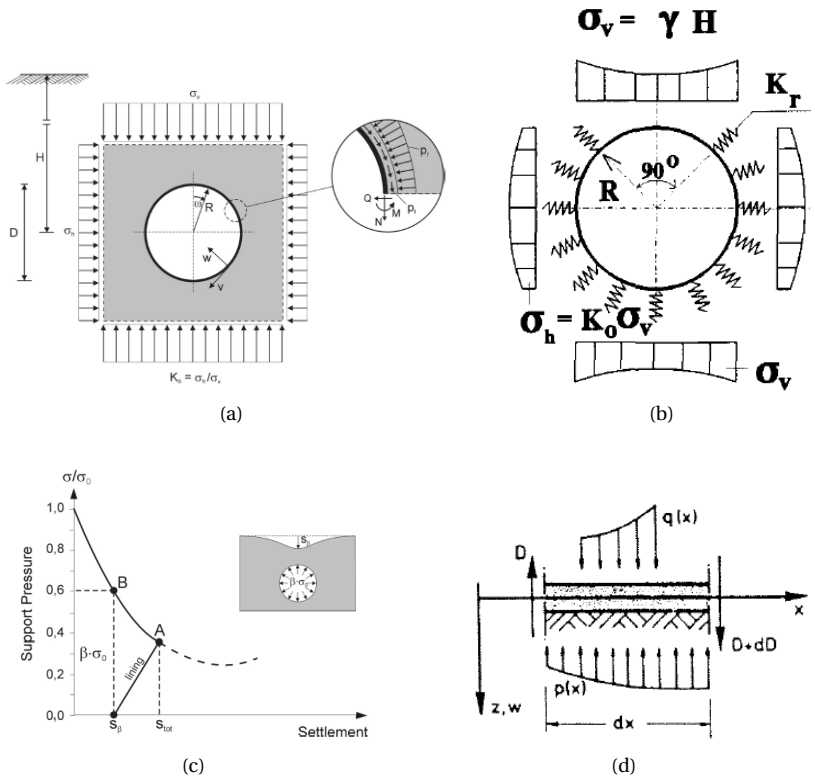


Figure 2.16: (a) Illustration of: continuum model (Möller and Vermeer, 2006), (b) Bedded-beam model (Jovanovic, 1995), (c) Convergence-confinement model (Möller and Vermeer, 2006), (d) Longitudinal bedded-beam model (Bogaards, 1998)

There are some main differences between these models, such as:

- The CM assumes a continuous distribution of the ground pressure and lining structure;
- The BBM discretizes the ground by means of springs;
- The CCM does not necessarily focus on the continuous or discontinuous distribution of ground-structure interaction, but takes into account the interaction between ground-structure response. In other words, the needed support and displacement of the ground depend on the extended pressures and displacements of the structure. The relaxation of the ground and delay in support installation can be taken into account in this model;
- The LBBM is an attempt to capture the longitudinal behaviour of the tunnel, by discretizing the ground in springs. With this solution, the lining is assumed to behave as beam, so that stiffness disparities or imposed differential settlements along the tunnel alignment can be taken;
- The EM is more commonly applied in NATM and open shield tunnels with a shotcrete lining. Therefore, the EN will not be implemented in this research, because of the preference to use analytical solutions for segmental bored tunnels.

The assmuptions and limitations that apply to the previously mentioned models are presented below:

- The lining is assumed to be purely elastic;
- The thickness of the lining is constant;
- The models take into account a homogeneous ground, which is not always the applicable in the Middle-East case;
- The stress state of the ground is equal to the initial stress state;
- Horizontal stresses are calculated in terms of $k_0$ principle;
- All the models calculate radial stresses in the lining;
- Models do not make a distinction of applicability for certain ground type (e.g. soft soil, sand or rock);
- All the models are assuming plain strain conditions, being parallel to the long. axis.

However, per author, there are differences in the assumptions of ground pressure, behaviour of ground, water pressure, ground-structure interaction, time effect, lining composition and the output. The assumptions per author are presented in table 2.1.

| *Solution* | $\sigma_v$ | $h_w$ | k | *gb* | *Interaction* | *Weight* | *Joints* | *M* | $\sigma_\theta$ | $\delta$ |
|---|---|---|---|---|---|---|---|---|---|---|
| Morgan | effect. | v | - | elastic | implicit[1] | - | - | v | - | input var.[2] |
| Muir-Wood | effect. | v | v | elastic | implicit[1] | - | v | v | v | input var.[2] |
| Curtis | effect. | v | - | elastic | slip-bond | - | - | v | v | input var.[2] |
| Erdmann | effect. | - | - | elastic | bond | - | - | v | v | - |
| Lo & Hefny | total | - | - | elastic | slip-bond | - | - | v | v | - |
| COB | total | v | - | elastic | implicit[1] | - | - | v | v | - |
| Einstein-Schwartz | total | v | - | elastic | slip | - | - | v | v | v |
| Palmstrom | total | - | - | plastic | slip | - | - | - | - | v |
| Duddeck-Erdmann | effect. | v | - | elastic | slip-bond | - | - | v | v | - |
| Blom/Hoefsloot | total | v | - | elastic | implicit[1] | v | v | v | - | v |

Table 2.1: Significant differences between several analytical solutions for a tunnel lining in terms of input and output, with v meaning the feature is considered and with - it is not

[1] the interaction takes into account either some implicit bonding between the surrounds and the lining or at least the subgrade reaction.
[2] the deformation of the lining is an input variable for the calculation of stresses in the lining.

Additional justification for the following parameters:

| | | |
|---|---|---|
| $\sigma_v$ | = | whether the analytical solution takes into account effective or total stress analysis for the ground; |
| $h_w$ | = | whether the analytical solution takes into account water pressures acting as a load; |
| k | = | whether the analytical solution takes into account the permeability of the ground; |
| *gb* | = | whether the type of ground behaviour the solution models is elastic or plastic; |
| *Interaction* | = | whether the analytical solution takes into account the interaction between the lining and the ground, in terms of bonding or subgrade reaction; |
| *Weight* | = | whether the analytical solution takes into account the weight of the lining; |
| Joints | = | whether the analytical solution takes into account the higher flexibility of the lining due to joints; |
| M | = | whether the output contains moment distribution in the lining or at critical points; |
| $\sigma_\theta$ | = | whether the output contains tangential stresses in the lining due to bonding; |
| $\delta$ | = | whether the output contains deformations of the lining. |

For this study, one solution is chosen to validate the results of the numerical ring models. The chosen solution is the one by Erdmann, which is quite simple and has proved its validity in practice over the many years of application (over 35 years). The Erdmann solution is explained in more detail in appendix F. The solution calculates normal forces and moments in the lining, based on an insitu stress in the ground and a deformability parameters (Young's modulus (E)).

## 2.4. Numerical modelling in Plaxis

One of the main objectives of this research is to model a tunnel lining in the most critical combination of rock mass behaviour in a fault zone in the final stage of the construction phase. The set up of the numerical model in Plaxis itself is described in this section 2.4. This will include the description of the dimensions and boundary conditions of the numerical model, the rock mass and the definition of lining properties.

### 2.4.1. General

A representative numerical model should be chosen depending on the type of ground one is modelling. This could be a Finite Element (FE), a Finite Difference (FD), a Discrete Element (DE) or a Boundary Element (BE) model (BTS, 2004). One model represents the behaviour of the ground and the structure better than the other. Usually, soft ground is considered to behave continuous and can be modelled with FE, FD and BE models. Moreover, discontinuous rock mass is sometimes best modelled using DE or BE to enable independent block movement. This knowledge has to be taken into account in the Middle-East case while using Plaxis to model the rock masses. The choice to use Plaxis is mainly based on its relevance worldwide.

### 2.4.2. Model

Each numerical model has a certain geometry, with its dimensions and boundary conditions. Depending on the distance necessary to minimize boundary effects, the geometry can be optimized to reduce the calculation time or the so called "running time". There are several rules of thumb to choose the width (X), height (Z), depth ($Z_0$) and length (Y) of the model as illustrated in figure 2.17. These dimensions typically depend on the radius (R) or depth ($Z_0$) of the tunnel. Some of these rules are proposed by the British Standard and in Möller, 2006. BTS suggests: Y = 15 R = 7.5 D. For deep tunnels Möller suggests: X = 4 à 5 D and Z = 1.3 à 2.2 D. However, no rules of thumb for $Z_0$ in the design of deep tunnels is provided. The general rule mentioned by Möller is that the upper boundary displacement should not surpass 1% of the center line displacement.

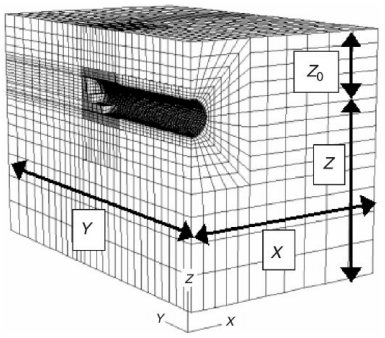


Figure 2.17: Illustration of model geometry to apply dimensions of model by means of rules of thumb (BTS, 2004)

Furthermore, the typical assumption for bored tunnels situated in a ground modelled as a continuum, is that the model is reduced to a symmetrical half space. This is due to the symmetric stresses and displacements of the ground and the lining as mentioned by Möller. This assumption leads to the boundary conditions as shown in figure 2.18.

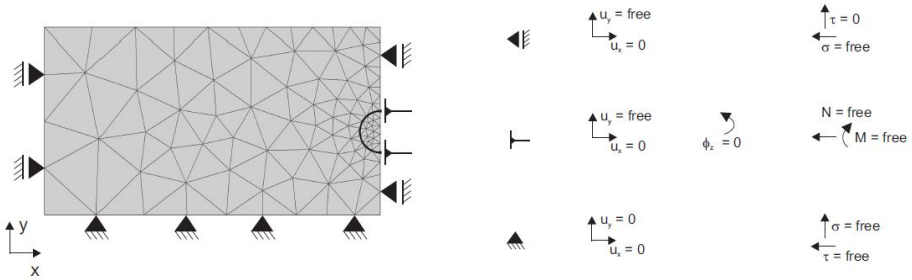


Figure 2.18: Illustration of boundary conditions in symmetrical half space model (Möller, 2006)

### 2.4.3. Material models

In general there are several types of rock masses, which can be divided into: (1) highly fractured / soil-like rock mass, (2) massive rock and (3) rock blocks. For these rock masses, the following behaviour is relevant to the final stage of the construction phase: (a) squeezing, (b) swelling and delayed (c) block fall. This section focuses on the description of constitutive models relevant to the previously mentioned rock masses and behaviour.

The most basic constitutive model is the **linear elastic (LE)** model, which does not involve any plasticity or non-linearity. This means no plastic potential has to be defined and the stiffness involves a constant Young's modulus.

The best known and most generally applicable constitutive model of the ground behaviour is the **Mohr-Couloumb (MC)** model. This is also known as the linear elastic perfectly plastic model. The main parameters are: the effective cohesion (c) and the effective angle of internal friction ($\phi$), as well as the Young's modulus (E), Poisson's ratio ($\nu$) and dilantancy angle ($\psi$). In the case the ground material can resist tension, there is the possibility to specify a tension cut off ($\sigma_t$). This model uses one stiffness parameter, independent on the state of stress. For undrained behaviour, the $\phi$ is set to zero and c is assumed to be equal to the undrained shear strength ($s_u$). The robust model gives a good first-order estimation of the soil behaviour.

In the case that one would favor considering material hardening behaviour, the **Hardening Soil (HS)** or **HS small strain model (HSsmall)** have been developed. The failure criteria are MC based with the possibility to adjust the stiffness of the material depending on the stress state. This is not possible with the traditional MC model and results in a non-linear stiffness distribution, whereas HSsmall can take into account the increased hardening (strain dependent) and generally well applicable for very small strains and in dynamic calculations. The additional parameters are $E_{50}$, $E_{ur}$ and $E_{oed}$. However, for the HSsmall model another two parameters make it possible to better estimate the strain-dependency of the ground which are $G_{0.7}$ and $\gamma_{0.7}$.

To model normally consolidated soft soils, the **Modified Cam Clay (MCC)** and **Soft Soil (SS)** models have been developed. In these models the failure criterion is again MC based. However, the MCC and SS models are stress dependent. The two models give the possibility to input the memory of pre-consolidation stress. An evolution of the SS model is the **Soft Soil Creep (SSC)** model, which takes into account the creep behaviour of soft soils, which is a stress independent increment of strains.

However, the previously mentioned constitutive models are typically implemented for modelling soils and not specifically for rock masses. There are models that are specified for the description of the behaviour of rock masses as well. These are the **Hoek and Brown (HB)**, **Jointed Rock (JR)** and **Swelling Rock (SR)**[1] models. The failure criterion of each of these models is MC based, though the following features are taken into account.

With **HB**, the non-linear stiffness of the rock masses depending on stress is adressed to by means of a hyperbolic distribution, is based on the Uniaxial Compressive Strength, the Geological Strength Index and the Disturbance factor. The HB criterion also takes into account the reduced tensile strength capacity depending on the classification of the rock mass.

The **JR** gives the opportunity to consider the anisotropy of rock and the stratification of the rock layers. The failure criterion of the discontinuities and the intact rock are both based on MC.

A quite new model that is not yet set as a standard model in Plaxis, is the **SR** model (for more detailed description one refers to Schädlich et al., 2013). As the name of the SR model already indicates, the model gives the opportunity to take into account the swelling potential of a rock mass. The swelling behaviour is modelled based on Grob's, 1972 swelling law. The swelling behaviour is a time-dependent (creep-like) behaviour, which is attempted to be described by this model.

[1] The Swelling Rock model is only applicable in the 2D PLAXIS, not yet in 3D

An overview of the application of the above mentioned constitutive models is presented in table 2.2. This overview is based on the descriptions of the material models in Brinkgreve, 2019. It was chosen to look at several types of ground material that clearly influence the relevance of previously mentioned models.

| *Constitutive model* | MR | HJR | PDR | SA | CNC | COC | SR | SS | CON |
|---|---|---|---|---|---|---|---|---|---|
| Linear Elastic | +/- | - | - | - | - | - | - | - | +/- |
| Mohr-Coulomb | +/- | +/- | - | +/- | +/- | +/- | - | - | + |
| Hardening Soil | - | - | - | + | + | + | +/- | + | - |
| HS small strain | - | - | - | + | + | + | +/- | + | - |
| Soft Soil | - | - | - | - | + | - | - | + | - |
| Soft Soil Creep | - | - | - | - | + | - | - | + | - |
| Jointed Rock | - | - | +/- | - | - | - | - | - | - |
| Modified Cam-Clay | - | - | - | - | + | - | - | + | - |
| Hoek-Brown | + | + | - | - | - | - | - | - | - |
| Swelling Rock | - | - | - | - | - | - | + | - | - |

Table 2.2: Usability of several relevant constitutive models to corresponding rock masses and soils. The relevancy of the models was rated in terms of + being the best applicable model, - not specifically applicable for the corresponding ground type and +/- means the model can be used as a first-order estimation of the ground behaviour

Additional description for the following parameters:

MR = Massive rock mass;
HJR = Highly jointed rock mass;
PDR = Predominantly discontinuous rock;
SA = Sand, loose to dense;
CNC = Clay, normally consolidated;
COC = Clay, over-consolidated;
SR = Swelling rock mass;
SS = Swelling soil;
CON = Concrete.

From the upper table, it is suggested that certain models are relevant to the ground in the Middle-East case, while others are not. In particular, the following ground types were found at the case site and are linked to the corresponding constitutive model as shown below:

- Fault material: in case of clayey squeezing conditions. This can best be modelled with HS. However, a first order estimate can be acquired with the MC model. The SS, SSC and MCC models are mainly used for normally consolidated (NC) soils, while it is expected that a faultzone with over 200 m overburden will behave like an over-consolidated soil, making this models not applicable;
- Fault material: that could have a potential for swelling. Unloading behaviour could be modelled with the HS model. However, the expected swelling of rock is not just due to unloading (open pores filling up with water), but also due to a chemical behaviour of swelling particles. The authors claim that the SR model can take this into account. However, the SR model is not yet applicable in the Plaxis 3D environment. For these reasons the HS and SR models are not considered in this study;
- Fault material: in the form of highly fractured rock with some clay-particles. This is perfectly modelled with the HB criterion. If there is no plasticity, the first- order estimation can be done with the LE model;
- For massive marl alternating with limestone swelling potential, the SR model is most appropriate. For the first order approximation implementation of HS or HSsmall models can be considered. The SS, SSC and MCC models are described to be applicable for NC soils;
- For highly fractured limestone the most suitable model is the one using the HB failure criterion. For elastic behaviour it can be approximated with with the LE model, in case of plasticity the MC model can be implemented.

### 2.4.4. Lining design

The input properties of a lining are among others the geometry, the material properties, the segment joints, the lining contraction and the interface between the lining and the ground.

The required characteristic for a lining design are the **lining material** properties. The reinforced concrete segments are generally modelled with a LE model, which is defined by the Young's modulus (E), Poisson's ratio ($\nu$) and the weight ($\gamma$). These properties are then translated into the lining resistance to shear (EA) and resistance to bending (EI).

The segment **joints** are modelled by either fixed or free connections or a spring. Free connections represent hinges, which can not resist rotations. Fixed connections resist against rotation entirely, leading to the full taking over of the bending moments. The spring connection is the most realistic one, which can resist some rotation depending on the assigned rotational stiffness. This rotational stiffness can be calculated with the Janßen relation as described in section 2.3.2.

In Plaxis, the **contraction** method is implemented to account for ground loss due to the TBM overcut (in Möller, 2006 this and other methods are elaborated). The input value for contraction represents the volume loss in percent. Bezuijen mentions values of TBM tapering that coincide with measured volume loss quantities, which vary between 0.2 to 1.0% (in Bezuijen and Talmon, 2008).

One of the most discussed parameter in modelling the lining behaviour is the **interface**. This describes the ground-structure interaction (transition of shear stresses from the ground to the lining, or slip and bond) as well as the permeability of the lining. In Plaxis, the interaction between ground and structure can be modelled through applying a reduction factor ($R_{inter}$) on the strength and stiffness parameters with which the lining interacts. It can be chosen to use either the strength and stiffness parameters from the adjacent ground, or assigning values manually. The lining is often modelled as being impermeable, to take into account the total water table acting on the lining (BTS, 2004).

# 3

# Case: Tunnel Middle-East

This chapter gives an overview of the experienced difficulties in the main tube (section 3.4), geological and geotechnical conditions of the project (sections 3.1 and 3.2) and the lining design (section 3.3).

## 3.1. General case information

The Middle-East project consisted of two main tunnel tubes, with roughly 15 m distance between each other, which were connected by cross passages located at approximately every 500 m along the alignment. The main tubes were bored using a 10.04 m diameter Double Shield TBM, while the cross passages were excavated by a conventional method. The northern tube was executed first, followed by the southern tube.

In the Middle-East case, it was observed that the lining of the southern main tunnel tube underwent ovalization directly after the construction phase. This meant that the clearance requirement of the tunnel as applicable for railway tunnels was compromised. The other issue was that excessive deformations were the cause of leakage in the tunnel. In the cross passages issues occurred in terms of failed tunnel lining and floor, which was claimed to be due to exceeding water pressures and inappropriate implementation of the concrete works. For this research, the focus was limited to the main tunnel because this was excavated with a TBM, while the cross passages were executed mechanically with a sequential excavation method.

The geology of the region was characterized by sediments originating from the early and late Cretaceous period (Albian 113-100 Ma[1] and Cenomanian 100-94 Ma respectively) of the Mesozoic era (252 to 66 Ma) based on Cohen et al., 2013. These geological units generally consist of sedimentary rock type material (Waltham, 2009). The geological formations were represented by limestones with marl embedded layers alternating with dolomite at an increasing depth. The following zones were established, based on geological mapping and core logging from continuous borehole cores:

| | | |
|---|---|---|
| gy | : | dolomite (Cenomanian) |
| K | : | dolomite, locally limestone (Albian-Cenomanian) |
| q | : | marl alternating with limestone (Albian) |
| eq | : | limestone (Albian) |

In the preliminary design stage of the project, a seismic survey was carried out by a geophysical institute. It was found that the region was marked by fault lines and possibly (moderate) subjected to seismic events. From the seismic survey a peak ground acceleration (PGA) equal to 0.13 g was estimated, which was considered to be harmless to the lining and a seismic hazard was irrelevant. Based on this result, the tunnel lining design did not consider seismic events and no further evaluation of the seismic risk was conducted.

[1] Ma is an abbreviation for Mega-annum, which means Million years ago

In figure 3.1, the complete geological profile for the tunnel alignment is presented. The rough locations of the 16 normal faults was given by the red lines. The faults were marked as single lines, whereas estimated width of the fault zones varied between 10 to 40 m. These zones were characterized by extremely abrupt changes in mechanical properties between two geotechnical units found between fault lines. For this research only one specific fault zone was analyzed, due to the difficulties encountered in this specific zone and the available monitoring data. The fault zone material was not encountered during the site investigation and therefore the parameters had to be estimated.

On the figure the overburden height encountered along the alignment of the tunnel can be estimated. Furthermore, the division in geotechnical units with almost homogeneous properties are shown in the figure. It is important to acknowledge that the estimated stratigraphical division and rock mass properties were based on exploratory boreholes (20 in total) that were between 150 to 1000 m apart from each other. Since the laboratory tests were only performed on samples obtained at the depth corresponding to the tunnel alignment, the properties were only known for limestone with marl interbeds (s), dolomite (gy), dolomite with locally limestone (k) and marl alternating with limestone (q). In case that unknown properties were needed for the analysis of this research, they will have to be estimated.

The in situ stresses in the Middle-East case were not measured in the field. This meant that assumptions had to be made to assess the state of stress of the rock mass. In particular, the lateral earth pressure coefficient (k), which is the ratio between horizontal and vertical stress, had to be estimated. As an upper limit, the k-ratio was assumed to be lower than unity, based on the measured vertical ovalization. However, the lower limit for the k-ratio at large depth was set to 0.3 based on worldwide measurements (Pei et al., 2016).

Transmissivity ranging between less than 1 $m^2$/day to maximal 4 $m^2$/day was found along the tunnel alignment. Based on water level measurements in the boreholes, it was concluded that a permanent aquifer was present. The measured hydraulic head was at a level of maximum 58 m above the invert ($\approx$ 580 kN/$m^2$) to a couple of meters underneath the invert of the tunnel. With the help of the pumping tests, the flow rate was expected to be equal to 45 $m^3$/hour in the summer and 90 $m^3$/hour in the winter (due to rainfall). This was based on a maximal inflow rate over 1000 m of tunnel length which lay below the water table and the aquifer had a gradient of 0.027.

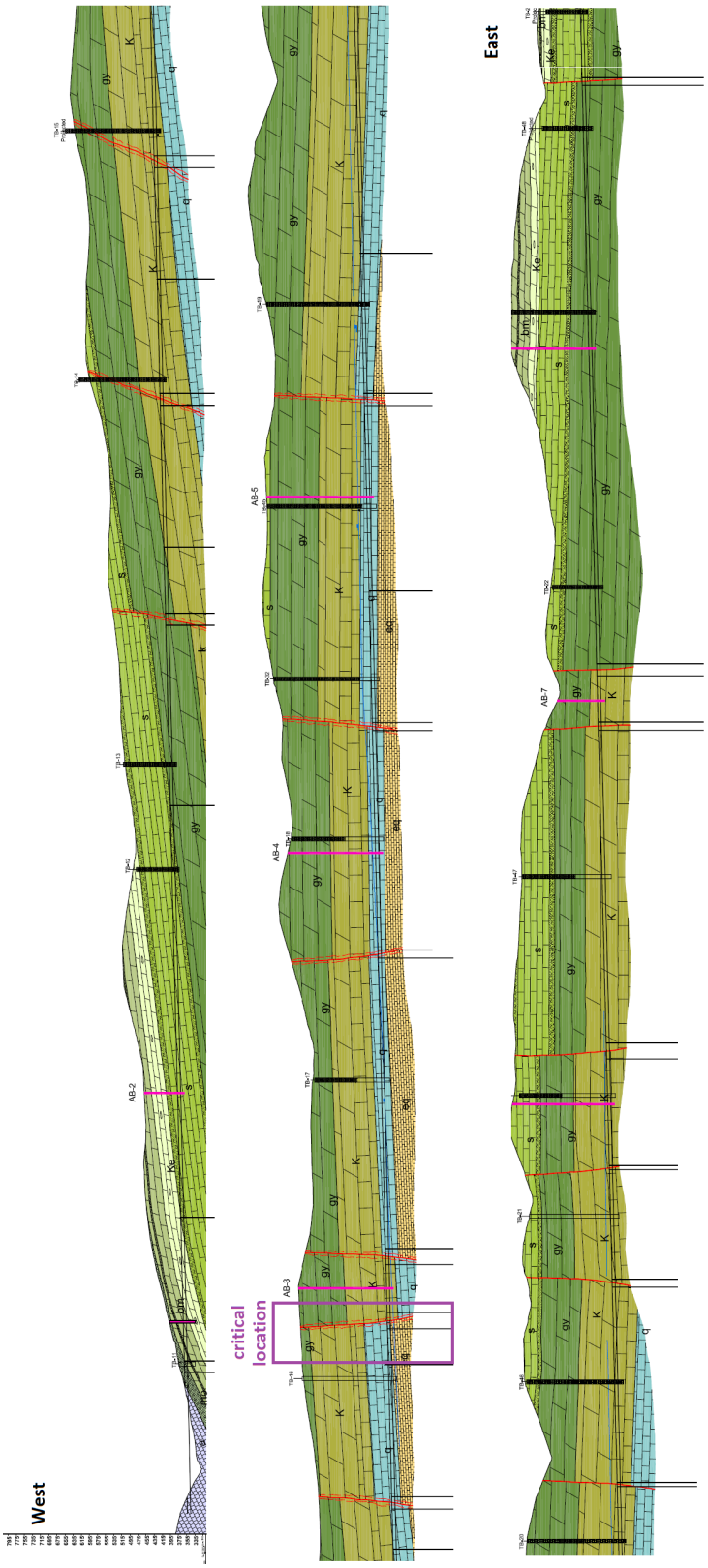


Figure 3.1: Geological profile shown in parts for the Middle-East case

## 3.2. Geotechnical conditions

In this section the geotechnical and -hydrological starting points for the tunnel and the tunnel lining design are described.

The **rock mass properties** in the fault zone of interest were estimated based on engineering experience and a GSI equal to 25, as no site investigation or sampling of the material in this zone was done. These properties were also not determined in the probe drills during excavation of the tunnel. The intact rock parameters of the fault zone were assumed to be equal to the adjacent geological formation. For the time being this hypothesis was assumed to be a reasonable and representative for the real fault zone material.

The measured **overburden thickness** at the studied area was equal to 215 m, based on the corresponding surface level above the tunnel lining (top lining: 460 m a.s.l.; surface level: 675 m a.s.l.).

The deformation issues were measured at 10 lining rings (which is equal to a width of 16 meters) and was believed to be less then the total **fault zone extent**. This assumption was supported by the probe drilling data from the boring stage, resulting in a zone width of roughly 40 m (figure 3.3).

During the design stage, the waterpressure was assumed to be ranging between 400 to 500 kN/m$^2$, which corresponded to a **water table** of 40 à 50 m above the lining.

The **fault zone** is shown in figure 3.2, where the red solid line represents the fault line with an angle of 5 to 15 degrees. The winding lines represent the fault zone boundary. Legend of the regarding rock units is indicated in the left bottom corner. The geology, relevant to the analyses in the studied area, was divided in 3 zones (as shown at the top of the figure). The nearest fault line at the west side of zone 1 was at a distance of over 400 meters, while at the east side of zone 3 at approximately 120 meters.

In figure 3.2 the location of measured rings indicated with a purple rectangle. The encountered fault zone is shown from a top view in figure 3.3 to indicate the distribution in the third dimension. The excessively deformed tunnel lining was in the southern tube, which was executed after the northern one. It was therefore assumed that the boring of the northern tube did not influence the behaviour of the southern tube, where difficulties were observed. The fault was just about parallel with the tunnel alignment, which made the extent of the crossed fault longer during the boring process.

The **joints** encountered in the core samples showed a constant direction over a large distance. According to Bell, 1981 these joints would be called planar and parallel. Random joints, hair cracks and stylolites were also common. The dip direction of the fractures was mainly towards west, while the striking was mainly east-west and north/north-west/south/south-east. No laboratory nor field tests were carried out to define the strength and deformation properties of the joints. However, several criteria were used to estimate the shear strength of discontinuities based on their characterisation (e.g. Mohr Coulomb, Barton and Patton described in Price, 2009). The characterisation of the joints was based on visual inspection of the obtained rock cores.

It was expected that the encountered rock mass would be affected by **karst** development and rock alteration. Dissolution along joints, leading to the development of cavities and caves common in limestone were frequently encountered during field works. In some cases of earlier performed earthworks in the surrounding area, caves were encountered with volumes of up to hundreds to several thousands cubic meters. These cavities were horizontally more developed than vertically. The walls of the caves seemed stable, however the secondary filling (clay and rock) might have collapsed during excavations.

At present, the points of departure for the rock mass parameters in the fault zone are summed up in table 3.1.

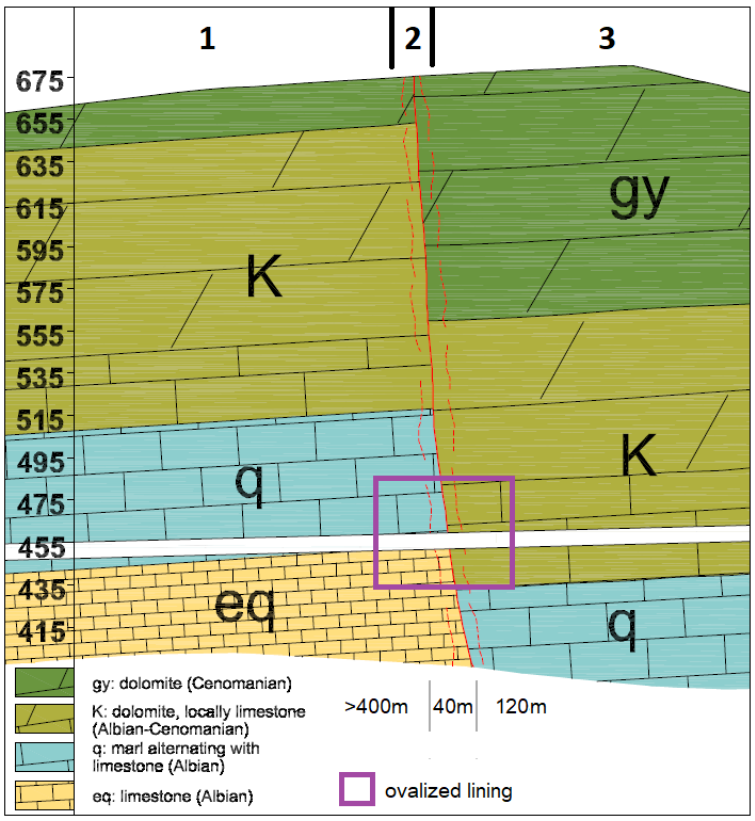


Figure 3.2: Critical fault zone, where exceeding deformations were observed in the southern tube in the Middle-East case

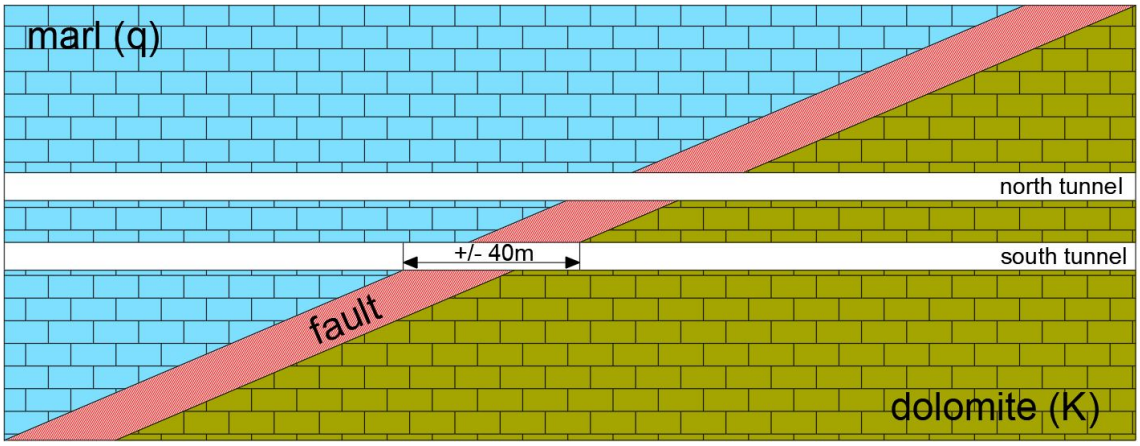


Figure 3.3: Identified fault zone from a top view where excessively deformed rings were measured in the Middle-East project

| $Zone$ [#] | 1 | | | | 2 | | 3 | | | |
|---|---|---|---|---|---|---|---|---|---|---|
| $Material$ [−] | q | | eq | | F * | | K | | q | |
| | min | max | min | max | min | max | min | max | min | max |
| $Width$ [$m$] | > 400 | | | | 10 | 40 | 120 | | | |
| $tunnel_{top}$ [$m$ $a.s.l.$] | 450 | 460 | 450 | 460 | 460 | | 460 | 465 | 460 | 465 |
| $h_{top}$ [$m$ $a.s.l.$] | 495 | 520 | 430 | 455 | 675 | | 560 | 570 | 430 | 440 |
| $h_{tot;top}$ [$m$ $a.s.l.$] | 635 | 675 | 635 | 675 | 675 | | 660 | 680 | 660 | 680 |
| $h_{low}$ [$m$ $a.s.l.$] | 430 | 455 | - | - | 400 | | 430 | 440 | - | - |
| $d_{above}$ [$m$] | 45 | 60 | - | - | 215 | | 100 | 105 | - | - |
| $d_{tot;above}$ [$m$] | 185 | 215 | 185 | 215 | 215 | | 200 | 215 | 200 | 215 |
| $d_{beneath}$ [$m$] | 10 | -5** | >50 | | >50 | | 20 | 15 | >50 | |
| $\gamma_d$ [$kN/m^3$] | 24.7 | 26.0 | 25.6 | | - | | 24.5 | 25.8 | 24.7 | 26.0 |
| $\sigma_c$ [$MN/m^2$] | 44 | 90 | 120 | | - | | 50 | 100 | 44 | 90 |
| $\sigma_t$ [$MN/m^2$] | 1.6 | 7.8 | - | | - | | 2.2 | 7.5 | 1.6 | 7.8 |
| $E_i$ [$MN/m^2$] | 9200 | 70600 | - | | - | | 20150 | 54550 | 9200 | 70600 |
| $S_p$ [$kN/m^2$] | 1600 | | - | | - | | 610 | | 1600 | |
| $RMR$ [−] | 45 | 65 | - | | - | | 30 | 69 | 45 | 65 |
| $RQD$ [−] | 80 | 100 | - | | - | | 33 | 100 | 80 | 100 |
| $GSI$ [−] | 40 | 60 | - | | - | | 45 | 70 | 40 | 60 |
| $m_i$ [−] | 5 | 11 | 6 | 12 | - | | 6 | 12 | 5 | 11 |
| $S_{dip}$ [°] | 10 | 30 | - | | - | | 25 | 30 | 10 | 30 |
| $S_{description}$ [−] | [1] | | - | | - | | [2] | | [1] | |
| $J_{dip}$ [°] | 30 | 90 | - | | - | | 40 | 90 | 30 | 90 |
| $J_{description}$ [−] | [3] | | - | | - | | [4] | | [3] | |

Table 3.1: Range for primary intact rock and rock mass parameters for layers corresponding to the tunnel depth

* This stands for fault;
** This is negative, because the top of the underlying layer was higher than the tunnel invert;
[1] thick strata of marl;
[2] crushed and weathered;
[3] planar, smooth and filled with marl or closed;
[4] planar to undular, smooth and closed.

Additional explanation for the following parameters:

| | | |
|---|---|---|
| Zone | = | This refers to the horizontal division as mentioned at the top of figure 3.2; |
| Material | = | Related to the rock unit as mentioned in section 3.1 |
| Width | = | Approximated width of the corresponding zone based on the geological length profile; |
| tunnel$_{top}$ | = | Level of the tunnel with respect to the sea level; |
| $h_{top}$ | = | This is the top of the layer where the tunnel is located; |
| $h_{tot;top}$ | = | This is the surface level at the highest and lowest point for the corresponding zone; |
| $h_{low}$ | = | This is the bottom of the layer where the tunnel is located; |
| $d_{above}$ | = | This is the thickness of the rock material above the tunnel top; |
| $d_{tot;above}$ | = | This is the total thickness of rock material above the tunnel top (until the surface); |
| $d_{beneath}$ | = | This is the thickness of the rock material below the tunnel invert; |
| $S_{dip}$ | = | The dip angle of the overall strata; |
| $S_{description}$ | = | The general description of the strata; |
| $J_{dip}$ | = | The dip angle of the joints; |
| $J_{description}$ | = | The general description of the joints. |

## 3.3. Lining ring design

The design of the lining takes into account the inner ring diameter, the ring thickness, the ring length, the amount of segments, the segment shape / the ring layout, the concrete characteristics, the reinforcement and joints. An overview of the design specification is shown in this subsection.

The lining design in a cross section and the lay-out of the ring are respectively shown in figure 3.4. From these figures it can be seen that each ring consisted of 7 segments including a keystone. The lay-out was based on the so called "Left-Right-Ring" lay-out. The inner and outer ring diameter were equal to respectively 8.9 and 9.7 meters. The segment thickness was 0.40 meters, whereas the width of the ring was equal to 1.6 meters. The Double Shield TBM that was used for this project had a diameter of 10.04 m, making the theoretical overcut approximately 17 cm all around the ring. The backfilling of the excess excavated ground was done using pea-gravel supplemented with grout. The characteristics of the concrete are C35/45 and reinforcement of quality S500. The joints were made watertight by using segmental gaskets, that provided enough resistance to the design water pressure.

For the design calculations, the Duddeck-Schultz model and the Convergence-Confinement model was used. The lining was designed with three different segment-types, which differ only in the provided reinforcement grade. The segments were for use in different ground conditions, being:

- Current-type, for normal ground conditions with a low level of thrust forces during re-gripping;
- Hybrid-type, for difficult ground conditions like faults or weak zones with a low level of thrust forces during re-gripping;
- Heavy-type, for difficult ground conditions like faults or weak zones with an elevated level of thrust forces in single-shield mode;

The difference between the segment-types was that the current-type provided less structural resistance for ground forces than hybrid- and heavy-type, while the heavy-type provided more resistance to normal/thrust forces than the hybrid-type.

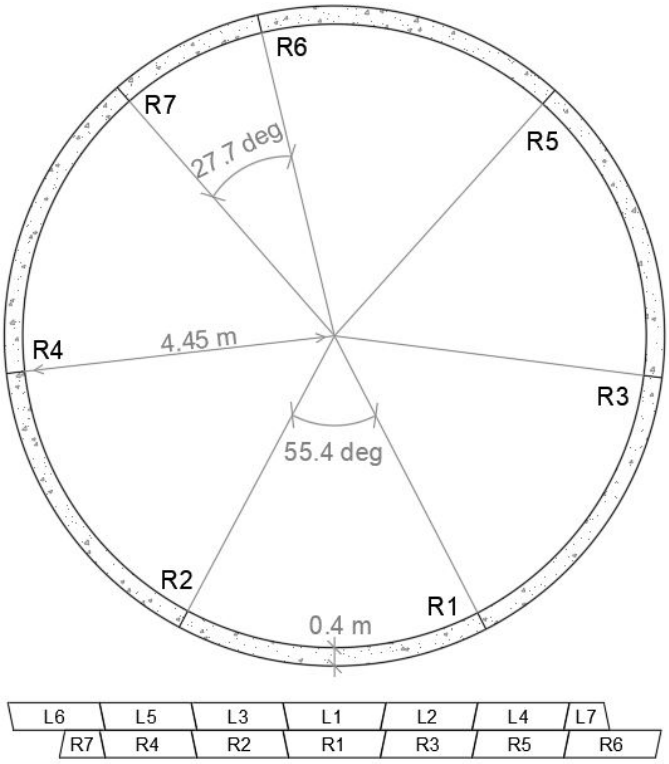


Figure 3.4: Design of the segmental bored tunnel lining in the Middle-East project: cross section (top) and "Left-Right-Ring" lay-out (bottom) not to scale

## 3.4. Difficulties with lining

Three main components did not meet the requirements or the original design assumptions of the tunnel lining and were detected after the boring process and installation of the rings. These are: (1) the measured exceeding deformations resulting in ovalization and settlement of several rings, (2) leakages and (3) implementation issues in terms of improper backfilling of rings. Each of these three components are explained in more detail below in this section.

### 3.4.1. Deformations

The measurements carried out after installation of the lining rings showed that the deformations of 10 rings did not meet the requirements. The maximal deformations of the central lining ring (nr. 3695), located in the fault zone, are shown in figure 3.5. The solid line represents the theoretical positioning of the ring, while the dotted line indicates the measured deformed ring. The shown deformations were in centimeters, in which the maximal total vertical and horizontal convergence were respectively 18 and 15 cm. The vertical and horizontal translational deformations of the entire tunnel were 14 and 4.5 cm.

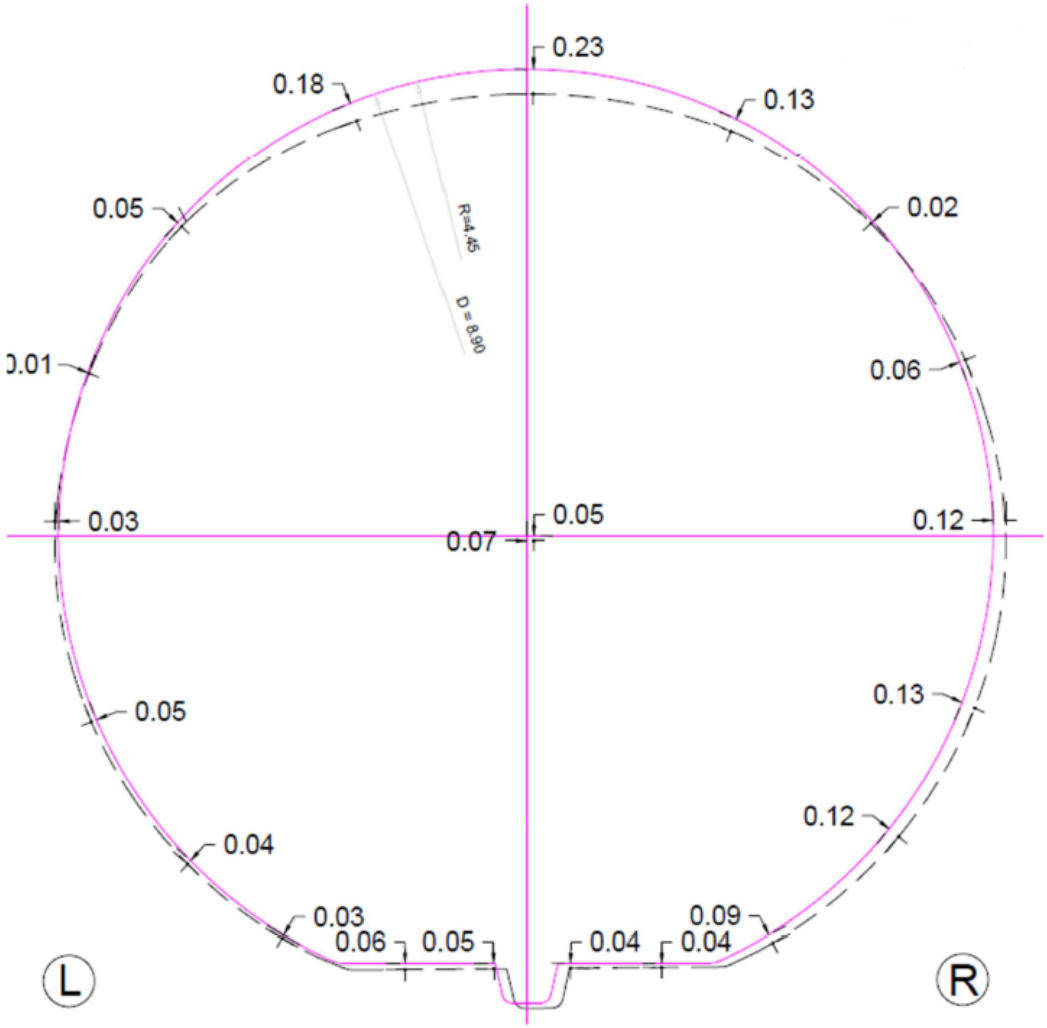


Figure 3.5: Measured maximal ovalization of lining ring nr. 3695
located in a fault zone in the Middle-East project

The total vertical convergence of the first and last rings (nr. 3690 and 3700) were equal to respectively 12 and 6 centimeters, which was determined based on the top and invert displacements shown in figure 3.6. The settlement of the first and last rings was respectively 9 and 7 centimeters, while the horizontal displacement for these rings remained unknown.

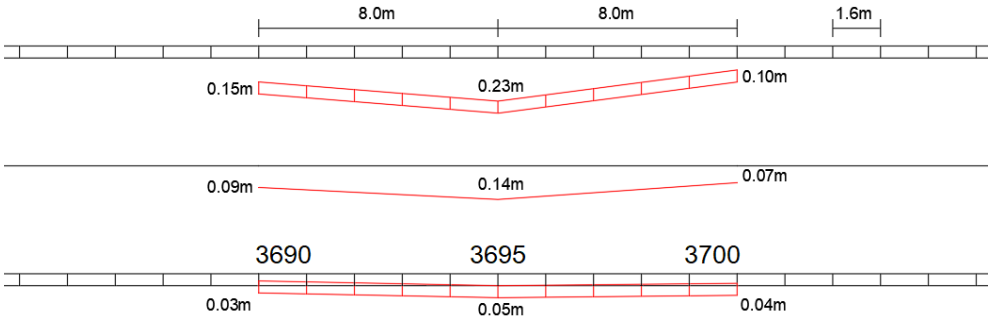


Figure 3.6: Measured maximal top and invert displacements and the settlements for rings 3690, 3695 and 3700

### 3.4.2. High water pressures

During investigation of the tunnel lining, serious water leakages were observed. Figure 3.7(a) shows the damage caused by high water pressures in some cross passages. Figure 3.7(b) is a picture of the video when workers drilled through the tunnel lining to measure the water pressures. The visible straight waterjet demonstrates the significant water pressure acting on the main tube. This information was used to confirm the pressure on the main tube. Based on the results from the pressure measurements, the water level was dropped from 58 to 30 meter which could be the cause of ring settlements.

(a) (b)

Figure 3.7: Observation of serious water pressure acting on tunnel lining in (a) cross-passages and (b) main tunnel tube in the Middle-East project

### 3.4.3. Implementation issues

An observation indicating there were implementation issues, was based on a video made by inspectors that drilled through the lining to measure present water pressures acting on the tunnel lining. At the moment of complete penetration of the lining, the drill jumped past the lining until the maximum level of penetration was reached. This illustrated that there was little resistance around the lining, which could have meant a gap (due to improper backfilling) or a weak/loose ground mass was present. Poor support might have resulted in non-uniformly distributed support or instabilities of the ground. As a result of the drilling activity, water gushed out of the hole which is shown in figure 3.7(b).

# 4

# Analysis

In this chapter the methodology to reliably model the tunnel lining and the ground behaviour in transversal and longitudinal direction is described. Moreover, the analysis was set up in such manner that the behaviour of the tunnel lining in both longitudinal and transversal directions was integrated in one three-dimensional model. The results from this analysis are presented and discussed in the next chapter (5).

## 4.1. Methodology

The general approach to come to the final three-dimensional model was set up in the form of a flowchart and presented in figure 4.1. The methodology principle contained two separate analysis for respectively the transverse and longitudinal direction of the lining in 2D. These models were used to predict the force distribution in a 3D environment, without knowing the 3D effects. This was followed by the set up of an integrated 3D model. After validation and calibration of the 2D and 3D models, the longitudinal and transversal behaviour of the ground and lining was assessed. In this section, each of these model is described in more detail.

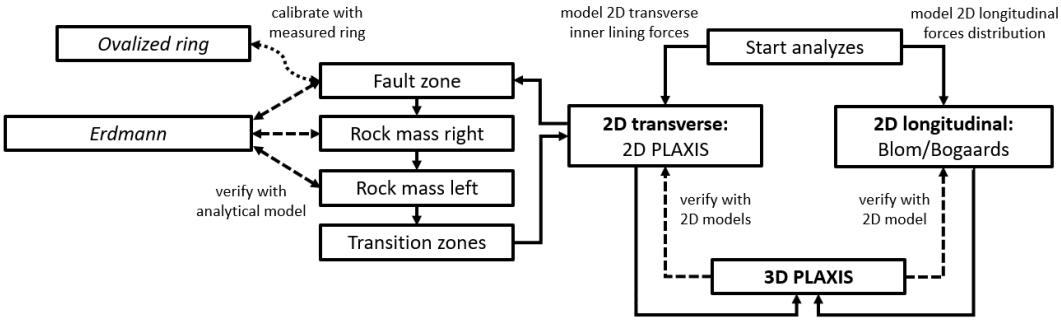


Figure 4.1: Research analysis methodology presented in the form of a flowchart, including validation and calibration steps of the numerical model

The validation of the 3D model in this research was done by comparing its results to validated 2D model results. The 2D models were validated by an analytical closed form solution and calibrated with the measured ring deformations in the Middle-East case. The longitudinal profile was divided into 3 transversal sections that were developed in Plaxis 2D. The cross sections for which Plaxis 2D models were elaborated to validate the 3D models, are shown in figure 4.2.

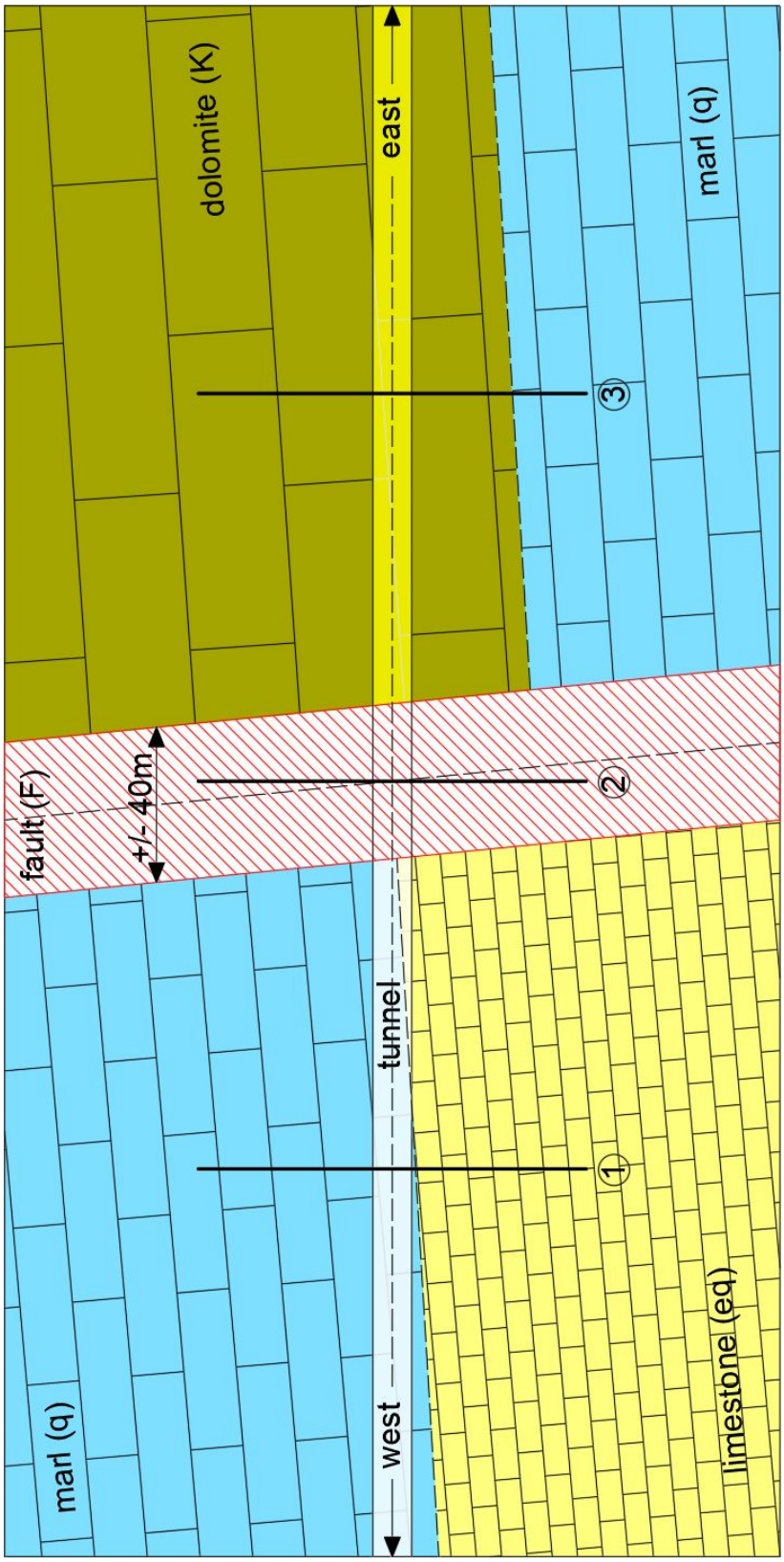


Figure 4.2: Longitudinal profile with designation of the locations for which 2D Plaxis models were made

## 4.2. 2D transversal model

The cross sections are indicated by thick vertical (black) lines and numbers 1 to 3 underneath each corresponding line (figure 4.2). The cross sections with their numbers correspond to the below mentioned locations:

1. Western adjacent geotechnical unit, which consisted of a layered system containing slightly weathered marl (q) and limestone (eq);
2. Fault zone, which consisted of a mixture of highly weathered rock mass originating from the adjacent rock (dolomite, limestone and marl) and was bounded by these adjacent geotechnical units (figure 4.2);
3. Eastern adjacent geotechnical unit, which consisted of a layered system containing highly fractured dolomite (K) and slightly weathered marl (q).

The modelling assumptions and methodology used to analyze the three different 2D sections in the transversal direction is described in this paragraph. Generally, the methodology followed six steps, which were:

1. Finding the optimal model geometry;
2. Finding the optimal mesh coarseness;
3. Analyzing the sensitivity of geotechnical parameters on the model;
4. Analyzing the sensitivity of lining parameters on the model;
5. Verifying the calculated models with an analytical solution and a different constitutive model;
6. Calibrating the model with measured data where possible.

An illustration of the general build up of a transversal model is presented in figure 4.3 on the following page. For explanation purposes, all geometrical parameters which were used in the analysis are shown in the drawing.

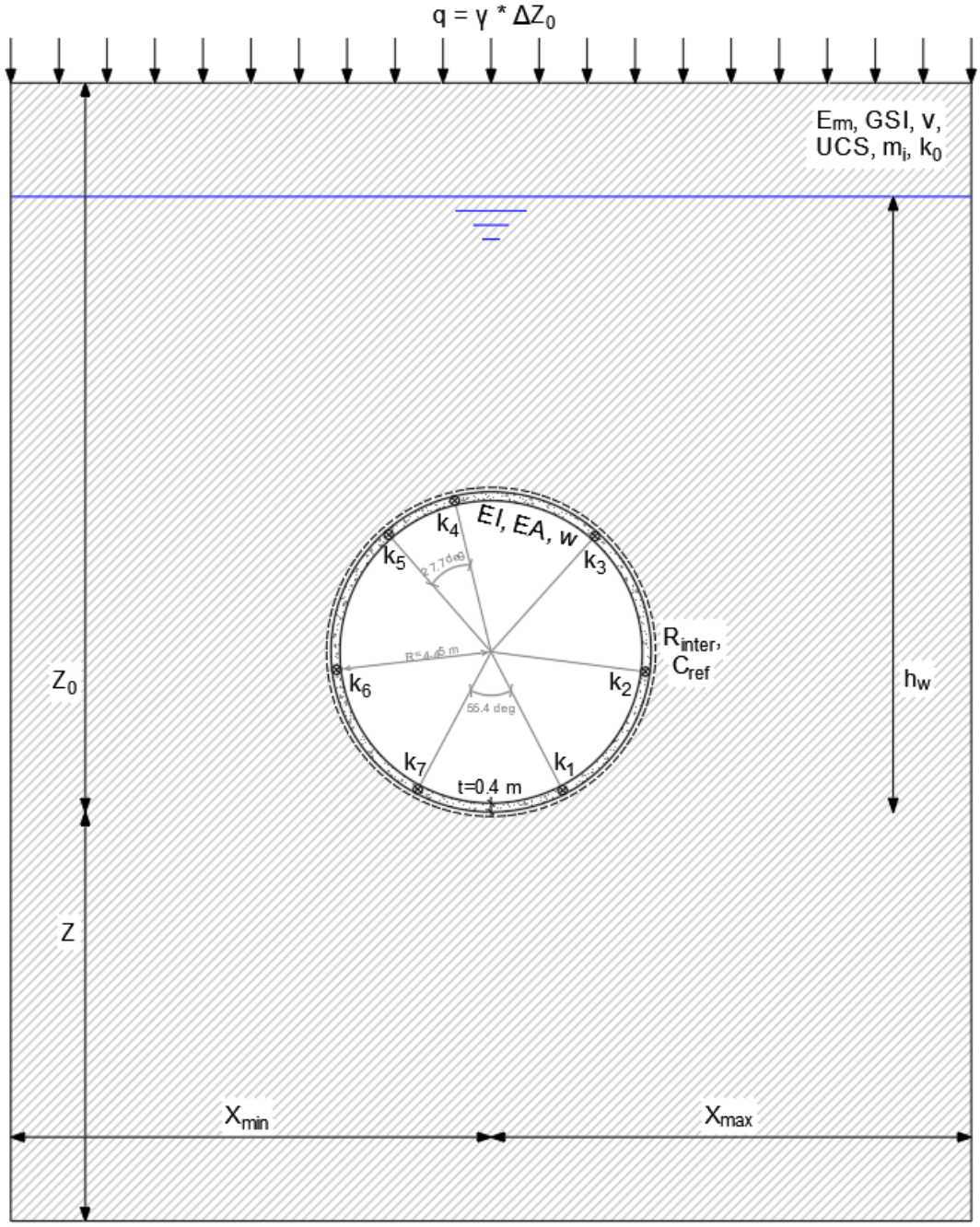


Figure 4.3: Model geometry with the clarification of corresponding parameters that are discussed in the modelling assumptions and parametric studies

The model had dimensions of: height Z + $Z_0$ and width $X_{min}$ + $X_{max}$. Z represented the depth of the model underneath the invert of the tunnel ring, while $Z_0$ was the modelled overburden. However, the overburden was reduced and compensated by a vertical load equal to the mass weight ($\gamma$) times the compensated overburden ($\Delta Z_0$). The water table ($h_w$) was modelled with respect to the tunnel invert. The ground model consisted of variable parameters for stiffness (E and $\nu$), lateral earth pressure coefficient ($k_0$), strength (UCS, $m_i$ or $\phi'$ and c') and rock mass characterisation (for Hoek-Brown this is the GSI). The lining ring with a 9.7 m outer diameter and 0.4 m thick walls, consisted of 6 segments with a key-stone with a certain stiffness (EI and EA) and weight (w). The joints between the segments were modelled as connection points with a rotational stiffness (k). The interface between the ground and ring was modelled through applying a reduction factor ($R_{inter}$). These parameters are developed in more detail in the following section.

### 4.2.1. Modelling assumptions

It was important to assess the limitations of the proposed model, as well as the assumptions taken for the analyses. For the 2D transversal models the following initial assumptions were applied:

- The rock mass (marl, limestone and dolomite) was best described by the Hoek and Brown (H-B) failure criterion, which meant;
  - it behaved as a continuum with random failure direction, due to "randomness" of the joints encountered in the corresponding rock masses;
  - it acted as an isotropic material, which meant that the rock mass properties were identical in all directions;
  - it was best modelled in terms of an effective stress analysis, due to the high permeability that was measured in the field no undrained behaviour leading to the need of total stress analysis was expected for limestone and dolomite. The permeability of marl was typically low. However, for the parametric study only drained analyses were implemented;
  - it did not show creep phenomena, because the large displacements occurred almost immediately after installation of the lining, one was not interested in the time-effect;
  - it behaved elasto-plastic, indicating that during loading there was an elastic and at the same time a plastic component in the development of strains;
  - the disturbance factor was equal to 0 for a TBM excavation method.
- The fault zone material was expected to be a weathered and crushed rock mass, where the intact rock material consisted of mainly marl. This was based on the faulting history, which showed that the marl layer had shifted normal to the fault (figure 4.2) and therefore the marl material should be spread throughout the fault. However, it was expected to be weathered because of the large width of the fault zone, resulting in fill material that behaved as a very stiff (sandy) clay rather than a rock mass. The high stiffness was accounted for by the large overburden and therefore the stress history of the material. This assumption led to the supposition that the fault material was best described by a soil model, which for this research was chosen to be Mohr-Coulomb. The translation from Hoek and Brown to Mohr-Coulomb parameters is explained in appendix B.
- The rock mass stiffness ($E_{rm}$) is a parameter that was estimated based on geological classification and intact rock parameters. For this research it was assumed that the Hoek-Diederichs solution was valid (referred to Hoek and Diederichs, 2006). This formulation is presented in equation 4.1 and depends on the Geological Strength Index (GSI), the disturbance factor (D) and the stiffness of the intact rock ($E_i$). However, the disturbance factor for rock mass cut by a TBM is equal to zero thus the new equation shown in 4.2:

$$E_{rm} = E_i * \left(0.02 + \frac{1 - D/2}{1 + e^{(60+15D-GSI)/11}}\right) \; [MN/m^2] \tag{4.1}$$

$$E_{rm} = E_i * \left(0.02 + \frac{1}{1 + e^{(60-GSI)/11}}\right) \; [MN/m^2] \tag{4.2}$$

- The overburden and depth of the tunnel were based on the longitudinal profile provided by the engineering party at the Middle-East case, but in order to facilitate the modelling, the surface level was set to 675 m a.s.l. and the depth of the center line of the tunnel at 455 m a.s.l. over the complete model. Additionally, the stratification was modelled as horizontal for all rock masses. The determined ground properties of the intact rock and the stratification of the area were mostly based on the existing site investigation and lab-testing. However, the volumetric weight ($\gamma_d$) for all the rock masses was set to 25 kN/m$^3$ being an average value, while in the fault zone it was expected to be much lower and set to 20 kN/m$^3$ (equal to a very stiff clay). Moreover, the mechanical properties of the undetermined geotechnical unit, being limestone (eq), were assumed to be comparable to the dolomite (K).
- The expected deformation behaviour of the fault material was assumed to be squeezing, this was based on the measured deformations. For the other rock masses, the behaviour was non-squeezing based on the measurements. Literature offered many conditions to define squeezing, but the one presented in Singh and Goel, 2011 was chosen, which implied that mild squeezing occurs when the radial displacement was at least 1% of the tunnel radius. For the Middle-East case, this implied the radial displacement

should have been at least 4.5 cm. Based on this assumption, the range of input parameters such as the compressive strength and deformability were found iteratively based on calculated deformations. In particular, the parameters of the marl were expected to be too low.

- The occurrence of dilatancy ($\psi$) was not taken into account in this study. Typically, in rock the dilatancy phenomena did not occur because grains were not densely distributed, rather they were connected by bonding material which broke and did not show dilation (Bell, 1981).

- The concrete lining segments were assumed to behave linear-elastic during loading, which led to an uncracked and unchanged stiffness of the concrete (E = 35*$10^6$ kN/$m^2$) throughout the analyses.

- Lining rings implemented in this analyses were as designed for the Middle-East tunnel. The thickness of the lining (t) was 0.4 m and the concrete strength was equal to 35 N/$mm^2$. The surface (A) and moment of resistance (I) were equal to respectively 0.4 $m^2$/m and 0.0053 $m^4$/m (based on an I per meter for a ring; I = $\frac{1}{12}$ * $t^3$). The Poisson's ratio ($\nu$) for concrete is typically 0.2. One ring was build up of 6 segments and 1 key-stone (figure 4.3).

- The stiffness of the joints in the lining rings was calculated according to Janßen's theorem. The stiffness was calculated as an open or closed joint (equation 4.3 and 4.4), depending on the ratio between the moment (M) and normal force (N) in the joint. This ratio represented the eccentricity (e = M/N) of forces acting in the joint. As a first approximation, the joint stiffness was seen as one of a closed joint. However, if the eccentricity (e) coming from the results of the calculations was larger than $\frac{1}{6}$ of the joint width (t), an iterative process to find the stiffness for which the input and output normal forces and moments match each other was needed. In the calibration with the measured ring, the joints had to be calculated as open based on leakage that was observed. Furthermore, due to the high overburden and therefore large normal forces, it was assumed that the joints were so compressed that full concrete to concrete contact was present. This assumption led to a stiffness parameter of the joint (E) being equal to that of concrete.

$$k_{r,closed} = \frac{b * t^2 * E}{12} \; [kNm/m/rad] \tag{4.3}$$

$$k_{r,open} = \frac{9 * b * t * E * M * \left(\frac{2*M}{N*t} - 1\right)^2}{8 * N} \; [kNm/m/rad] \tag{4.4}$$

- The analyses focused on the final stage of construction, when the lining was installed and the backfilling was hardened, and was based on the difficulties that occurred in the Middle-East case. Furthermore, the backfilling in the reference case contained pea-gravel and post-grouting. The boring process consisted only of the cutting of a hole and installation of the lining rings. Therefore, the staged construction in the analyses consisted of three stages, namely:

  1. the initial stage, in which the initial vertical and horizontal stresses were based on the k0-procedure. No (shear) failure in the rock mass was expected here;
  2. the first stage, in which the excavation of the hole together with the installation of the lining ring were executed in one step;
  3. the second stage, in which the volume loss due to incomplete annular gap filling or subsidence of pea-gravel was modelled by means of contraction.

- No explicit three-dimensional effects were taken into account in the 2D transversal models. By this was meant e.g. the effect of adjacent rock masses with highly deviating properties or the influence of longitudinal effects.

Furthermore, a prediction of the rock behaviour was done prior to model it in Plaxis (appendix A). This prediction showed that typical failure modes of the different rock masses and fault material relevant to the Middle-East case were block fall and unravelling of blocks in limestone, dolomite and marl and additionally squeezing or swelling for marl as well as for the fault material. However, using Plaxis, or other FEM software, did not give the opportunity to model block movement by default. For this, the blocks had to be generated manually for which the location and properties were chosen arbitrarily. Although, block failure was not modelled in this research, limited insight of this phenomenon was obtained by analyzing the load case of a boulder acting on top of the lining in the fault zone (section 4.2.7).

### 4.2.2. Optimal model geometry

From the preliminary analyses, it was established that the normative geometry of the model was that for which the ground properties were the lowest. Based on this, the optimal geometry was chosen based on the cross section with fault material (cross section 2) and applied to all the other cross sections.

To find the optimal geometry, one started by choosing a very large area so that boundary effects were excluded. The width of this model was $X_{max}$ = -$X_{min}$ ≈ 10 D = 100 meters. The thickness of the rock mass underneath the tunnel ring (Z) was set to 10 D as well. The overburden $Z_0$ was modelled as the real overburden height, which was 215 m above the tunnel top. In the 2D Plaxis models 15-nodal elements were implemented.

The optimal geometry for the model was determined by reducing the geometry size per direction to the point where the maximal ring forces and displacements deviated more than 1% from the initial model. It was chosen to first reduce the overburden thickness ($Z_0$) until expected divergence of the result was obtained. The reduction of $Z_0$ had to be compensated by a vertical load at the top boundary, that was quantified by the multiplication between the volumetric weight of the rock mass ($\gamma$) times the reduced overburden thickness ($\Delta Z_0$). Then the search of the optimal geometry proceeded based on the model dimensions before divergence occurred, this by implementing a comparable analysis for the bedding thickness (Z) and for the model width (X).

Doing the above mentioned analysis, resulted in a model with minimal influence of boundary effects on the lining ring as explained in subsection 2.4.2. At this stage of the analysis it was chosen to implement a full model, instead of a half plane symmetric model, in order to take into account the asymmetric displacements that were measured in the rings from the Middle-East case.

### 4.2.3. Optimal mesh coarseness

Due to the large geometry of the numerical model, it was chosen to refine the mesh around the tunnel ring in the form of a circle or multiple circles. Thereby, the radius of the circle had to be chosen in such way that no unnecessary inaccuracy near the strata transition occurred. Generally, the boundary of the circle (filled with a denser mesh) had to be at a sufficient distance from the strata transition (1D and more). In figure 4.4 the mesh quality for a insufficient (left) and sufficient (right) mesh is illustrated, which was quantified in terms of "mesh quality" ranging between 1.0 for the best mesh element and 0 for the worst element. The horizontal blue line in the figure represented the strata transition and the smallest blue circle was the tunnel lining.

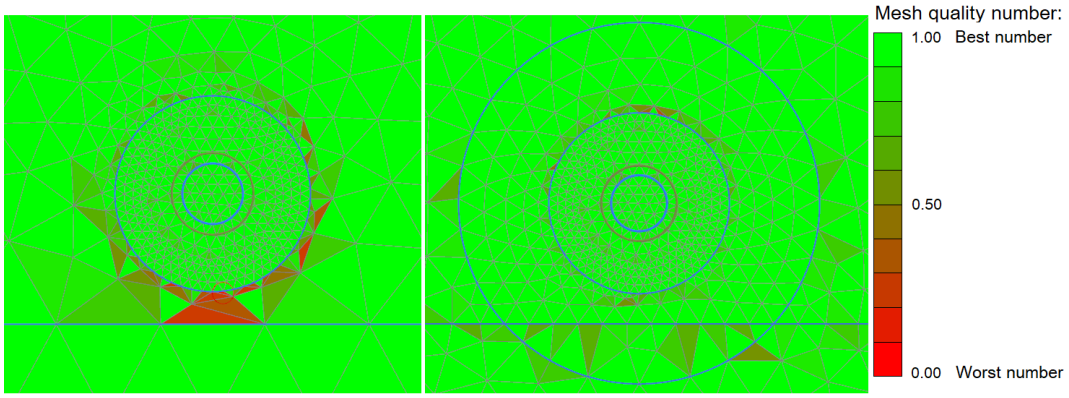


Figure 4.4: Mesh quality which depended on the meshing technique in a layered system,
where a mesh with insufficient element quality (left) was compared to a more sufficient quality mesh (right)

Actually, this meshing technique should be chosen separately for each cross section, depending on the stratification. In the case of cross section 2, the circle had a radius of approximately 3 times the tunnel diameter. After the choice of the optimal geometry was made, the sensitivity of the mesh coarseness was measured. Comparable to the search for the optimal geometry, the optimal mesh coarseness was chosen based on the point prior to the occurrence of large deviation (more than 1%) in the calculated results.

### 4.2.4. Sensitivity geotechnical parameters

Within geotechnical engineering, there were a lot of uncertainties on the ground parameters due their spatial variation. Therefore, most often a range of values for different parameters was given to perform parametric or sensitivity analysis. For this research, several parameters for which the influence on the calculation results was analyzed, were selected and subsequently a parametric study was carried out. Because this research focuses on extreme conditions, the initial model was based on the lowest parameters. The parametric analysis was done by varying one parameter at a time. In this section, the parameter determination was described. An overview of the parameters of the different geotechnical units and their ranges is presented in table 4.1.

| *Rock mass* | marl (q) | | limestone (eq) | | fault (F) | | dolomite (K) | |
|---|---|---|---|---|---|---|---|---|
| | min | max | min | max | min | max | min | max |
| $\Delta h_w$ [*m b.m.w.l.*] [1] | 0 | 60 | 0 | 60 | 0 | 60 | 0 | 60 |
| $E_i$ [$MN/m^2$] | 2000 | 9200 | 18000 | 70600 | 2000 | 9200 | 18000 | 54450 |
| $E_i/\sigma_c$ [−] | 100 | 300 | 300 | 500 | 100 | 300 | 400 | 500 |
| $\sigma_c$ [$MN/m^2$] | 7 \| 13 [2] | 20 | 60 | 140 | 7 | 20 | 45 | 135 |
| $GSI$ [−] | 40 | 60 | 40 | 60 | 15 | 25 | 45 | 70 |
| $E_{rm}$ [$MN/m^2$] | 319 | 4784 | 2874 | 36712 | 73 | 551 | 4026 | 39975 |
| $m_i$ [−] | 5 | 9 | 6 | 12 | 5 | 9 | 6 | 12 |
| $\phi'$ [°] [3] | 21 \| 25 | 39 | 38 | 55 | 16 \| 27.5 [4] | 30 \| 32.5 [4] | 37 | 56 |
| $c'$ [$kN/m^2$] [3] | 260 \| 340 | 730 | 700 | 2300 | 1100 \| 0 [4] | 300 \| 150 [4] | 700 | 3600 |
| $\nu$ [−] | 0.35 | 0.15 | 0.35 | 0.1 | 0.35 | 0.2 | 0.35 | 0.1 |
| $k_0$ [−] | 0.5 | 1.0 | 0.5 | 1.0 | 0.3 | 0.7 | 0.5 | 1.0 |

Table 4.1: Geotechnical parameters with corresponding ranges used to do a sensitivity analysis on the calculated lining forces and displacements

[1] m b.m.w.l. = meter below the maximal water level, which 510 m a.s.l. or 60 m above tunnel invert
[2] assuming the marl was in the non-squeezing condition, the lower bound value of intact strength was determined as in appendix A
[3] these Mohr-Coulomb parameters were determined based on the Hoek and Brown criterion as described in section 4.2.6 and appendix B
[4] the second values were quantities for a highly over-consolidated clayey material and not determined from the Hoek and Brown criterion

The maximum water level ($h_w$) was based on insitu measurements, and was mentioned in section 3.1. However, the influence of groundwater lowering was the most relevant factor to be analyzed in this research. It was assumed that the groundwater could have been lowered until the level of the tunnel invert, which was assumed to have happened in the Middle-East case if the backfilling of the bored tunnel acted as a dewatering system.

The determined intact rock stiffness ($E_i$) and strength ($\sigma_c$) is presented in table 3.1. However, the determined strength and stiffness for marl showed very high and unrealistic values for this type of rock. According to worldwide test data, the average stiffness of marl is 2000 MN/m$^2$ (Palmstrom and Stille, 2014). This value was kept as the lower bound value, while the upper bound value was kept at 9200 MN/m$^2$ according to the SI data from the case. The strength of marl was determined based on a typical rock stiffness-strength ratio ($E_i/\sigma_c$). This ratio typically varies between 100 and 300 for mudstones (Vallejo and Ferrer, 2011). However, based on the assumption that marl was in a non-squeezing condition (section 4.2.1) the lower bound strength was expected to be larger and calculated in appendix A. The strength of limestone and dolomite were also based on a typical ratio introduced by Vallejo, although the determined values are more realistic. This ratio varies between 300 and 500 for limestone and 400 and 500 for dolomite. The stiffness parameters for these rocks were kept the same as in table 3.1. The fault zone material was considered as either a residual marl (use intact parameters of marl) or a clay-like material (use Mohr-Coulomb). In the case that it was modelled as a clay, the parameters varied between 0 to 150 for effective cohesion (c') and 27.5 to 32.5 for the effective friction angle $\phi$.

The Geological Strength Index was determined for the marl and dolomite. However, the limestone and fault material were not encountered nor presented. Therefore, an assumption of the GSI for these formations was made. The weathering and fracturing degree of the limestone was expected to be comparable to the marl which layed above it. However, the fault material had a GSI of typically between 15 to 25. Compared to the GSI graphs presented in Marinos and Hoek, 2000, these values looked realistic. Limestones and dolomites showed GSI values between 35 and 60 for thin bedded masses, while massive units varied between 45 and 90. Silt- and claystones showed GSI values between 5 and 30 for sheared and brecciated rock, which were applicable in the fault zone.

The stiffness parameters of the rock mass were determined based on equation 4.2. Here, the minimal and maximal values for the $E_i$ and the GSI were inserted. It should be noticed, that during the analysis the $E_{rm}$ with the correct corresponding GSI were entered simultaneously.

The range for a realistic Poisson's ratio ($\nu$) and material parameter ($m_i$) for limestone, marl and dolomite were found in Marinos and Hoek, 2000. Typically, the very strong and stiff rock masses were closer to the behaviour of a concrete with a maximum value of $\nu$ is 0.1, while the fault material went down to 0.35 as for a clayey material.

The minimal and maximal values for the lateral earth pressure coefficient were mentioned in section 3.1. In the practice, the value that was most frequently applied for deep tunnels is $k_0 = 0.5$. However, based on the observed vertical ovalization the value could not have been larger than 1.0. On the other hand the $k_0$ could have been as low as 0.3 for deep tunnels, especially in softer materials (such as for the fault zone material).

Based on the objective to analyze the sensitivity of upper mentioned geotechnical parameters, the second cross section (as numerated in figure 4.2) was modelled as if the fault zone was infinitely wide and deep. However, in reality the fault width and depth was bounded by the adjacent rock, which were the marl - limestone from cross section 1 and dolomite - marl from cross section 3 (in figure 3.3 the topview and non-perpendicular course of the fault is shown). The model with realistic width of the fault zone was analyzed in the model calibration as described in section 4.2.7.

### 4.2.5. Sensitivity lining parameters

A few lining parameters were unknown, such as the joint stiffness ($k_r$), the interface parameter ($R_{inter}$) and the contraction ($C_{ref}$). However, their sensitivity on the analysis still had to be assessed. The analysis of the lining parameters was carried out by fixing all but one parameter, which was varied between the min and max values. An overview of the parameter ranges is presented in table 4.2, the ranges are explained in this section.

| $Parameter$ | min | max |
|---|---|---|
| $k_r$ $[kNm/m/rad]$ | 1E5 | fixed |
| $R_{inter}$ $[-]$ | 0.25 | 1.00 |
| $C_{ref}$ [%] | 0.0 | 2.0 |

Table 4.2: Tunnel lining parameters with corresponding ranges for the sensitivity analysis of lining forces and displacements

In Plaxis, the interaction between the backfill material and the lining was represented by the interface (defined as the adjacent material reduced by the parameter $R_{inter}$). From this starting point, the strength and stiffness of the backfill material was assumed to be equal to the connecting material as it is described in section 2.2.4, which in this case was assumed to be the adjacent rock mass. The case of a partly bonded connection between the backfill material and the lining, resulted in a $R_{inter}$ smaller than unity. However, in reality there is always some bonding present, meaning that $R_{inter}$ was always larger than zero. The lowest value that could be inserted in Plaxis is $R_{inter} = 0.01$, to find a numerically stable solution (because $R_{inter} = 0$ gives an infinitely weak and soft interface, resulting in infinitely high forces and displacements in the lining). From preliminary analyses it was found that a realistic lower bound value was equal to 0.25, therefore the sensitivity of the maximal forces and displacements was analyzed for a $R_{inter}$ between 0.25 and 1.0.

The contraction method to model relaxation of the ground was defined by one parameter in Plaxis which was $C_{ref}$. The contraction could vary between zero (meaning no contraction was present) for a very stiff ground and properly backfilled overcut and improper backfilling. The situation with no backfilling was seen as unrealistic and it was assumed that maximal contraction occurred for a volume loss caused by the tapered shape of the TBM. Typically, the tapering of the TBM is 5 cm over the whole circumference and results in 2.0 % volume loss. For a TBM with an outer diameter of 10.04 m such as in the Middle-East case this meant: $(100\% - A_{tapered}/A_{initial} = 100\% - \pi/4 * (10.04 - 9.94)^2)$.

Starting with Janßen's assumption to model the joint as a block which offered a certain rotational stiffness depending on the eccentricity in the joint (ratio between the moment and normal forces; e = $\frac{M}{N}$ [m]), the joint behaved as open or closed. The transition from a closed to an open joint occurred when the eccentricity (e) was larger than $\frac{1}{6}$ times the joint width (t). Results from preliminary analysis showed that, in case of stiff rock, the maximum calculated eccentricity was much lower than this transition value ($\frac{t}{6}$). This could be explained by the thick overburden which resulted in high normal forces (N), combined with the reduction of the moment (M) with increasing ground stiffness ($E_{rm}$), thereby reducing the eccentricity. However, in case of soft material, such as in the fault zone, this ratio increased beyond the transition value. In the case of e > $\frac{t}{2}$, the rotational stiffness of the connection was nil. Any ratio between $\frac{t}{2}$ and $\frac{t}{6}$, resulted in a $k_r$ between 0 and $467*10^3$ kNm/m/rad (assuming $E_{joint} = E_{concrete}$; b = 1.0 m and t = segment width (w) = 0.4). Figure 4.5 shows an illustration of the joint stiffness distribution with the corresponding eccentricity. Moreover, to study the sensitivity of the joint stiffness on the maximal forces in the lining, the range of $k_r$ was varied between 100 MNm/m/rad (a free connection is unrealistic because this would imply full instability of the ring, which is a structural issue that was not analyzed in this study) and fixed (infinitely large).

Additionally, the impact of global reduction of the lining stiffness due to joints was analyzed. This analysis was done by implementing a reduction factor $\xi_x$ varying between 0.2 and 1.0 (reduced stiffness: $EI_{eff} = \xi_x$ * EI). The use of global reduction was a convenient approach to take into account the effect of joints on the integral ring and precluding the need of an iterative procedure in case of the Janßen approach. This was most convenient in large and complex models, such as the three-dimensional one.

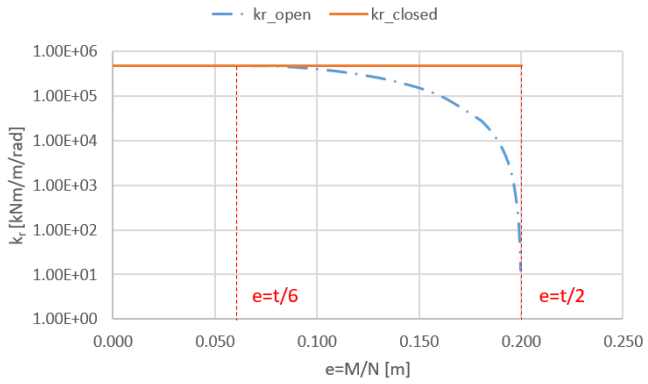


Figure 4.5: Distribution of the joint stiffness with respect to the eccentricity of forces in the joint according to Janßen (based on lining parameters from the Middle-East case

### 4.2.6. Model validation

The model validation in this study was done by comparing the calculated results with two other analysis. The first validation was an analysis where a different constitutive model was implemented, in this study chosen to be Mohr-Coulomb. The second validation was the closed form solution, developed by Erdmann. With this solution the maximal normal force and moment in the lining were calculated.

For the Mohr-Coulomb analysis, fitted parameters from the Hoek and Brown failure criterion were used. These were the effective internal friction angle ($\phi$') and effective cohesion (c'), which were determined in appendix B. The reference depth to calculate the corresponding Mohr - Coulomb parameters was at the center line of the tunnel. This was at 220 m depth which corresponded to effective vertical stresses of 3850 kN/m$^2$ and 4950 kN/m$^2$ in respectively the fault zone and the rock masses (based on a water level of 55 m above the center of the tunnel). The M-C parameters determined for the upper and lower bound values of H-B are shown in table 4.1.

The analytical solution introduced by Erdmann, documented concisely in Möller and Vermeer, 2006, assumed full bonding between the ring and the ground. The equations to calculate the maximal normal forces and maximal moment per unit meter are presented in appendix F. For the validation, it was needed to compare the results from Plaxis implementing $R_{inter}$ = 1.0, to account for the full bonding case. The calculations were based on the stress level at the center line of the tunnel.

### 4.2.7. Model calibration

The model calibration was meant to make the numerical model output fit the real measured deformations of the lining from the Middle-East case. This was done by changing several uncertain or undetermined parameters, until the best fit was found. However, the only location where lining deformation measurements were available, was in the fault zone, consisting of lining deformations (section 3.4.1). Therefore, the calibration of the model was only executed for the numerical model of the fault, while the model for the adjacent rock mass was not calibrated. To make the calibration more convenient, two models were set up; one for the homogeneous fault model (section 4.2.4) and the other as the heterogeneous model which took into account the effect of adjacent rock (figure 4.6).

The homogeneous fault model was used to find possible conditions that accounted for the vertical displacement of the ring in the Middle-East. However, the horizontal eccentricity could only be found by a model with non-homogeneous conditions which was represented by the heterogeneous model. Some variable parameters were defined and mentioned in figure 4.6, which were the fault width (W), the lining parameters (k, $R_{inter}$ and $C_{ref}$) and the layer boundaries ($Z_1$ and $Z_2$). Besides these, the ground parameters and the maximal water level and water table lowering of the whole model were variable as well, but limited in the ranges as presented in table 4.1 and 4.2.

An additional starting point for the model calibration was that the joints in the measured rings were open, this assumption was based on the observed water leakages in the joints. This meant that the eccentricity present in some of the joints, should be larger than $\frac{t}{6}$.

Furthermore, the volumetric weight and therefore the vertical and horizontal pressures in the different layers were not the same at the same depth. Because the layers were modelled separately as homogeneous layers, the transition of the stresses between adjacent layers was unrealistically abrupt. To make the transition of stresses more realistic, an additional calculation stage was added after the initial stage ($k_0$-procedure). This was called "the plastic stage", where the ground found an equilibrium for stress-strain distribution over the model. After resetting the displacements from this extra stage, the following stage was the excavation of the tunnel and the installation of the lining, followed by the stage where contraction occurred.

The parameters of the fault zone model that were calibrated are the following:

- The rock mass stiffness ($E_{rm}$), which was an uncertain property due to the lack of data of the fault zone material and for all the types of intact rock, had a very wide range;
- The water table lowering, which was an unknown quantity and was approximated, assuming the water table in the initial stage, was 60 m above the tunnel invert;
- The width of the fault zone (W), which was unknown due to the unknown course of the fault (figure 3.3);
- The depth of the layer transition ($Z_1$ and $Z_2$) from marl to limestone and dolomite to marl (in table 3.1 the values found in the longitudinal profile were presented);

- The interface between the backfilling and the lining ($R_{inter}$), which modelled the bonding between the two identities. It was assumed that $R_{inter}$ was a constant parameter over the tunnel circumference and the initial backfilling stiffness and strength were equal to that of the ground adjacent to the lining;
- The contraction of the lining ($C_{ref}$), which was a rather theoretical approach to simulate volume loss due to the TBM overcut. However, the contraction did not necessarily mean an uniform shrinkage of the lining, but because of the modelling limitations in Plaxis, was modelled as uniform;
- The input and output for the joint stiffness ($k_r$) should have matched each other (in terms of N and M). Additionally, a global reduction factor ($\xi_x$) for the lining stiffness based on the calibrated joint stiffness which matched the calculated displacements should have been found;
- The homogeneity of the fault material in previous modelling assumed a homogeneous fault zone. However, in many cases, boulders (which are large rock blocks) could be encountered. The effect of such rock block acting on the tunnel top was analyzed as well.

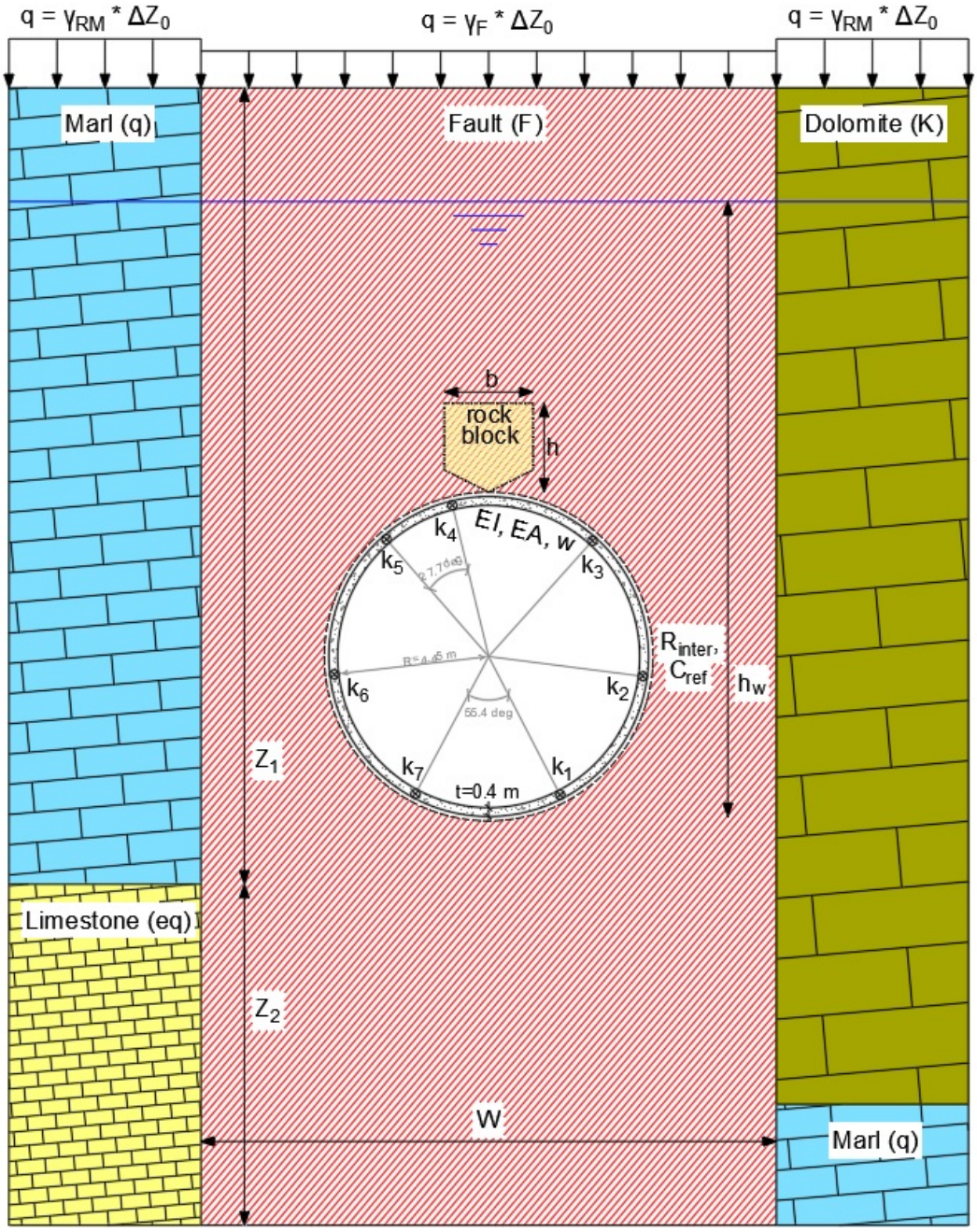


Figure 4.6: Ground model with a realistic stratification based on the geological profile from the Middle-East case and some defined variable parameters

## 4.3. 2D longitudinal model

For this research, the longitudinal model was set up based on the beam model, an assumption introduced in Blom, 1995. The beam model was a traditional method used to calculate the force distributions in a beam supported by springs, which was a typical structural engineering approach to model tunnels (described in Bouma, 1993). Subsequently, the vertical springs in fact represented the ground response to the tunnel displacement. The assumptions of the beam model are explained in this section. This is followed by the description of the method used to obtain an optimal geometrical model, the parameter variability for the sensitivity analyses and the model validation.

For this longitudinal model, the geological profile was divided into 3 zones, limited by thick vertical lines and shown in figure 4.7. The zones with their numbers correspond to the locations mentioned below:

1. Western adjacent geotechnical unit, which consisted of a layered system containing slightly weathered marl (q) and limestone (eq);
2. Fault zone, assumed to consist entirely of a mixture of highly weathered rock masses coming from the adjacent rock (dolomite, limestone and marl);
3. Eastern adjacent geotechnical unit, which consisted of a layered system containing highly fractured dolomite (K) and slightly weathered marl (q).

The modelling assumptions and methodology used to analyze the longitudinal tunnel lining behaviour are described in this section. Generally, the methodology consisted of three steps, which are:

1. Finding the optimal geometrical model;
2. Analyzing the sensitivity of the geotechnical parameters on the model;
3. Analyzing the sensitivity of the lining parameters on the model;
4. Comparing the calculated models with an analytical solution.

An illustration of the set up of the longitudinal beam model is presented in figure 4.7. All the variables relevant to the beam model analyses are shown in this figure.

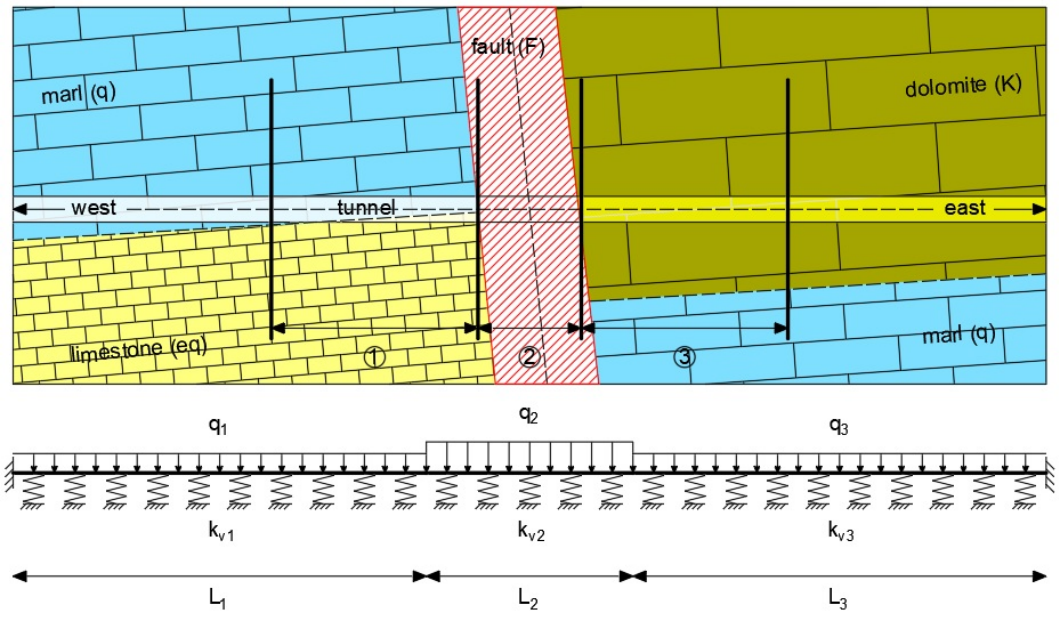


Figure 4.7: Translation from the geological profile to the beam model schematization, with according model parameters

### 4.3.1. Modelling assumptions

Implementing the beam model to model the longitudinal behaviour of a segmental tunnel lining, automatically implied certain basic assumptions. Besides these basic assumptions, additional assumptions were made for this specific research. These additional assumptions are described below.

- The tunnel segments and rings were connected to each other and work as one system. The connection at the tunnel ring joints (located between adjacent rings at each 1.6 m) could translate normal forces, shear forces and moments. This implied that the connection could be modelled as a rotational spring ($k_r$). Additionally, an assumption was made that the spring could be modelled implementing Janßen's theory for the segment joints.
- The rock mass was represented by elastic springs ($k_v$), which by itself assumed that the rock mass behaviour was fully linear elastic (Bouma, 1993). The spring captured the support stiffness of the entire tunnel circumference and was assumed to be equal to the ground stiffness ($E_{rm}$ calculated with equation 4.2). In equation 4.5, the formula to calculate the spring stiffness per unit length is shown, where $d_o$ is the outer diameter of the tunnel.

$$k_v = E_{rm} * d_o \; [kN/m/m^1] \tag{4.5}$$

- The longitudinal horizontal stiffness or frictional resistance of the ground was assumed to be infinitely large, which resulted in a model where the springs were only defined in terms of vertical stiffness.
- The vertical ground pressure acting on the tunnel lining was calculated assuming Singh's empirical determination of tunnel support pressure (Singh and Goel, 2011). This was a modification of the Terzaghi's arching theory, which depended on rock mass quality (Terzaghi, 1946). The ground pressure corresponded to the rock mass quality, which based on Terzaghi was the geological parameter RQD and is shown in table 4.3. To calculate the ground pressure per unit length of the tunnel ($q_v$), the pressure ($P_v$) was multiplied by the outer diameter of the tunnel ($d_o$) as shown in equation 4.6. As a simplification it was assumed that the tunnel weight was equal to the removed ground, so no additional pressure from the tunnel structure was taken into account.

$$q_v = P_v * d_o \; [kN/m^1] \tag{4.6}$$

| *Rock class* | I | II | III | IV | V | VI | VII | VIII |
|---|---|---|---|---|---|---|---|---|
| *RQD* [%] | 95-100 | 90-99 | 85-95 | 75-85 | 30-75 | 3-30 | 0-3 | -* |
| $P_v$ $[kN/m^2]$ | 0 | 40-70 | 0-40 | 40-100 | 100-200 | 200-300 | 300-600 | 600-2000 |

Table 4.3: Support pressure as defined by Singh representing the ground pressure that was resting on the tunnel lining and depends on the rock mass quality

* Did not depend on the RQD, but was valid for squeezing or swelling conditions.

- The bending resistance of the lining was assumed to be determined by the uncracked concrete stiffness (E) and the moment of resistance of the tube ($I = \frac{\pi(d_o^4 - d_i^4)}{64}$). The implemented moment of resistance was for a tube that acted as a beam with an outer ($d_o$) and inner ($d_i$) diameter of resp. 9.7 m and 8.9 m. The full bending resistance was EI = E x I = $35 * 10^6$ x 126.6 = $4430 * 10^6$ [kNm$^2$].

### 4.3.2. Model geometry

In the beam model, the only variable parameters for the geometry were the tunnel lengths located in zones 1 to 3 and represented by $L_1$ to $L_3$ as shown in figure 4.7. To obtain a valid model, the boundary effect on the force and moment distribution on the lining in and around the fault zone should have been negligible. To find the distance for which the boundary effects were negligible, the fault width ($L_2$) was set to a maximum of 40 m. The boundary condition was set to fully fixed, but had no influence as the boundary effects should be excluded. As an approximation, the wave length (Bouma, 1993) could be calculated to set an upper boundary value for $L_1$ and $L_3$ (equation 4.7). Based on preliminary analyses, the remaining parameters should have been set to a normative combination defined as follows:

- maximal rotational stiffness in the ring joints ($k_r$) and the lining stiffness (EI) over the whole tunnel;
- minimal stiffness values of the rock mass ($k_v$) in zones 1 to 3;
- minimal ground pressure (q) in zones 1 and 3 and maximal ground pressure in zone 2;

$$\lambda = \frac{2\pi}{\beta} \; [m] \tag{4.7}$$

$$\beta = \left(\frac{1}{4}\frac{k_v}{EI}\right)^{\frac{1}{4}} \; [m^{-1}] \tag{4.8}$$

### 4.3.3. Sensitivity geotechnical parameters

In the geometrical model, there were only a few input parameters that needed to be defined. However, the sensitivity of these parameters was of great importance for the results of the calculations due to their variability. The analysis of the sensitivity of the ground parameters was done by selecting different values in different zones for one parameter, while the other parameters were kept constant. The parameters for which the sensitivity was analyzed, were the ground stiffness ($k_v$) and the ground pressure ($q_v$) acting on the lining. The main purpose of the analysis was to find the critical loading combination. Additionally, the fault width ($L_2$) was varied. An overview of the parameter ranges was presented in table 4.4.

The ground stiffness ($k_v$) representing the rock mass was based on the rock mass stiffness ($E_{rm}$). The spring took into account the support of the rock mass for the entire tunnel width. The spring stiffness range was calculated based on the rock mass stiffness as described in section 4.2.4.

The ground pressure ($P_v$) depended on the rock mass classification (which in Terzaghi's theory was the rock quality designation (RQD)). As a first estimate, $P_v$ was calculated as a total pressure not taking into account the water pressure.

The width of the fault zone was varied between 10 and 40 meters. These quantities were based on the expected width of the fault zone and its uncertain character (non-perpendicular course of the fault and possibly non-abrupt transition from rock mass to fault zone).

| *Rock mass* | marl (q) | | limestone (eq) | | fault (F) | | dolomite (K) | |
|---|---|---|---|---|---|---|---|---|
| | min | max | min | max | min | max | min | max |
| $E_{rm}$ $[MN/m^2]$ | 319 | 4784 | 2874 | 36712 | 73 | 551 | 4026 | 39975 |
| $k_v$ $[MN/m^1]$ | 3094 | 46405 | 27878 | 356106 | 708 | 5345 | 39052 | 387758 |
| *RQD* [%] | 84 | 100 | - | - | - | - | 33 | 100 |
| *Rockclass* [%] | I | VIII | I | IV | VII | VIII | I | V |
| $P_v$ $[kN/m^2]$ | 0 | 600 | 0 | 100 | 300 | 2000 | 0 | 200 |
| $q_v$ $[kN/m^1]$ | 0 | 5820 | 0 | 970 | 2910 | 19400 | 0 | 1940 |

Table 4.4: Geotechnical parameters with corresponding ranges used for a sensitivity analysis on the calculated lining forces and displacements

### 4.3.4. Sensitivity lining parameters

The only two structural input parameters for the tunnel lining were the bending resistance (EI) and the rotational stiffness of joints ($k_r$). The sensitivity analysis was carried out by changing the rotational stiffness of the joints and the bending stiffness separately. With this analysis, the effective bending resistance $EI_{eff} = \xi_y$ * EI for different $k_r$ was determined. This analysis was used in the Plaxis 3D model, to estimate the influence of the ring joints on the results of the lining forces and displacements.

The input stiffness and calculated output were validated with the Janßen theory. Based on equation 4.9, where $E_{joint} = E_{concrete}$ and b = t = 8.6 m (assuming the width and height of the joint was the equivalent diameter for a rectangle), the maximal rotational stiffness for full joint contact was: $k_r = 1.85 * 10^9$ kNm/rad.

$$t = \sqrt{\pi \left(\frac{d_o}{2}\right)^2} \; [m] \tag{4.9}$$

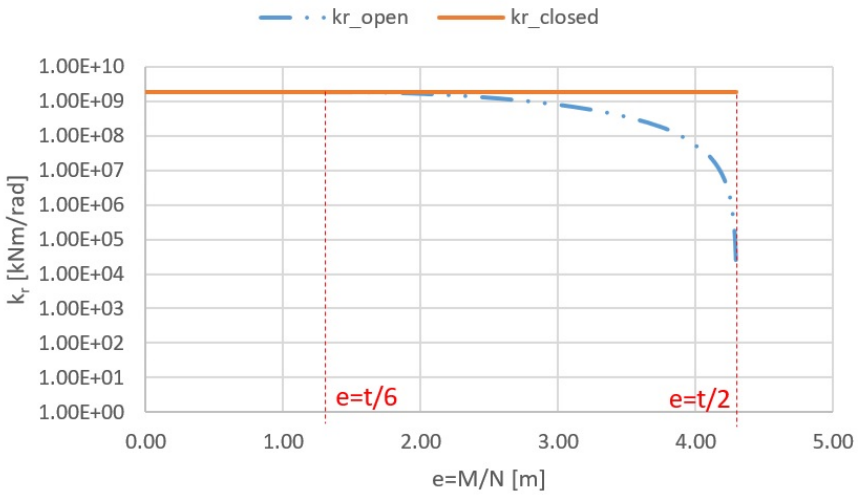


Figure 4.8: Distribution of the joint stiffness with respect to the eccentricity of forces in the joint according to Janßen (based on lining parameters from the Middle-East case

Furthermore, the normal force that was active in the lining joints was not an output parameter. In this model, it was assumed that the normal force was equal to the total jacking force (approximated by using diagram 4.9). Based on this diagram and a reference diameter of the TBM of 9.7 m, the total jacking force was expected to vary between 50000 and 120000 kN.

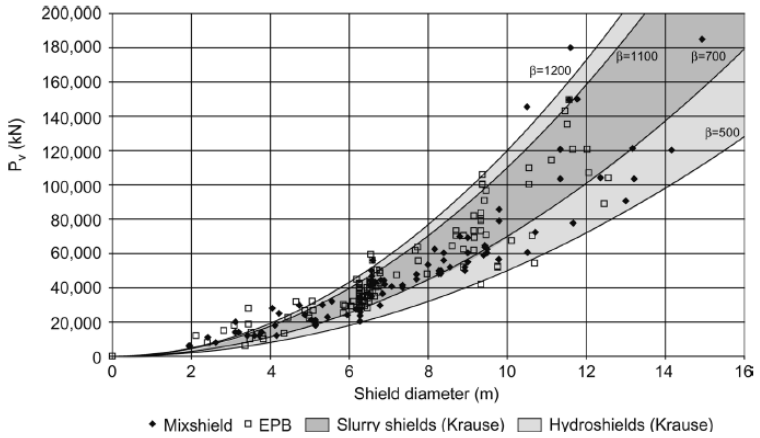


Figure 4.9: Diagram to empirically determine the total jacking forces acting on the lining (Maidl et al., 2012)

### 4.3.5. Model validation

For elastic supported beams, Bouma had determined standard load cases that could be used to verify simple load cases. For this research, one load case was used to support the validity of the method for analysis of the parameter sensitivity as described in sections 4.3.3 and 4.3.4. This load case consisted of an infinite beam supported by constant springs and charged by a constant load over a finite width (figure 4.10). Using this case, the maximal beam displacement and maximal bending moment were calculated.

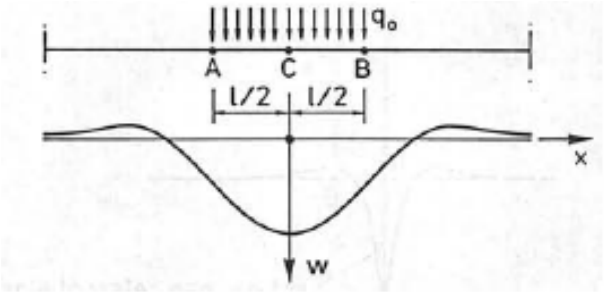


Figure 4.10: Most relevant standard load case as defined by Bouma, being an infinite beam supported by constant springs and charged by a constant load over a finite width

The derived formulas are shown in equations 4.10 and 4.11. These equations were used to calculate respectively the maximal deformation and bending moment of the beam.

$$w_{max} = \frac{q_v}{k_v}\left(1 - e^{-\beta\frac{L_2}{2}} * cos(\beta\frac{L_2}{2})\right) \; [m] \tag{4.10}$$

$$M_{max} = \sqrt{\frac{EI}{k_v}} * q_v * e^{-\beta\frac{L_2}{2}} * sin(\beta\frac{L_2}{2}) \; [kNm] \tag{4.11}$$

## 4.4. 3D model

After that all models relevant to this study were analyzed apart from each other in the 2D transversal and 2D longitudinal directions, a full 3D model was set up. The modelling assumptions, model geometry, mesh coarseness and geotechnical and lining parameters in the 3D analysis corresponded to the ones in the 2D Plaxis models. The methodology to analyze the 3D tunnel lining behaviour consisted of three main steps, which were:

1. Finding the representative model geometry and mesh;
2. Verifying the 3D model by comparing results with the 2D models;
3. Calibrating the 3D model with measured data by means of a parametric study.

These three steps resulted in three main 3D models. The first 3D model was used to validate the calibrated fault model from section 4.2.7. The second model was set up to match the 2D Plaxis models in the adjacent rock of the fault zone and to find a reliable y-axis of the 3D model. The final model was set up to analyze variable parameters and calibrate the calculated displacements to the measured data.

Figure 4.11 illustrates the definition of the coordinate system used in the 3D model, as the horizontal transversal direction of the tunnel was the x-axis, the horizontal longitudinal direction was the y-axis and finally the vertical direction was the z-axis.

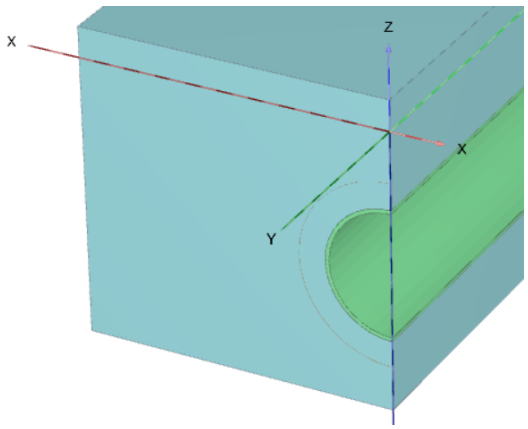


Figure 4.11: Coordinate system which was applied in the 3D Plaxis model, x-axis was the transversal direction with respect to the tunnel, y-axis was the longitudinal direction and z-axis was the depth

### 4.4.1. General for 3D models

In Plaxis 2D the elements can be 6-nodal or 15-nodal, while Plaxis 3D has the single possibility to implement 10-nodal elements. This could have led to discrepancies between 2D and 3D results, although the whole model set up matched each other. Therefore, the objective of the 3D geometry and mesh analyses was to find the output that corresponded to the 2D Plaxis results, which were used as reference calculations.

The transversal meshing method for the 3D model was kept exactly the same as in section 4.2.7, thus for the whole tunnel over its length. The deviation of the output at certain reference points was analyzed by changing the mesh coarseness.

The model geometry was kept as small as possible, due to the extensive running time of 3D models. Additionally, it was chosen to calculate a half space model which was used for all three models with exception of the model where the fault was modelled as non-perpendicular to the tunnel (with course angle $\alpha$).

The lining in the 3D analysis was modelled as a monolith tube without explicitly modelling the rings and longitudinal joint connections. It was chosen to use a reduction factor ($\xi_y$) on the lining stiffness parameter (EI) for modelling convenience and because it is often applied in engineering practice. The effect was only analyzed in the y-axis of the tunnel, as the x-axis was analyzed in the 2D Plaxis models. The limitation of this technique was the inability to calculate local displacements and forces from stress accumulation near joints, but gave reliable results for maximal displacements and forces.

Preliminary analysis of the 2D beam model showed that the critical conditions in terms of peak forces and moments in the lining were found for a combination of the following conditions:

- The largest stiffness of the lining ($k_r$ = fixed, or $EI_{eff}$ = EI);
- The smallest stiffness ($E_{rm}$) of the whole ground (fault and rock masses);
- The minimum ground pressures in the first and third zone combined with largest ground pressure in the second zone.

This meant that in the Plaxis 3D analyses, the case in which zone 1 and 3 had the largest stiffness and the case in which zone 1 and 3 had the smallest stiffness (figure 4.2) have to be analyzed separately. In both cases, the ground stiffness in the second zone (representing the fault zone) should be a lower bound value.

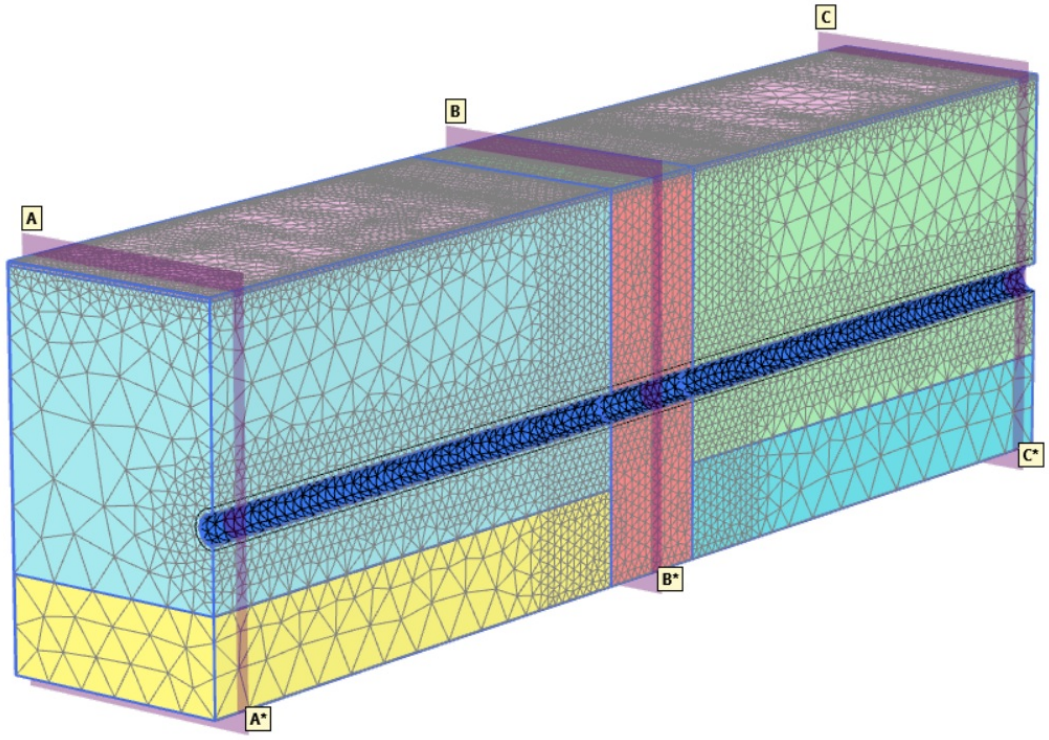


Figure 4.12: Full 3D Plaxis model with a perpendicular non-inclined fault zone, with designation of reference cross sections A-A*, B-B* and C-C* that correspond to 2D Plaxis models

### 4.4.2. Homogeneous model

The starting point for this model was that the dimensions in the x- and z-axis of the 3D model were equal to the optimal 2D geometry. The heterogeneous model was split up in three zones in the y-axis (figure 4.7). However, for the fault model validation only the middle zone ($L_2$) was of interest. For this reason, the model was set up of one zone, which represented the fault zone and in which the y-dimension was irrelevant (red volume in figure 4.12). The ground and lining parameters were fixed to the values found in the calibrated homogeneous fault 2D model described in section 4.2.7. The outcome of these models was compared and the mesh coarseness was adapted such that the 2D and 3D output matches each other as much as possible.

### 4.4.3. Heterogeneous model

After the homogeneous model was validated, the full model with multiple ground layers was set up as shown in figure 4.12. This model was used to find a representative y-dimension and to validate the 3D output with 2D output (cross sections A-A* and C-C* to 1 and 3 as in figure 4.2).

The reliable y-dimension was found based on the model with minimal boundary effects. In this heterogeneous model, the normative feature that defined the boundary effects was the horizontal stress distribution ($\sigma'_{yy}$). Therefore, the stress distribution was analyzed for different fault width and different stiffness ratios between the fault and adjacent rock mass. This analyses was carried out for a fault width ($L_2$) varying between 80 to 10 meters, while the stiffness ratio varies between 0.2 and 0.015 (extreme ratios between the fault and marl stiffness).

To reduce the risk to compare results bearing a numerical error, the calculated displacements and force distributions in the lining at cross sections A-A* and C-C* were taken 10 meters away from the real model boundary. These results were compared to those in cross sections 1 and 3 of the 2D model.

### 4.4.4. Calibration model

The calibration of the 3D model was done by comparing the displacements of the middle ring in the fault zone with the measured displacements (section 3.5). The values used in this parametric study are shown in table 4.5.

The preliminary analyses showed that a fault zone width between 10 and 80 meters was most relevant to this analysis. This is explained in more detail in the next chapter where the results are presented.

The normative loading conditions can be found in case of either minimal or maximal stiffness parameters of the rock mass and minimal stiffness of the fault. Therefore, both these combinations were analyzed in the this parametric study in search for the best calibrated model.

Based on the results of the parametric analysis, the impact of a reduced fault stiffness was further studied. While the minimal stiffness used in the 2D analysis was equal to E = 73 MN/m$^2$, the impact of a lower stiffness of E = 10 MN/m$^2$ was analyzed as well (typical value for soft clay in Palmstrom and Stille, 2014).

The global longitudinal lining stiffness was unknown, but was assumed to behave in a similar manner to the transversal direction (section 4.2.5). Therefore, a reduction factor ($\xi_y$) was used to define the stiffness reduction, applied to the lining stiffness (E) and shear modulus (G), which depends on E and $\nu$ (equation 4.12). However, the longitudinal stiffness of the lining depends on the transversal stiffness by means of the Poisson's ratio ($\nu$), shown in equation 4.13.

$$G = \frac{E}{2(1+\nu)} \tag{4.12}$$

$$\frac{E_y}{E_x} > \nu^2 \tag{4.13}$$

Assuming $E_x = 35 * 10^6$ kN/m$^2$ and $\nu = 0.2$, the minimal value for $E_y$ was $1.4 * 10^6$ kN/m$^2$. This meant that the minimal possible reduction factor was $\xi_y = \nu^2 = 0.04$, rounded up to a reduction factor of 0.1.

Finally, the effects of a different fault inclination angle ($\beta$) and a non-perpendicular fault course angle ($\alpha$) were analyzed. In this final step, the course of the fault was changed with respect to the longitudinal center point of the tunnel. The fault inclination and course angle took into account are shown in figures 4.13 and 4.14.

| *Parameters* | min | max |
|---|---|---|
| $E_{rm;fault}$ $[MN/m^2]$ | 10 | 73 |
| $k_{0;fault}$ [−] | 0.5 | 1.0 |
| $L_2$ $[m]$ | 10 | 80 |
| $\alpha$ [°] | 0 | 45 |
| $\beta$ [°] | 0 | 30 |
| $\xi_y$ [−] | 0.1 | 1.0 |

Table 4.5: Ranges of the variable parameters to find the calibrated 3D model based on the measured lining deformations

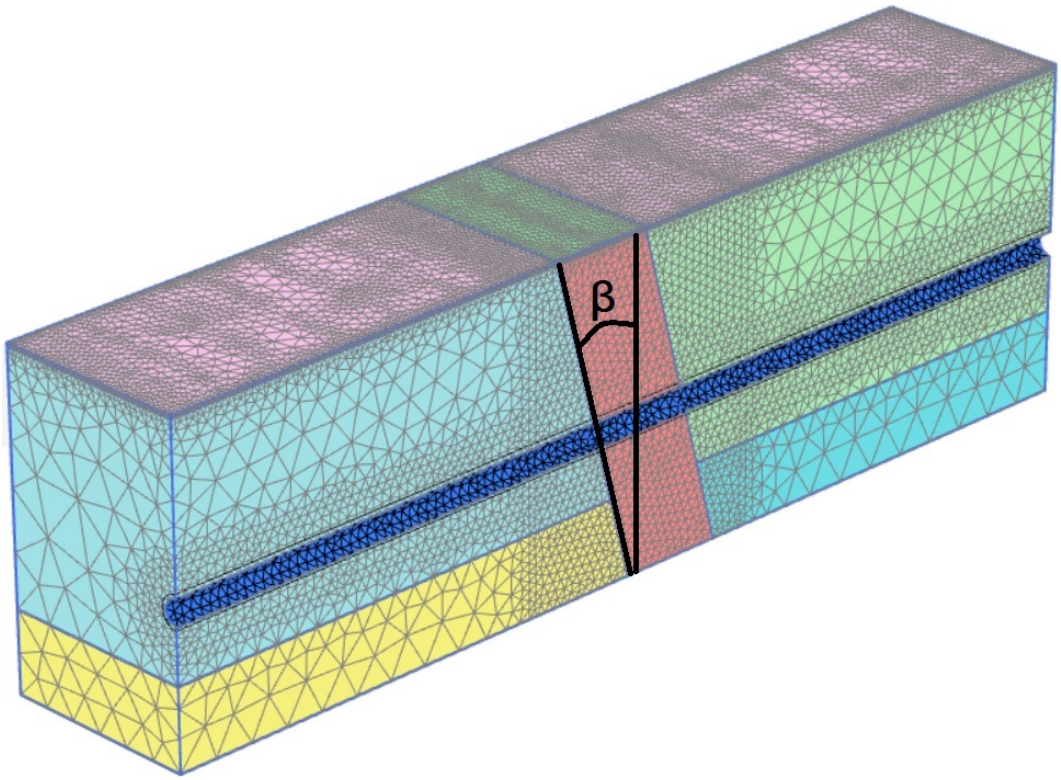


Figure 4.13: Geological profile in longitudinal direction showing the inclination angle of the fault ($\beta$)

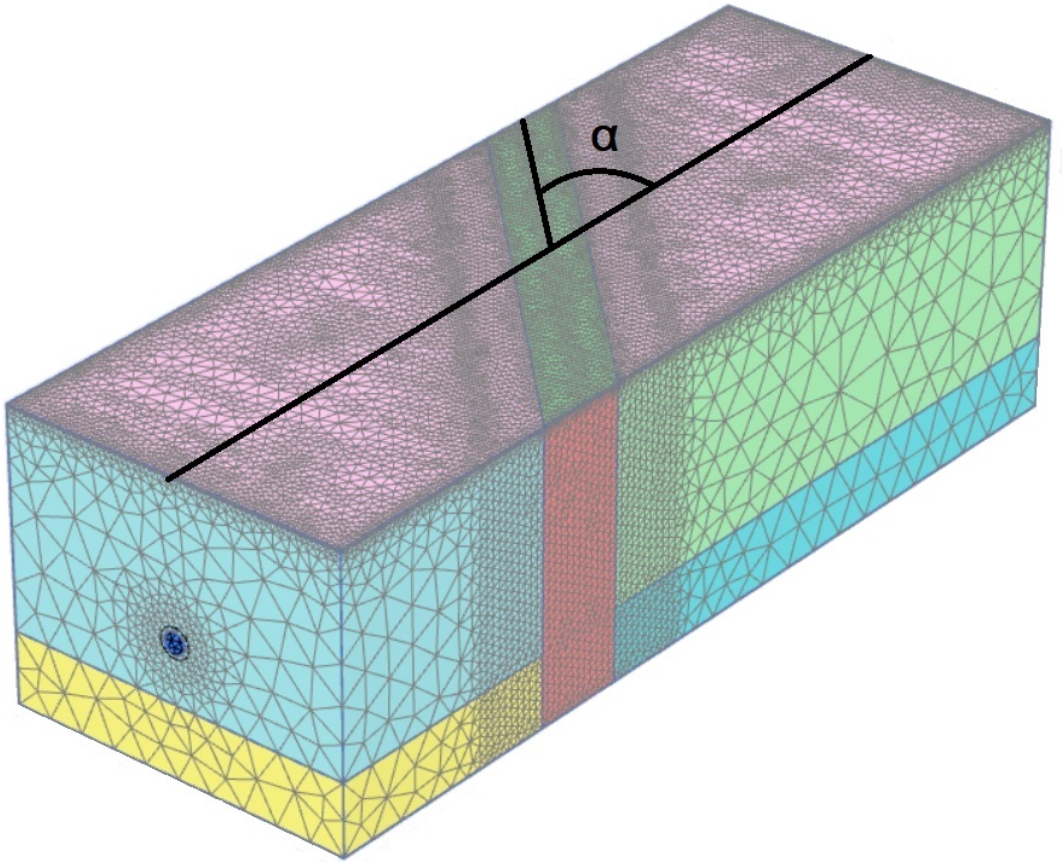


Figure 4.14: Top view of the model with a non-perpendicular fault showing the angle of the fault ($\alpha$)

# 5

# Discussion of results

In this chapter the results of the executed analyses are presented and discussed in the same order as the previous chapter. Additionally, the limitations of the studied models are mentioned per section.

## 5.1. 2D transversal model

The model set up and the results of the parametric study, the model validation, the model calibration and the limitations of the analyses are presented here in that order.

### 5.1.1. Initial model

Initially, the strategy was to model all the ground layers with Hoek and Brown. However, the fault zone material (GSI of 15) collapsed due to shear failure (shear strength $\tau$ exceedance) during the $k_0$-procedure, resulting in erroneous horizontal stresses ($\sigma_{xx}$).

The ratio between horizontal and vertical stress ($k_0$) is constant with depth in Mohr-Coulomb, because the internal friction angle ($\phi'$) is assumed to be constant for homogeneous material (equation 5.1). These relations were used to calculate the shear stress at failure for a material in given stress conditions (equation 5.2). This way it was calculated for which $k_0$, for a given c' and $\phi'$, failure occurred.

$$\sigma_3 = \sigma_1 * k_0 = \sigma_1 * \left(1 - sin(\phi')\right) \tag{5.1}$$

$$\tau = c' + \sigma_n * tan(\phi') \tag{5.2}$$

In Hoek and Brown the $k_0$ ratio is non-linear (equation 5.3). Therefore, it was impossible to define a constant ratio. Additionally, the shear stress at failure for certain $\sigma_{ci}$ and $m_i$ is non-linear with respect to coupled to the $k_0$ ratio. Plaxis iteratively searches for $k_0$ at failure, defined by the development of plastic points in the model. The ratio $\sigma_{3max}$ / $\sigma_{1max}$ gave values close to the $k_0$ resulting in shear failure and was used as a first estimation. Table 5.1 shows the analytically and numerically calculated $k_0$ ratios at failure. The vertical stress level for these calculations was set to 4.4 MN/m$^2$, based on a model height of 275 meters, volumetric weight of 20 kN/m$^3$ and water level of 110 meters from the bottom of the model.

$$\sigma_{1max} = \sigma_{3max} + \sigma_{ci} * \left(\frac{m_b * \sigma_{3max}}{\sigma_{ci}} + s\right)^a \tag{5.3}$$

| $Parameters$ | | | | | | | | | |
|---|---|---|---|---|---|---|---|---|---|
| $\sigma_{ci}$ $[MN/m^2]$ | 7 | 13 | 20 | 7 | 13 | 20 | 7 | 13 | 20 |
| $m_i$ $[-]$ | 5 | 5 | 5 | 9 | 9 | 9 | 9 | 9 | 9 |
| $GSI$ $[-]$ | 15 | 15 | 15 | 15 | 15 | 15 | 25 | 25 | 25 |
| $k_{0,estimate}$ $[-]$ | 0.55 | 0.48 | 0.44 | 0.47 | 0.41 | 0.36 | 0.41 | 0.34 | 0.30 |
| $k_{0,plaxis}$ $[-]$ | 0.60 | 0.51 | 0.44 | 0.49 | 0.40 | 0.34 | 0.40 | 0.31 | 0.25 |

Table 5.1: Calculated relation between vertical and horizontal stress using Hoek and Brown failure criterion

The results from table 5.1 showed that the range of Hoek and Brown parameters for the fault material can not be used for modelling with $k_0$ = 0.3, while Mohr-Coulomb parameters from the table can. Therefore, it was chosen to model the fault with Mohr-Coulomb.

The results of the search for an optimal model geometry are plotted and presented in appendix C. The optimal model geometry was found for dimensions: $Z_0$ = 100 m; Z = 50 m; X = 75 m. The optimal mesh coarseness in the denser mesh circle (with a radius of 15 m) was for coarseness c = 0.5. With this model geometry and mesh (figure 5.1) the 2D Plaxis analyses were executed.

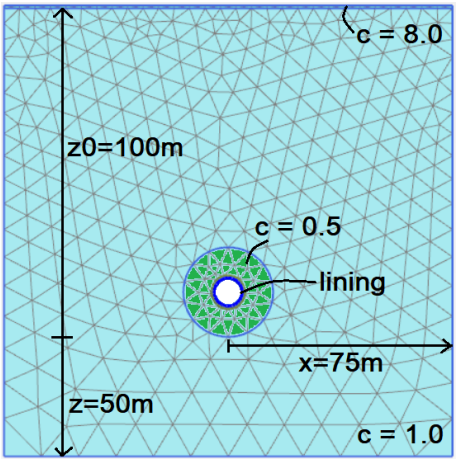


Figure 5.1: Optimal model geometry and mesh used in the 2D Plaxis analyses

### 5.1.2. Parametric study

The output that was analyzed with this parametric study were the vertical and horizontal stresses in the ground model and the displacement of the tunnel ring, divided into ovalization and translational displacements. Additionally, the influence of the parameters on the force distribution in the lining (needed for structural analyses) the normal forces and moments was analyzed as well.

#### Fault (cross section 2)

The results led to the conclusion that particularly E, $k_0$ and $k_r$ or $\xi_x$ affected the output the most. Decreasing $R_{inter}$ resulted in an exponential increase of lining ovalization and moments. In addition, low interface factor led to heaving of the tunnel ring, which was not observed in the case. The illustrations of the parameter sensitivities are presented in appendix E. An overview of the calculated factors of increase/decrease with respect to the initial model is presented in table 5.2. The initial model consisted of lower bound values, except for $R_{inter}$ = 1.0, $k_r$ = fixed and $\xi_x$ = 1.0. The results from the table concluded that the normal force deviated the least, while the ovalization and maximal moment was affected the most.

| *Factor* | vertical ovalization ($u_y$) | horizontal ovalization ($u_x$) | normal force ($N$) | moment ($M$) |
|---|---|---|---|---|
| **Ground stiffness** ($E$) | **0.22** | **0.16** | 0.88 | **0.19** |
| Poisson's ratio ($\nu$) | 1.11 | 1.11 | 1.02 | 1.09 |
| Effective cohesion ($c'$) | 0.91 | 0.90 | 1.01 | 0.87 |
| **Stress ratio** ($k_0$) | **0.42** | **0.33** | 1.10 | **0.34** |
| Water level lowering ($\Delta h_w$) | 1.03 | 1.05 | 1.02 | 1.03 |
| Interface red. factor ($R_{inter}$) | 1.17 | 1.23 | 0.88 | 1.15 |
| Lining contraction ($C_{ref}$) | 1.32 | 0.72 | 0.86 | 1.01 |
| **Joint rotational stiffness** ($k_r$) | **1.85** | **1.73** | 0.96 | **0.51** |
| **Lining stiffness red. factor** ($\xi_x$) | **1.56** | 1.23 | 0.91 | **0.28** |

Table 5.2: Overview of the growth factor of each parameter on the output of the calculated displacement and force distribution in the lining ring with respect to the initial model

The horizontal ovalization for these analyses was almost symmetrical, with negligibly small deviation due to non-symmetric placement of lining segments. Vertical settlements of the ring were only observed in case of ground water lowering, which resulted in settlements proportional to the drop of the ground water level (figure D.10 in appendix E).

Figure 5.2 shows the typical deformation pattern for vertical ovalization, in which the center of the ring stayed in its initial position. The ovalization ratio in the figure was extreme, because $k_0$ was a lower bound value. The tunnel invert came up due to the compensation of the deformations of the ring and the ground displacements that occurred around the ring. The ground squeezed upward by means of a sort of wedge effect, due to increased vertical stresses at the sides of the ring. The maximal displacement and moment occurred at the tunnel top and invert and the maximal normal force at the sides of the ring.

Most of the parameters affected these distributions by proportional increase or decrease, except for $k_0$ and $C_{ref}$. Smaller $k_0$ resulted in larger ratios between vertical and horizontal displacements, while the vertical ground pressure stayed the same. Larger $C_{ref}$ led to the same observation as with $k_0$ (figure D.20 in appendix E).

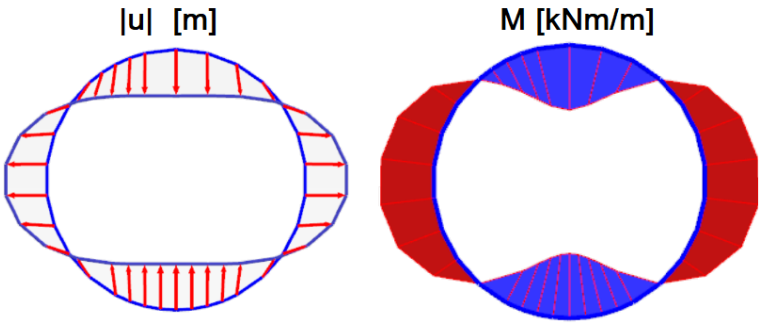


Figure 5.2: The typical distribution of displacements and moments along the lining ring

The change in vertical effective stress due to groundwater lowering is shown in figure 5.3. This indicates that the ground water drop resulted in approximately a linear increase in vertical stress, e.g. for $\Delta h_w$ = 60 m is $\Delta\sigma_{yy}$ = 60 m x 10 kN/m$^3$ = 600 kN/m$^2$. Moreover, this effective stress increase resulted in global ground settlements that corresponded to this change in stress.

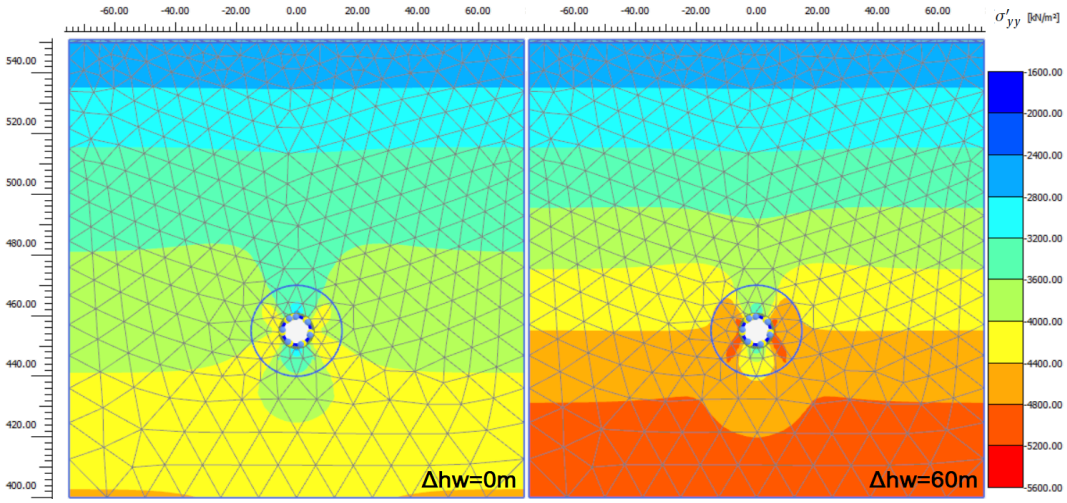


Figure 5.3: The change of vertical effective stress distribution due to ground water lowering over the model domain, on the left side without water lowering and right side with maximal water lowering

### West and East (cross section 1 and 3)

The overall influence of the parameters on the results was comparable to the fault zone material, only the ratio of influence and the extreme values for displacements and lining forces were different. Two exceptional cases were observed, namely when $C_{ref} > 0.5$ and when $k_0 = 1.0$.

For $C_{ref} > 0.5$, the horizontal displacement due to contraction exceeded the expanding deformation, yet it was relatively low in the stiff rock formations. For $k_0 = 1.0$, the horizontal deformation of the lining was equal to the vertical one (both contracting) and therefore uniform. Both exceptions are shown in figure 5.4.

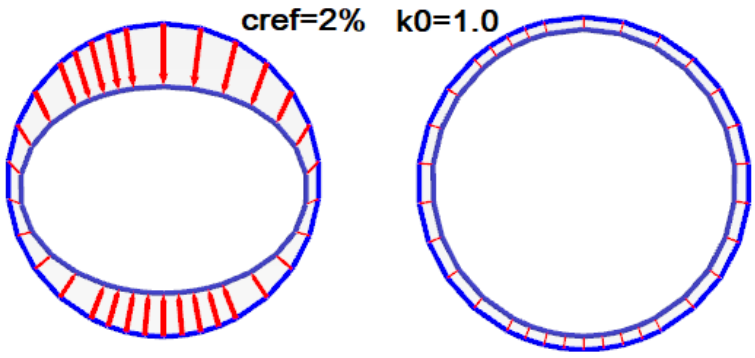


Figure 5.4: Distribution of absolute displacement for $C_{ref} = 2.0\%$ (left) and for $k_0 = 1.0$, which shows a deviating distribution compared to other cases

The results for lower bound values except for $\Delta h_w = 60$ m, $R_{inter} = 1.0$, $k_r$ = fixed and $\xi_x = 1.0$, are shown in table 5.3. The displacements in the fault model were larger then were measured in the Middle-East case. Moreover, the displacement in the rock agreed on the non-squeezing conditions, that ovalization should not exceed 1% of the tunnel radius which was 0.045 m. This meant that the lower bound parameters for the rock masses were valid for the 2D models. These results were later used for the validation of the 3D model.

| *Cross section* | 1 | 2 | 3 |
|---|---|---|---|
| Max. top displacement ($u_{y,top}$) [m] | -0.08 | -0.43 | -0.05 |
| Max. invert displacement ($u_{y,invert}$) [m] | 0.01 | -0.19 | -0.04 |
| Max. vertical radial ovalization ($u_{y,oval}$) [m] | 0.04 | 0.12 | 0.01 |
| Max. vertical settlement ($\delta_y$) [m] | -0.04 | -0.31 | -0.04 |
| Max. horizontal radial ovalization ($u_x$) [m] | 0.03 | 0.11 | 0.00 |
| Max. normal force ($N$) [kN/m] | 22190 | 19130 | 13760 |
| Max. moment ($M$) [kNm/m] | 1061 | 3028 | 135 |

Table 5.3: Calculated maximal displacements and forces in the lining in all 3 cross sections

### 5.1.3. Validation

As the fault zone was modelled with Mohr-Coulomb parameters, the only validation was with Erdmann. The rock masses were validated with both Erdmann, as well as Mohr-Coulomb.

### Mohr-Coulomb

From the comparison between Hoek and Brown and Mohr-Coulomb, it was concluded that no deviation (0.0%) developed in any combination of parameters. This observation underlined that tunnel modelling in stiff ground was a pure stiffness related problem, because the strength of the ground and failure criterion was irrelevant. Additionally, this meant that the rock masses could have been modelled with elastic behaviour.

### Erdmann

In appendix F, the formulation of Erdmann's solution combined with the calculated results are presented. Tables 5.4 and 5.5 show the deviation percentage between the output calculated with the analytical solution and with Plaxis for section 1 and 2. Like with the parametric study, the initial model properties were assumed to be lower bound values except for $R_{inter}$ = 1.0, $k_r$ = fixed and $\xi_x$ = 1.0.

| *Varied parameter* | $E$ [$MN/m^2$] | | $\nu$ [−] | $k_0$ [−] | | $\xi_x$ [-] |
|---|---|---|---|---|---|---|
| | 73 | 551 | 0.15 | 0.5 | 0.7 | 0.2 |
| Max. normal force $N$ [kN/m] | 5% | 7% | 8% | 1% | 1% | 12% |
| Max. moment $M$ [kNm/m] | 26% | 35% | 28% | 6% | 7% | 36% |

Table 5.4: Comparison of the maximum N and M in a ring with corresponding parameters in the fault zone between Erdmann and Plaxis

| *Varied parameter* | $E$ [$MN/m^2$] | | $\nu$ [−] | $k_0$ [−] | $\xi_x$ [-] |
|---|---|---|---|---|---|
| | 319 | 4784 | 0.15 | 1.0 | 0.2 |
| Max. normal force $N$ [kN/m] | 3% | 6% | 4% | 1% | 22% |
| Max. moment $M$ [kNm/m] | 4% | 19% | 8% | 100% | 19% |

Table 5.5: Comparison of the maximum N and M in a ring with corresponding parameters in the marl (west to fault) between Erdmann and Plaxis

This comparison showed that there was significant deviation between the Erdmann solution and the Plaxis results. Especially for fault material, the deviation in terms of moments was significant (36%). With marl the deviation was smaller, especially for a low stiffness. Additionally, it was observed that Erdmann gave the best results for cases $k_0$ = 0.5 and low E. Overall, Erdmann gave results that could be used as a first of results calculated with Plaxis, considering the limitations. The limitations were the increasing deviations with: stiffer ground, low $k_0$ and reduced ring stiffness.

## 5.1.4. Calibration

The measured ring in the Middle-East case was assumed to be located in the middle of the fault zone, as the maximal deformations were expected in the middle of the zone. The homogeneous fault was a relatively simple model, which gave a first impression of model properties that fitted the measured ring displacements. The heterogeneous model provided more insight about the effect of adjacent rock on the fault zone.

### Homogeneous fault

The $k_0$ ratio which resulted in fitting horizontal to vertical displacement ratio with the measured displacement was $k_0$ = 0.5. In figure G.1, the calculated displacements were compared to the measured ring data from the case. The parameters which resulted in a calibrated model, except for horizontal translation, were:
$E_{rm}$ = 150 MN/m$^2$; $\nu$ = 0.2; c' = 0 kN/m$^2$; $\phi'$ = 27.5°; $k_0$ = 0.5; $R_{inter}$ = 0.5; $C_{ref}$ = 0.2%; $\Delta h_w$ = 43 m

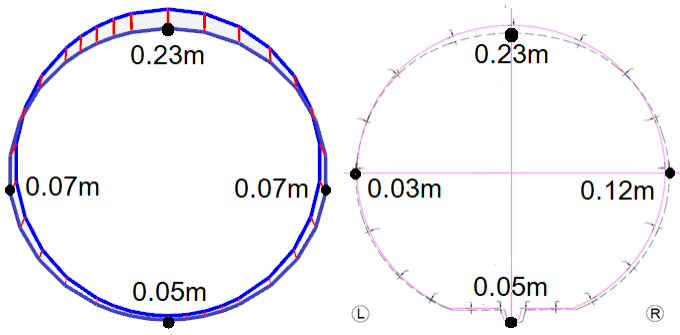


Figure 5.5: Comparison between the calculated displacements (left) and the measured displacements (right)

The displacements fitted precisely except for the horizontal translation. As the horizontal ovalization was assumed to be symmetric, the measured horizontal ovalization was actually $u_x$ = (0.03 + 0.12)/2 = 0.075m, which was found in the Plaxis output as well. Then the rotational joint stiffnesses were iteratively changed until the in- and output eccentricity corresponded to each other (Janßen's theorem). In table 5.6, the found joint stiffnesses are presented (appendix G). The numeration of the connection points was kept according to one illustrated in figure 4.3.

| *Joint #* | Stiffness ($k_r$) [*$10^3$ kNm/rad/m] | Moment (M) [kNm/m] | Normal force (N) [kN/m] | open/closed joint |
|---|---|---|---|---|
| k1 | 452 | 1086 | 13426 | open |
| k2 | 355 | 1887 | 17301 | open |
| k3 | 467 | 208 | 14453 | closed |
| k4 | 260 | 1576 | 12281 | open |
| k5 | 467 | 103 | 14258 | closed |
| k6 | 357 | 1884 | 17354 | open |
| k7 | 452 | 1088 | 13428 | open |

Table 5.6: Calculated joint stiffnesses with Janßen's theorem for the calibrated ring

Based on Janßen's approach, most of the joints were open due to the ovalization that occurred from large moments in the joints. This conclusion corresponded to the observation of water leakages due to open joints in the Middle-East case.

Table 5.7 presents the calculated maximal displacements and lining forces based on fitting $k_r$ and corresponding $\xi_x$. The range of realistic outcome was between the measured deformations +/- 3 cm (an assumed measurement error). Including this error, $\xi_x$ could have varied between 0.2 and 1.0 based on calculated displacements. The calculated maximal moment reduced by a factor 4 for $\xi_x$ = 0.2, which was significant and should have been taken into account in the structural design.

| $\xi_x$[−] | cal. | 1.0 | 0.8 | 0.6 | 0.4 | 0.2 | 0.1 |
|---|---|---|---|---|---|---|---|
| Max. top displacement ($u_{y,top}$) [m] | -0.23 | -0.23 | -0.23 | -0.24 | -0.25 | -0.26 | -0.28 |
| Max. invert displacement ($u_{y,invert}$) [m] | -0.05 | -0.05 | -0.05 | -0.04 | -0.03 | -0.02 | 0.00 |
| Max. horizontal displacement ($u_x$) [m] | 0.07 | 0.07 | 0.07 | 0.07 | 0.07 | 0.07 | 0.05 |
| Max. normal force ($N$) [kN/m] | 17350 | 17420 | 17220 | 16940 | 16470 | 15330 | 13480 |
| Max. moment ($M$) [kNm/m] | 2030 | 2138 | 1787 | 1389 | 973 | 519 | 279 |

Table 5.7: Comparison between the calibrated joints model and monolith ring model including a global reduction factor ($\xi_x$)

## Heterogeneous model

This calibration resulted in insight of the impact of adjacent rock masses on the fault zone behaviour. Preliminary analyses showed that the event with lower bound values for all geotechnical units, the ring displacements did not reach the amount of measured horizontal translation. This was mainly due to the reason that there was not enough horizontal displacement of the ground mass.

Therefore, the calibration was done by changing six parameters within a certain range, which were the E and $\nu$ of the marl, the $\Delta h_w$, the $W_{left}$ and $W_{right}$ and the $Z_2$ (appendix H). The combination of parameters which resulted in a fitting displacement pattern, was:

For the fault zone material:
E = 73 MN/m$^2$; $\nu$ = 0.35; $k_0$ = 0.5; $W_{left}$ = 5 m; $W_{right}$ = 30 m;
For the marl:
$E_{rm}$ = 200 MN/m$^2$; $\nu$ = 0.2; $\Delta h_w$ = 70 m; $Z_2$ = 400 m a.s.l.
For the lining ring:
$R_{inter}$ = 1.0; $C_{ref}$ = 0.0%; $k_r$ = fixed; $\xi_x$ = 1.0;

These parameters showed three features that contradicted assumptions earlier made for this geology. Firstly, the horizontal translation was only found in case of marl softer than predicted, namely 200 MN/m$^2$ instead of 319 MN/m$^2$, which seemed unrealistic because implied squeezing conditions in the marl according to Singh and Goel, 2011. Secondly, the layer transition between marl and limestone with respect to the tunnel depth was 30 m lower than determined by site investigation. The amount of boreholes was scarce and the nearest borehole was over 500 m away from the location, so this seemed realistic. Lastly, the ground water level was lowered further than expected initially, which was also possible.

The absolute displacements in the ground showed large displacements near to the top of the model (figure 5.6), which was mainly due to vertical settlement from ground water lowering. Zooming in on the horizontal displacements, the larger displacements (between 5 and 11 cm) turned out to be very locally distributed next to the ring.

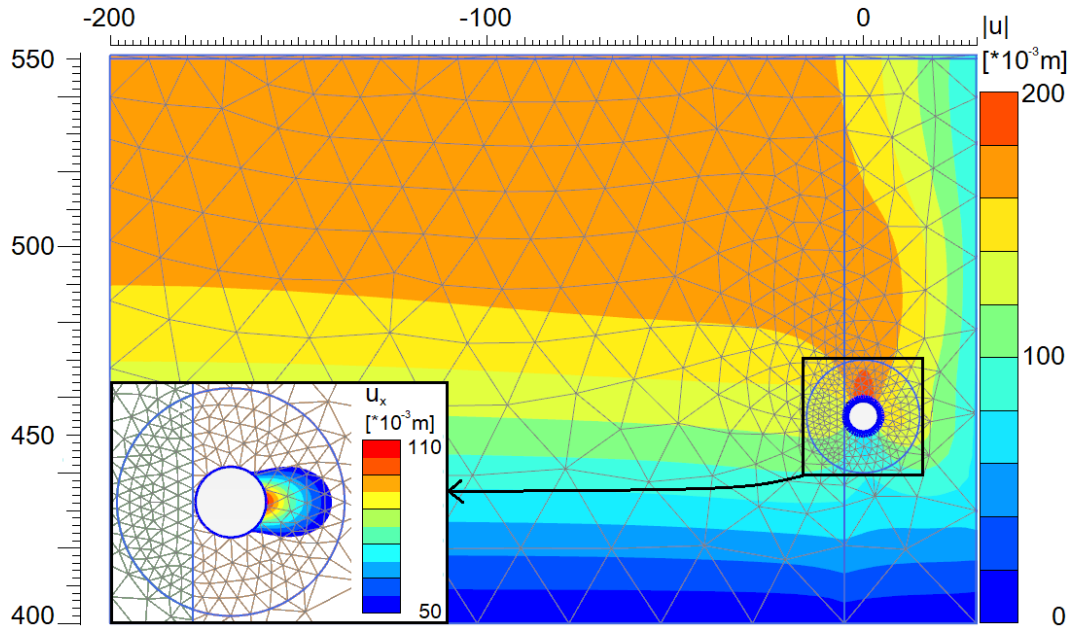


Figure 5.6: Absolute ground displacements (|u|) in the left half of the model domain, with a zoom-in on the larger horizontal displacements which developed next to the ring

The calibrated model outcome is presented in figure 5.7. Based on the four measurement points, the calculated displacements fit well. No further analysis of ring stiffness reduction was executed, as it was already studied for the homogeneous fault.

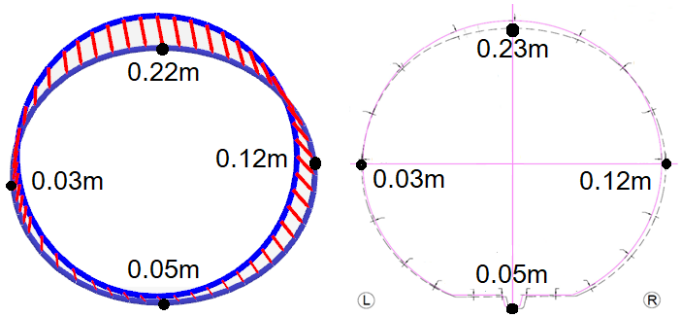


Figure 5.7: Displacement distribution for the calibrated ring, in which the deformations were A = 0.22/0.23 m; B = 0.12 m; C = 0.05 m; D = 0.03 m

Considering the maximal moments in the lining ring (figure 5.8), the maximal calculated value was 10% larger than in the homogeneous fault. This was justified by the lower fault stiffness, which resulted in larger moments.

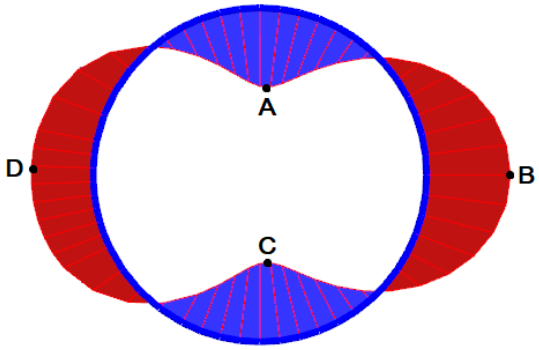


Figure 5.8: Moment distribution for calibrated ring, in which the moments were
A = 2186 kNm/m; B = 2342 kNm/m; C = 2185 kNm/m; D = 1729 kNm/m

### 5.1.5. Limitations

- Hoek and Brown and Mohr-Coulomb implied that the stiffness response was linear, while in reality the stiffness often depends on the stress history;
- The reliability of the determined properties in the Middle-East was questionable, as the calculated results based on lower bound values were too advantageous compared to the measured rings;
- The time-aspect of the ring displacement measurements was unknown, which counteracted the possibility to consider non-linear time-dependent behaviour;
- It was unknown whether initial misplacement of the lining was considered in the reference measurement of the lining position;
- It was assumed that the behaviour of the material in the fault zone was drained, due to the ignorance of the measurements and ground classification;
- Modelling the improper backfilling by means of lining contraction ($C_{ref}$) and stiffness reduction ($R_{inter}$), did not take into account initial relaxation of the ground after excavation;
- The manual calibration of the homogeneous and heterogeneous model led to one combination of parameters for which the calculated and measured ring displacements fit each other, while multiple combinations might have resulted in a fit.

## 5.2. 2D longitudinal model

The model was set up with a calculated wave length, which excluded boundary effects, validated with a standard load case (Bouma, 1993) and examined by means of a parametric study for several variable properties.

### 5.2.1. Initial model

Calculating the wave length for different geological units, led to the normative value of 80 m in case of soft fault material. This implied that the total model width should be 160 m to exclude boundary effects. However, the model consisted of multiple zones so the boundary effects were analyzed by reducing the $L_1$ and $L_3$, while keeping $L_2$ at 40 m. This analysis resulted in an optimal model with dimensions: $L_1$ = 30 m and $L_3$ = 20 m (appendix J). A typical moment distribution is presented in figure 5.9, where M1 and M3 are "clamping" moments and M2 is the field moment.

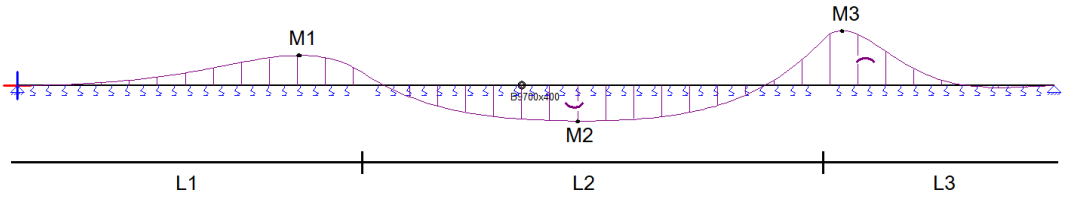


Figure 5.9: Typical longitudinal moment distribution for stiff adjacent rock and soft fault zone

### 5.2.2. Validation

Particularly, one standard load case of Bouma was suitable for the validation of the model in this research, presented in section 4.3.5. This case gave the possibility to calculate the maximal field moment and displacement in the fault zone ($L_2$). The load case considered a beam with an infinite length and a uniform vertical load over a fixed length (L = 40 m). The assumed conditions were lower bound stiffness of the fault material and upper bound ground pressure acting on the beam. These properties resulted in $w_{max}$ = 0.028 m and $M_{max}$ = M2 = 306 MNm. The length of the beam was set to 160 m, as the wave length for this spring stiffness was 80 m. Comparing the Matrix Frame solution with Bouma resulted in 2% deviation for the calculated moment and 0% for the deformation.

### 5.2.3. Parametric study

Firstly, the parametric study for extreme cases of lower and upper bound ground stiffnesses was executed. This concluded that the maximal global field moment (M2) was reached in upper bound stiffnesses for the adjacent rock combined with maximal pressure in zone $L_2$ and no pressure in $L_1$ and $L_3$. The maximal clamping moments (M1 and M3) were found when the same loading condition was present, but all the ground stiffnesses were lower bound values. The reduction of the fault width ($L_2$) to 10 m was analyzed as well and presented in appendix I.

Secondly, the impact of non-fixed ring joint stiffnesses was analyzed in the fault zone. The largest joint stiffness was set to $k_r$ = 1.85 * $10^9$ kNm/rad modelling a closed joint. The calculated stiffness was based on Janßen's approach, which initially can not directly be applied for the ring joints. However, the results showed that the moments were almost the same as for a fixed joint, which was realistic and also observed in Plaxis 2D models. The decrease of moments showed that the extreme load case corresponded to the predicted one (figure 5.10).

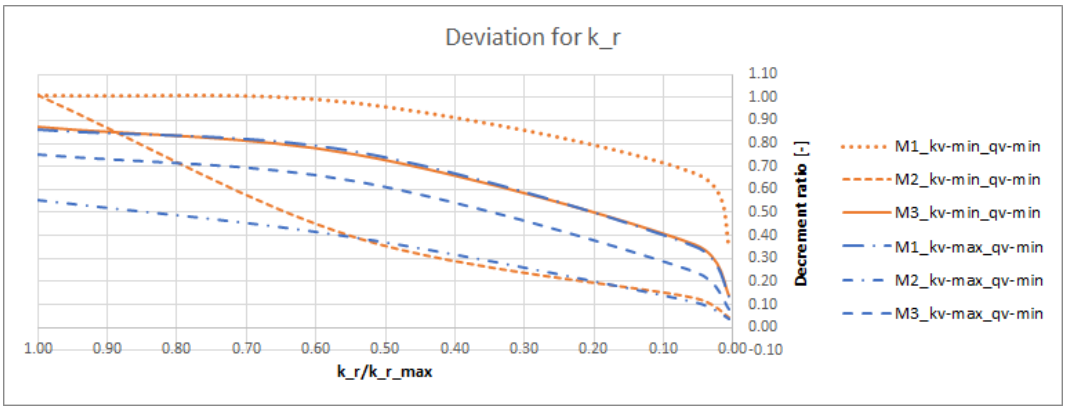


Figure 5.10: Decrement ratio of moments due to joint stiffness reduction for two extreme geotechnical cases

The most rapid decrease occurred for the field moment ($M_2$). Joint stiffness of half the closed joint stiffness, decreased by a factor 0.4. In figure 5.11 a comparable analysis is presented, only with a global reduction factor ($\xi_y$) for the lining stiffness instead of joint stiffness ($k_r$). The decrease in moments was almost linear with global reduction, while for a reduced joint stiffness this was not. Additionally, it was found that the estimation of a stiffness for a closed joint in the beam model could be done using Janßen's theorem.

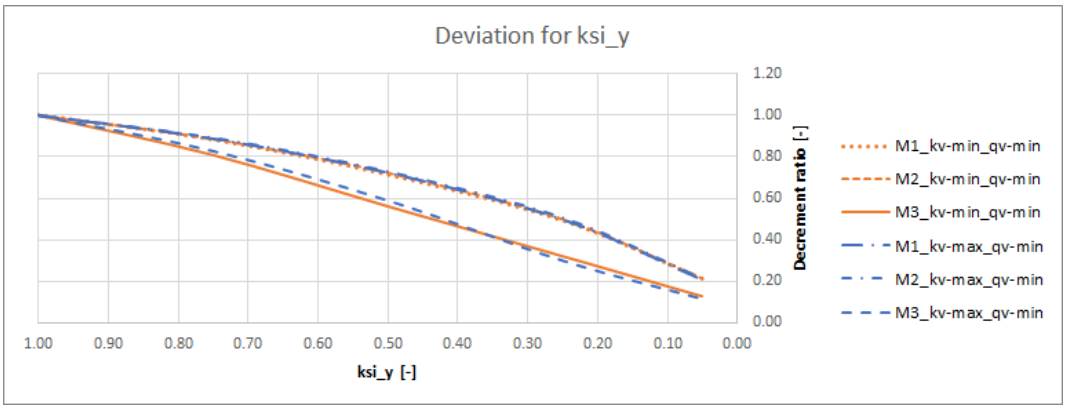


Figure 5.11: Decrement ratio of moments due to global lining stiffness reduction ($\xi_y$) for two extreme geotechnical cases

### 5.2.4. Limitations

- This model ignored the transversal behaviour of the tunnel (such as ovalization), which implied pure vertical loading and support of the structure;
- Particular aspects, such as groundwater lowering and ground-structure interaction, were not implicitly taken into consideration in this modelling approach;
- The ground pressures were based on Terzaghi's arching effect, but the correctness was not validated.

## 5.3. 3D model

After the 2D behaviour in both transversal and longitudinal direction of the lining was analyzed separately, an integrated 3D model was made. The objectives of the 3D analyses were to find critical loading conditions for the lining, calibrate the model based on case measurements and investigate the applicability of Plaxis.

### 5.3.1. Model set up

In general, the model set up in terms of geometry was the same as the optimal model that was found for the Plaxis 2D models (figure 5.1). The third dimension, being in the longitudinal direction of the tunnel, was chosen based on the horizontal effective stress distribution ($\sigma'_{yy}$) that was found (appendix K). The normative case for the longitudinal geometry was in which the marl and limestone consisted of upper bound properties and fault zone of lower bound properties (figure 5.12). The distribution of $\sigma'_{yy}$ is shown along the domain, with on the horizontal and vertical axis respectively the Y- and Z-axis is plotted.

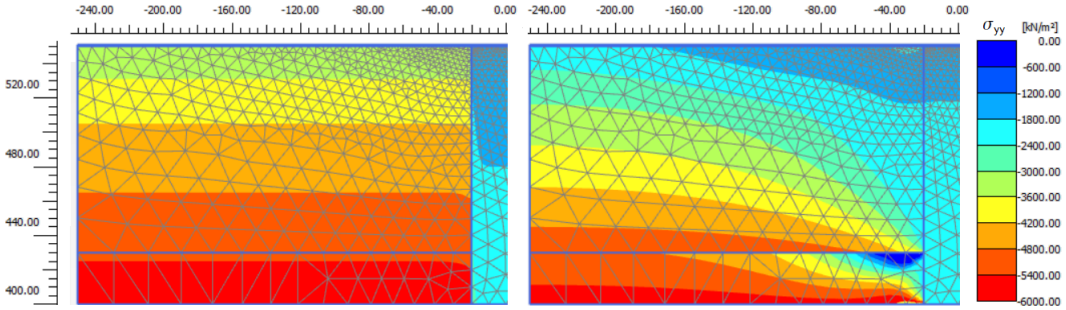


Figure 5.12: Horizontal effective stress ($\sigma'_{yy}$) distribution assuming upper bound properties for marl and limestone and lower bound properties for the fault zone, in the initial stage (left) and plastic stage (right)

From this figure it was concluded that the distribution of $\sigma'_{yy}$ did not reach the point were the stresses were equal to far field stresses at the side boundaries (Y = +/-250 m). Despite that, the distribution in and near the fault zone was expected to be accurate and not effected by the (vertical) boundary effect. As the main focus of the results was on the lining in the fault zone, the domain was considered as large enough.

Based on the distribution of $\sigma'_{yy}$, it was decided to refine the mesh coarseness in the fault zone and up to 30 meters outside the transition between rock and fault. However, results showed that this was not fine enough, so c = 0.25 was applied (figure 5.13). Still normal forces showed discrepancy even for c = 0.1.

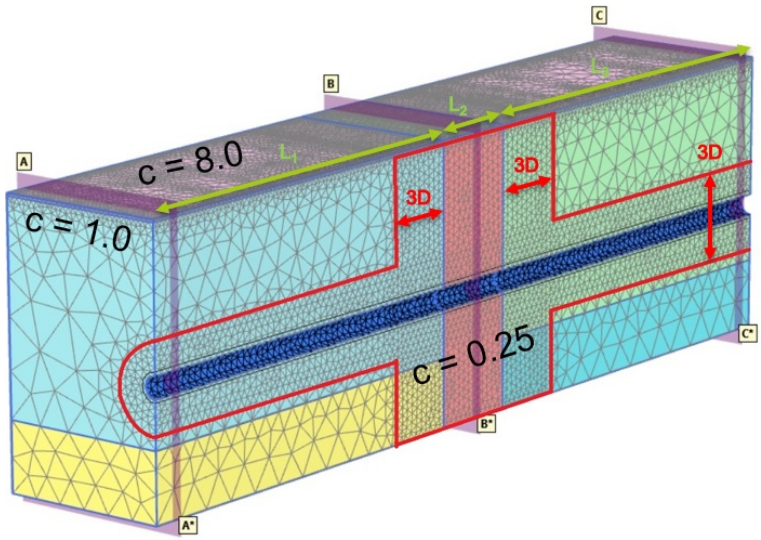


Figure 5.13: Final 3D model showing the finer mesh surrounding the tunnel and in and next to the fault zone

### 5.3.2. Validation

Prior to analyzing the full 3D model, the volume in Plaxis that represented purely the fault (pink colored volume at B-B* in figure 5.13) was validated with the results of the calibrated 2D homogeneous model. The results as presented in table 5.8 were found.

| *Cross section* | Fault | |
|---|---|---|
| | 2D | 3D |
| Max. top displacement ($u_{y,top}$) [m] | -0.23 | -0.23 |
| Max. invert displacement ($u_{y,invert}$) [m] | -0.05 | -0.05 |
| Max. vertical radial ovalization ($u_{y,oval}$) [m] | 0.09 | 0.09 |
| Max. vertical settlement ($\delta_y$) [m] | 0.14 | 0.14 |
| Max. horizontal radial ovalization ($u_x$) [m] | 0.07 | 0.07 |
| Max. normal force ($N$) [kN/m] | 17530 | 18930 |
| Max. moment ($M$) [kNm/m] | 2015 | 2018 |

Table 5.8: Calculated maximal lining displacements and forces in the fault zone (cross section B-B* and 2 for resp. 3D and 2D) for the calibrated homogeneous model

The output for the 3D homogeneous fault model showed 8% deviation for the calculated maximal normal force. This initiated to look at the distribution of the calculated normal forces in longitudinal and transversal direction, discussed in the next part. The maximal displacements and moment did match the 2D output very accurately.

The normal force distribution is shown in respectively figures 5.14(a) and 5.14(b). The longitudinal maximal normal force distribution contained a deviation of 1.8 MN/m for a homogeneous material, which was over 16%. This resulted in the need for acceptance of the error, as the 3D model was already quite extensive in terms of running time. This error was expected to increase in the model with abrupt layer transitions, in which the calculations became even more extensive. The deviation found for the maximal moment in this model was 15 kNm/m, which was less than 1% and therefore very accurate.

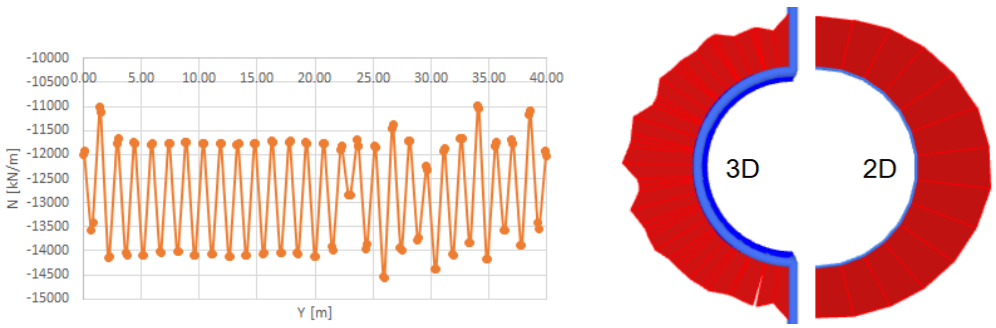


(a) (b)

Figure 5.14: Longitudinal maximal normal force distribution (a) and transversal normal force distribution along the ring in the middle of the fault zone (b) for $E_{fault}$ = 150 MN/m$^2$

After the model conditions were set equal to the ones for which the output in table 5.3 was obtained and $L_2$ = 40 m, the results of the calculated 3D models as shown in table 5.9 were found.

| $Cross\ section$ | A-A* | | B-B* | | C-C* | |
|---|---|---|---|---|---|---|
| $L_2 = 40m$ | 2D | 3D | 2D | 3D | 2D | 3D |
| Max. top displacement ($u_{y,top}$) [m] | -0.08 | -0.07 | -0.43 | -0.13 | -0.01 | -0.01 |
| Max. invert displacement ($u_{y,invert}$) [m] | 0.01 | 0.00 | -0.19 | -0.02 | 0.00 | 0.00 |
| Max. vertical radial ovalization ($u_{y,oval}$) [m] | 0.04 | 0.04 | 0.12 | 0.08 | 0.01 | 0.01 |
| Max. vertical settlement ($\delta_y$) [m] | -0.04 | -0.03 | -0.31 | -0.06 | -0.01 | -0.01 |
| Max. horizontal radial ovalization ($u_x$) [m] | 0.03 | 0.03 | 0.11 | 0.07 | 0.00 | 0.00 |
| Max. normal force ($N$) [kN/m] | 22170 | 20570 | 19130 | 16190 | 13500 | 11460 |
| Max. moment ($M$) [kNm/m] | 1058 | 977 | 3028 | 2229 | 129 | 115 |

Table 5.9: Calculated maximal lining displacements and forces in all cross sections for resp. 3D and 2D, as presented in section 5.1.2, for $E_{fault}$ = 73 MN/m$^2$ and $L_2$ = 40 m

These results showed a small deviation in the 3D output compared to 2D at cross section A-A* and C-C*. The displacements seemed to fit, but the forces decreased in the 3D output. This was clarified by looking at the distribution of the 3D forces, which turned out to contain a significant discrepancy. In the fault zone, which corresponded to cross section B-B*, the displacements and forces reduced. However, this feature was analyzed in more detail in the next subsection.

### 5.3.3. Calibration

After validation of the geotechnical cross sections in the 3D model, the search for a calibrated model is presented. The illustration and explanation of all set up models is given in appendix L, while the most relevant results are discussed in this section.

Prior to executing the calibration of the lining, the ground behaviour for different fault widths was analyzed. In figure 5.15, the longitudinal arching effect for lower bound ground properties and groundwater lowering is presented for changing $L_2$. The displacements in the fault zone showed not to be dominant for $L_2$ = 10 m. The displacement distribution transited from one rock mass to the other without a local increase in the fault zone. This simple analysis, which can be done with a 2D model, was used to predict the impact of the soft fault zone on the lining. When the fault zone has no impact, the lining design can be based on the rock mass stiffness.

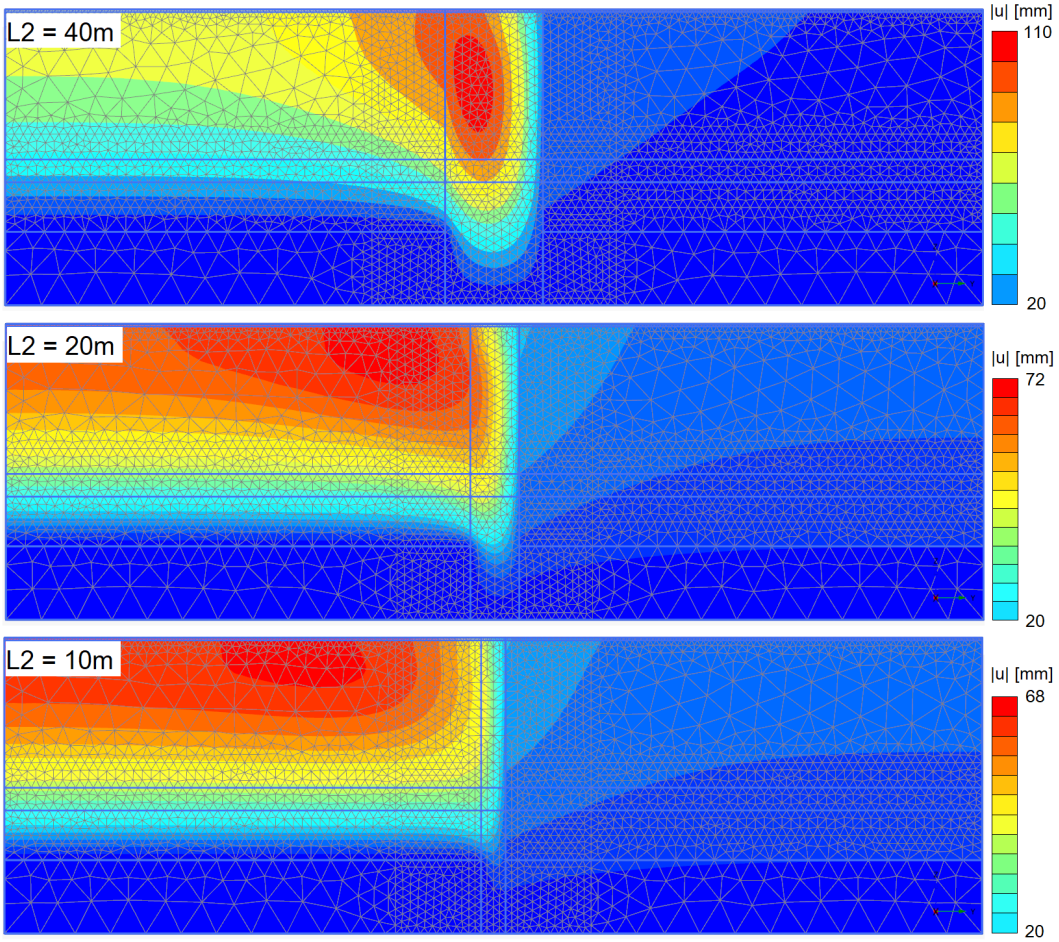


Figure 5.15: Ground displacements for lower bound properties after lowering of the groundwater level in the longitudinal direction

Figure 5.16 compared the tunnel invert displacement for lower and upper bound parameters of the adjacent rock. The results showed two noticeable features, namely that invert displacement of the middle ring (Y = 200 m) shifted from settlement to uplift between $L_2$ = 60 m and 40 m and an abrupt bump in the fault zone directly behind the transition from rock. Both these features were justified by one argument, which was that at a certain fault width the lining behaviour was dominated by transversal behaviour (ovalization). Directly after the transition from the rock mass to the fault zone, the settlement of the lining was negligible and the ovalization increased rapidly with increasing tunnel length towards the middle of the fault zone.

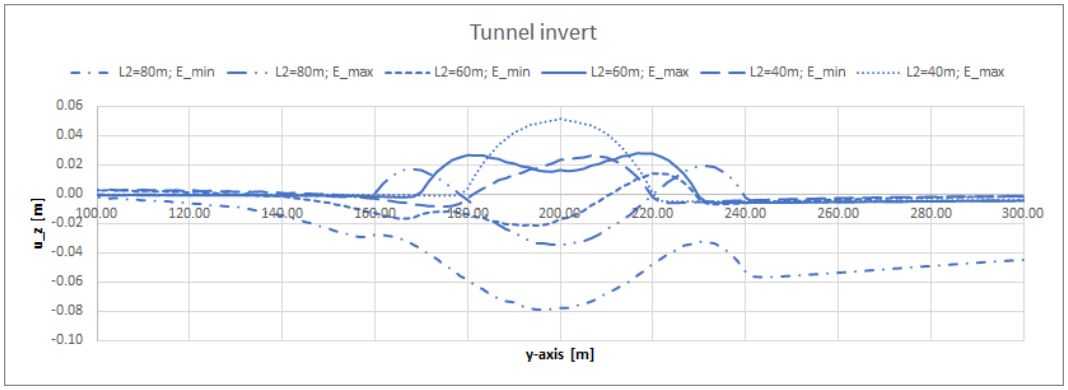


Figure 5.16: Comparison of different fault width and effect of adjacent rock stiffness (lower and upper bound properties) on the tunnel invert displacement for $E_{fault}$ = 73 MN/m$^2$

Analyzing the ovalization behaviour, keeping in mind the previously mentioned feature, it was confirmed that the ovalization increased rapidly after the transition to the fault zone (figure 5.17). However, a fault width of 1D ≈ 10 m showed a plain transition from one rock mass to the other, without a concave in the faultzone. Assuming lower bound ground properties still did not result in a fit with the measured ovalization. The amount of ovalization was not reached, nor the steep concave distribution in the fault zone.

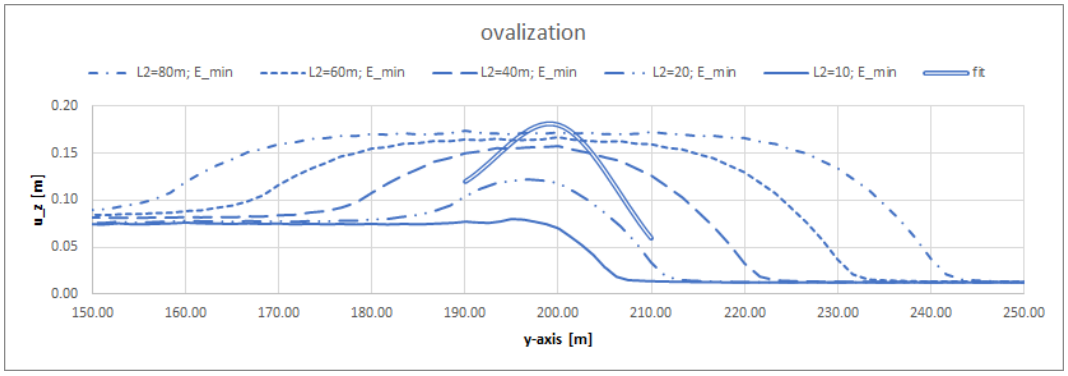


Figure 5.17: Comparison of different fault width and effect of adjacent rock stiffness (lower bound properties) on the tunnel ovalization for $E_{fault}$ = 73 MN/m$^2$

Furthermore, the impact of global lining stiffness reduction in the longitudinal direction ($\xi_y$) was analyzed. The result of calculated settlements shown in figure 5.18 indicated that a reduced lining stiffness led to increased settlements. On the other hand, the ovalization decreased as presented in appendix L. This analysis also showed that a very small $\xi_y$, results in difficulties for Plaxis calculations. Particularly, finding a converging solution became hard or even impossible, as the nodal strains became too large for finite elements. Based on these conclusions, it was decided to proceed the calibration without lining stiffness reduction, as the significance of $\xi_y$ was found to be minor for $\xi_y$-values that yet provide converging solutions ($\xi_y \geq 0.1$).

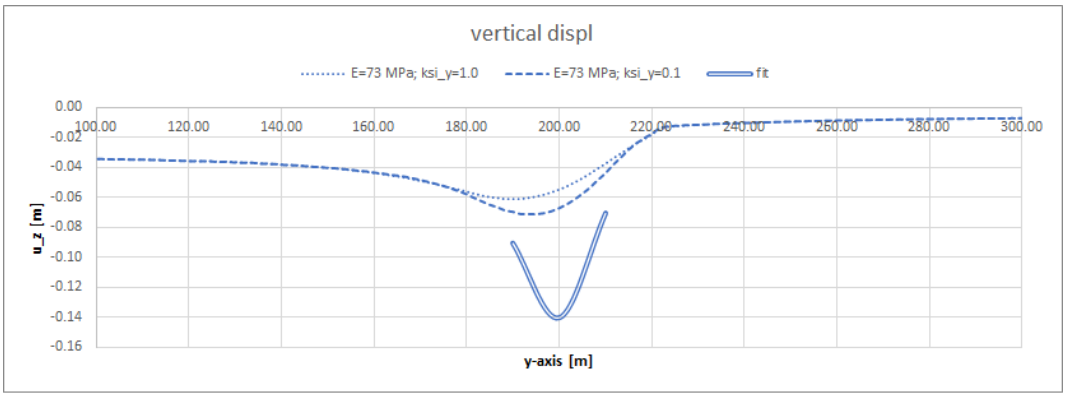


Figure 5.18: Influence of lining stiffness reduction ($\xi_y = 0.1$) on the tunnel settlement for $E_{fault}$ = 73 MN/m$^2$

However, the calculated results still did not satisfy the very abrupt and local behaviour of the measured rings in the faultzone. Therefore, the material stiffness in the fault zone was reduced to that of a soft clay, with E = 10 MN/m$^2$ (Palmstrom and Stille, 2014). This resulted in a moderate ovalization for $L_2$ = 1D = 10 m, which still agreed to the deformation requirements (figure 5.19). The calculated ovalization did fit the measured ovalization very well for $L_2$ = 20 m, independent of the adjacent rock stiffness. Based on this specific analysis, with corresponding assumptions, it was found that the impact of the fault zone on the tunnel lining displacements is negligible for $L_2 \leq$ 1D.

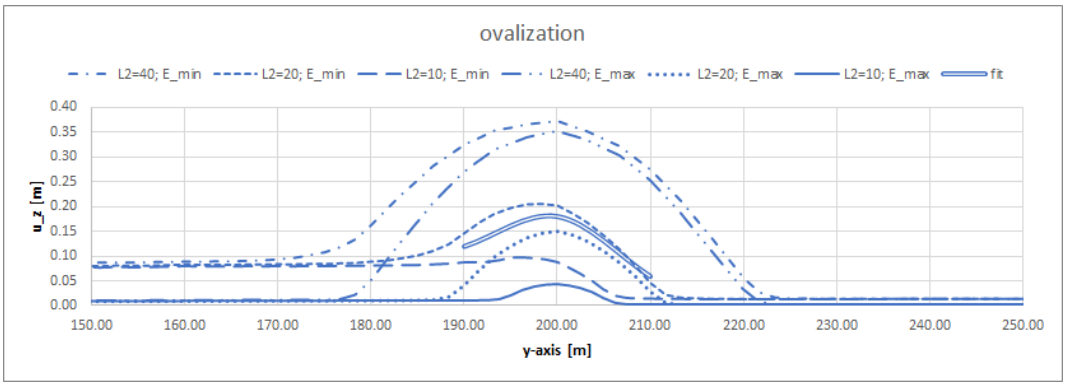


Figure 5.19: Comparison of different fault width and effect of adjacent rock stiffness (upper bound properties) on the tunnel ovalization for $E_{fault}$ = 10 MN/m$^2$

Because the ground stiffness reduction resulted in a fit for the ovalization, the settlements for this case were analyzed as well. Unfortunately, the corresponding settlements did not fit the measured settlements. Figure 5.20 shows that the calculated results were not large enough, nor was the distribution steep enough to fit the measured displacements. It was suspected that a Finite Element model in which the tunnel composed of a monolith plate, would not result in a calibrated model. Rather, as a suggestion, explicit joint modelling or the application of a method that allows for abrupt or discontinuous displacements (e.g. Discrete Element method) could be analyzed in future studies.

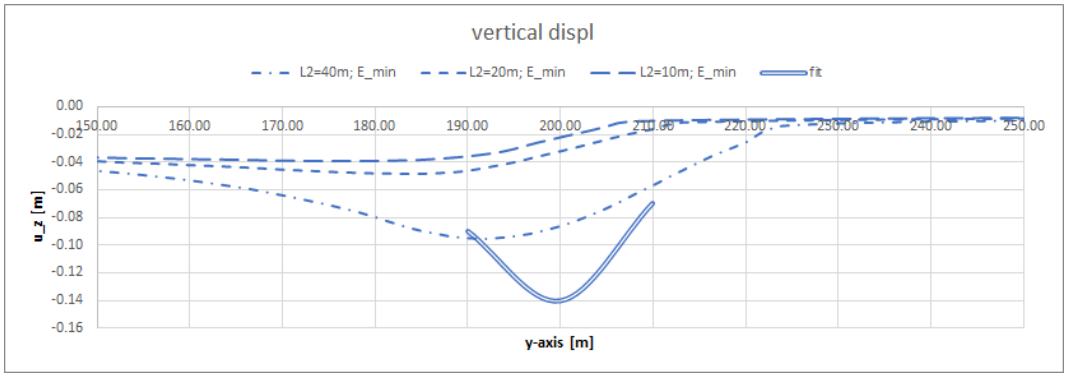


Figure 5.20: Comparison of different fault width and effect of adjacent rock stiffness (upper bound properties) on the tunnel settlement for $E_{fault}$ = 10 MN/m$^2$

The previously calculated models assumed a fault zone perpendicular to the tunnel alignment. Then the cases in which the fault was non-perpendicular or inclined were studied. The calculated vertical deformations showed distributions that were comparable to the perpendicular fault. The horizontal displacements for a non-perpendicular fault, showed a small horizontal shift (figure 5.21). However, there was no global translation that fitted the displacements as measured in the Middle-East case. The event of a softer fault zone gauge would have led to a larger shift, as shown in appendix L. Despite that, increased horizontal ovalization made such an event very unlikely. Another cause for this shift could be initial misplacement of the lining rings, which was not reported in the measurements.

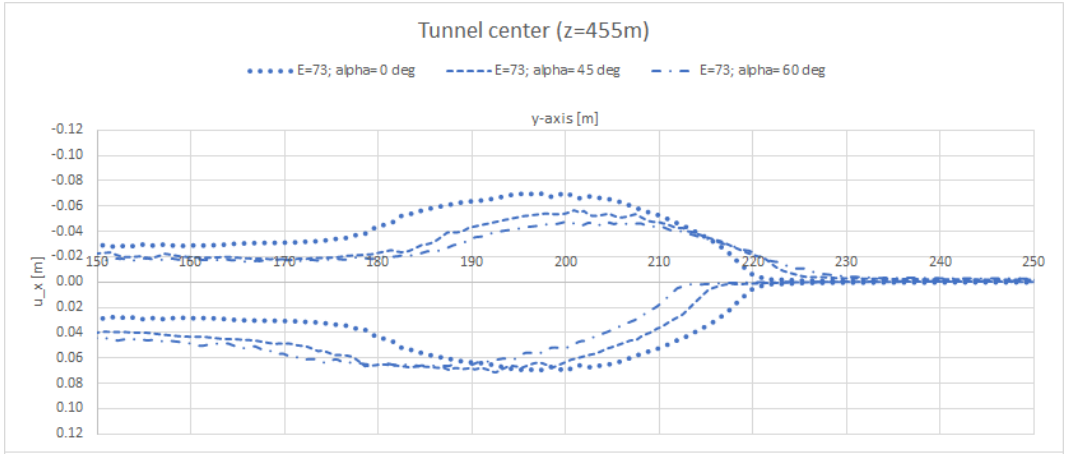


Figure 5.21: Effect of a non-perpendicular fault course ($\alpha$ = 45 and 60°) for lower bound properties of adjacent rock stiffness on the horizontal tunnel displacement at Z = 455 m

Based on the results from the previous analyses, it was concluded that the translational displacements were not calibrated. Additionally, as the insitu forces in the rings were not measured, the forces could not be calibrated. However, in the event that the lining would be modelled as a monolith structure, the maximal moment distributions would be as shown in figure 5.22 and 5.22 for respectively E = 73 MN/m$^2$ and E = 10 MN/m$^2$.

The most notable feature was that at $L_2$ = 10 m, the maximal moment transited from marl to dolomite without a significant increase in the fault zone with E = 73 MN/m$^2$ (figure 5.22). For E = 10 MN/m$^2$ and $L_2$ = 10 m, a slight increase of maximal moments was observed (figure 5.23). Comparing the calculated moments between 3D and 2D, led to the conclusion that the maximal moments obtained from 2D analysis could be set as upper bound values for realistic parameter sets. By this is meant, the parameters for which the calculated and measured ovalization fit each other.

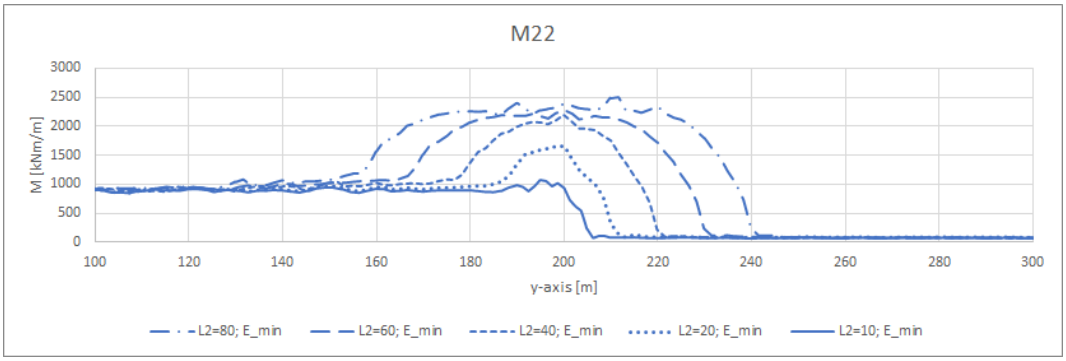


Figure 5.22: Comparison of different fault width and effect of adjacent rock stiffness (lower bound properties) on the maximal transversal moment (M22) distribution along the tunnel alignment for E$_{fault}$ = 73 MN/m$^2$

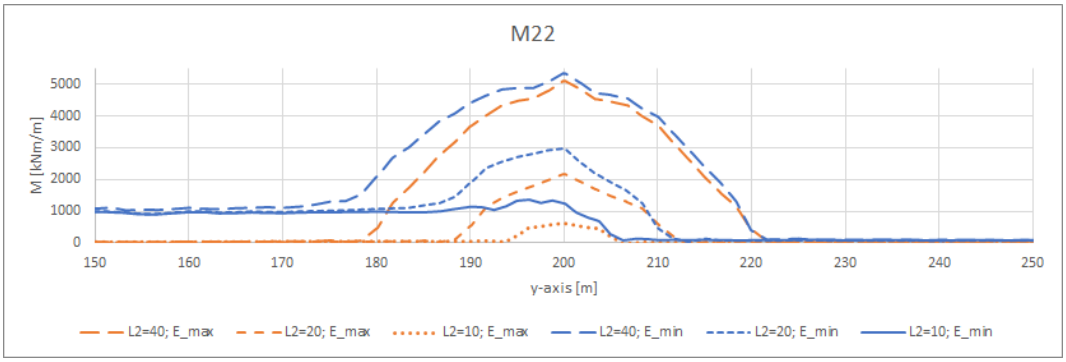


Figure 5.23: Comparison of different fault width and effect of adjacent rock stiffness (lower and upper bound properties) on the maximal transversal moment (M22) distribution along the tunnel alignment for E$_{fault}$ = 10 MN/m$^2$

The longitudinal normal force distribution (N1) illustrated that the peak normal forces were at the transition from the rock mass to the faultzone (figure 5.24). This corresponded to the distributions which were found in the 2D longitudinal beam model. This feature was justified by the fact that the normal force is the first derivative of the moment and the steepest inclination of the moment distribution was found directly after the zone transitions. In structural engineering terms, this phenomena is called a "clamping moment". The very stiff adjacent rock results in an almost fixed connection of the lining, whereas the tunnel section located in the fault zone was loaded as a beam. However, the peak force did not exceed the maximal transversal normal force (N2), as shown in figure 5.24, so that N2 remained normative.

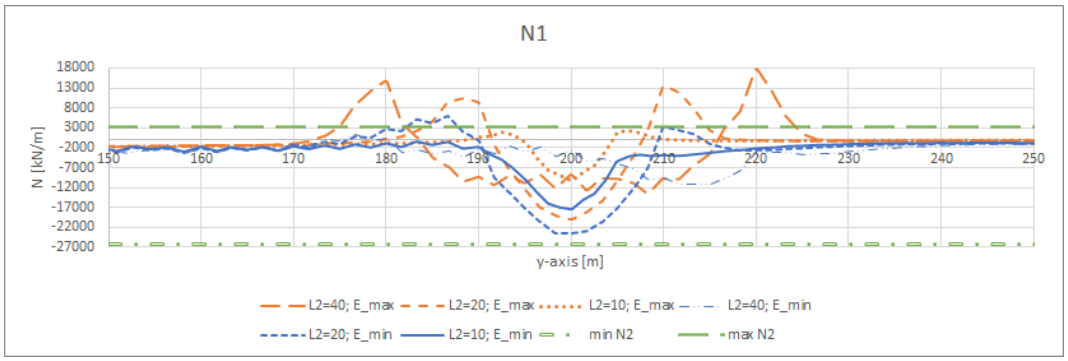


Figure 5.24: Comparison of different fault width and effect of adjacent rock stiffness (lower and upper bound properties) on the maximal longitudinal normal force (N1) distribution along the tunnel alignment for $E_{fault}$ = 10 MN/m$^2$

### 5.3.4. Limitations

For the 3D model, three limitations were discovered which were particularly relevant to the 3D Plaxis model, while the limitations in the 2D Plaxis were implicitly valid here.

- The calculated effective horizontal stress ($\sigma_{yy}$) in the plastic stage showed a boundary effect at the side boundaries (Y = -250 and 250 m), as the calculated stress was not equal to the stress in the initial stage (figure 5.12);
- The calculated transversal normal forces showed a significant inaccuracy of more than 10%, which resulted in a substantial discrepancy with respect to 2D results;
- The use of a Finite Element program restricted the allowable amount of strains and did not allow differential strains between nodes, which led to difficulties in finding numerical convergence for very abrupt transition of ground stiffnesses;
- Applying global lining stiffness reduction, instead of explicit joint modelling, disabled calculating local peak forces due to stress accumulation near joints, which was required for several detailed structural design such as the reinforcement;
- The set up models considered a single tunnel tube without the effect of an adjacent tunnel, while two tunnel were constructed next to each other in the Middle-East case.

# 6

# Conclusions

In this section the research questions are presented, followed by the corresponding answer. The first three questions are subquestions, which were set up to answer the main and final question.

### Subquestion 1: Which critical conditions, specifically in the Middle-East case study, make a bored tunnel construction difficult?

The two most critical factors, that governed the lining behaviour in the Middle-East case, were the submerged conditions and the soft gauge material in the fault zone. Described in more detail below:

- Underwater conditions imply the need for a delicate execution of the backfilling to provide support and water tight sealing around the lining, which was not guaranteed in this case based on water pressure measurements. Improper backfilling resulted in increased drainage conditions, which led to ground water flow around the tunnel and lowering of the water level. Consequently, the effective stresses increased which conducted settlement of the ground, causing the significant translational deformations observed in the tunnel rings.
- Tunnel excavations result in a redistribution and local increase of effective stresses in the ground, which can cause large displacements in ductile ground such as the faultzone of the Middle-East case. The installed lining had to provide resistance to these ground displacements, as it was placed immediately after excavation, resulting in large ring forces. Particularly, development of eccentric forces (bending moments) resulted in ovalization and joint opening, provoking leakages in the joints.

### Subquestion 2: What are the available analytical and numerical methods to design tunnel linings, specifically in and around fault zones?

Traditionally, the design of a tunnel lining is based on two-dimensional analytical solutions for transversal behaviour with division of pre-assigned geotechnical zones. However, comparing 3D Plaxis to transversal models showed that a narrow fault zone results in significantly reduced lining forces, due to longitudinal arching of the ground. Explanation is given below:

- Results of multiple 3D Plaxis models, indicated that the lining action in a ductile fault zone is governed by transversal behaviour. In particular, fault widths smaller than four times the tunnel diameter (<4D) did not result in lining settlements in the fault zone, just ovalization, substantiating the transversal action.
- The longitudinal beam model was found to be inapplicable for abruptly varying ground properties in narrow zones. Structural engineers, as a rule of thumb, consider beam effect in case the length of the studied structure is larger than ten times the diameter of the structure. The studied fault widths varied between 1D to 8D, which does not meet the previous rule of thumb.
- A fault zone as narrow as the tunnel diameter (1D) did not show increased lining deformations or lining forces in the zone. In such an event, the lining behaviour was basically dominated by the geotechnical

zones adjacent to the fault zone, because the deformations and forces transmitted between adjacent rock without being impacted by the fault.

- Plaxis 2D allowed for more detailed modelling of several components compared to Erdmann's analytical solution. More specifically, the backfilling ($R_{inter}$) and reduced lining stiffness due to joints ($k_r$ or $\xi_x$) gave reliable results, comparing them to measured ring ovalization. Also, the vertical ground settlement is not accounted for by the analytical solution. However, 2D analysis resulted in overestimated ground pressures, as it did not take into account longitudinal arching. Therefore, 2D transversal analysis can be applied to approximate upper bound lining forces, but will generally result in oversized rings (in terms of reinforcement).

### Subquestion 3: Can the stress and displacement distribution around and of the tunnel lining in and around fault zones under critical loading combinations be reliably modelled in Plaxis?

Results of this study showed that transversal lining forces and displacements can be calculated accurately with Plaxis. However, settlements in the longitudinal direction of the tunnel were not calibrated with the measured displacements. Clarification is given below:

- The tunnel rings in Plaxis 2D were modelled with plate elements, taking into account stiffness reduction due to joints by means of a global reduction factor ($\xi_x$) or rotational connections ($k_r$) implementing Janßen's theory. Calibration of the Plaxis models with the measured ring displacements resulted in a credible fit. Additionally, validation with Erdmann's analytical solution produced lining forces with a matching order of magnitude. Therefore, it was concluded that reliable results were obtained in homogeneous ground (without 3D effect).

- Setting up Plaxis 3D models to capture the longitudinal effect by including all geotechnical zones, did not result in a model that fitted the measured lining settlements. The most crucial limitation was the inability to explicitly model ring joints using plate elements for the lining in Plaxis, which did not allow for abrupt lining settlements in the fault zone. However, the outcome of the models gave ovalizations that did correspond to the measured rings. Consequently, modelling realistic lining behaviour in very narrow and soft fault zones is suggested with a program that enables explicit design of ring joint and discrete nodal displacements.

### Main question: What is the behaviour of a segmental bored tunnel lining in hardened backfill material in fault zones between different unfavorable geotechnical units in saturated rock formations at the end of the construction phase?

- The behaviour of a segmental lining in a narrow fault zone between different unfavorable geotechnical units is governed by the transversal behaviour, such as ovalization.

- Depending on the stiffness ratio between adjacent geotechnical units and the fault width, the ground pressures acting on the lining, can reduce as a result of increased longitudinal arching. Therefore, considering two-dimensional behaviour in narrow fault zones would lead to an overestimation of the lining forces.

- Overall, the normative components for the calculation of ovalization and moments are: the ground stiffness (E), the lateral earth pressure coefficient ($k_0$), the lining stiffness reduction ($\xi_x$) and the interface factor ($R_{inter}$).

- Additionally, excavation in saturated rock formations led to groundwater lowering, resulting in settlement of the ground and exceedingly large transversal lining deformations.

- The longitudinal behaviour in geotechnical units with abruptly developed settlements, as was observed in the Middle-East case, was not modelled well as a monolith structure. The lining rings rather act as separate structures, that are connected by ring joints.

# 7

# Recommendations

The previously mentioned conclusions and limitations of the analysis resulted in the formulation of four recommendations for future research. Below, in each subsection the corresponding recommendation is explained.

### Modelling of ring joints

It was concluded from the measured deformations of the rings in the Middle-East case that the rings settled very abruptly over a very short distance. Implementing Plaxis did not result in a realistic global reduction of the longitudinal lining stiffness which would fit such settlements. Therefore, it is recommended to look at a different modelling approach to take into account the local behaviour of the ring joints. This could be done by either modelling a very thin structural plate with joint properties, or not modelling the lining as a plate but rather as a volume. However, it is known that modelling lining as volumes includes a significant numerical discrepancy compared to plates.

### Implementation of a discontinuous model

In this research software based on Finite Elements was applied. This implied that the modelled materials behave as a continuum. It is suggested to model the abrupt differential settlement of rings in the Middle-East case by a method that allows for discontinuous deformations, such as with discrete elements.

### Analyzing longitudinal pre-stress effect

The longitudinal prestressing of the lining was not accounted for in this research. In reality the behaviour of the lining rings could be dominated by the individual behaviour of single rings, which are connected to each other by means of longitudinal compression. This compression would lead to increased shear resistance between the rings, but would not imply continuous deformation and force distribution along the lining. The more suitable way to model the lining behaviour is by modelling each lining ring as a separate element and loading these with a longitudinal force coming from the hydraulic jacks of the TBM.

### Taking into account the boring process

The focus of this research was to model the behaviour of the tunnel lining at the end of the construction phase. However, the time aspect of the measured data from the Middle-East case was unknown which led to uncertainties with regard to the construction factors that could have influenced the behaviour of the lining. Features such as misplacement of the lining were unknown and would change the displacement and force distribution pattern. Therefore, it is recommended to implement this research strategy to a case where real-time data is available and re-analyze longitudinal behaviour of the rings, taking into account among others initial displacements of rings.

# Bibliography


Barla, G. and S. Pelizza
2000. *TBM Tunneling in Difficult Ground Conditions.* Technical report, Politecnico di Torino.

Bell, F. G.
1981. *Properties of Soils and Rocks,* 1st edition. Butterworths.

Bell, F. G.
2000. *Engineering Properties of Soils and Rocks,* 4rd edition. Blackwell Sciense Ltd.

Bezuijen, A. and A. Talmon
2008. Processes around a tbm. *GEC international.*

Bieniawski, Z. T.
1973. Engineering Classification of Jointed Rock Masses. *Transaction of the South African Institution of Civil Engineers,* 15:335–344.

Blom, C.
1995. *Liggerwerking van boortunnels.* Technical report, Technische Universiteit Delft.

Blom, C.
2002. *Design philosophy of concrete linings for tunnels in soft soils.* Technical report, Technische Universiteit Delft.

Bogaards, P.
1998. *Liggerwerking Boortunnels.* Technical report, Technische Universiteit Delft.

Bouma, A.
1993. *Mechanica van constructies: elasto-statica van slanke structuren,* 2nd edition. Delftse Uitgevers Maatschappij.

Brinkgreve, R.
2019. *PLAXIS 2D manual.* PLAXIS.

Brown, E. and B. Brady
2006. *Rock Mechanics for Underground Mining,* 3rd edition. Springer-Verlag New York Inc.

BTS, B. T. S.
2004. *Tunnel lining design guide.* Institution of Civil Engineers.

Carranza-Torres, C. and C. Fairhurst
1999. General formulation of the elasto-plastic response of openings in rock using the hoek-brown failure criterion. *Int. J. Rock Mech. Min. Sci.,* 36:777–809.

COB-L500
2000. *Toetsingsrichtlijn voor het ontwerp van boortunnels voor weg- en railinfrastructuur.* Technical report, Centrum Ondergronds Bouwen.

Cohen, K. M., S. C. Finney, and P. L. Gibbard
2013. The ICS International Chronostratigraphic Chart. *Episodes 36,* 3:199–204.

DAUB
2010. *Recommendations for the selection of tunnelling machines.* German Tunneling Committee (ITA-AITES).

DAUB
2013. *Recommendations for the design, production and installation of segmental rings*. German Tunneling Committee (ITA-AITES).

Goodman, R. E.
1981. *Introduction to Rock Mechanics*, second edition. John Wiley and Sons.

Hoefsloot, F.
2009. Analytical solution of longitudinal behaviour of tunnel lining. *Geotechnical Aspects of Underground Construction in Soft Ground*, Ng, Huang & Liu.

Hoek, E., C. Carranza-Torres, and B. Corkum
2002. Hoek-Brown Failure Criterion. *Proc. NARMS-TAC Conference*, 1:267–273.

Hoek, E. and M. Diederichs
2006. Empirical estimation of rock mass modulus. *International Journal of Rock Mechanics and Mining Sciences*, 43:203–215.

Hoek, E., P. Kaiser, and W. Bawden
2000. *Support of Underground Excavations in Hard Rock*, 1st edition. CRC Press.

Hudson, J. and J. Harrison
2000. *Engineering Rock Mechanics*, 1st edition. Butterworth-Heinemann.

ITA WG2
2000. Guidelines for the Design of Shield Tunnel Lining. *Tunnelling and Underground Space Technology*, 15:303–331.

Janßen, P.
1983. *Load capacity of segmental joints*. Technical report, Braunsweigh university.

Jovanovic, P.
1995. *Bored Railway Tunnels in The Netherlands*. Technical report, COB.

Kunst, D.
2017. *Modelling construction phases of bored tunnels with respect to internal lining forces*. Technical report, Technische Universiteit delft.

Lengkeek, A.
1996. *Analyse grond-tunnelinteractie*. Technical report, Technische Universiteit Delft.

Lo, K. and A. Hefny
1996. Design of tunnels in rock with long-term time-dependent and nonlinearly stress-dependent deformation. *TAC annual conference proceedings*, Pp. 179–214.

Luttikholt, A.
2007. *ULS Analysis of a Segmented Tunnel Lining*. Technical report, Technische Universiteit Delft.

Maidl, B., M. Herrenknecht, U. Maidl, and G. Wehrmeyer
2012. *Mechanised Shield Tunelling*, 2nd edition. Wilhelm Ernst and Sohn.

Maidl, B., L. Schmid, W. Ritz, M. Herrenknecht, G. Wehrmeyer, and M. Derbort
2008. *Hardrock Tunnel Boring Machines*, 2nd edition. Wilhelm Ernst and Sohn.

Maidl, B., M. Thewes, and U. Maidl
2013. *Handbook of Tunnel Engineering volume 2*, 1st edition. Wilhelm Ernst and Sohn.

Marinos, P. and E. Hoek
2000. Gsi: A geologically friendly tool for rock mass strength estimation. *Proceedings of the GeoEng 2000 at the International Conference on Geotechnical and Geological Engineering, Melbourne*, Pp. 1422–1446.

Marinos, V., P. Marinos, and E. Hoek
2012. The Geological Strength Index: Applications and Limitations. *Bull Eng Geol Environ*, 64:55–65.

Mortier, H., M. Brugman, and T. Schubert
2018. The difference is in the detail. *Tunnels and Tunnelling*.

Möller, S.
2006. *Tunnel induced settlements and structural forces in linings*. Technical report, Institut fur Geotechnik der Universität Stuttgart.

Möller, S. and P. Vermeer
2006. Prediction of settlements and structural forces in linings due to tunnelling. *Taylor & Francis Group*.

Palmstrom, A. and H. Stille
2014. *Rock Engineering*, 2nd edition. Ice Publishing.

Pei, Q., X. Ding, B. Lu, Y. Zhang, S. Huang, and Z. Dong
2016. An improved method for estimating in situ stress in an elastic rock mass and its engineering application. *Open Geosciences*, 8:523–537.

Price, D. G.
2009. *Engineering Geology: Principles and Practice*, 1st edition. Springer-Verlag Berlin Heidelberg.

Saraglou, H. and G. Tsiambaos
2008. A modified hoek - brown failure criterion for the anisotropic intact rock. *International Journal of Rock Mechanics and Mining Sciences*, 45:223–234.

Schädlich, B., H. F. Schweiger, and T. Marcher
2013. *Modelling Swelling Rock Behaviour in Tunnelling*. PLAXIS.

Singh, B. and R. Goel
2011. *Engineering Rock Mass Classification*, 1st edition. Butterworth-Heinemann.

Terzaghi, C.
1946. *Introduction to tunnel geology*, 1st edition. Youngstown, OH: Commercial Shearing & Stamping Co.

Thewes, M. and C. Budach
2009. *Grouting of the annular gap in shield tunnelling*. Technical report, Ruhr-University Bochum.

Vallejo, L. G. and M. Ferrer
2011. *Geological Engineering*, 1st edition. CRC Press.

van der Horst, E.
1998. *Invloed van voegmaterialen op de krachtswerking in gesegmenteerde betonnen boortunnels*. Technical report, Technische Universiteit Delft.

van Oosterhout, G., C. Blom, and P. S. Jovanovic
1999. Analysis of tunnel lining behaviour in soft soil during the construction stage, second heinenoord tunnel. *12th European Conference on Soil Mechanics and Geotechnical Engineering*, 3:57–61.

Waltham, T.
2009. *Foundations of Engineering Geology*, 3th edition. Taylor and Francis.

Wood, A. M.
1975. The circular tunnel in elastic ground. *Geotechnique*, 25:115–127.

Zhang, L.
2016. *Engineering Properties of Rocks*, 2nd edition. Butterworth-Heinemann.

Zhou, X. and J. Li
2011. Hoek-brown criterion applied to circular tunnel using elastoplasticity and in situ axial stress. *Theoretical and Applied Fracture Mechanics*, 56.

# A

# Failure prediction

Based on table A.2 (Singh and Goel, 2011) a prediction of the type of failure to occur in certain rock masses was made based on the ratio between insitu stress ($sig_v$ or $\sigma_1$) to the uniaxial compressive strength of intact rock (UCS or $q_c$) and the Rock Mass Rating value (RMR). Using the available data of the rock as presented in table 4.1 and assuming that the correlation of GSI with RMR as shown in figure 2.5 was valid, the values as presented in table A.1 were found. The insitu stress for marl, limestone and dolomite was based on 200 m overburden of dry rock with a volumetric weight of 25 kN/m$^3$. For the fault material the insitu stress with the same overburden was assumed but with a volumetric weight of 20 kN/m$^3$.

Comparing the correlation as presented in figure 2.5 and the GSI and RMR as observed in the field (table 3.1), showed that the marl corresponds quite well. While the dolomite had a much lower observed RMR than obtained with the correlation. This is explained by the significantly lower RQD, which is not directly accounted for in the correlation to GSI. However, implementing the low RMR as observed in the field, still resulted in the same failure prediction as found with the correlation for the dolomite because the RMR was below 50 in both cases.

Knowing that squeezing was only observed in the fault zone, the other rock masses were expected to be non-squeezing. Using this as a starting point, led to observation that the compressive strength of the marl was underestimated and would rather be larger than UCS = $sig_v$ / 0.4 = 13. This was based on the condition that the $sig_v$ / UCS ratio would be smaller than 0.4 for a non-squeezing rock.

| geo.unit | marl | | limestone | | fault | | dolomite | | |
|---|---|---|---|---|---|---|---|---|---|
| *parameters* | *min* | *max* | *min* | *max* | *min* | *max* | *min* | *max* | *unit* |
| sig_v | 5000 | | 5000 | | 4000 | | 5000 | | kN/m2 |
| GSI | 40 | 60 | 40 | 60 | 15 | 25 | 45 | 70 | - |
| RMR | **48** | **65** | **48** | **65** | **28** | **36** | **53** | **73** | - |
| UCS | **7** | **20** | **60** | **140** | **7** | **20** | **45** | **135** | MN/m2 |
| sig_v/UCS | 0.25 | 0.71 | 0.04 | 0.08 | 0.20 | 0.57 | 0.04 | 0.11 | - |

Figure A.1: Table to predict rock failure mechanisms based on the ratio of insitu stress to intact rock strength and the RMR of the rock mass (GSI-RMR correlation in figure 2.5 and range of values for the different geotechnical units from table 4.1

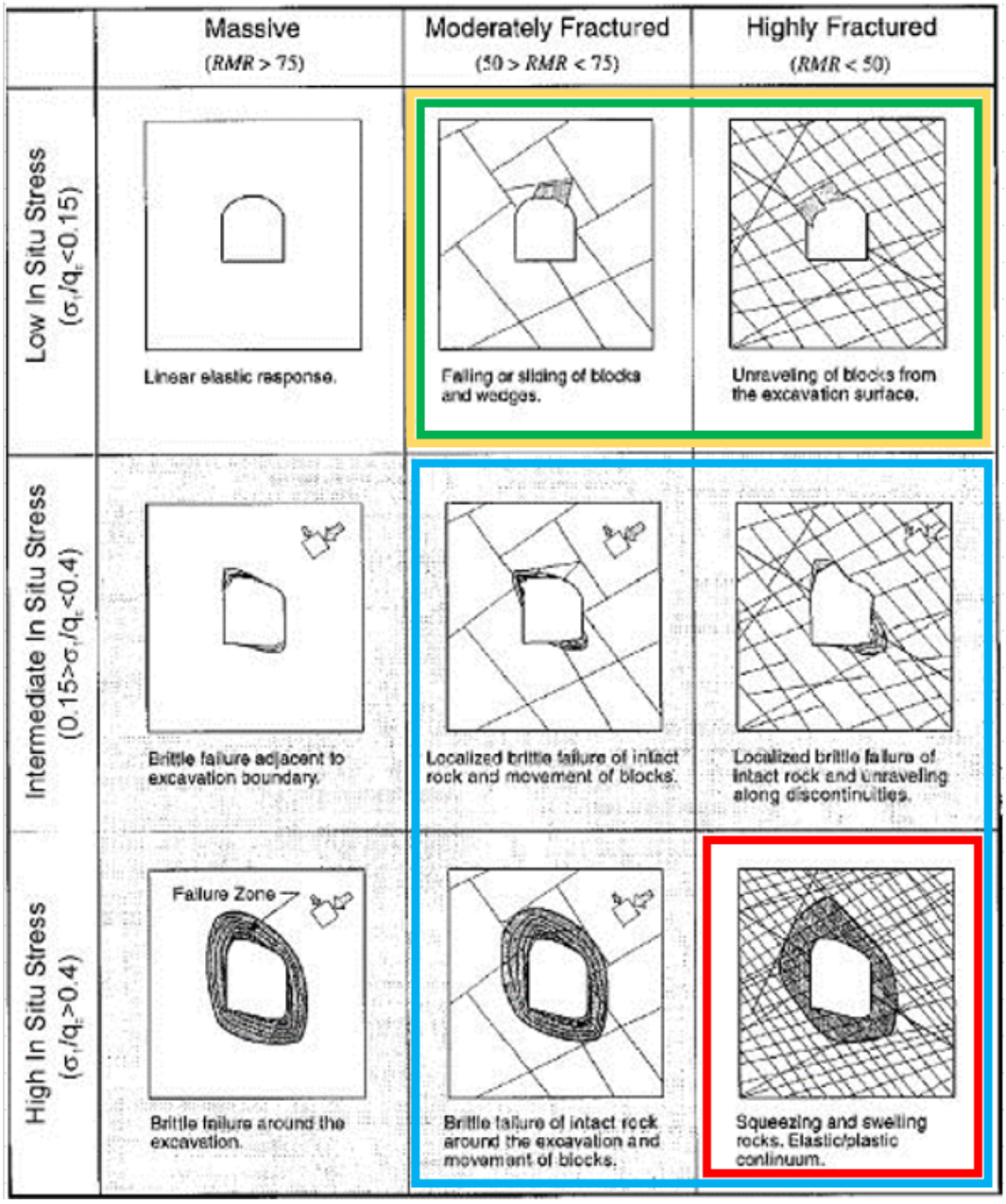


Figure A.2: Diagram to predict rock failure modes based on correlations between the stress ratio and the RMR (Singh and Goel, 2011). The colored rectangles correspond to the rock mass indicated with the same color in table A.1

# B

# Translation Hoek-Brown to Mohr-Coulomb

Detailed explanation about the determination of Mohr-Coulomb (M-C) parameters based on Hoek and Brown is given in Hoek et al., 2002. In this appendix the determined Mohr-Coulomb parameters and approximated $k_0$ based on Hoek and Brown (H-B) are presented.

In table B.1, the calculated M-C parameters which were used to validate the calculated results with the H-B model are shown. The H-B parameters correspond to the quantities presented in table 4.1 in section 4.2.4. The disturbance factor D is zero in all cases because the rock was excavated by means of a TBM. The reference (effective) stress level in this translation was chosen at the depth corresponding to the center of the tunnel, being 3850 kN/m$^2$ for the fault zone and 4950 kN/m$^2$ for rock. This was one of the limitations of using M-C based on H-B, because a homogeneous material could be stress dependent with HB and with for M-C. However, results of the validation with M-C showed that the parameters were representative (section 5.1.3).

| *Rock mass* | marl (q) | | limestone (eq) | | fault (F) | | dolomite (K) | |
|---|---|---|---|---|---|---|---|---|
| | min | max | min | max | min | max | min | max |
| $\sigma_c$ $[MN/m^2]$ | 7 \| 13 | 20 | 60 | 140 | 7 | 20 | 45 | 135 |
| $m_i$ $[-]$ | 5 | 9 | 6 | 12 | 5 | 9 | 6 | 12 |
| $GSI$ $[-]$ | 40 | 60 | 40 | 60 | 15 | 25 | 45 | 70 |
| $s$ $[-]$ | 0.0013 | 0.0117 | 0.0013 | 0.0117 | 0.0001 | 0.0002 | 0.0022 | 0.0357 |
| $a$ $[-]$ | 0.511 | 0.503 | 0.511 | 0.503 | 0.561 | 0.531 | 0.508 | 0.501 |
| $m_b$ $[-]$ | 0.587 | 2.157 | 0.704 | 2.876 | 0.240 | 0.618 | 0.842 | 4.110 |
| $\sigma'_{cm}$ $[MN/m^2]$ | 0.70 \| 1.29 | 4.17 | 6.52 | 33.15 | 0.32 | 1.80 | 5.50 | 40.71 |
| $\sigma'_{3max}$ $[MN/m^2]$ | 2.07 \| 2.15 | 2.30 | 2.37 | 2.61 | 1.56 | 1.73 | 2.34 | 2.64 |
| $\sigma'_{3n}$ $[MN/m^2]$ | 0.26 \| 0.17 | 0.12 | 0.04 | 0.02 | 0.22 | 0.09 | 0.05 | 0.02 |
| $\phi'$ $[°]$ | 21 \| 26 | 39 | 38 | 55 | 16 | 30 | 37 | 56 |
| $c'$ $[kN/m^2]$ | 260 \| 320 | 730 | 700 | 2300 | 110 | 300 | 700 | 3600 |

Table B.1: Translation of Hoek and Brown parameters to Mohr-Coulomb parameters based on a stress level at the tunnel center

The calculation of $k_0$ based on the ratio between $\sigma'_3$ and $\sigma'_1$ for the Hoek and Brown parameters of the fault zone, is presented in table B.2. The $\sigma'_v$ was calculated based on a reference level at 400 m a.s.l., which corresponded to a depth of 275 meter below surface level. The water table at this level was equal to 110 m (510 m a.s.l.). This resulted in a vertical effective stress of 4400 kN/m$^2$.

| *Parameters* | | | | | | | | | |
|---|---|---|---|---|---|---|---|---|---|
| $\sigma_c$ $[MN/m^2]$ | 7 | 13 | 20 | 7 | 13 | 20 | 7 | 13 | 20 |
| $m_i$ $[-]$ | 5 | 5 | 5 | 9 | 9 | 9 | 9 | 9 | 9 |
| $GSI$ $[-]$ | 15 | 15 | 15 | 15 | 15 | 15 | 25 | 25 | 25 |
| $s$ $[-]$ | 0.0001 | 0.0001 | 0.0001 | 0.0001 | 0.0001 | 0.0001 | 0.0002 | 0.0002 | 0.0002 |
| $a$ $[-]$ | 0.561 | 0.561 | 0.561 | 0.561 | 0.561 | 0.561 | 0.531 | 0.531 | 0.531 |
| $m_b$ $[-]$ | 0.240 | 0.240 | 0.240 | 0.432 | 0.432 | 0.432 | 0.618 | 0.618 | 0.618 |
| $\sigma'_{cm}$ $[MN/m^2]$ | 0.32 | 0.59 | 0.91 | 0.44 | 0.82 | 1.26 | 0.63 | 1.17 | 1.80 |
| $\sigma'_{3max}$ $[MN/m^2]$ | 1.77 | 1.83 | 1.88 | 1.80 | 1.87 | 1.92 | 1.84 | 1.91 | 1.96 |
| $\sigma'_1$ $[MN/m^2]$ | 3.22 | 3.78 | 4.27 | 3.85 | 4.61 | 5.28 | 4.51 | 5.55 | 6.48 |
| $k_0$ $[-]$ | 0.55 | 0.48 | 0.44 | 0.47 | 0.41 | 0.36 | 0.41 | 0.34 | 0.30 |

Table B.2: Calculation of the vertical to horizontal stress ratio at the bottom of the optimal geometry as defined in appendix C

# C

# Plaxis 2D geometry and mesh

The dimensions of the model domain were defined as illustrated in figure 4.3 in section 4.2. In other words, $Z_0$ and Z were respectively the overburden and bedding thickness with respect to the tunnel invert (+450 m a.s.l.). X = -$X_{min}$ = $X_{max}$ was the distance from the tunnel center to the vertical boundary of the model. The ground parameters were the minimal values of the fault material as shown in table 4.1 presented in section 4.2.4. This analysis was to observe the increase of deviation of the vertical ovalization ($u_y$), horizontal ovalization ($u_x$), the normal forces (N) and the moments (M) of the lining. In the search for the optimal model two interesting features were observed.

Firstly, the decrease of the model geometry did not always result in an increase in deviation. This features were observed in the figures below, where the distribution waved up and down. It was explained by the fact that a fixed mesh coarseness implied that the shape of the elements were fixed. Therefore, a decrease in model geometry while creating elements with the same shape resulted in the need of more elements and thereby resulting in more nodes.

Secondly, the decrease of model dimensions (when keeping the mesh coarseness fixed) resulted in an increase of elements and nodes. Therefore, the optimal model was not necessarily a model with decreased dimensions, rather the optimal mesh was a model with the minimal amount of nodes while still producing results with small deviation compared to a very dense mesh.

The optimal mesh found from this analyses was at: $Z_0$ = 100 m; Z = 50 m; X = 75m. The maximal deviation in this model geometry compared to the initial one, was just 0.5%. Reducing the model geometry with one step results in a much larger deviation for the moment (M) and normal forces (N).

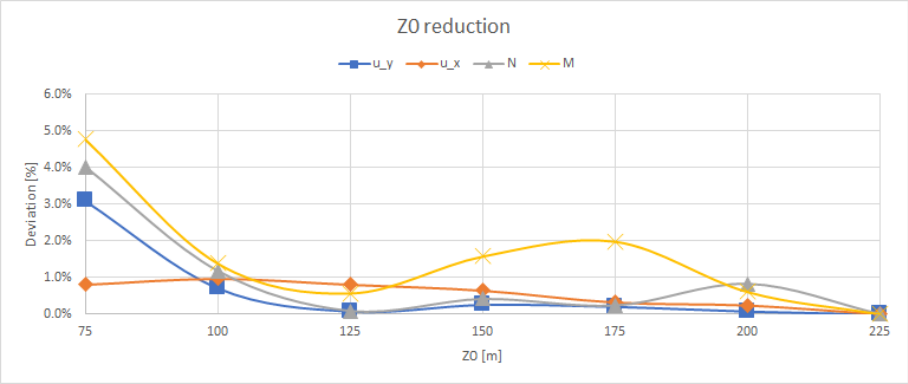


Figure C.1: Reduction of the overburden thickness above the tunnel invert ($Z_0$)

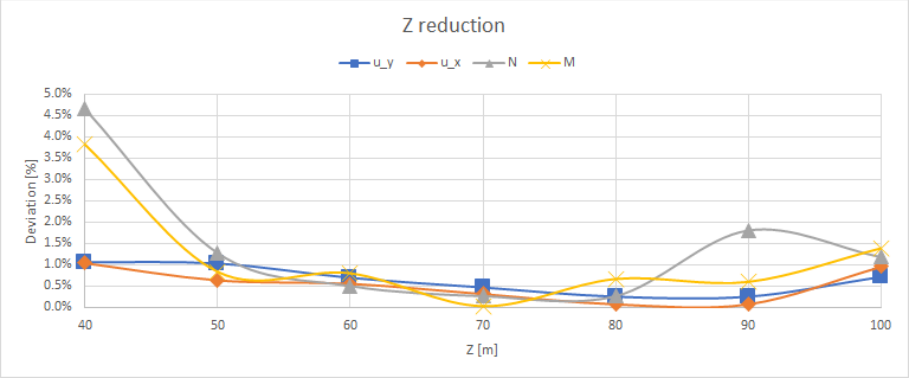


Figure C.2: Reduction of the bedding thickness underneath the tunnel invert (Z)

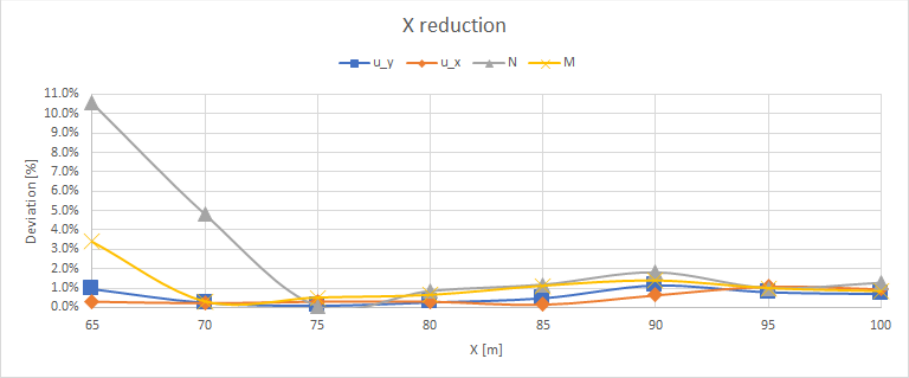


Figure C.3: Reduction of the model domain width with respect to the tunnel center (X)

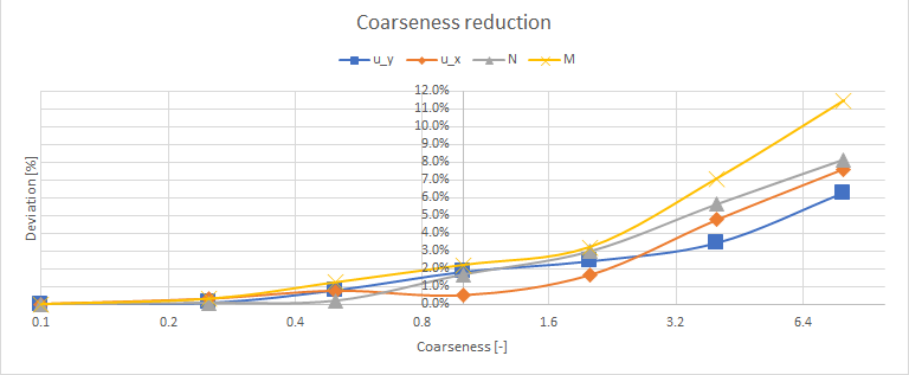


Figure C.4: Reduction of the coarseness of the denser mesh, radius of 15 m around the tunnel center (c)

# D

# Plaxis 2D fault sensitivity

The parametric study for the fault zone was based on the parameters presented in table D.1. In figures D.1 to D.9 the ratio of increase or decrease of displacements and forces are presented. In most of figures, on the horizontal axis the normalized parameter is shown which was analyzed. This parameter is either normalized to the minimal or maximal value of the range, which is indicated with a min / max subscript. The vertical axis is a normalized value of the maximal vertical ovalization ($u_y$ [m]), the maximal horizontal ovalization ($u_x$ [m]), the maximal normal force (N [kN/m]) and the maximal moment (M [kNm/rad/m]), which is indicated as the parameter Y. This always normalized to the calculated value which corresponds to the minimal variable on the horizontal axis (indicated as $Y_{min}$). For example, the $Y_{min}$-value in $Y/Y_{min}$ at $E/E_{max}$, is the value that corresponds to the lower bound E (which is $E_{min}$ = 73 MN/m$^2$).

| *Parameters* | min | max |
|---|---|---|
| $\Delta h_w$ [*mb.m.w.l.*] | 0 | 60 |
| $E$ [$MN/m^2$] | 73 | 551 |
| $\phi'$ [°] | 27.5 | 32.5 |
| $c'$ [$kN/m^2$] | 0 | 150 |
| $\nu$ [−] | 0.35 | 0.2 |
| $k_0$ [−] | 0.3 | 0.7 |
| $k_r$ [$kNm/rad/m$] | 1E5 | fixed |
| $R_{inter}$ [−] | 0.25 | 1.00 |
| $C_{ref}$ [%] | 0.0 | 2.0 |

Table D.1: Geotechnical and structural parameters in the fault zone material with corresponding ranges used in the parametric study

It was chosen to present the sensitivity of the parameters in this way because the quantity was not analyzed, but rather the increment of the output. However, to get an insight on the quantity that was calculated, one can back calculate the results based on the initial values (which correspond to the lower bound range of table D.1, except for $k_r$ = fixed and $R_{inter}$ = 1.0). The calculated results for the combination of all lower bound values are presented in table D.2.

| $Parameters$ | output |
|---|---|
| $u_y$ $[m]$ | 0.166 |
| $u_x$ $[m]$ | 0.147 |
| $N$ $[kN/m]$ | 17670 |
| $M$ $[kNm/m]$ | 4438 |

Table D.2: Output for the combination of lower bound values from table D.1 except for $k_r$ and $R_{inter}$

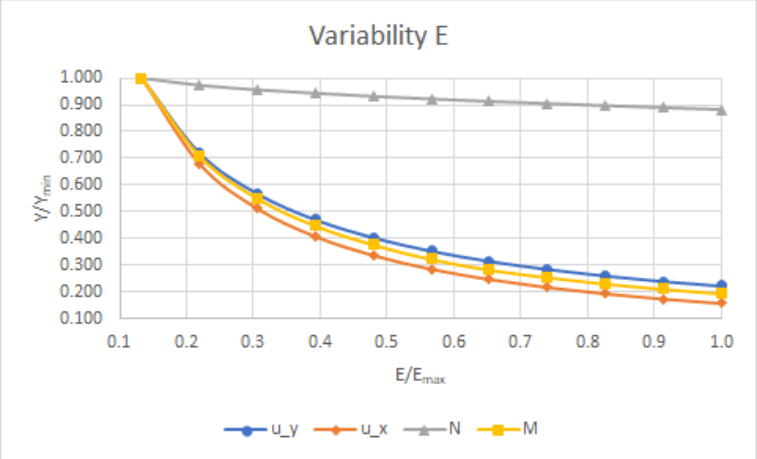


Figure D.1: Variability of calculated results for a different ground stiffnesses (E)

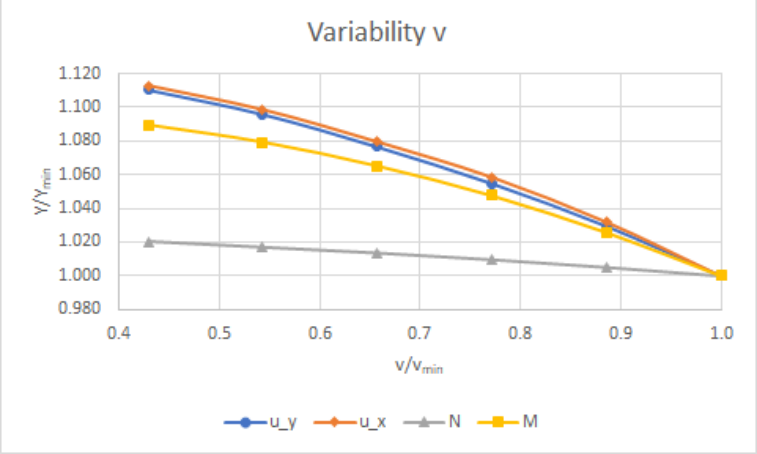


Figure D.2: Variability of calculated results for a different Poisson's ratio's ($\nu$)

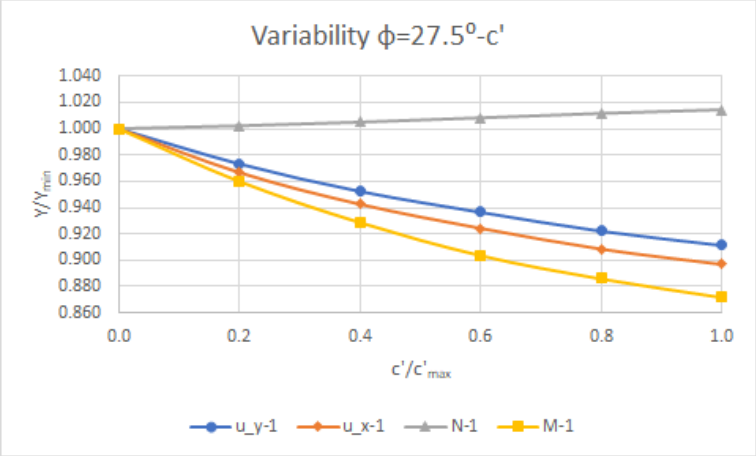


Figure D.3: Variability of calculated results for different effective cohesion's (c')

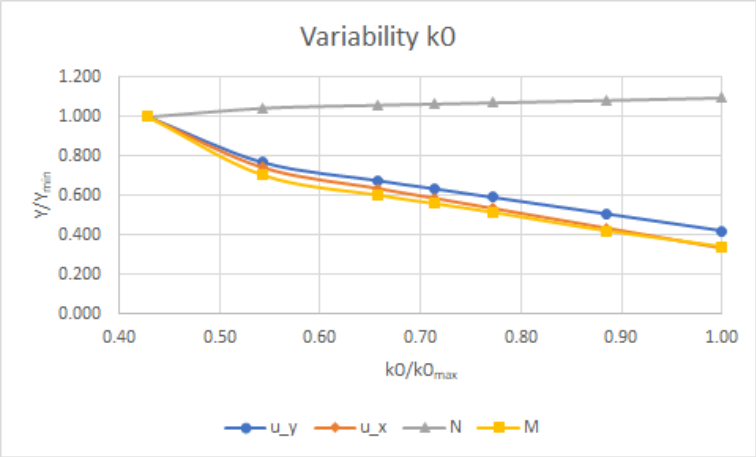


Figure D.4: Variability of calculated results for different lateral earth pressure coefficients ($k_0$)

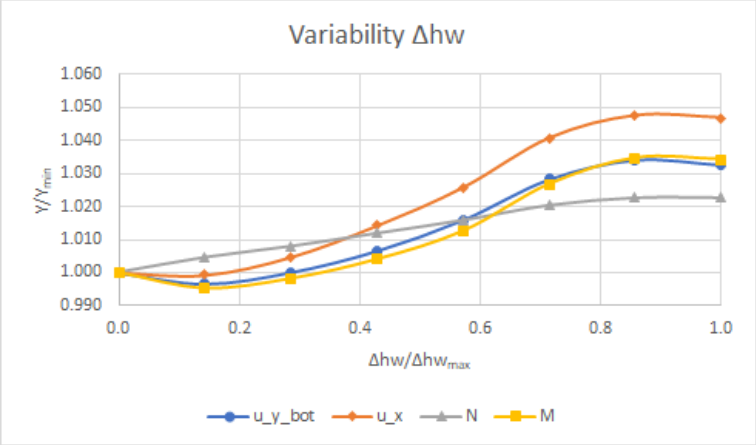


Figure D.5: Variability of calculated results for different groundwater level lowering ($\Delta h_w$)

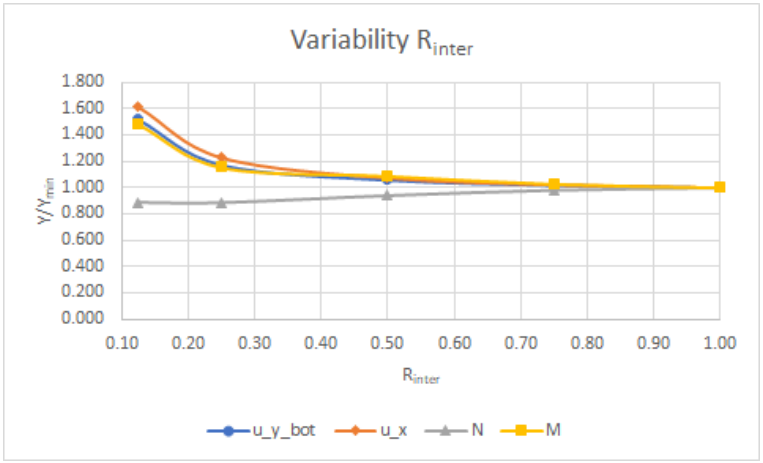


Figure D.6: Variability of calculated results for different interface reduction factors ($R_{inter}$)

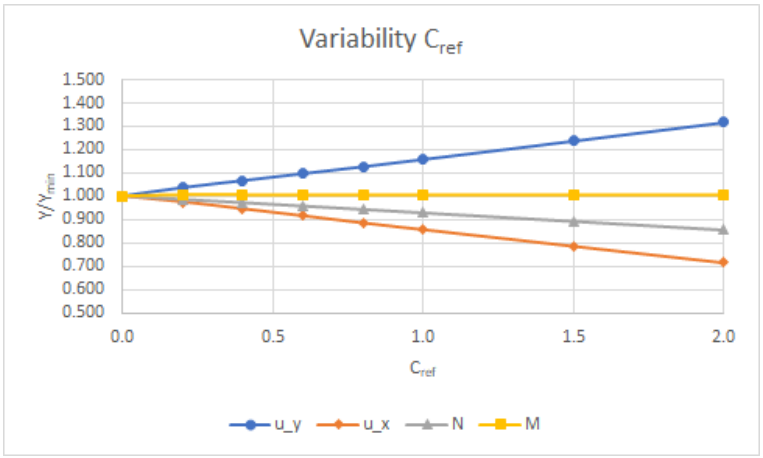


Figure D.7: Variability of calculated results for different contractions ($C_{ref}$)

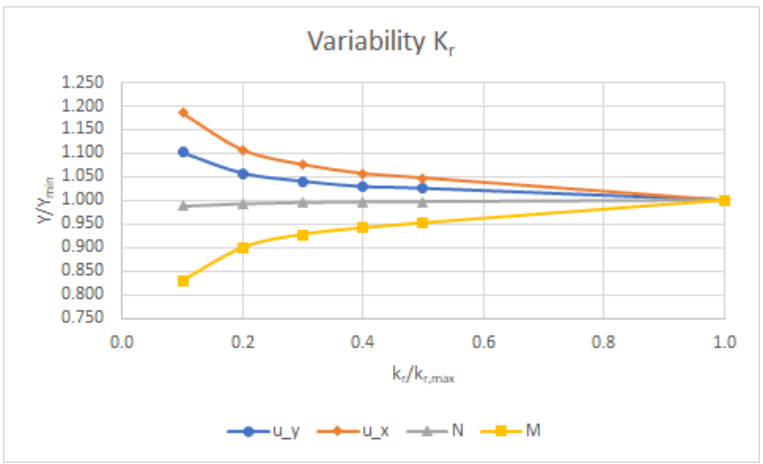


Figure D.8: Variability of calculated results for different rotational segment joint stiffnesses ($k_r$)

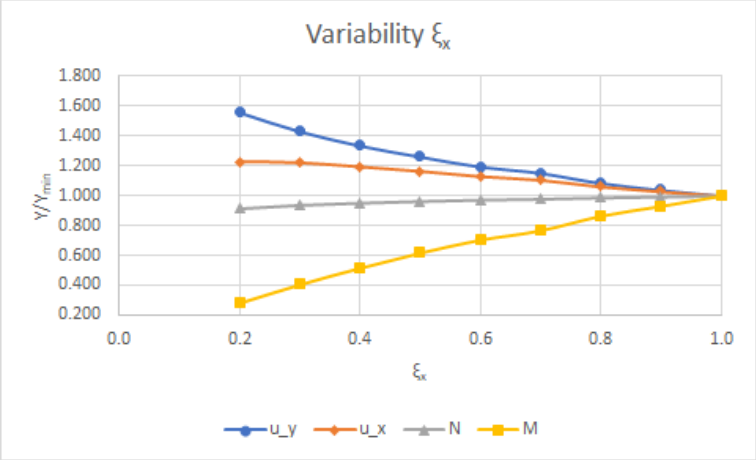


Figure D.9: Variability of calculated results for different global ring stiffness reduction factors ($\xi_x$)

From these plots it was determined which parameters (with the corresponding range relative to the Middle-East case) had the most influence on the ground and tunnel lining behaviour. As was mentioned earlier the most interesting feature was whether the parameter increases or decreases: the vertical ovalization, the horizontal ovalization, the normal forces and the moments in the lining. Per parameter it was notified whether it had influence on the output and is presented in table D.3.

| $Factor$ | $u_y$ | $u_x$ | $N$ | $M$ |
|---|---|---|---|---|
| $E$ | 0.22 | 0.16 | 0.88 | 0.19 |
| $\nu$ | 1.11 | 1.11 | 1.02 | 1.09 |
| $c'$ | 0.91 | 0.90 | 1.01 | 0.87 |
| $k_0$ | 0.42 | 0.33 | 1.10 | 0.34 |
| $\Delta h_w$ | 1.03 | 1.05 | 1.02 | 1.03 |
| $R_{inter}$ | 1.17 | 1.23 | 0.88 | 1.15 |
| $C_{ref}$ | 1.32 | 0.72 | 0.86 | 1.01 |
| $k_r$ | 1.85 | 1.73 | 0.96 | 0.51 |
| $\xi_x$ | 1.56 | 1.23 | 0.91 | 0.28 |

Table D.3: Overview of the growth factor of each parameter on the output of the calculated displacement and force distribution in the lining with respect to the initial model

It was concluded that for the vertical and horizontal ovalization and the calculated moment the normative parameter was the Young's modulus (E) of the ground, the lateral earth pressure coefficient ($k_0$) and the lining stiffness indicated by the rotational joint stiffness ($k_r$) and the global reduction factor ($\xi_x$). The maximal normal force was a quite constant value when indicating the ratio. However, as an absolute value it deviated much due to the large quantity.

Moreover, the vertical translation of the ring was only observed with ground water lowering. This phenomena is plotted in figure D.10. From this figure it was concluded that the vertical settlement of the ring was a roughly linear distribution. An increased ground water lowering resulted in an increased settlement. In this analyses no horizontal translation was observed due to the symmetric loading conditions in this model.

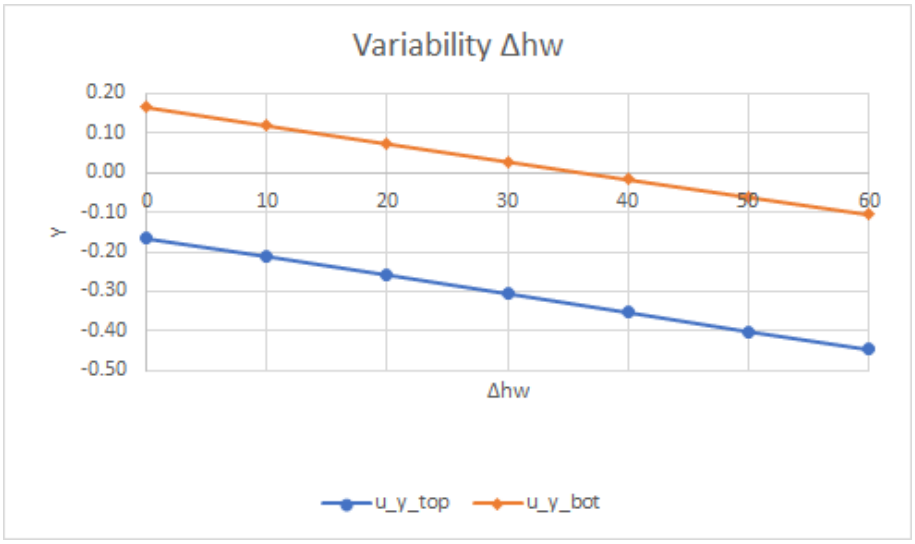


Figure D.10: Variability of calculated lining settlements for different groundwater level lowering ($\Delta h_w$)

Analyzing the effective stress distribution in the ground for different quantities of E, showed the different amount of arching that occurred in the ground. Namely, the area of reduced stress above and below the ring was larger for stiffer material. The vertical stress distribution for the minimal stiffness (left) and maximal stiffness (right) is illustrated in figure D.11. As a result of the same phenomena the horizontal stress redistributed in a comparable matter as shown in figure D.12. These figures combined with the fact that a larger E results in smaller displacements (figure D.13) and moments (figure D.14), concluded that stiffer material resulted in more arching. It was observed that the reduction of displacements and moments along the ring reduces in terms of a ratio, while the shape of the distribution stayed roughly same.

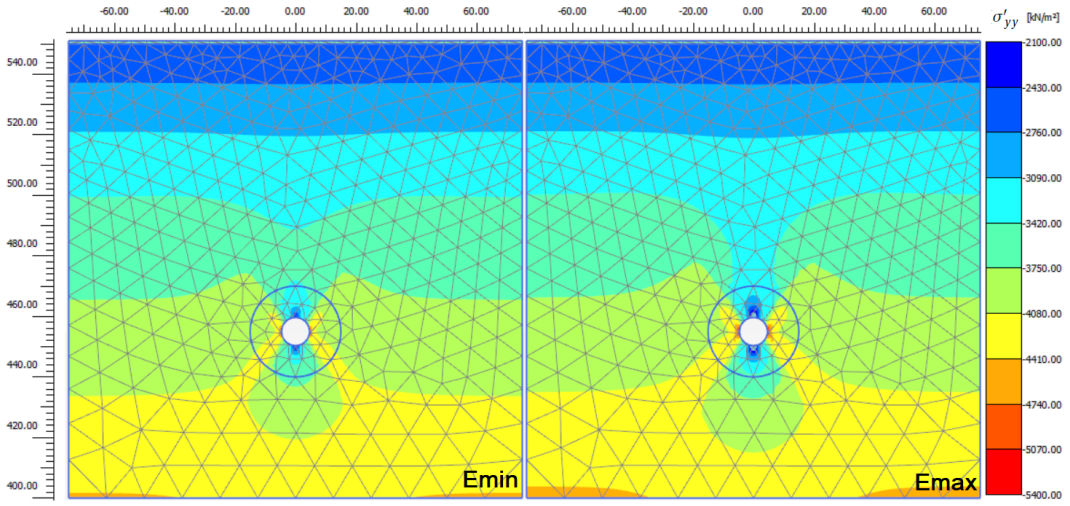


Figure D.11: Comparison between calculated vertical effective stresses ($\sigma'_{yy}$) after the final construction phase for upper and lower bound stiffnesses (E)

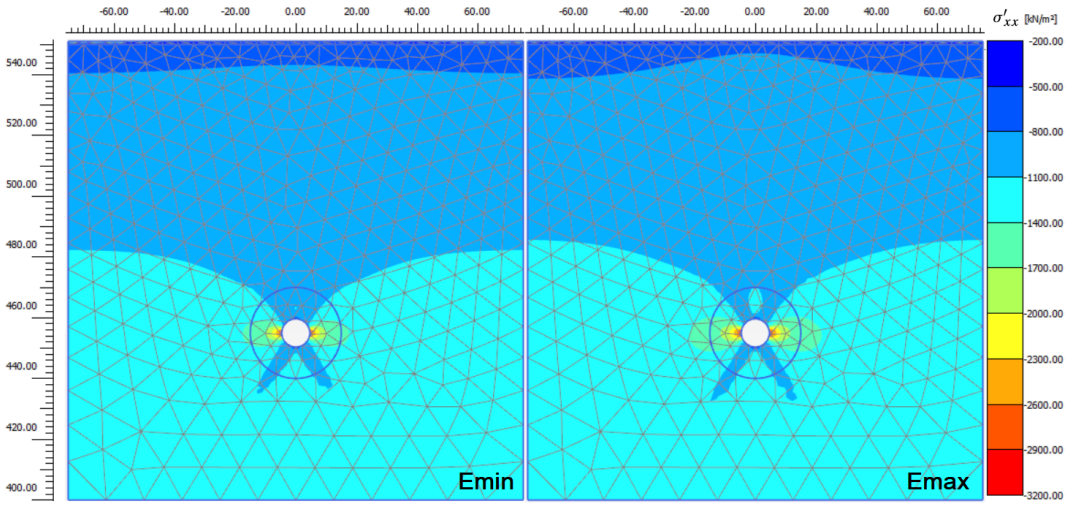


Figure D.12: Comparison between calculated horizontal effective stresses ($\sigma'_{xx}$) after the final construction phase for upper and lower bound stiffnesses (E)

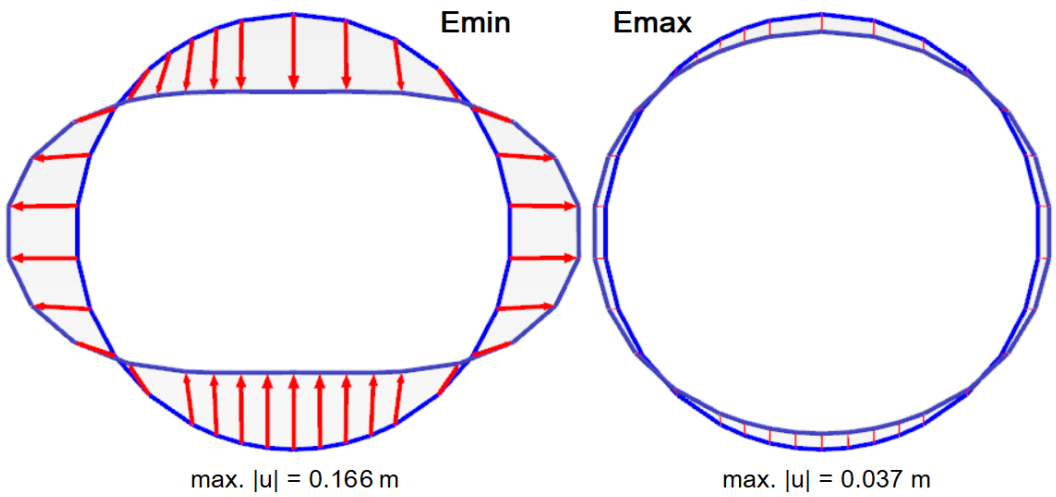


Figure D.13: Comparison between calculated ring displacements (|u|) after the final construction phase for upper and lower bound stiffnesses (E)

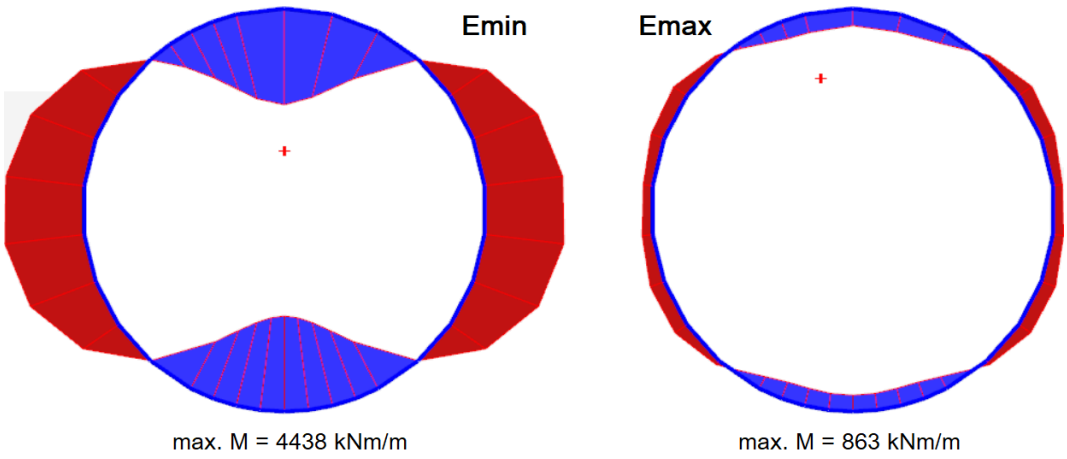


Figure D.14: Comparison between calculated bending moments in the ring (M) after the final construction phase for upper and lower bound stiffnesses (E)

Low lateral earth pressure coefficients ($k_0$) resulted in less horizontal resistance from the ground. While the vertical stress that acted on the lining ring is dependent on the amount of arching in the ground, the amount of horizontal stress at the sides of the ring was lower. This phenomena was observed in figures D.15 and D.16. In terms of vertical stress, it looked like more arching occurred for a low $k_0$. However, in terms of horizontal stress, a low $k_0$ resulted in very local stress increase at the sides of the ring.

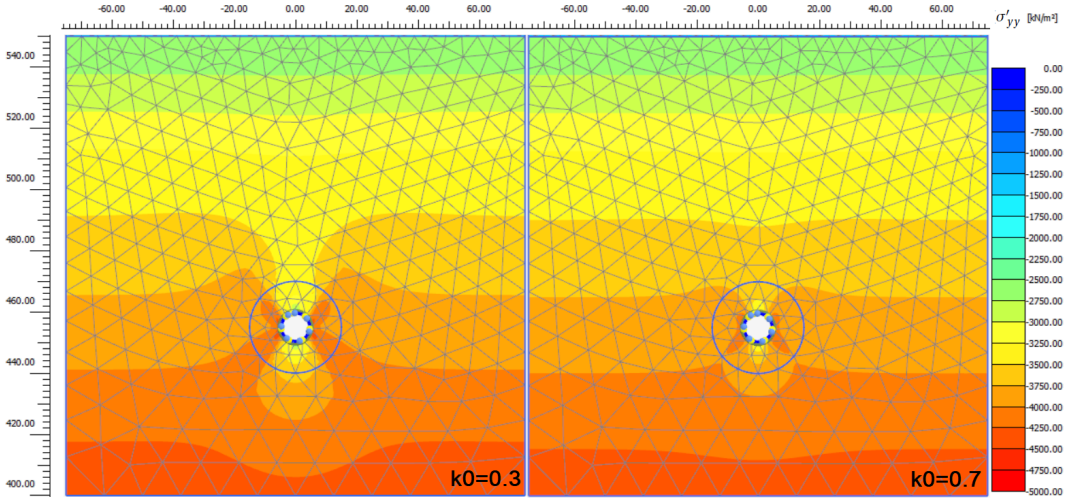


Figure D.15: Comparison between calculated vertical effective stresses ($\sigma'_{yy}$) after the final construction phase for upper and lower bound lateral earth pressure coefficients ($k_0$)

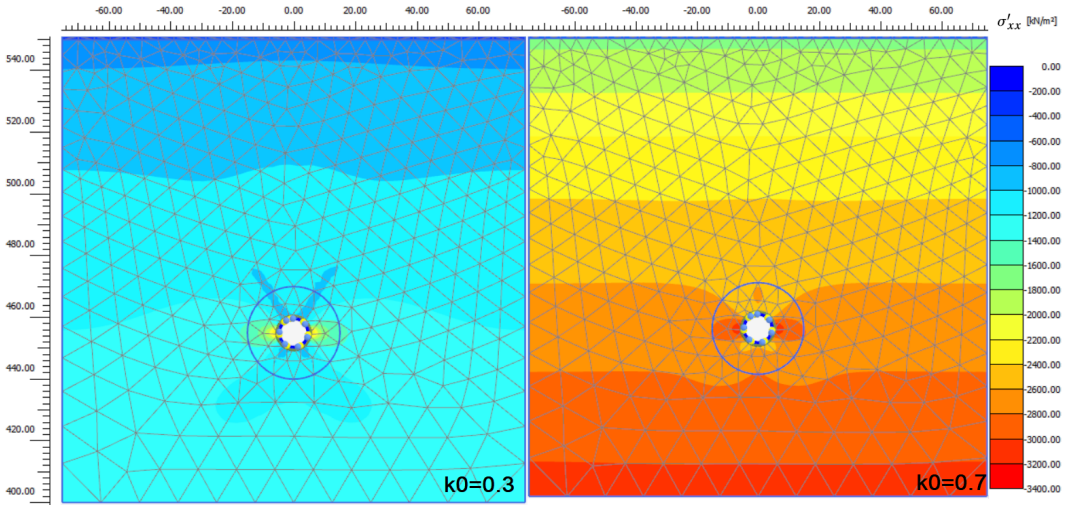


Figure D.16: Comparison between calculated horizontal effective stresses ($\sigma'_{xx}$) after the final construction phase for upper and lower bound lateral earth pressure coefficients ($k_0$)

Ground water lowering did not affect the arching effect in ground, nor the ovalization and moment distribution of the lining. The ground water lowering only resulted in an increase of effective stresses along the whole depth, where ground water was lowered (so from 510 to 450 m a.s.l.). This increase in effective stress resulted in settlements of the entire ground, which implicitly resulted in settlement of the entire ring. This can also be seen in figure D.19, where the ovalization of the ring was almost the same as in the case without ground water lowering, only the ring settled vertically.

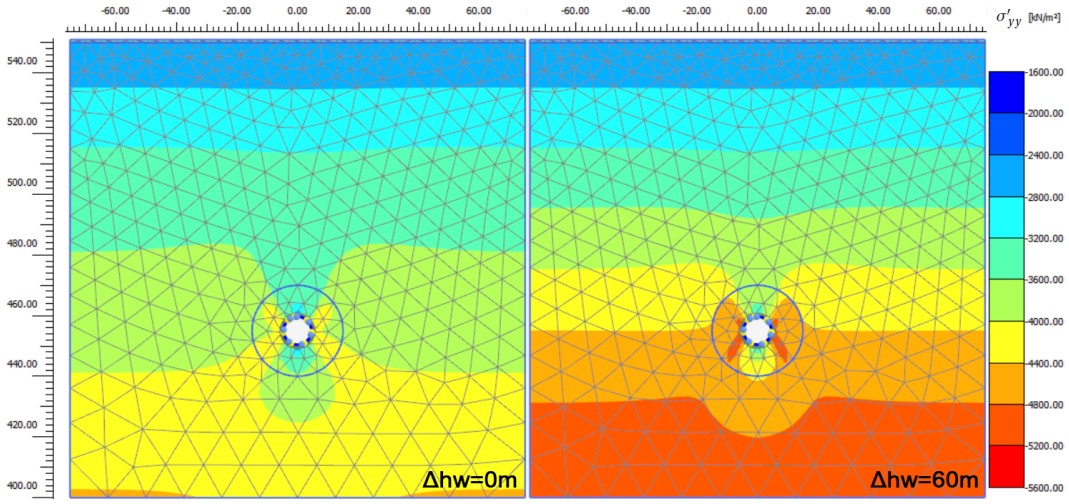


Figure D.17: Comparison between calculated vertical effective stresses ($\sigma'_{yy}$) after the final construction phase without and with lowering of the groundwater level ($\Delta h_w$)

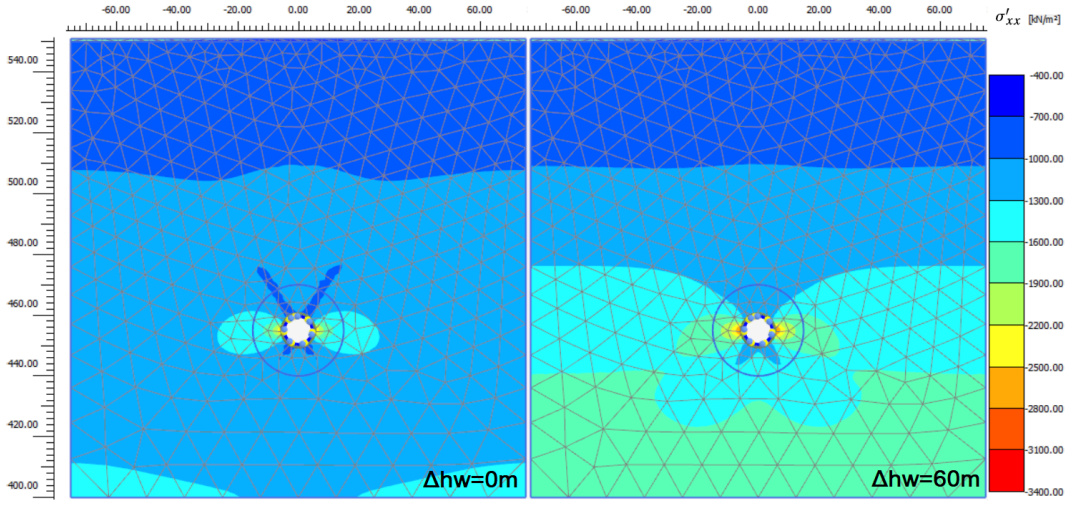


Figure D.18: Comparison between calculated horizontal effective stresses ($\sigma'_{xx}$) after the final construction phase without and with lowering of the groundwater level ($\Delta h_w$)

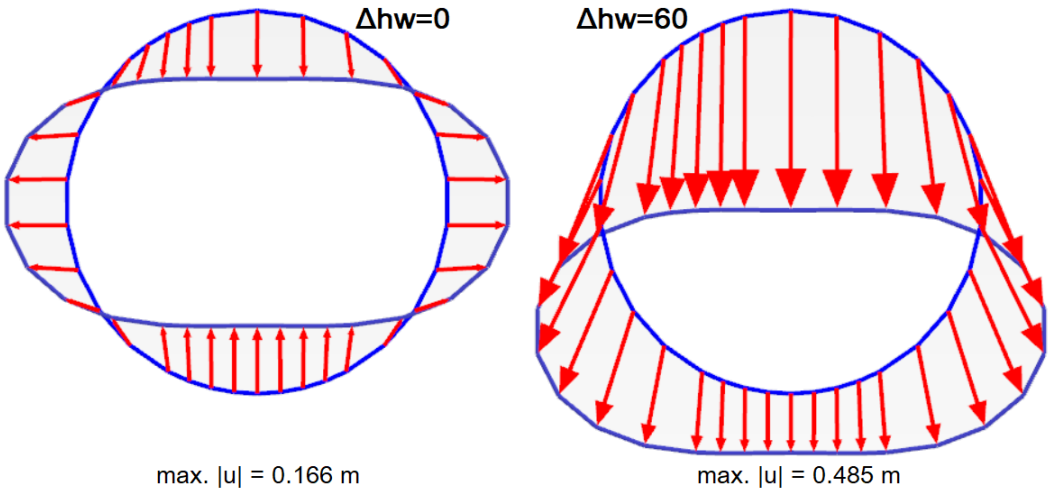


Figure D.19: Comparison between calculated ring deformations (|u|) after the final construction phase without and with lowering of the groundwater level ($\Delta h_w$)

Whereas all other analyzed parameters resulted in an increase or decrease of the displacements of the ring along the entire circumference, the lining contraction ($C_{ref}$) resulted something different. The displacement of ring increased in terms of vertical ovalization and decreased in terms of horizontal ovalization. This was mainly due to the fact the the contraction acted over the entire circumference which resulted in an increase of deformation towards the center of the lining. While the initial ovalization resulted in horizontal expansion.

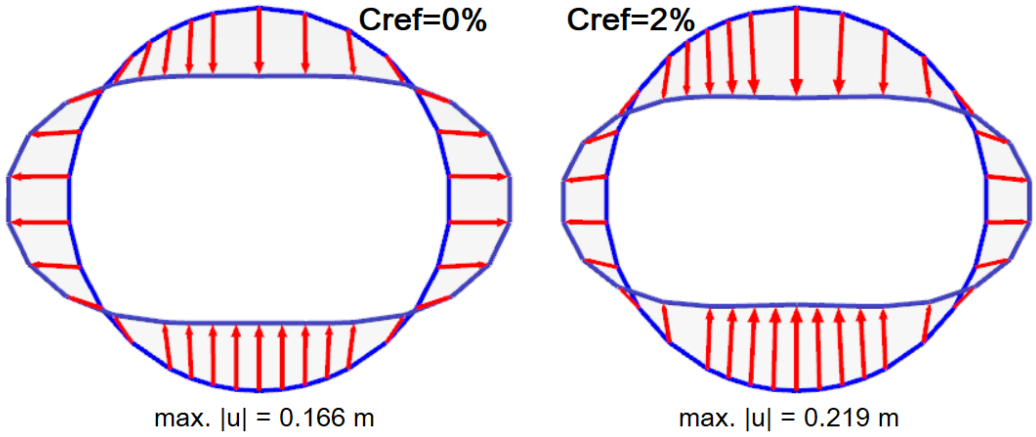


Figure D.20: Comparison between calculated ring deformations (|u|) after the final construction phase without and with lining contraction ($C_{ref}$)

As part of the analyses, the effect of a block load in soft fault material was analyzed. The shape of the block had a point below, which was modelled as such to created a concentrated load on the ring (figure D.21). For this study, the block was modelled with a total height and width of respectively 4 and 6 meter. The properties of the block were equal to the upper bound values of the limestone, which was comparable to an intact concrete block. However, results showed that the loading from the fault and the behaviour of the ring was dominated by the soft fault material along the circumference of the ring. The outcome of the these calculations were compared to the case without a block, with a fault material with corresponding properties. The horizontal ovalization, maximal normal force and moment for different stiffnesses showed exactly the same output. The largest deviation was observed in the vertical ovalization with water lowering of 60 m, which is illustrated in figure D.22. Contrary to the expectations, the case without a rock block showed larger displacements. This might have been due to improper redistribution of stresses through the very stiff block, which reduced the vertical stress acting on the lining.

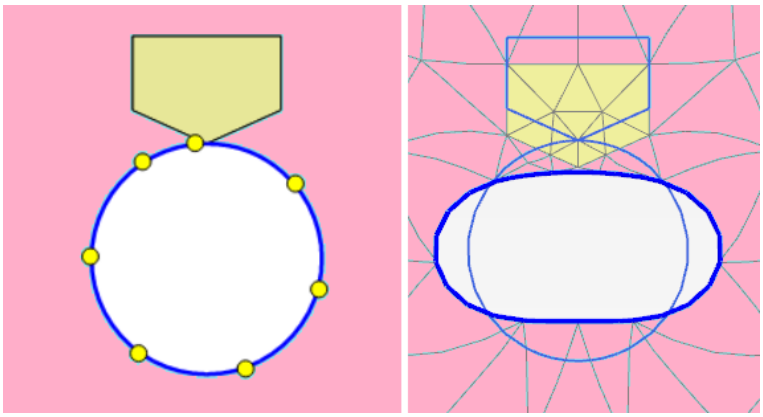

Figure D.21: Rock block modelling in a homogeneous fault (left) with the resulting deformation pattern of the model (right)

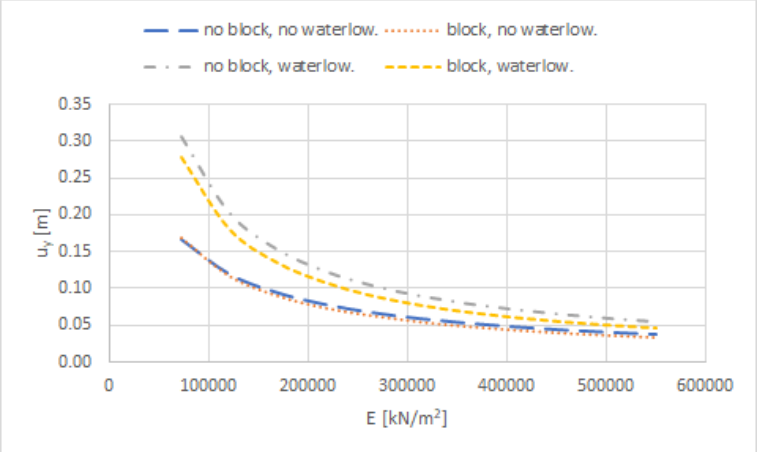


Figure D.22: Variability of calculated vertical displacements for a different ground stiffnesses (E) with and without considering a rock block in the homogeneous fault

# E

# Plaxis 2D west sensitivity

The parametric study for cross section 1, which was located at the west side of the considered fault zone, was executed based on Hoek and Brown parameters only. However, due to the fact that the tunnel lining was located in mainly the marl and this material resulted in the largest displacements and forces in the lining (figure E.1 showed the effect of different depth of the transition from marl to limestone with respect to the center line of the tunnel), the study was executed by changing just the parameters of the marl. The parameters of limestone were fixed at the lower bound values at any time of the parametric study. The analyses were executed and presented in the same manor as done for the fault zone material. Therefore, one refers to appendix D for explanation of the presentation of the calculated output of the parametric study. The ranges of parameters applied in this study are presented in table E.1.

| *Parameters* | marl (q) | | limestone (eq) | |
|---|---|---|---|---|
| | min | max | min | max |
| $\Delta h_w$ [*m b.m.w.l.*] | 0 | 60 | 0 | 60 |
| $GSI$ [−] | 40 | 60 | 40 | 60 |
| $E_{rm}$ [$MN/m^2$] | 319 | 4784 | 2874 | 36712 |
| $\sigma_c$ [$MN/m^2$] | 13 | 20 | 60 | 140 |
| $m_i$ [−] | 5 | 9 | 6 | 12 |
| $\nu$ [−] | 0.35 | 0.15 | 0.35 | 0.1 |
| $k_0$ [−] | 0.5 | 1.0 | 0.5 | 1.0 |
| $k_r$ [$kNm/rad/m$] | 1E5 | fixed | - | |
| $R_{inter}$ [−] | 0.25 | 1.00 | - | |
| $C_{ref}$ [%] | 0.0 | 2.0 | - | |

Table E.1: Geotechnical and structural parameters in the western rock material with corresponding ranges used in this study

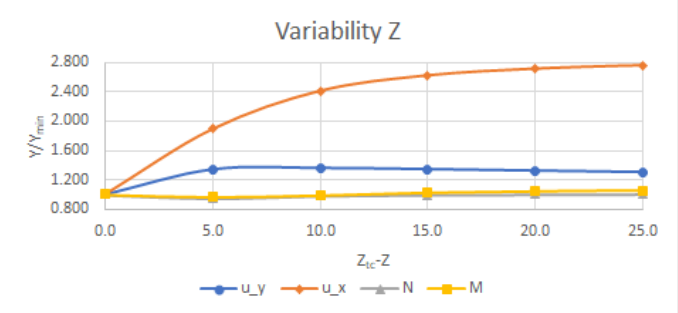


Figure E.1: Variability of calculated results for different depth of the transition from marl to limestone with respect to the tunnel center line ($Z_c$-Z)

The output for the lower bound parameters are presented in table E.2. It was noted that the displacements and moments were relatively low and agree to the non-squeezing conditions as described in section 4.2.4 (radial displacement was lower than 1% = 4.5 cm). However, due larger volumetric weight compared to the fault material (25 instead of 20 kN/m$^3$) combined with the larger lower bound $k_0$-value, the normal forces were larger than for the fault material.

| *Parameters* | output |
|---|---|
| $u_y$ $[m]$ | 0.041 |
| $u_x$ $[m]$ | 0.025 |
| $N$ $[kN/m]$ | 21730 |
| $M$ $[kNm/m]$ | 892 |

Table E.2: Output for the combination of lower bound values from table E.1 except for $k_r$ and $R_{inter}$

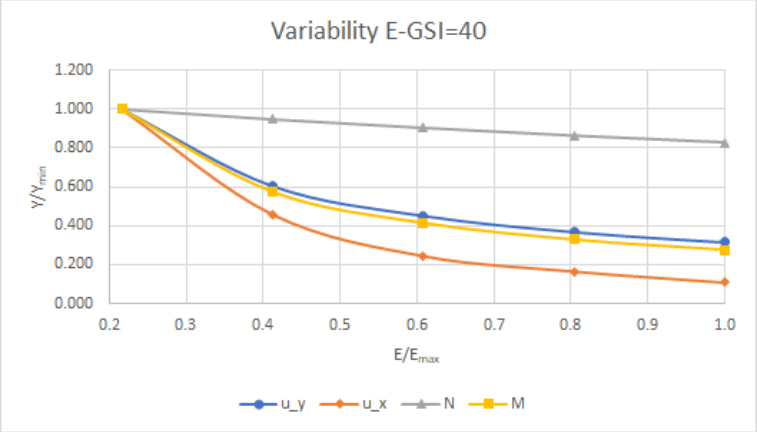


Figure E.2: Variability of calculated results for a different ground stiffnesses (E)

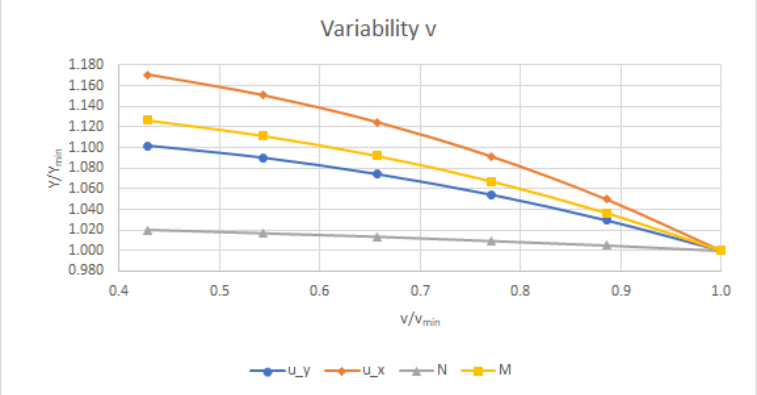


Figure E.3: Variability of calculated results for a different Poisson's ratio's ($\nu$)

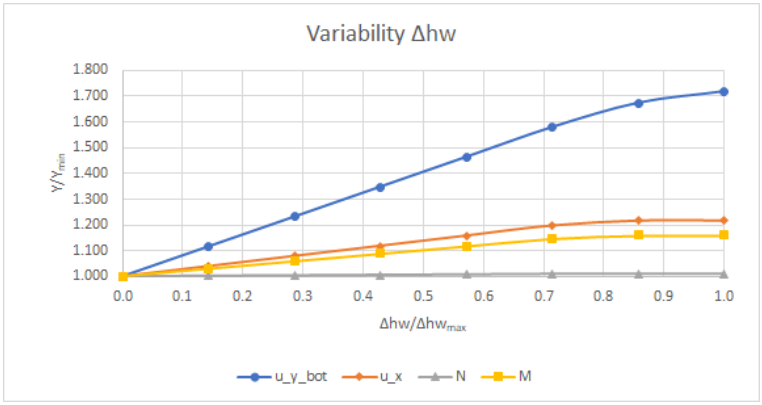


Figure E.4: Variability of calculated results for different groundwater level lowering ($\Delta h_w$)

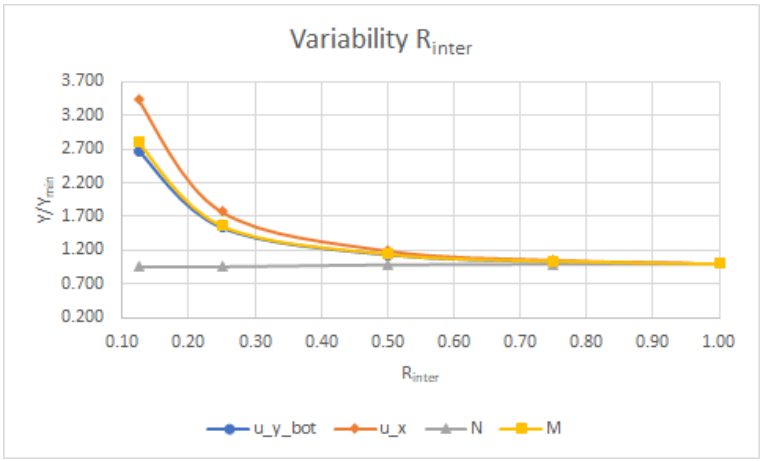


Figure E.5: Variability of calculated results for different interface reduction factors ($R_{inter}$)

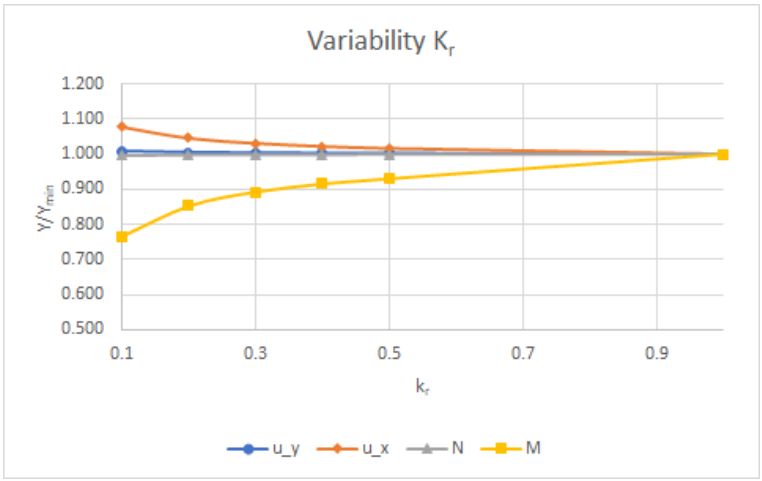


Figure E.6: Variability of calculated results for different rotational segment joint stiffnesses ($k_r$)

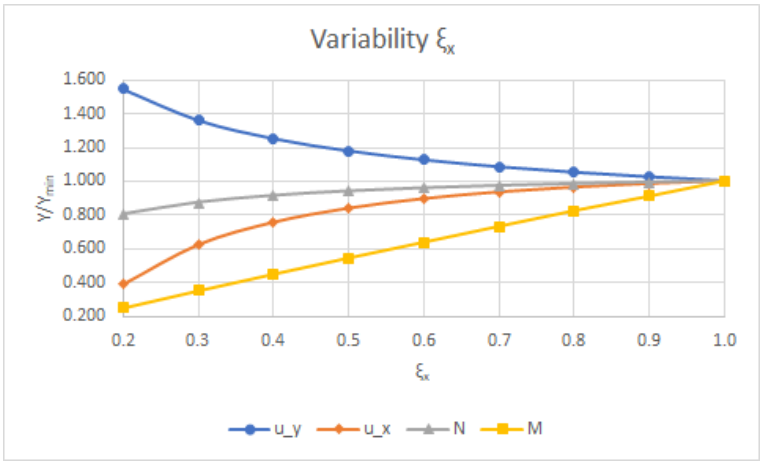


Figure E.7: Variability of calculated results for different global ring stiffness reduction factors ($\xi_x$)

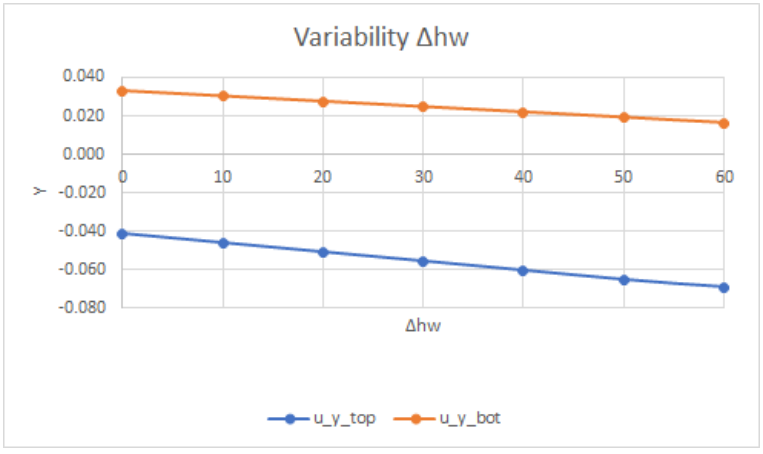


Figure E.8: Variability of calculated lining settlements for different groundwater level lowering ($\Delta h_w$)

Figures E.2 to E.8 showed distributions that were comparable qualitatively to that of the fault material. The vertical translation due to groundwater lowering did show a much lower quantity, namely a settlement of approximately 2cm at the tunnel invert ($u_{y,bot,min}$ - $u_{y,bot,max}$). The figures E.9 and E.11 do show an interesting feature for $k_0$ and $C_{ref}$.

The $k_0$ resulted in a reduction of horizontal ring displacements, except for $k_0$ = 1.0. The the horizontal displacement for $k_0$ = 0.9 was smaller, than for $k_0$ = 0.8 and 0.9. The reason for this was that for $k_0$ = 1.0 the displacements along the whole lining ring was uniform because of a uniform loading condition, shown in figure E.10.

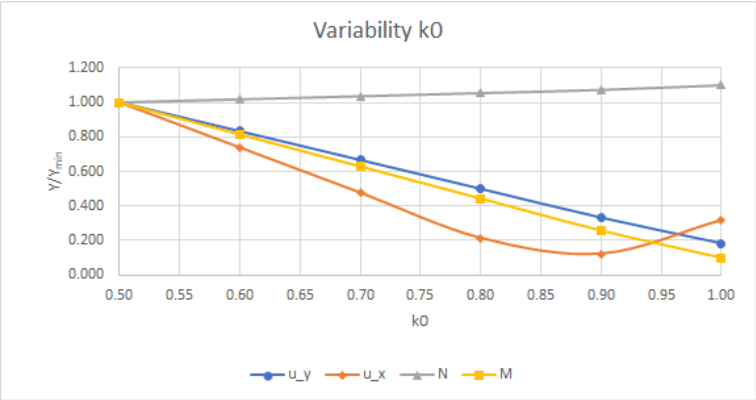


Figure E.9: Variability of calculated results for different lateral earth pressure coefficients ($k_0$)

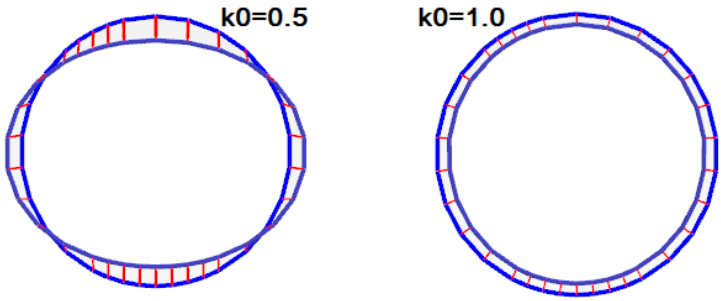


Figure E.10: Comparison between calculated ring deformations (|u|) after the final construction phase for upper and lower bound lateral earth pressure coefficients ($k_0$)

The horizontal displacement decreased in case of an increasing $C_{ref}$ until a certain point. At $C_{ref} > 0.8\%$ the horizontal displacement started to increase. This was declared by the fact that the horizontal displacement was an expansion in the first place due to the ovalization, but due to the contraction there was a certain point when the whole line contracted to the inward of the ring. The contraction was a uniform displacement along the circumference of the ring, however the initial ovalization was so small that the contraction exceeded the limit number of expansion after $C_{ref} > 0.8\%$. This phenomena is shown in figureE.12.

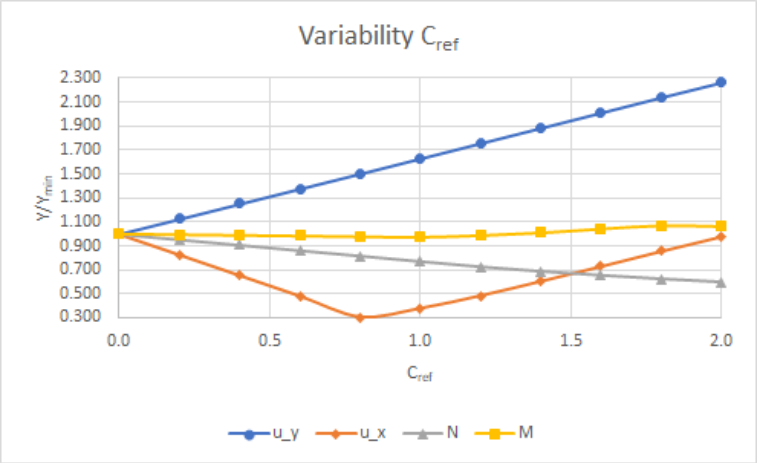


Figure E.11: Variability of calculated results for different contractions ($C_{ref}$)

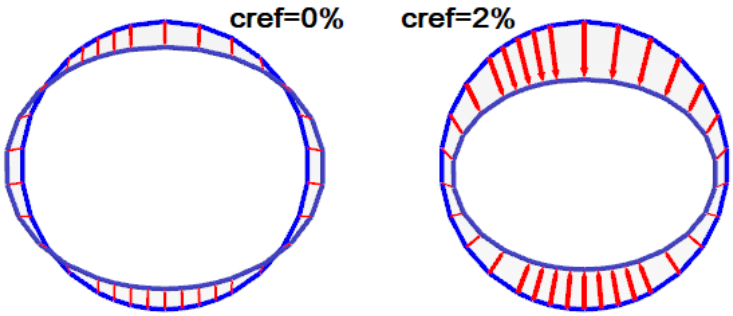


Figure E.12: Comparison between calculated ring deformations (|u|) after the final construction phase without and with lining contraction ($C_{ref}$)

# F

# Plaxis 2D validation - Erdmann

By using equation F.1, the maximal normal force was calculated. The first term of the summation was the normal force due to pressure of the ground at rest, while the second term accounted for the shear stresses translated into normal forces due to a $k_0$ not equal to 1.0. The maximal moment, that was calculated using equation F.2, was generated by translated shear stresses from the ground as well. For a partial slip between the lining and the ground, the second N-term and M would decrease. Equations F.3 and F.4 calculated a dimensionless factor to account for the ratio between ground - bending stiffness (EI) and ground - shear stiffness (EA) respectively. The parameter R was the radius of the center line of the lining ring.

$$N = (\gamma' H \frac{1+K_0}{2} + \gamma_w H_w) \frac{R}{1+\frac{1}{1+\nu}\beta+\frac{\beta}{\alpha}} + \frac{\gamma' H \frac{1-K_0}{2} R\left(1+\frac{1}{12(1+\nu)}\alpha+\frac{1}{4(1+\nu)}\beta\right)}{1+\frac{3-2\nu}{12(3-4\nu)(1+\nu)}\alpha+\frac{5-6\nu}{4(3-4\nu)(1+\nu)}\beta+\frac{1}{12(3-4\nu)(1+\nu)^2}\alpha\beta} \; [kN] \tag{F.1}$$

$$M = \frac{\gamma' H \frac{1-K_0}{2} R^2\left(1+\frac{1}{2(1+\nu)}\beta\right)}{2+\frac{3-2\nu}{6(3-4\nu)(1+\nu)}\alpha+\frac{5-6\nu}{4(3-4\nu)(1+\nu)}\beta+\frac{1}{6(3-4\nu)(1+\nu)^2}\alpha\beta} \; [kNm] \tag{F.2}$$

$$\alpha = \frac{E_{rm} R^3}{(EI)_l} \; [-] \tag{F.3}$$

$$\beta = \frac{E_{rm} R}{(EA)_l} \; [-] \tag{F.4}$$

The analytical validation of the calculated Plaxis 2D models was done with the Erdmann solution. It was chosen to only validate the lower and upper bound values for all parameter, while the rest of the parameters was fixed at the lower bound value. This meant that the minimal and maximal results of the parametric study for $E_{rm}$, $k_0$, $\nu$ and $\xi_x$ in appendix D and E were validated. The reference stress level was kept at 455 m a.s.l., same as in the validation with Mohr-Coulomb (appendix B). The total stresses were 4400 and 5500 kN/m$^2$, while the effective stresses were 3850 and 4950 kN/m$^2$ for respectively the fault and rock. The only other variables needed to calculate the maximal normal force and moment in the ring, were: $E_{rm}$, $k_0$, $\nu$, tunnel radius (R) and lining stiffness (E). The lining radius was fixed at 4.65 m and the stiffness at 35E6 kN/m$^2$. The calculated results were presented in table F.1 for the fault zone and table F.2 for the marl on the west side of the fault.

| *Parameters* | $E\ [MN/m^2]$ | | $\nu$ [−] | $k_0$ [−] | | $\xi_x$ [-] |
|---|---|---|---|---|---|---|
| | 73 | 551 | 0.15 | 0.5 | 0.7 | 0.2 |
| $\alpha$ [−] | 39 | 297 | 39 | 39 | 39 | 197 |
| $\beta$ [−] | 0.024 | 0.183 | 0.024 | 0.024 | 0.024 | 0.024 |
| $N_{Erdmann}\ [kN/m]$ | 18668 | 16682 | 19590 | 19087 | 19487 | 18371 |
| $N_{Plaxis}\ [kN/m]$ | 17670 | 15580 | 18030 | 18810 | 19340 | 16100 |
| $M_{Erdmann}\ [kNm/m]$ | 3269 | 565 | 3495 | 2335 | 1401 | 796 |
| $M_{Plaxis}\ [kNm/m]$ | 4438 | 863 | 4835 | 2475 | 1504 | 1247 |

Table F.1: Comparison of the maximum N and M in a ring with corresponding parameters in the fault zone between Erdmann and Plaxis

| *Parameters* | $E\ [MN/m^2]$ | | $\nu$ [−] | $k_0$ [−] | $\xi_x$ [-] |
|---|---|---|---|---|---|
| | 319 | 4784 | 0.15 | 1.0 | 0.2 |
| $\alpha$ [−] | 172 | 2577 | 172 | 172 | 859 |
| $\beta$ [−] | 0.106 | 1.589 | 0.106 | 0.106 | 0.106 |
| $N_{Erdmann}\ [kN/m]$ | 22349 | 11760 | 23133 | 23700 | 22270 |
| $N_{Plaxis}\ [kN/m]$ | 21730 | 12540 | 22160 | 23980 | 17450 |
| $M_{Erdmann}\ [kNm/m]$ | 852 | 88 | 929 | 0 | 179 |
| $M_{Plaxis}\ [kNm/m]$ | 892 | 109 | 1005 | 87 | 222 |

Table F.2: Comparison of the maximum N and M in a ring with corresponding parameters in the marl (west to fault) between Erdmann and Plaxis

# G

# Plaxis 2D calibration - homogeneous fault

The homogeneous fault calibration was basically the same simple model as used for the parametric study. For this model, it was assumed that the fault was perpendicular to the tunnel, not inclined and implicitly that the fault width was infinite. Based on the geological cross section, this was not the case in the Middle-East. However, to have a better understanding of the combination of parameters that would result in the amount of displacements this analysis was done. Analysis was done by fitting the vertical and horizontal ovalization, as well as the vertical translation. The iterative determination of the rotational joint stiffness ($k_r$) was accounted for, which was compared to a corresponding global reduction factor ($\xi_x$) for the lining. Obtaining these results, an idea of the corresponding maximal normal force and moment was created.

The combination of parameters for which a match with the displaced ring from the case was found are:
$E_{rm}$ = 150 MN/m$^2$; $\nu$ = 0.2; c' = 0 kN/m$^2$; $\phi'$ = 27.5°; $k_0$ = 0.5; $R_{inter}$ = 0.5; $C_{ref}$ = 0.2%; $\Delta h_w$ = 43 m

In figure G.1 the fitted displacements of the calculated ring is compared to the real measured ring. The points based on which the fit was made, were the tunnel top and invert and the horizontal ovalization (where the assumption was made that the measured ring had symmetric horizontal ovalization of (12 + 3) / 2 ≈ 7.5 cm).

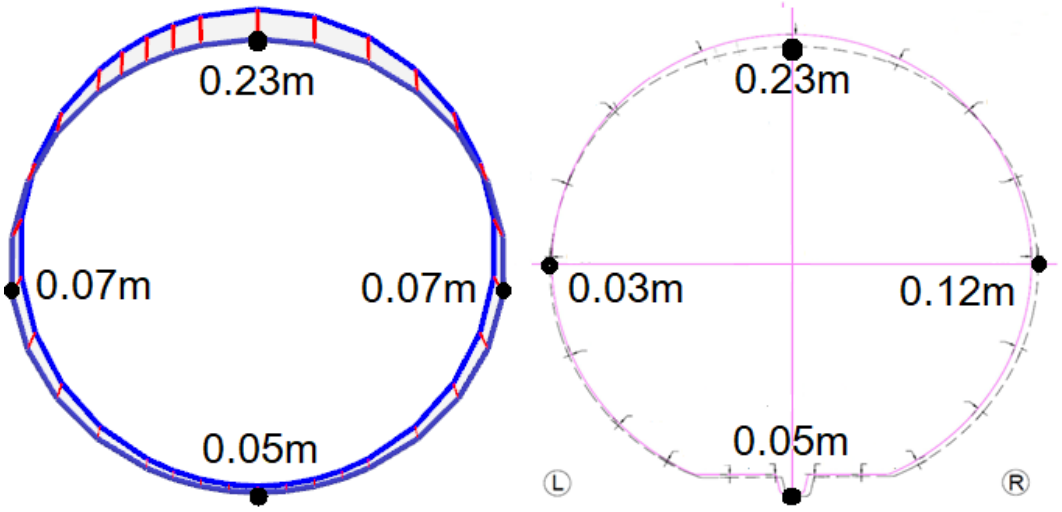


Figure G.1: Comparison between the calculated displacements for the homogeneous model (left) and the measured displacements (right)

The iteratively found parameters for the rotational stiffness of the joint are shown in table G.1. The locations of the joints with corresponding number in the Plaxis model are shown in figure G.2. As a reminder, the closed joint stiffness was equal to $k_r$ = 467 MNm/rad/m. As it was observed in the Middle-East case, the joints underwent leakages. It was not clear were the leakages were observed, but based on this calibration most of the joints were open.

| *Joint #* | Stiffness ($k_r$) [*$10^3$ kNm/rad/m] | Moment (M) [kNm/m] | Normal force (N) [kN/m] | eccentricity e [m] | open/closed joint |
|---|---|---|---|---|---|
| k1 | 452 | 1086 | 13426 | 0.081 | open |
| k2 | 355 | 1887 | 17301 | 0.109 | open |
| k3 | 467 | 208 | 14453 | 0.014 | closed |
| k4 | 260 | 1576 | 12281 | 0.128 | open |
| k5 | 467 | 103 | 14258 | 0.007 | closed |
| k6 | 357 | 1884 | 17354 | 0.109 | open |
| k7 | 452 | 1088 | 13428 | 0.081 | open |

Table G.1: Calculated joint stiffnesses with Janßen's theorem for the calibrated ring

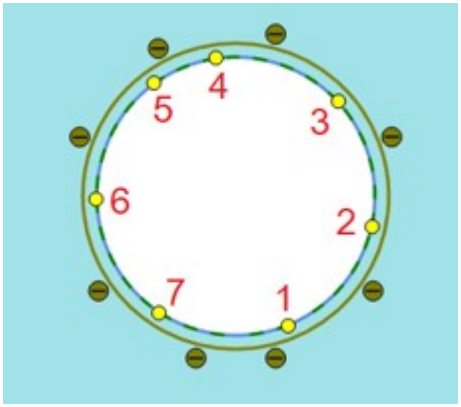


Figure G.2: Locations of the corresponding joint numbering is shown in this figure

Analyzing a monolith lining ring for which the stiffness was reduced by means of a global reduction factor which resulted in the same displacements, it was found that an $\xi_x$ between 1.0 to 0.8 fitted the displacements exactly. However, it was unknown what the error of the measurements was. This could have be typically 3 cm, which implied that $\xi_x$ could be as low as 0.2. Additionally, as the observed issues in the Middle-East case did not include structural damage, the force distribution would be lower than the capacity of the ring. On the other hand, the assumption of a monolith ring resulted in normative values for the maximal normal force and moment.

| $\xi_x$[−] | cal. | 1.0 | 0.8 | 0.6 | 0.4 | 0.2 | 0.1 |
|---|---|---|---|---|---|---|---|
| Max. top displacement ($u_{y,top}$) [m] | -0.23 | -0.23 | -0.23 | -0.24 | -0.25 | -0.26 | -0.28 |
| Max. invert displacement ($u_{y,invert}$) [m] | -0.05 | -0.05 | -0.05 | -0.04 | -0.03 | -0.02 | 0.00 |
| Max. horizontal displacement ($u_x$) [m] | 0.07 | 0.07 | 0.07 | 0.07 | 0.07 | 0.07 | 0.05 |
| Max. normal force ($N$) [kN/m] | 17350 | 17420 | 17220 | 16940 | 16470 | 15330 | 13480 |
| Max. moment ($M$) [kNm/m] | 2030 | 2138 | 1787 | 1389 | 973 | 519 | 279 |

Table G.2: Comparison between the fitted model with joints and the calculated results using a global reduction factor ($\xi_x$) for the stiffness of a monolith ring

# H

# Plaxis 2D calibration - heterogeneous model

The calibration of the heterogeneous model assumed the aspects as the homogeneous fault in terms of the third dimension. The difference was that in this model the influence of adjacent rock masses were taken into account (figure H.1). The principle in this model was that the fault had a non-perpendicular course with respect to the tunnel. However, the width and course of the fault zone were unknown and could be theoretically back calculated from this model.

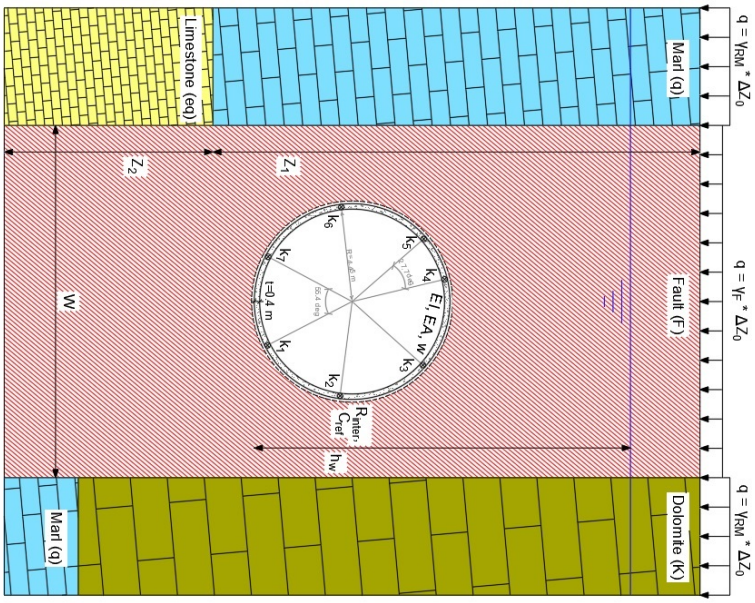


Figure H.1: Ground model with a realistic stratification based on the geological profile from the Middle-East case and some defined variable parameters

As it had been observed from preliminary analyses, it was very hard to "make" the tunnel translate vertically and especially horizontally in this model. The reason for this was mainly the redistribution of stresses in the fault zone due to the very stiff adjacent rock masses. This resulted in a stiffness ratio varying from 0.22 (lower bound values of fault material and marl) to 0.002 (lower bound value of fault material and upper bound value of dolomite) between the fault material and the adjacent rock. Based on this feature the calibration was started with the assumptions of minimal stiffness and strength parameters in the fault zone. The dolomite and limestone had such large lower bound properties, that these were also adopted from the start of the calibration. This led to the only variable parameters, being the ones mentioned in table H.1.

The parameters in table H.1 were predefined based on preliminary analyses. These analyses showed that the ovalization of the tunnel was calibrated to the fitted output by setting the fault parameters to the lower bound values as mentioned in table 4.1 in section 4.2.4, except for $k_0$ which was set to 0.5. The vertical settlement of the tunnel was hard to reach with an upper value for ground water lowering of $\Delta h_w$ = 60m, therefore it was increased to 70 m. This was considered as realistic, because the perched water could have easily dropped to an infinitely low water table if the tunnel acted as a drain. In terms of lining parameters, the joints were assumed to be fixed and the backfilling as fully bonded with the lining ($R_{inter}$ = 1.0 and $C_{ref}$ = 0 %). As it was observed that the difference between closed joints and a monolith ring was very small, for sake of simplicity, the ring was modelled as monolith. Moreover, the assumption that the measured ring was located in the middle of the fault zone was set loose. The reason for this was that the ring was displaced non-symmetrically in the horizontal direction. Instead, the width with respect to the tunnel center for which the right horizontal shift was encountered was analyzed in terms of $W_{left}$ and $W_{right}$. Lastly, the lower bound stiffness for marl was reduced to 200 MN/m$^2$ and the upper bound to 319 MN/m$^2$ and the vertical transition from marl to limestone was varied between 400 m and 430 m a.s.l. instead of 430 m and 455 m a.s.l. as mentioned in table 3.1.

| *Parameters* | min | max |
|---|---|---|
| $\Delta h_w$ [*m b.m.w.l.*] | 40 | 70 |
| $E_{marl}$ [$MN/m^2$] | 200 | 319 |
| $\nu_{marl}$ [−] | 0.35 | 0.2 |
| $W_{left}$ [*m*] | 5 | 15 |
| $W_{right}$ [*m*] | 30 | 40 |
| $Z_2$ [*m*] | 0 | 30 |

Table H.1: Geotechnical parameters of the marl layer at the west side with corresponding ranges used in the calibration

After all the combinations of the parameters were analyzed, the best fit was found for:
E = 200 MN/m$^2$; $\nu$ = 0.35; $\Delta h_w$ = 70 m; $W_{left}$ = 5 m; $W_{right}$ = 40 m; $Z_2$ = 400 m a.s.l.

The calculated displacements of the lining ring were compared to the measured ones and presented in figure H.2. The calculated displacements fitted the measured displacements almost rounded up to centimeters, only the vertical displacement at the top of the ring (A) was 1 cm less. Furthermore, the points of maximal horizontal displacement in the calculated ring seemed to be located lower than in the measured ring.

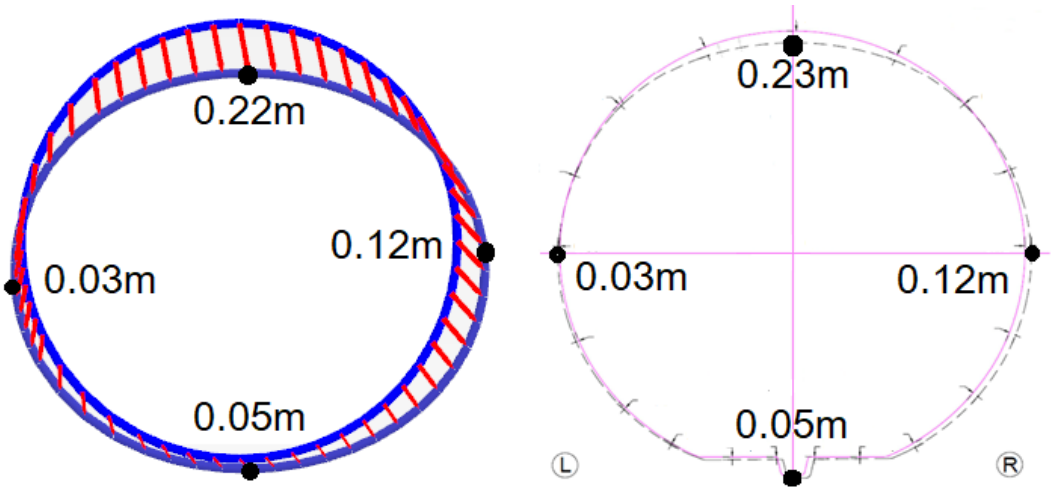


Figure H.2: Displacement distribution for a ring calibrated based on displacements, where the deformations were A = 0.22 m; B = 0.12 m; C = 0.05 m; D = 0.03 m

Although, the normal force and moment distribution showed a small non-symmetry (figure H.3), the calculated values were a little lower than for exactly the same ground parameters for a homogeneous fault (calculated in appendix D). The case of E = 73 MN/m$^2$ and $k_0$ = 0.5 resulted in a maximum moment of 2475 kNm/m, while the calibrated model resulted in a maximum moment of 2342 kNm/m.

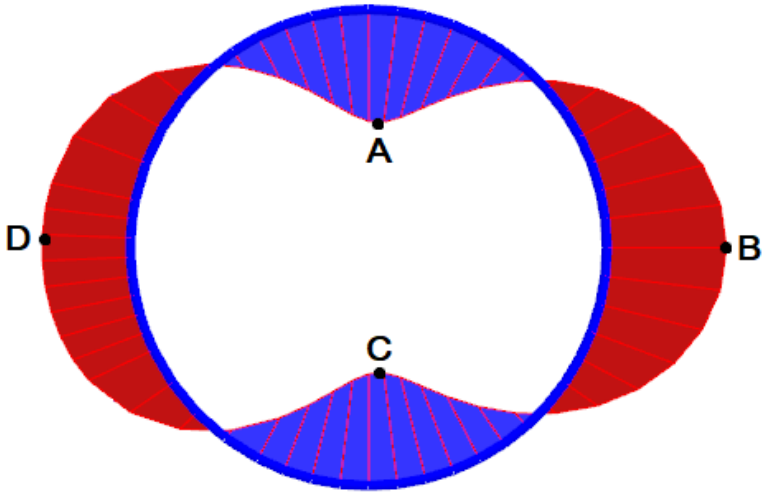


Figure H.3: Moment distribution for a ring calibrated based on displacements, where the moments were A = 2186 kNm/m; B = 2342 kNm/m; C = 2185 kNm/m; D = 1729 kNm/m

To properly show the vertical and horizontal stress distribution for the calibrated model, the domain width of the model was expanded. Looking at the effective vertical stress, as shown in figure H.4, the distribution was dominated by the ground water lowering which resulted in a quantitative increase of stress over depth. Due to the non-symmetric ground model with respect to the tunnel center, the stress increase next to the tunnel due to excavation was dominated at the side of the marl.

The horizontal stress distribution showed some boundary effects at the top and bottom of the model, in terms of a not so smooth distribution of stresses at the bottom and attraction of larger stress at the top of the model (figure H.5). Furthermore, the stress distribution showed results which were comparable to a symmetric ground build up (appendix D).

Due to the soft marl and fault material the absolute displacements of the ground model were large (figure H.6). The maximal displacement above the tunnel top was equal to the displacements of the ring (which was 22 cm). The absolute displacement of the ground was equal to 18 cm from 490 m to 550 m a.s.l, which was dominated by vertical displacements due to ground water lowering. The horizontal displacements were very local and are shown in the zoomed in box within figure H.6. The maximal horizontal displacement was 11 cm, equal to the horizontal ovalization at the right side of the ring.

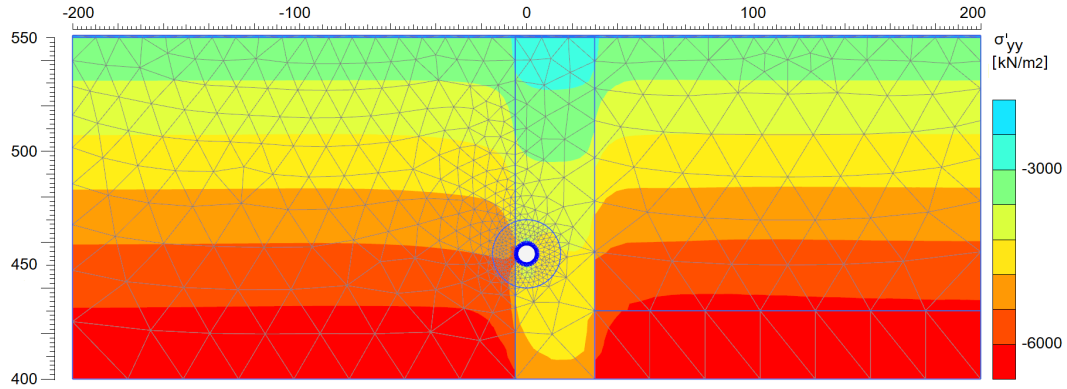


Figure H.4: Calculated vertical effective stresses ($\sigma'_{yy}$) after the final construction phase with lowering of the groundwater level ($\Delta h_w$)

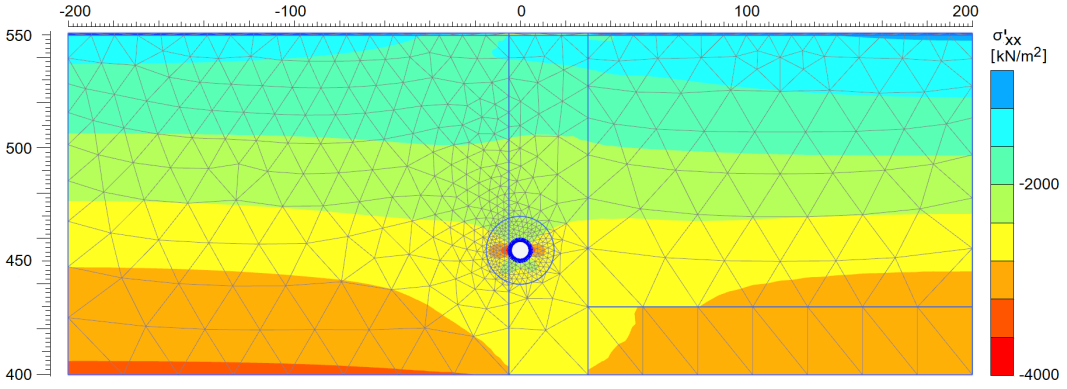


Figure H.5: Calculated horizontal effective stresses ($\sigma'_{xx}$) after the final construction phase with lowering of the groundwater level ($\Delta h_w$)

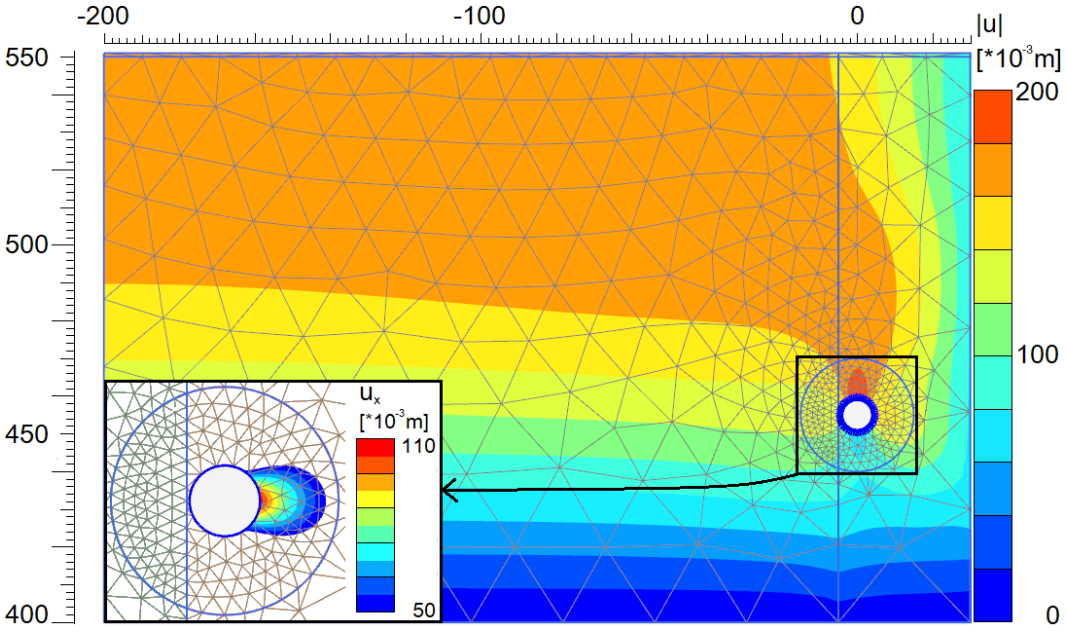


Figure H.6: Absolute ground displacements (|u|) in the left half of the model domain, with a zoom-in on the larger horizontal displacements which develop next to the ring

# Beam model sensitivity

kr = fixed

| L2 [m] | | | max | | | | max | | | |
|---|---|---|---|---|---|---|---|---|---|---|
| kv [kN/m] | min | min | max | max | min | min | max | max | | |
| qv [kN/m] | min | max | min | max | min | max | min | max | | |
| M1 [kNm] | **419361** | 388193 | 779147 | 775682 | 75613 | 31482 | 86383 | 81712 | | |
| M2 [kNm] | 492141 | 475491 | **597226** | 595809 | 301240 | 287576 | 206302 | 205974 | | |
| M3 [kNm] | **766280** | 762510 | 1045807 | 1045422 | 210543 | 251449 | 171975 | 178173 | | |
| w [m] | 0.0248 | 0.0249 | 0.0215 | 0.0216 | 0.0031 | 0.0041 | 0.0010 | 0.0011 | | |
| | | | | | | | | | ksi_y | E |
| | | | | | | | | | 1.00 | 35.00 |
| | | | | | | | | | 0.75 | 26.25 |
| | | | | | | | | | 0.50 | 17.50 |
| | | | | | | | | | 0.25 | 8.75 |
| | | | | | | | | | 0.05 | 1.75 |
| M1 | 0% | 7% | -86% | -85% | 82% | 92% | 79% | 81% | | |
| M2 | 18% | 20% | 0% | 0% | 50% | 52% | 65% | 66% | | |
| M3 | 0% | 0% | -36% | -36% | 73% | 67% | 78% | 77% | | |

| L2 [m] | | | max | | | | max | | | |
|---|---|---|---|---|---|---|---|---|---|---|
| kv [kN/m] | | | min | | | | max | | | |
| qv [kN/m] | | | min | | | | min | | | |
| kr | fixed | 1.85E+09 | 1.00E+09 | 1.00E+08 | 1.00E+07 | fixed | 1.85E+09 | 1.00E+09 | 1.00E+08 | 1.00E+07 |
| M1 [kNm] | 419361 | 423324 | 408844 | 280382 | 145083 | 779147 | 668783 | 593650 | 273582 | 104105 |
| M2 [kNm] | 492141 | 496506 | 191584 | 63275 | 21593 | 597226 | 329789 | 232181 | 65098 | 21921 |
| M3 [kNm] | 766280 | 668250 | 575255 | 275329 | 106276 | 1045807 | 785356 | 662243 | 250658 | 80226 |
| w [m] | 0.0248 | 0.0271 | 0.0281 | 0.0290 | 0.0286 | 0.0215 | 0.0255 | 0.0272 | 0.0293 | 0.0286 |
| | | | | | | | | | | |
| M1 | | 1.01 | 0.97 | 0.67 | 0.35 | | 0.86 | 0.76 | 0.35 | 0.13 |
| M2 | | 1.01 | 0.39 | 0.13 | 0.04 | | 0.55 | 0.39 | 0.11 | 0.04 |
| M3 | | 0.87 | 0.75 | 0.36 | 0.14 | | 0.75 | 0.63 | 0.24 | 0.08 |
| w | | 1.09 | 1.13 | 1.17 | 1.15 | | 1.19 | 1.27 | 1.36 | 1.33 |
| | | | | | | | | | | |
| | | 1.00 | 0.54 | 0.05 | 0.01 | | 1.00 | 0.54 | 0.05 | 0.01 |

| | | | | | | | | | | |
|---|---|---|---|---|---|---|---|---|---|---|
| | | | | | | | | | | |
| | | | | | | | | | | |
| ksi_y | 1.00 | 0.75 | 0.50 | 0.25 | 0.05 | 1.00 | 0.75 | 0.50 | 0.25 | 0.05 |
| M1 [kNm] | 419361 | 371623 | 303397 | 210161 | 91032 | 779147 | 695550 | 569264 | 396642 | 168951 |
| M2 [kNm] | 492141 | 397985 | 276332 | 157916 | 62679 | 597226 | 494639 | 352437 | 179984 | 69463 |
| M3 [kNm] | 766280 | 675248 | 546682 | 378220 | 164000 | 1045807 | 928584 | 757767 | 522137 | 218863 |
| w [m] | 0.0248 | 0.0259 | 0.0274 | 0.0291 | 0.0290 | 0.0215 | 0.0232 | 0.0255 | 0.0284 | 0.0293 |
| | | | | | | | | | | |
| | 1.00 | 0.89 | 0.72 | 0.50 | 0.22 | 1.00 | 0.89 | 0.73 | 0.51 | 0.22 |
| | 1.00 | 0.81 | 0.56 | 0.32 | 0.13 | 1.00 | 0.83 | 0.59 | 0.30 | 0.12 |
| | 1.00 | 0.88 | 0.71 | 0.49 | 0.21 | 1.00 | 0.89 | 0.72 | 0.50 | 0.21 |
| | 1.00 | 1.04 | 1.10 | 1.17 | 1.17 | 1.00 | 1.08 | 1.19 | 1.32 | 1.36 |

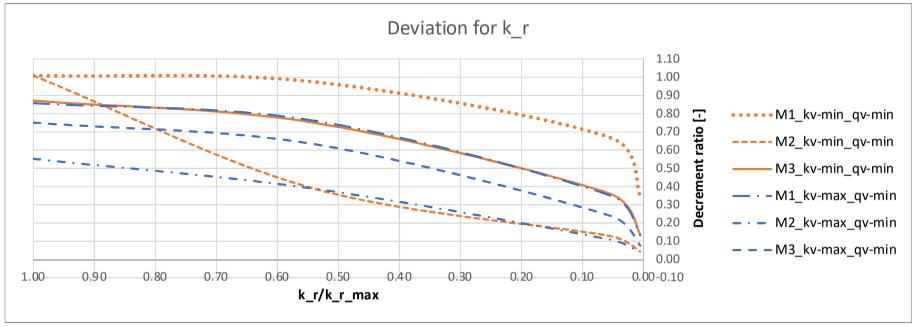


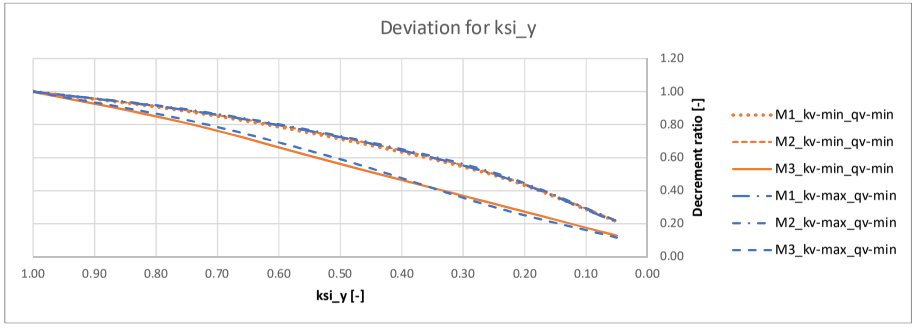

# J

# Beam model validation - Bouma

**Wavelength**

| | q | | eq | | F | | K | |
|---|---|---|---|---|---|---|---|---|
| kv [kN/m] | 3.09E+06 | 4.64E+07 | 2.79E+07 | 3.56E+08 | **7.08E+05** | 5.35E+06 | 3.91E+07 | 3.88E+08 |
| EI [kN/m2] | 4.43E+09 | 4.43E+09 | 4.43E+09 | 4.43E+09 | **4.43E+09** | 4.43E+09 | 4.43E+09 | 4.43E+09 |
| beta [1/m] | 0.11495 | 0.22622 | 0.19916 | 0.37651 | **0.07950** | 0.13179 | 0.21667 | 0.38461 |
| lambda [m] | 55 | 28 | 32 | 17 | **79** | 48 | 29 | 16 |

**Boundary effect** ----------> Kv => Left: marl-min; Middle: fault-min; Right: dolomite-min

qv => Left: marl-min; Middle: fault-max; Right: dolomite-min

| | M_L [kNm] | M_M [kNm] | M_R [kNm] |
|---|---|---|---|
| 60 - 40 - 60 | 419715 | 492064 | 766387 |
| 50 - 40 - 50 | 419735 | 492065 | 766387 |
| 40 - 40 - 40 | 419605 | 492048 | 766385 |
| 30 - 40 - 30 | 419361 | 492155 | 766427 |
| **30 - 40 - 20** | **419361** | **492141** | **766279** |
| 20 - 40 - 20 | 436071 | 492356 | 765913 |
| 20 - 40 -10 | 435806 | 493202 | 786258 |
| 10 - 40 -10 | 251668 | 478898 | 786881 |

| | | | | | | | |
|---|---|---|---|---|---|---|---|
| 60 - 40 - 60 | - | - | - | 160 | 0% | 0% | 0% |
| 50 - 40 - 50 | 0% | 0% | 0% | 140 | 0% | 0% | 0% |
| 40 - 40 - 40 | 0% | 0% | 0% | 120 | 0% | 0% | 0% |
| 30 - 40 - 30 | 0% | 0% | 0% | 100 | 0% | 0% | 0% |
| **30 - 40 - 20** | **0%** | **0%** | **0%** | 90 | 0% | 0% | 0% |
| 20 - 40 - 20 | 4% | 0% | 0% | 80 | 4% | 0% | 0% |
| 20 - 40 -10 | 4% | 0% | 3% | 70 | 4% | 0% | 3% |
| 10 - 40 -10 | -40% | -3% | 3% | 60 | 40% | 3% | 3% |

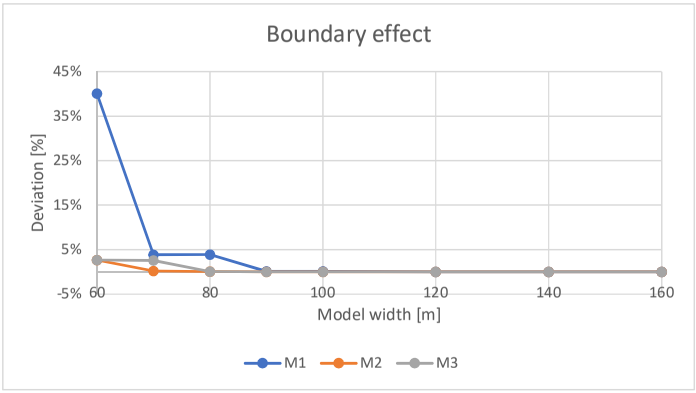


**Validation**

| | F-min |
|---|---|
| EI [kN/m2] | 4.43E+09 |
| kv [kN/m] | 7.08E+05 |
| beta [1/m] | 0.07950 |
| L2 [m] | 40 |
| qv [kN/m] | 19400 |
| wmax [m] | **0.0275** |
| Mmax [kNm] | **312851** |

| | MatrixFrame | |
|---|---|---|
| Ltot [m] | **160** | 80 |
| | **0.0276** | 0.0276 |
| | **306006** | 293950 |
| | 0% | 0% |
| | 2% | 6% |

# K

# Plaxis 3D validation

Prior to doing a validation of the output in 3D with 2D results, the set up of the 3D model was justified. As it was mentioned earlier in section 4.4.3 the dimension of the y-axis should have been chosen such that minimal boundary effect was observed or at least the effects should be acknowledged. This was done by setting up a 2D Plaxis ground model which represented the ground stratification in the longitudinal direction of the tunnel. Figures K.1 and K.2 showed the difference in effective horizontal stress distribution, between the initial stage (left), which was the $k_0$-procedure, and the plastic phase (right), which resulted in displacements of the ground due to its own weight and differences in stiffness between layers. In both cases the fault existed of lower bound properties, except for the $k_0$ which was equal to 0.5, and half of the fault width was 20 meters.

In figure K.1 the adjacent rock mass consisted of marl and limestone with lower bound values. It was observed that there was a boundary effect in the limestone layer, where the stresses were reduced. This is explained by horizontal displacements of the marl layer towards the fault zone mainly occurring at the top of the layer, which led to a reduction of horizontal stresses at the interface between the marl and limestone layer. From y = -150 m the stresses stayed almost constant and the dimension was large enough to prevent horizontal boundary effects.

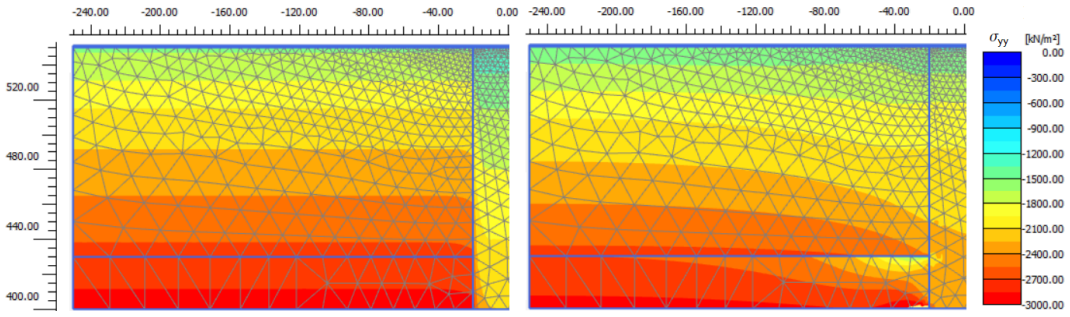


Figure K.1: Horizontal effective stress ($\sigma'_{yy}$) distribution assuming lower bound properties for marl and limestone and lower bound properties for the fault zone, in the initial stage (left) and after the plastic stage (right)

In figure K.1 the adjacent rock mass consisted of marl and limestone with upper bound values. The same feature as in the other case was observed. Additionally, the horizontal stresses were larger (because $k_0$ = 1.0 in the rock) and the transition to a constant horizontal stress in the rock mass needed a larger distance due to the high stiffness ratio between the rock and fault material. Therefore, the required y-dimension was larger, up to 1000 m from the fault. To prevent the calculation of a very large model, this limitation was accepted and taken into account for further analysis.

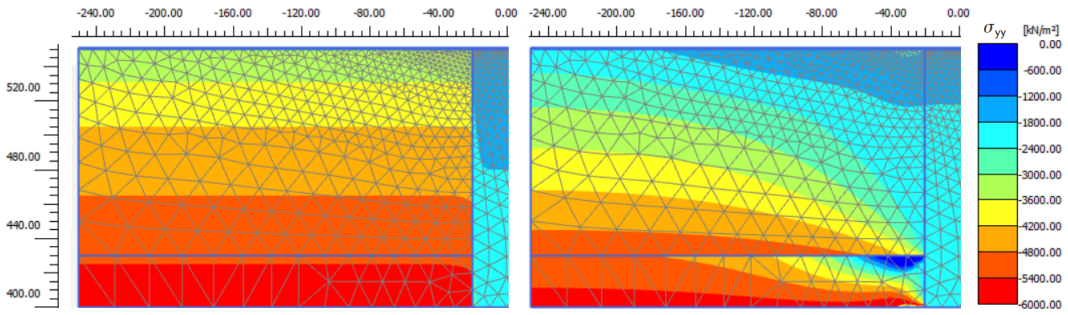


Figure K.2: Horizontal effective stress ($\sigma'_{yy}$) distribution assuming upper bound properties for marl and limestone and lower bound properties for the fault zone, in the initial stage (left) and after the plastic stage (right)

Figure K.3 illustrates the locations of the relevant cross sections that were used to validate the 3D model. The first model that was validated was the fault model, where the 3D homogeneous fault was validated with the calibrated homogeneous fault model in 2D (appendix G). The second model that was validated was the full 3D model, where the other 2D models, from cross sections 1 and 3, were used for validation. These models corresponded to cross sections A-A* and C-C* and were chosen at these locations to prevent the effect of the soft fault zone as much as possible.

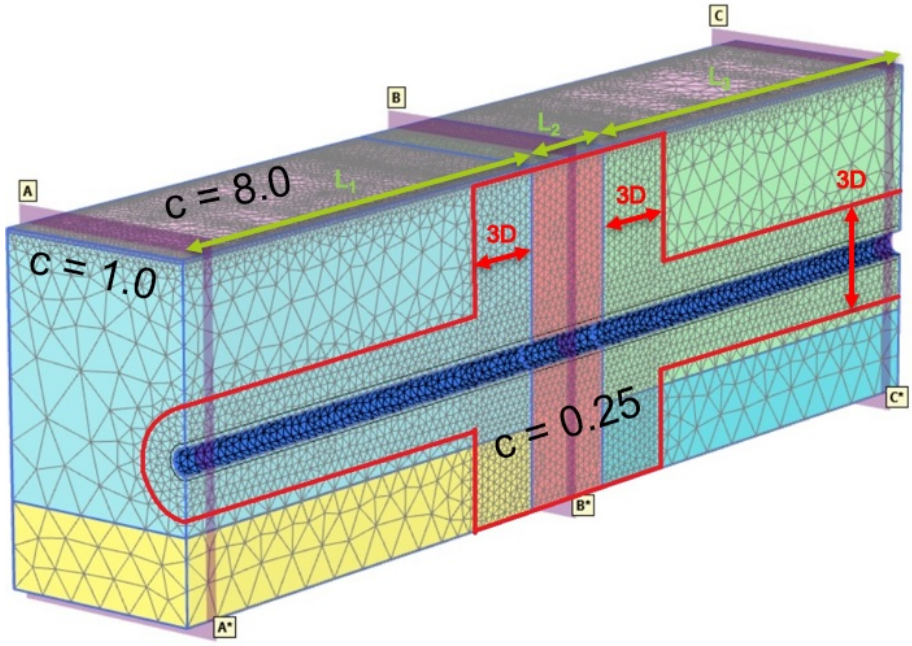


Figure K.3: Final 3D model showing the volume with a finer mesh coarseness of c = 0.25 surrounding the tunnel lining with a diameter of 3 * tunnel diameter = 3D ≈ 30 m and in and 3D next to the fault zone, while the rest had a mesh of 1.0

The set up of the 3D fault model was exactly the same as the homogeneous 2D fault model. This not only included all ground and lining properties, but included the model dimensions and meshing coarseness as well. The results of this comparison is shown in table K.1. Here the parameters $u_{y,top}$, $u_{y,invert}$ and $u_{y,oval}$ were the vertical displacement of the tunnel top and invert as well as half of the total symmetric ovalization ($|u_{y,top}$-$u_{y,invert}|/2$). The vertical displacement of the center of the ring was calculated as $\delta_y = u_{y,top} + u_{y,oval}$. The horizontal displacement was the horizontal ovalization ($u_x$) at one side of the ring. The comparison was also made between max. normal force (N) and moment (M) in the ring.

| *Cross section* | Fault | |
|---|---|---|
| | 2D | 3D |
| $u_{y,top}$ $[m]$ | -0.23 | -0.23 |
| $u_{y,invert}$ $[m]$ | -0.05 | -0.05 |
| $u_{y,oval}$ $[m]$ | 0.09 | 0.09 |
| $\delta_y$ $[m]$ | 0.14 | 0.14 |
| $u_x$ $[m]$ | 0.07 | 0.07 |
| $N$ $[kN/m]$ | 17530 | 18930 |
| $M$ $[kNm/m]$ | 2015 | 2018 |

Table K.1: Calculated maximal lining displacements and forces in the fault zone (cross section B-B* and 2 for resp. 3D and 2D) for the calibrated homogeneous model

All the calculated displacements and moment for 2D and 3D fitted each other precisely. The normal force did not and was explained by the deviation of its distribution in the 3D model (figure K.4). It should be acknowledged that even for a mesh coarseness of 0.25 (relatively fine mesh), there was a significant deviation in the calculated normal force distribution along the ring. In figures K.5(a) and K.5(b) an illustration of the normal force and moment distribution in the longitudinal direction of the tunnel is presented. Here it was observed that not only the normal force deviated significantly, but the moment as well. Based on this output, the normal force ranged between 11.0 and 14.6 MN/m (deviation: 1.8 MN/m) and the moment between 1905 and 1935 kNm/m (deviation: 15 kNm/m). This knowledge justified the results in table K.1.

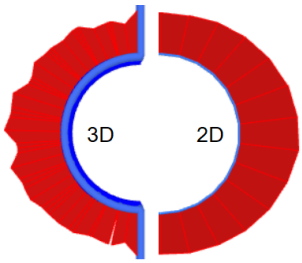


Figure K.4: Transversal normal force distribution along the ring in the middle of the fault zone for $E_{fault}$ = 150 MN/m$^2$

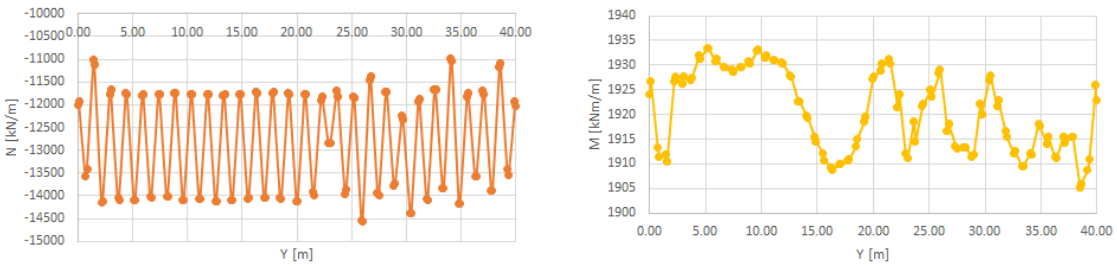


(a) (b)

Figure K.5: Longitudinal distribution of the maximal normal force (a) and the bending moment (b) for $E_{fault}$ = 150 MN/m$^2$

Then the 3D models were set up, where the ground properties were lower bound values as presented in table 4.1 in section 4.2.4 (except for the $k_0$ in the fault zone which was 0.5). The lining was modelled as a monolith structure, without stiffness reduction ($\xi_x = \xi_y = 1.0$), nor contraction ($C_{ref} = 0\%$) or reduction of the interface stiffness and strength ($R_{inter} = 1.0$). In tables K.2 and K.3 these 3D results were compared to results of 2D models, for a fault zone width ($L_2$) of respectively 80 m and 40 m.

Comparable to what was observed for the validation of the homogeneous fault zone model, without longitudinal stiffness effects of the adjacent rock, the displacements of cross sections A-A* and C-C* from the 3D models were almost identical to the 2D models. However, the forces and especially the maximal normal forces deviated significantly (up to 2.4 MN/m for $L_2$ = 80 m in cross section A-A*).

The results in cross section B-B* were the most significant. Not only did it show less vertical settlement which was expected due to the resistance from the adjacent rock mass (which acted as a sort of fixation at the sides of the lining beam), but also the vertical and horizontal ovalization and moment was reduced compared to 2D. This is typically the result of the redistribution of stress in the fault zone due to the much stiffer adjacent rock mass. On top of this, the case of $L_2$ = 80 m showed larger displacements and moment because the stiffness effect of the adjacent rock mass was less tangible in the middle of the fault zone compared to $L_2$ = 40 m. Exclusively, an increase of normal forces in the fault zone was observed for $L_2$ = 80 m, which was unrealistic and should actually be lower than the 2D case. This was again proof of the inaccuracy in the resulting normal forces.

| *Cross section* | A-A* | | B-B* | | C-C* | |
|---|---|---|---|---|---|---|
| $L_2 = 80m$ | 2D | 3D | 2D | 3D | 2D | 3D |
| $u_{y,top}$ $[m]$ | -0.08 | -0.07 | -0.43 | -0.25 | -0.01 | -0.01 |
| $u_{y,invert}$ $[m]$ | 0.01 | 0.00 | -0.19 | -0.08 | 0.00 | 0.00 |
| $u_{y,oval}$ $[m]$ | 0.04 | 0.04 | 0.12 | 0.09 | 0.01 | 0.01 |
| $\delta_y$ $[m]$ | -0.04 | -0.04 | -0.31 | -0.16 | -0.01 | -0.01 |
| $u_x$ $[m]$ | 0.03 | 0.03 | 0.11 | 0.08 | 0.00 | 0.00 |
| $N$ $[kN/m]$ | 22170 | 19790 | 19130 | 23340 | 13500 | 11460 |
| $M$ $[kNm/m]$ | 1058 | 1008 | 3028 | 2438 | 129 | 115 |

Table K.2: Calculated maximal lining displacements and forces in all cross sections for resp. 3D and 2D, as presented in section 5.1.2, for $E_{fault}$ = 73 MN/m$^2$ and $L_2$ = 80m

| *Cross section* | A-A* | | B-B* | | C-C* | |
|---|---|---|---|---|---|---|
| $L_2 = 40m$ | 2D | 3D | 2D | 3D | 2D | 3D |
| $u_{y,top}$ $[m]$ | -0.08 | -0.07 | -0.43 | -0.13 | -0.01 | -0.01 |
| $u_{y,invert}$ $[m]$ | 0.01 | 0.00 | -0.19 | -0.02 | 0.00 | 0.00 |
| $u_{y,oval}$ $[m]$ | 0.04 | 0.04 | 0.12 | 0.08 | 0.01 | 0.01 |
| $\delta_y$ $[m]$ | -0.04 | -0.03 | -0.31 | -0.06 | -0.01 | -0.01 |
| $u_x$ $[m]$ | 0.03 | 0.03 | 0.11 | 0.07 | 0.00 | 0.00 |
| $N$ $[kN/m]$ | 22170 | 20570 | 19130 | 16190 | 13500 | 11460 |
| $M$ $[kNm/m]$ | 1058 | 977 | 3028 | 2229 | 129 | 115 |

Table K.3: Calculated maximal lining displacements and forces in all cross sections for resp. 3D and 2D, as presented in section 5.1.2, for $E_{fault}$ = 73 MN/m$^2$ and $L_2$ = 40 m

# L

# Plaxis 3D calibration

To find a calibrated 3D model that fits the measured displacements of the ring from the Middle-East case, several model conditions were analyzed. It started with the analysis of different fault zone widths ($L_2$). The longitudinal arching effect in the ground due to settlement from groundwater lowering is shown in figure L.1. All the ground properties were lower bound values and the tunnel excavation was not considered, to understand the ground behaviour prior to looking at the lining behaviour.

Now, the effect of different fault widths and the comparison between lower and upper bound properties of the adjacent rock mass on the tunnel behaviour was analyzed. The longitudinal displacements of the center of the ring over the relevant part of the tunnel are shown in figures L.2 to L.4. In this analysis the fault zone material was kept constant at the lower bound properties (except for a $k_0$ of 0.5). The lining was modelled as a monolith structure ($\xi_x$=$\xi_y$ = 1.0), with proper backfilling ($R_{inter}$ = 1.0 and $C_{ref}$ = 0 %) as the impact of these features was already analyzed in 2D.

As the fault width in the Middle-East case was mapped and assumed to be no more than 40 m, the effect of a global lining stiffness reduction in the longitudinal direction ($\xi_y$ = 0.1) was analyzed. The plots of the longitudinal vertical displacements are shown in figures L.5.

As the effect of stiffnesses of the lining was analyzed, the other parameter that affected the calculated results significantly was the fault stiffness E (which was concluded from the 2D sensitivity analysis) and was studied here. The fault stiffness was reduced to a value which was representative for a soft clay and was equal to E = 10 MN/m$^2$ (Palmstrom and Stille, 2014). The results of the calculated ovalization and settlement for different fault widths are shown in figure L.6.

The impact of an inclined and non-perpendicular fault was analyzed. It was chosen to only look at the extreme cases, where the maximal inclination was $\beta$ = 30° and the fault course $\alpha$ = 60° (illustrated in figures L.7. The ground properties were lower bound for the rock as well as the fault, where the fault stiffness was 73 MN/m$^2$ and a width of $L_2$ = 40 m. In addition to the effect on horizontal displacements for an $\alpha$ = 60° and E = 10 MN/m$^2$ is presented in figure L.9. This plot shows the horizontal displacements at the center line of the tunnel at z = 455 m.

Finally, the calculated longitudinal force distribution of transversal moments ($M_{22}$) and longitudinal normal forces ($N_1$) is presented and discussed in figures L.10 to L.12. In these analyses, the fault width ($L_2$) and stiffness (E) was varied between respectively 80 to 10 m and 73 to 10 MN/m$^2$.

Analyzing the ground displacement due to ground water lowering, without considering the construction of the tunnel, led to an interesting observation. Reduction of the fault width ($L_2$), showed negligible increase of displacement in the fault zone at $L_2$ = 10 m. This led to the conclusion that a relation was found between fault width and the ratio between fault and rock stiffness for which the softer fault material did not result in increased displacements. This knowledge could help preventing the need for complex 3D lining analyses. Using this simple 2D ground model, could predict the impact of the fault zone on the global ground mass behaviour. If no increased displacements were found in the fault zone, the lining could be designed based on the adjacent rock material. As the the rock was stiffer than the fault zone material, the active lining forces would be lower in the rock and therefore the needed lining dimensions could be optimized.

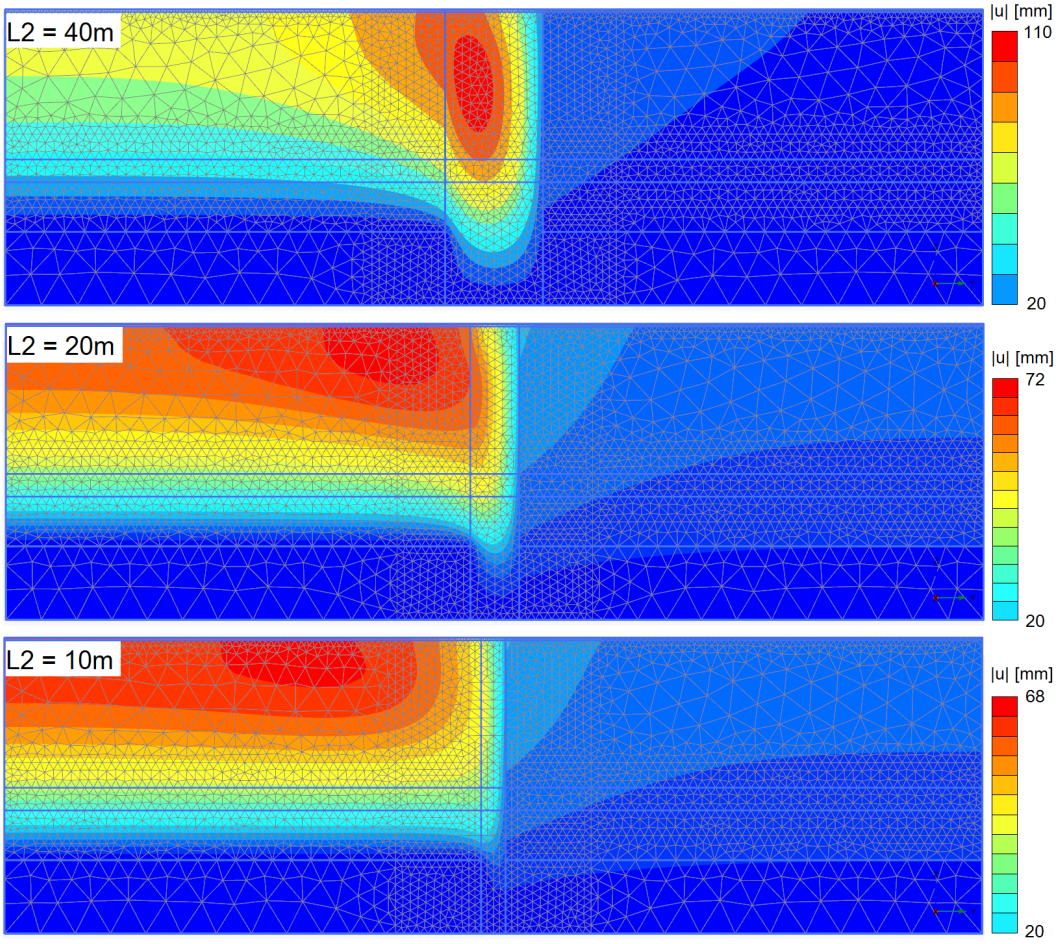


Figure L.1: Ground displacements for lower bound properties after lowering of the groundwater level in the longitudinal direction

In figures L.2 from the top down: the tunnel top displacement, invert displacement and vertical ovalization are shown. The most important conclusion made based on these figures, was that the reduction of fault width influences the displacement of the tunnel as a whole, but the ovalization stayed almost the same. The notable feature observed in the invert displacement was that for $L_2$ = 80 m, there was a upward jump directly after the transition from the rock to the fault zone. This feature was justified by the abrupt increase in ovalization of the lining, while the settlement of the lining increased less abrupt. For $L_2$ = 40 m, no settlement was observed (invert displacement is positive/upward), just ovalization.

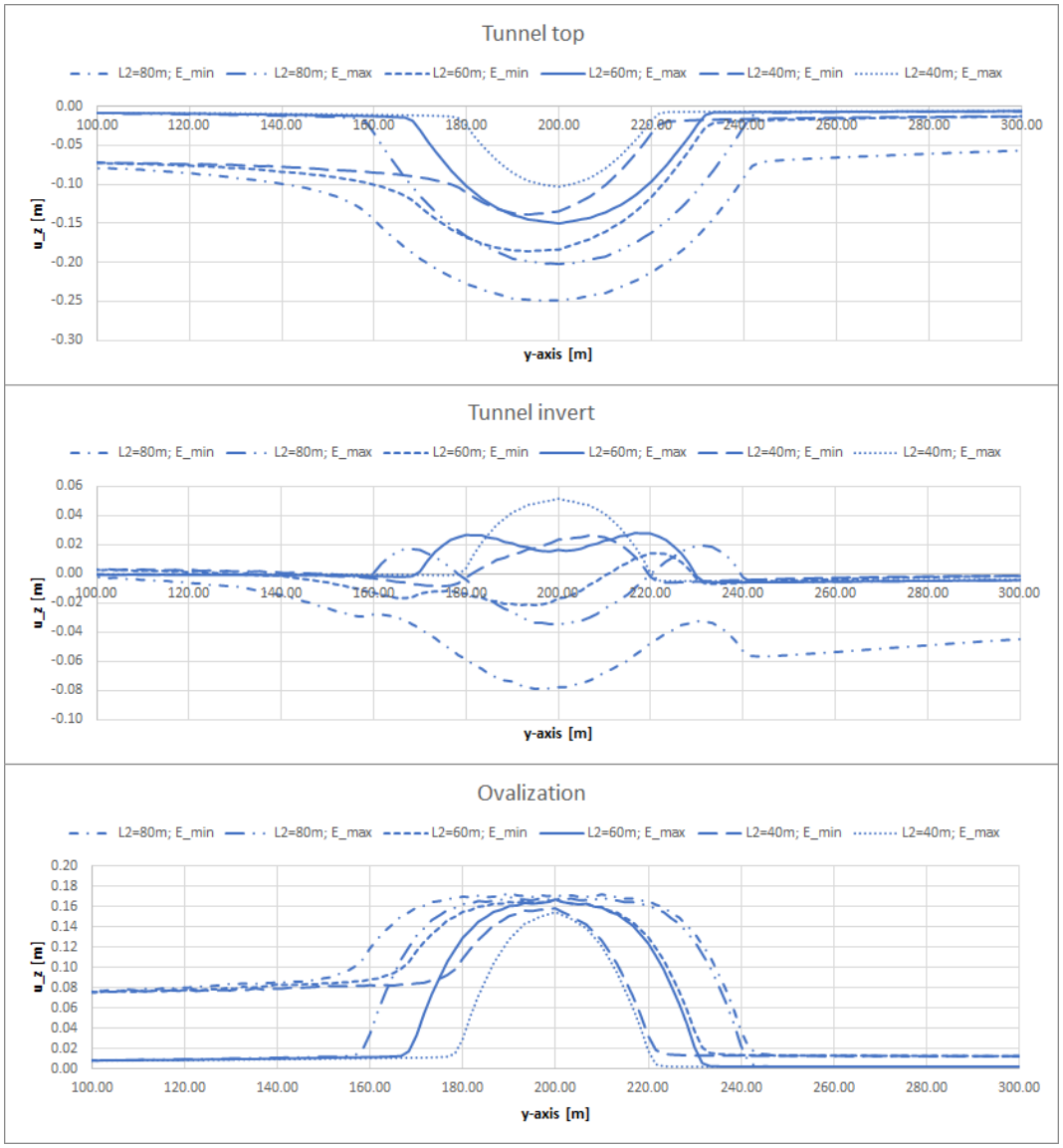


Figure L.2: Comparison of different fault width and effect of adjacent rock stiffness (lower and upper bound properties) on the tunnel displacements for $E_{fault}$ = 73 MN/m$^2$

Figure L.3 indicated the comparison between calculated lining ovalization at different $L_2$, with a constant ground and lining stiffness, and measured ring displacements. It was noticed that measured ovalization had an abrupt increase of 0.06 à 0.12 m over a short distance of 10 m compared to the calculated increase of the ovalization. From these plots it was clear that a fault zone width of 20 m would not result in an ovalization that corresponded to the measured ovalization. Additionally, it was observed that for a lower bound rock and fault stiffness, the displacement for $L_2$ = 10 m transited smoothly without a local increase from marl to dolomite. This feature was already predicted with the longitudinal ground model in the previous section (figure L.1).

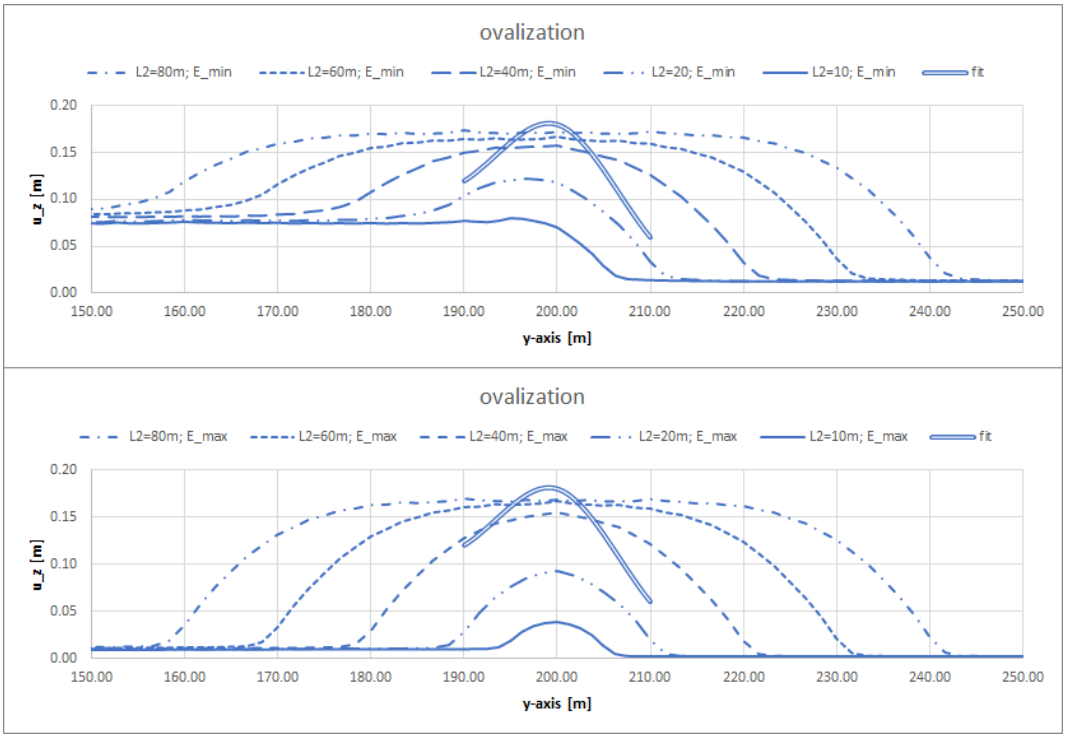


Figure L.3: Comparison of different fault width and effect of adjacent rock stiffness (lower and upper bound properties) on the tunnel ovalization for $E_{fault}$ = 73 MN/m$^2$

The settlement of the tunnel showed (figure L.4) results comparable to the ovalization presented in the figure above. In short, the settlement increases was very abrupt and the amount of settlement was only reached for $L_2$ = 80 m. However, such fault width was considered as unrealistic.

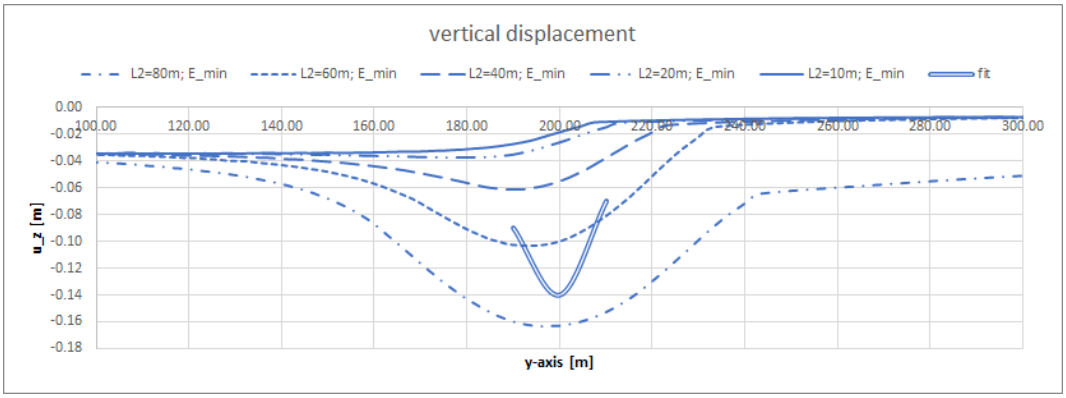


Figure L.4: Comparison of different fault width on the tunnel settlement for $E_{fault}$ = 73 MN/m$^2$

The reduced longitudinal lining stiffness ($\xi_y < 1.0$) resulted in smaller displacements than without reduction, in terms of ovalization. On the other hand, the settlement of the lining was larger. However, the impact of such significant stiffness reduction did not show a large impact on the result and it was decided to proceed the analysis with $\xi_y = 1.0$. As the reduction factor became smaller, difficulties to obtain results from the numerical model were observed. This was due to the exceedingly large differential deformations, which could not be handled by the finite elements.

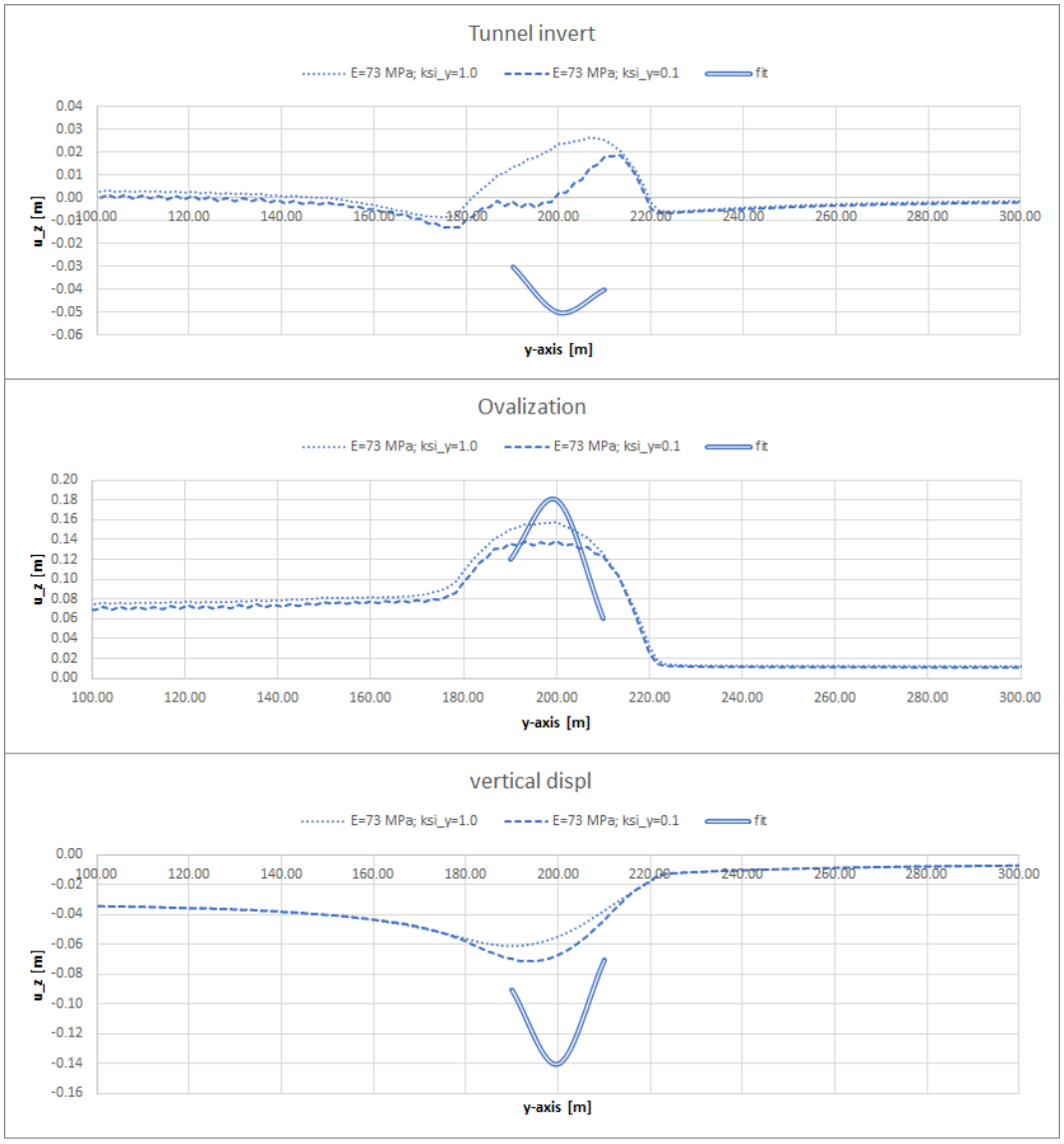


Figure L.5: Comparison longitudinal lining stiffness reduction on the tunnel displacements for $L_2$ = 40 m

The effect of upper and lower bound stiffness of the adjacent rock and the reduction of lining stiffness had been analyzed. The next analysis related to the case in which the fault gauge material was softer than initially approximated and was equal to a soft clay with E = 10 MN/m$^2$. Results in which such material was applied, showed that for $L_2 \approx 20$ m the calculated ovalization fitted the measured ovalization (figure L.6). In this case, even the distribution towards the adjacent rock seemed to fit, with a more abrupt increase at the dolomite-side (between y = 200 and 210 m). However, the settlements were not calibrated in this manor because the maximal calculated settlement was less than measured and the increase was very abrupt.

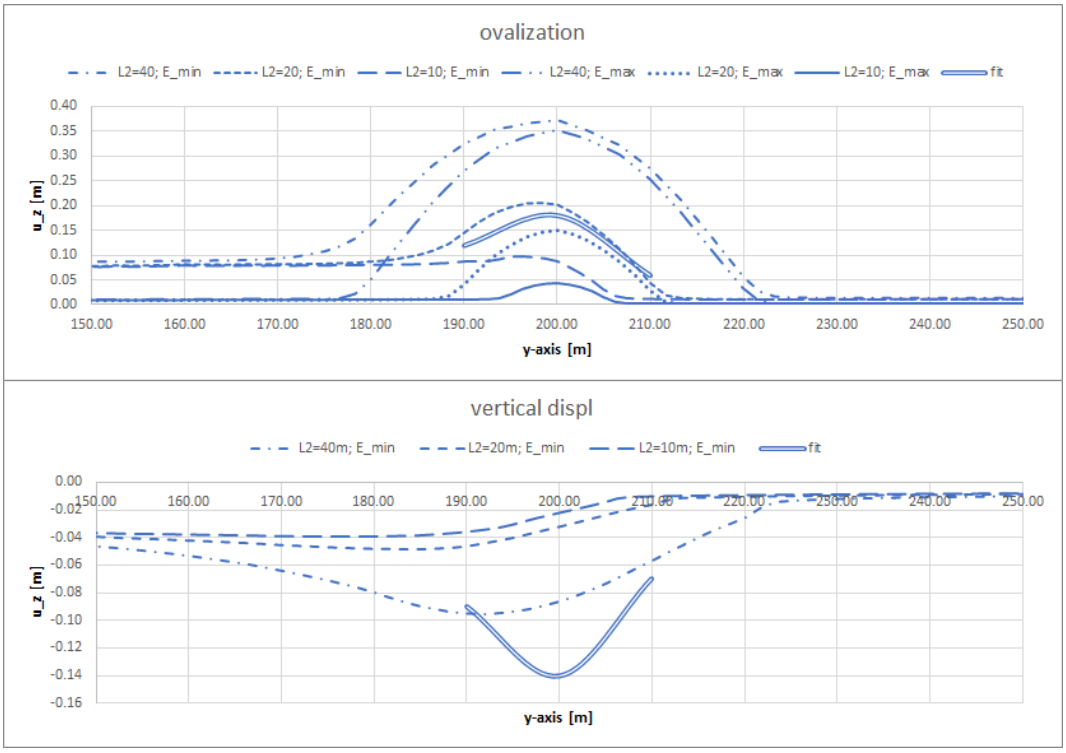


Figure L.6: Ovalization and settlement of the lining in case of a fault material with E = 10 MN/m$^2$

The circumstances in which the fault was inclined showed a decreased displacement of the tunnel top and an increased displacement of the invert, while the vertical ovalization was the same as the perpendicular fault. The diagonal fault resulted in less displacements, for the top, the invert as well as the ovalization. In other words, for a realistic case with a non-perpendicular and inclined fault, the calculated displacements were lower than a perpendicular fault. This meant it was even more difficult to find the calibrated model.

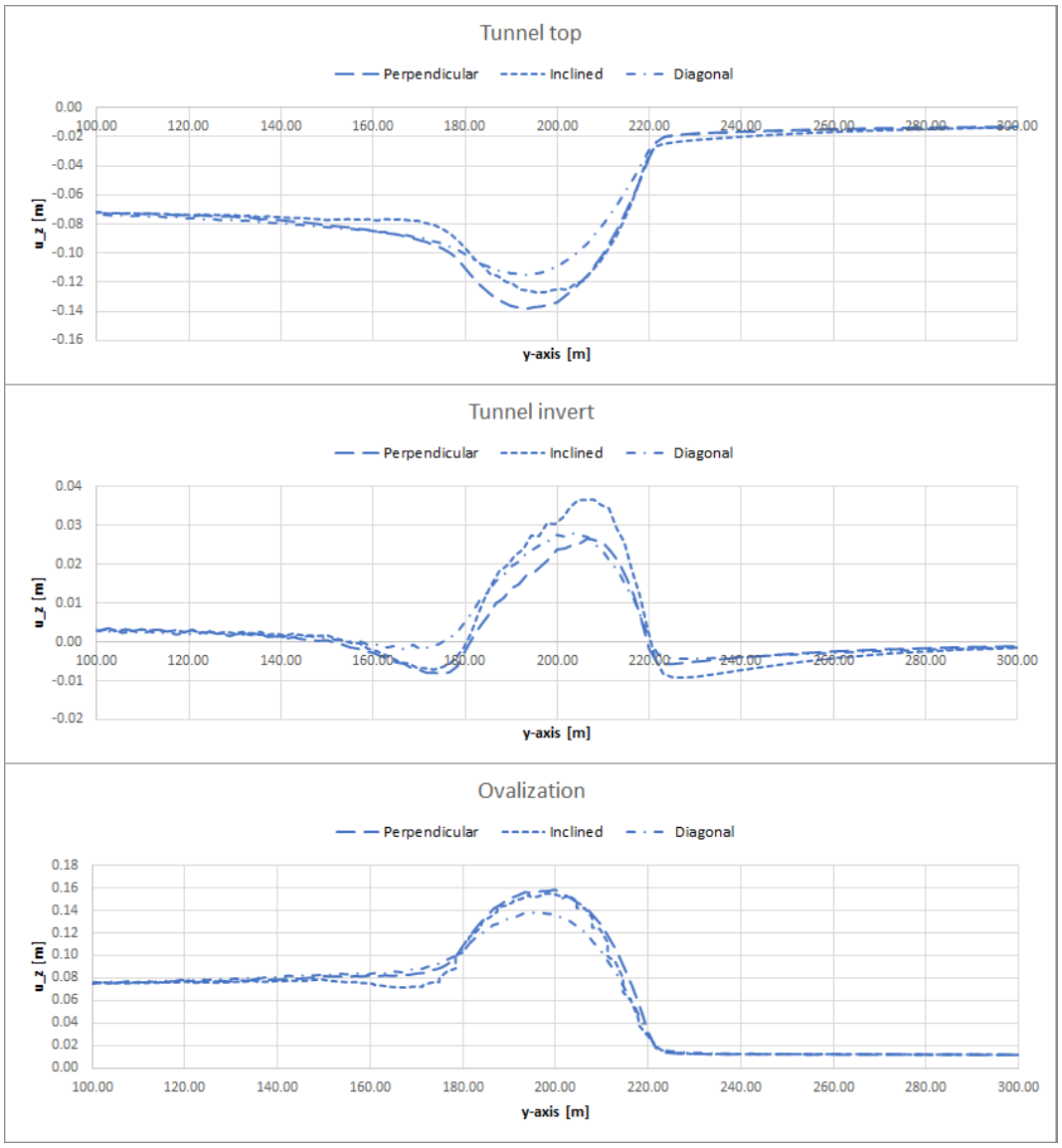


Figure L.7: Calculated tunnel displacements for an inclined and non-perpendicular fault, in both cases $L_2$ = 40 m

The calculated lining settlement for an inclined and non-perpendicular fault resulted in the same image as with the other tunnel deformations. It was observed that the case of an inclined fault resulted in a settlement distribution containing a significant discrepancy. The settlement of a perpendicular fault compared to a diagonal fault showed a reduction of approximately 15%.

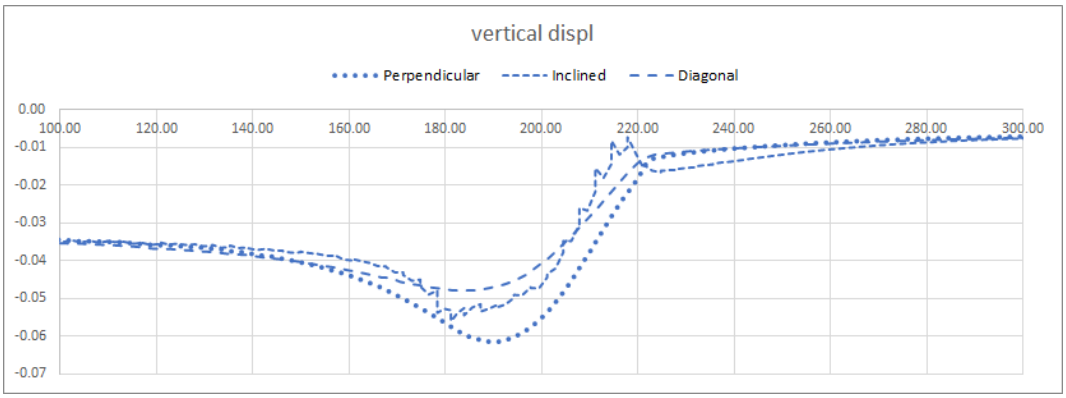


Figure L.8: Calculated tunnel settlement for an inclined and non-perpendicular fault, in both cases $L_2$ = 40 m

The largest difference between the perpendicular, the diagonal and the perpendicular fault, was the horizontal displacement of the lining as shown in figure L.9. The lining showed a horizontal shift, especially towards the positive x-direction and slightly in the diagonal course. However, the calculated horizontal ovalization was much more than the measured ovalization (0.15 m) in the center of the fault zone.

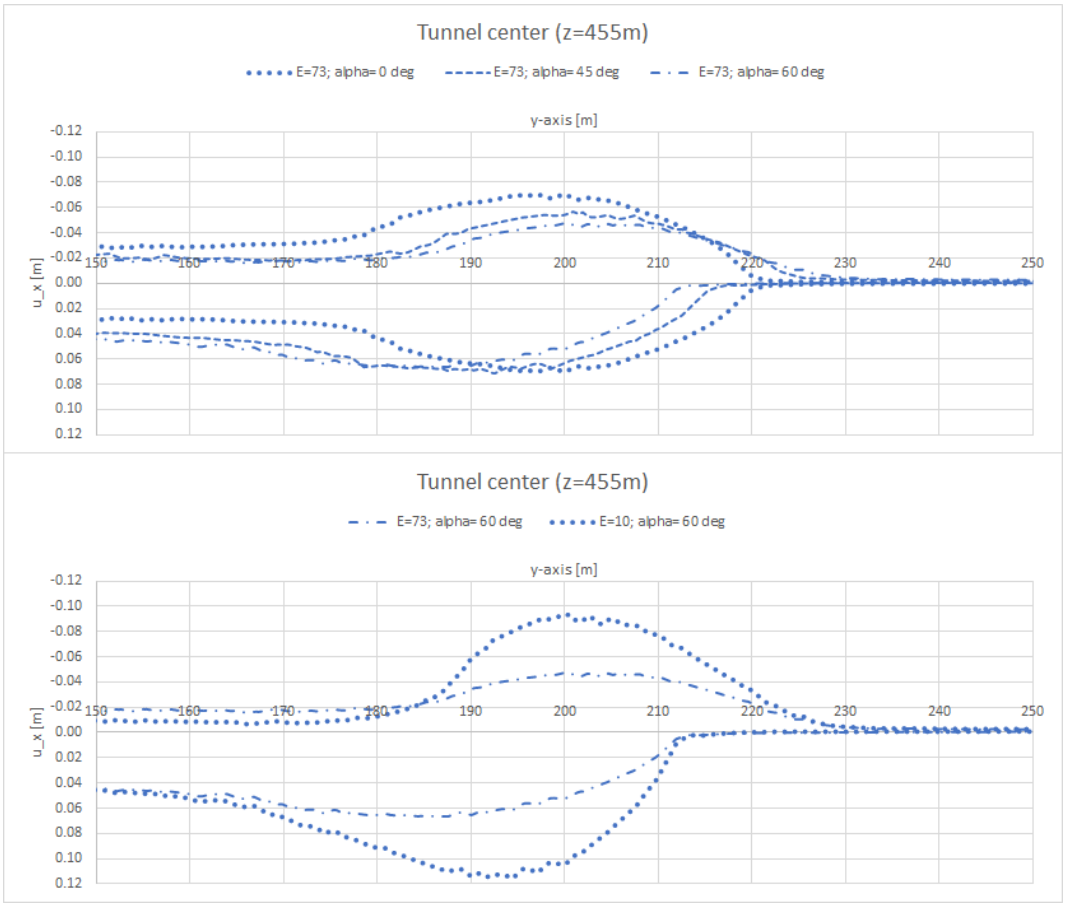


Figure L.9: Comparison of different fault course and inclination angle (resp. $\beta$ and $\alpha$) on the tunnel displacements for $L_2$ = 40 m

The transversal moment ($M_{22}$) distribution along the tunnel alignment in figures L.10 and L.12 for resp. fault stiffness E = 73 MN/m$^2$ and 10 MN/m$^2$ showed a comparable distribution to the vertical ovalization in the previous figures. It was noticed that in the case that no longitudinal arching effect was observed, which was for a large $L_2$, the maximal calculated moment was equal to that of a 2D calculation. Therefore, the upper bound limits of moments were not exceeded in a 3D analyses and could be approximated with a 2D model.

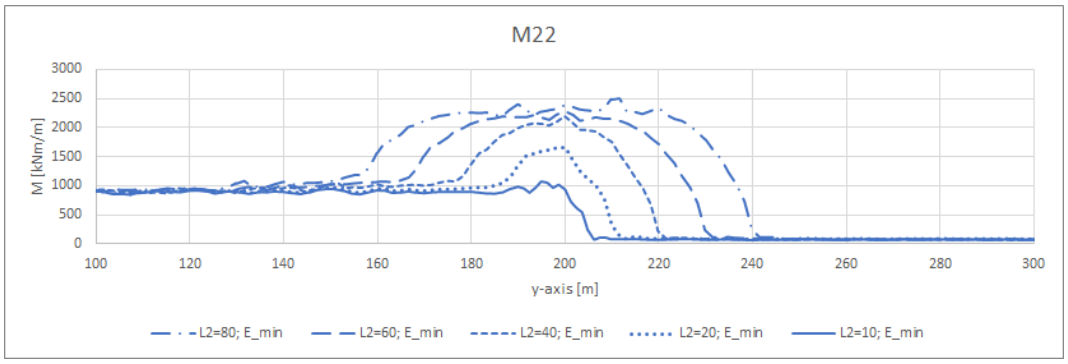


Figure L.10: Maximal transversal moment ($M_{22}$) distribution along the tunnel alignment for lower bound properties

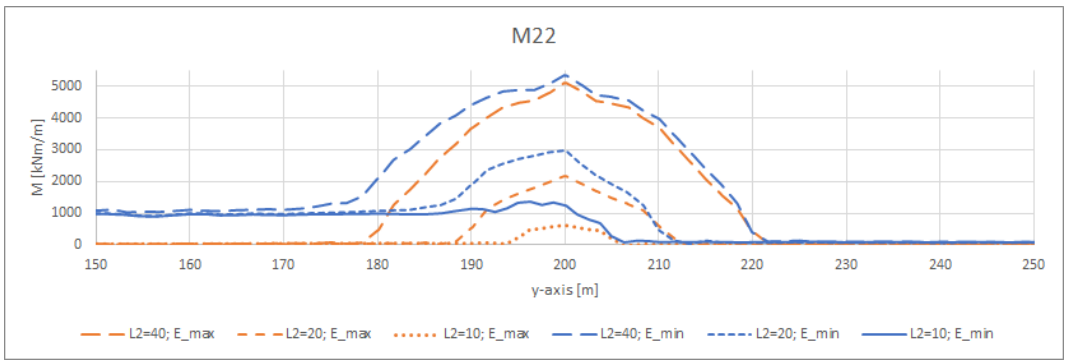


Figure L.11: Maximal transversal moment ($M_{22}$) distribution along the tunnel alignment for lower and upper bound stiffness of adjacent rock and fault stiffness E = 10 MN/m$^2$

The longitudinal normal force shows peaks at the transition from adjacent rock to the fault zone in figure L.12. As the normal force is the first derivative of the moments, the peak force is maximal at the location were the slope of the moment distribution is maximal, which explains this feature.

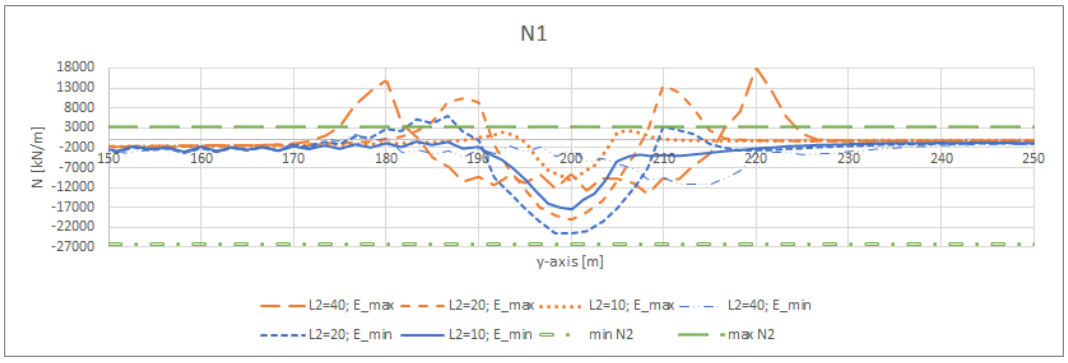


Figure L.12: Maximal longitudinal normal force ($N_1$) distribution along the tunnel alignment for lower and upper bound stiffness of adjacent rock and fault stiffness E = 10 MN/m$^2$